Towards an anthropogenic nitrogen cycle based on nitrite

Giacomo Cioncoloni

Submitted in fulfilment of the requirements for the

Degree of Doctor of Philosophy

School of Chemistry

College of Science and Engineering

University of Glasgow

August, 2018

ABSTRACT

The overall goal of this thesis was to investigate the feasibility of a new route to anthropogenic nitrogen fixation based on the oxidation of nitrogen (to give primarily nitrite), and then electrocatalytic conversion of nitrite to other N-containing species of interest, such as nitrate and nitric oxide (NO). In pursuit of this goal, the synthesis of metal-ligand coordination complexes that could act as electrocatalysts for the oxidation of nitrite to nitrate was attempted, as was the synthesis of metal-ligand coordination complexes that could act as electrocatalysts for the reduction of nitrite to NO. As a corollary to this, routes for the initial fixation reaction were also investigated, of which the ultrasonic generation of nitrite from aerated aqueous solutions was found to be the most promising.

The work detailed in this thesis is organized in the following manner: In **Chapter 1** we discuss coordination complexes that mimic the enzymes promoting the redox reactions of the nitrogen cycle involving nitrite as a substrate or product. During this introduction we will also give an overview of topics that are relevant to the following chapters, such as proton-coupled-electron transfer and basic kinetic treatment of catalytic reactions.

Chapter 2 is a description of the different techniques used throughout this thesis. Once having set the bases, we shall start with the actual research, which corresponds to **Chapters 3** to **6**.

Chapter 3 deals with the synthesis, characterization and catalytic properties of a copper coordination compound mimicking the active site of the copper nitrite reductase (CuNiR) class of enzymes. This chapter includes a detailed study of the kinetics and electrocatalytic properties of this complex towards the mono-electronic reduction of nitrite to nitric oxide.

Chapters 4 and **5** deal with the unusual structures and spectroscopic properties of a number of new cobalt complexes that we isolated whilst trying to develop Mo(bis-dithiolene) coordination complexes that might act as analogues of the molybdenum nitrite oxidoreductase (MoNiOR), which oxidises nitrite to nitrate in nature. Our original Mo-containing targets proved impossible to obtain and are not discussed in this thesis. However, we found that cobalt readily makes coordination complexes with these bis-dithiolene ligands, which allowed us to isolate the compounds we present in **Chapters 4** and **5.** Hence in **Chapter 4** we show the synthesis and the solvatochromic properties of mixed-ligand mono-nuclear Co-diimine o-catecholato complexes and compare these complexes with the analogous compounds prepared with o-benzenedithiolato ligands. **Chapter 5** then discusses the synthesis and redox properties of a mixed-ligand di-cobalt

coordination complex in which the two cobalt centres have (unprecedented) inequivalent metal coordination environments.

Finally, in **Chapter 6** we describe a much-underexplored way to fix nitrogen based on a sonochemical reaction. After a brief introduction we describe the optimisation of the procedure and comparisons with previous reports.

Table of contents

List of conferences attended and posters/talks presented

- **Inorganic Colloqua Seminars** School of Chemistry, University of Glasgow

Oral presentations (2015-2017)

a) Sustainable ways to NO_2^- Production, May 2015

b) Photoinduced way to NO_2^- Production, February 2016

c) The electronic and solvatochromic properties of $[Co(L)(Bypiridine)_2]^+$ species: a combined study, November 2016

d) Potentially Renewable Routes to Nitrogen Fixation, October 2017

- RSC Scotland and North of England Regional Electrochemistry Symposium, April 20th 2016 University of Glasgow

- One-day Symposium on Nanoscience & Materials Chemistry
  13th June 2016 University of Glasgow

- UK-India Symposium on Functional Materials
  21 June 2016 University of Edinburgh
  Presenting a poster titled: "The facile synthesis of [Co(bipyridine)2(X)]+ species (X=catecholate or benzenedithiolate) and their electronic and solvatochromic properties"

- Universities of Scotland Inorganic Chemistry Conference
  29-30 August 2017
  Presenting a Talk with the title: "A SERIES OF NEW Co-DIIMINE o-CATECHOLATO (& o-BENZENEDITHIOLATO) COMPLEXES WITH UNUSUAL STRUCTURES ANDSPECTROSCOPIC PROPERTIES"

- RSC Scotland and North of England Regional Electrochemistry Symposium, April 25th 2018 University of Aberdeen

List of publications

- Versatile control of the submolecular Motion of Di(Acilamino)piridine-based [2]Rotaxanes. Martinez-Cuezva, A. Pastor, **G.Cioncoloni**, R.-A. Orenes, M. Alajarin, M. D. Symes and J. Berna. *Chem. Sci.* **2015**, *6*, 3087-3094
(paper not presented in this thesis)

- The Electronic and Solvatochromic Properties of [Co(L)(bipyridine)2]+ (L = *o*catecholato, *o*-benzenedithiolato) Species: a Combined Experimental and Computational Study. **G. Cioncoloni**, H. M. Senn, S. Sproules, C. Wilson and M. D. Symes. *Dalton Trans.* **2016**, *45*, 15575-15585

- Unprecedented Inequivalent Metal Coordination Environments in a Mixed-Ligand Dicobalt Complex. **G. Cioncoloni**, S. Sproules, C. Wilson and M. D. Symes. *Eur. J. Inorg. Chem.* **2017**, 3707–3713

- Ligand-directed synthesis of {MnIII5} twisted bow-ties.
M. J. Heras Ojea, M. A. Hay, **G. Cioncoloni**, G. A. Craig, C. Wilson, T. Shiga, H. Oshio, M. D. Symes and M. Murrie *Dalton Trans.* **2017**, *46*, 11201–11207
(paper not presented in this thesis)

- Proton-Coupled-Electron Transfer Enhances the Electrocatalytic Reduction of Nitrite to NO. **Giacomo Cioncoloni**, Isolda Roger, Stephen Sproules, Paul S. Wheatley, Claire Wilson, Russell E. Morris, & Mark D. Symes *ACS Catal.* **2018**, 8, 5070−5084

Acknowledgements

I am not really good in this part since I cannot find the right words to say what I would like to say but I try. Firstly I would like to thank Dr. Mark Symes first of all for choosing me as PhD student, for all the new thigs he teach to me and (most important) for the patience he had with me.

Big thanks to the fantastic actual and past and present members of the Symes group: Isolda, a great source of help and good advises when I just started my PhD and I had to settle here (and also about synthesis when I restart to do it). Mike, I'll miss the coffee you was making in the office every day and Alex (I do not know how you can have fun doing skydiving)

A would like to thank Ross, Francois, and Isabel because they help me to settle in the new environment and also because I spent really good time with them both in the lab and outside the lab. I would also like to thank Simon and Davide, good friends also and very pleasant people to spend time with.

A special thanks to JiaJia and Niall for his availability and for helping me with potentiostats and other instruments I have to use in the lab.

I would also like to thank my mum and my father for the help and the support they always gave me.

Author’s declaration

I declare that, except where explicit reference is made to the contribution of others, this dissertation is the result of my own work and has not been submitted for any other degree at the University of Glasgow or any other institution.

Printed Name: GIACOMO CIONCOLONI

Signature:

List of abbreviatioins:

H-B: Haber-Bosch Process

PCET: Proton Coupled Electron Transfer

CPET: Concerted Proton Electron Transfer

PET: Proton Electron Transfer

EPT: Electron Proton Transfer

DNRA: Dissimilatory Nitrate reduction to Ammonium

CSNiR: sirohaem-containing Nitrite reductase

HAOR: and hydroxylamine oxidoreductase

MoNiOR: Molybdenum Nitrate Oxido-Reductase

CuNiR: Copper Nitrite Reductase

NO: Nitric Oxide

NO_2: Nitrite

TPP: Tetraphenylporphrine

TIC: hydrotris(3,5-dimethylpyrazolyl)methane

TPM: tris(3,5-dimethylpyrazolyl)methane

TREN: Tris(2-aminoethyl)amine

LSV: Linear Sweep Voltammetry

CV: Cyclic Voltammetry

C.E: Counter Electrode

W.E: Working Electrode

R.E: Reference Electrode

NHE: Normal Hydrogen Electrode

UV: Ultraviolet

IR: Infrared

UV-Vis: Ultraviolet-Visible

HOMO: Highest Occupied Molecular Orbital

LUMO: Lower Unoccupied Molecular Orbital

EPR: Electronic Paramagnetic Resonance

NMR: Nuclear Magnetic Resonance

DFT: Density functional theory

TD-DFT: Time-dependent density functional theory

ESBO: edge-sharing bi-octahedron

Bipy: Bypyridine

Me_2Bipy: 5,5'-dimethyl-2,2'-BiPyridine

Bdt: 1,2-Benzenedithiol

$TBAPF_6$: Tetrabutylammonium nexafluorophosphate

$TBANO_2$: Tetrabutylammonium nitrite

MeOH: Methanol

MeCN: Acetonitrile

DMSO: Dimethyl sulfoxide

DCM: Dichloromethane

MeOD: Deuterated methanol

Et_2O: Diethyl ether

T: Temperature

R: Resistance

E: Potential

C: Charge

1: meso-tetrakis(4-N-methylpyridiniumyl)porphyrin ($[Fe^{(III)}(TMPyP)]^{5+}$)

2: $[Et_4N][Mo^{IV}(SPh)(PPh_3)(mnt)_2$

3: $(TIC)Cu(NO_2)$

4: $(TPM)Cu(NO_2)$

5: $[Cu(NO_2)$-(TREN)][PF_6]

6: $[Cu(NO_2)$-(Tris-[(benzimidazol-2-yl)methyl]amine)][PF_6]

7: $[Cu(ONO)_2$(Tris-(2-pyridyl)phosphine)]

8: Cu(tris[(2-pyridyl)-methyl]amine)]$^+$

9: (Cu[6-methyl-tris(2-pyridyl)methoxide]$(NO_2)_2$

10: Cu(bis(6-methyl-2-pyridylmethyl)amine-ethyl-sulphide)

11: $[Cu^{II}(6\text{-}eTMPA)(H_2O)]^{2+}$

12: $[N(afa^{Cy})_3Fe(O)][OTf)$

13: $CuF(H_3thpa)$

14: $[Fe(H^{DEA}PDI)(CO)_2]^+$

15: ((6-methoxycarbonyl-2-pyridyl)methyl)bis(2-pyridylmethyl)amine

16: ((6-carboxyl-2-pyridyl)methyl)bis(2-pyridylmethyl)amine

17: $[Cu^{II}(\mathbf{15})]^{2+}(ClO_4)_2$

18: $[Cu^{II}(\mathbf{16})]^{+}(ClO_4)$

19: $[Co^{III}$(o-catecholate)(2,2'-bipyridine$)_2]^{+}$

20: $[Co^{III}$(o-catecholate)(5,5′-dimethyl-2,2′-bipyridine$)_2]^{+}$

21: $[Co^{III}$(o-benezenedithiolate)(5,5′-dimethyl-2,2′-bipyridine$)_2]^{+}$

22: $[(bpy)_2Ni(bdtO_4)Ni(bdt)]$

23: $Zn_3(tdt)_3(bpy)_2$

24: $[Co^{III}{}_2(bdt)_2(Me_2bpy)_3](NO_3)_2$, $[24](NO_3)_2$

Coordination complexes mimicking the active sites of enzymes which handle nitrite

Synopsis

The natural nitrogen cycle is fundamental for life and compounds like ammonia, nitrite, nitrate and nitric oxide are key components in a wide range of processes of fundamental importance for the environment and in biology. In this introductory chapter are briefly described the redox processes forming the nitrogen cycle and the classes of enzymes promoting them with particular attention to the processes involving nitrite as a substrate and product, and with particular attention to the structure of the CuNiR (as this relates specifically to a large part of the experimental work presented in this thesis). Since all these reactions involve the transfer of one or more electrons, electrochemical methods are of fundamental usefulness to investigate and describe the reaction kinetics and the methodology used is also briefly described. Moreover, also described is proton coupled electron transfer (PCET) which is of great importance since in all the described reactions hydrogen transfer is observed together with electron transfer. Finally are described a series of metal coordination complexes that mimic the active site of the enzymes promoting reactions involving nitrogen. Specifically described are: Fe-haem complexes mimicking Cytochrome C nitrite reductase that promotes the six-electron reduction of nitrite to ammonia, the Mo-bis dithiolene complexes that mimic the molybdenum nitrite oxidoreductase class of enzymes promoting two-electron reduction of nitrate to nitrite and finally the monoelectronic reduction of nitrite to nitric oxide promoted by Cu-tripodal coordination compound mimicking the active site of the copper nitrite reductase (CuNiR) class of enzymes.

1.1 Introduction

1.1.1 Enzymatic catalysis of the biological nitrogen cycle

Nitrogen is the most abundant element in the earth's atmosphere and although one of the first names given to this element means literally “no life” (from the Greek άζωτικός or azote) it is indispensable in all living organisms since it is one of the essential constituents of the most important biological molecules like amino-acids, nucleobases and Adenosine Triphosphate (ATP). Moreover, nitrogen is the key component of several inorganic compounds like Ammonia, Nitrate, Nitrite, and Nitric Oxide, simple small inorganic molecules fundamental for life, the environment and industry since they can act as building blocks to create more complex structures or be part of the life cycle in various organisms.

Elemental nitrogen is present in nature as dinitrogen (N_2), a diatomic molecule that under standard conditions appears as a colourless and odourless gas that is not very soluble in water. The very high strength of the triple bond between the two nitrogen atoms dominates N_2 chemistry since this causes difficulty for both organisms and industry in converting N_2 into useful compounds. Another exploitable reservoir of nitrogen present in nature is nitrate, mainly found in salts such as KNO_3 and $NaNO_3$ but also as $Ca(NO_3)_2$ and $Mg(NO_3)_2$. The nitrate reservoirs originate from organic materials (guano) and are located in arid regions like deserts since these salts are soluble in water.

Ammonia, or ammonium salts depending on the pH, forms the other main important nitrogen reservoir present in nature and is the main source of nitrogen for living organisms since it is the only one which can be taken up by the majority of organisms. The natural series of processes whereby nitrogen species are transformed from one form to another is known as the Nitrogen Cycle.

Many of these reactions are promoted by microorganisms, either in their efforts to harvest energy or to accumulate nitrogen in a form needed for their growth. For example, the nitrogenous wastes in animal urine are broken down by nitrifying bacteria in the soil so that the nitrogen they contain can be reused. Atmospheric dinitrogen must be processed, or "fixed", into a form possible to be taken up by plants and the most of this fixation is done by microorganism known as diazotrophs. These are archea or bacteria, either free-living or living in symbiosis in the roots of some class of plants, like for example legumes.

N_2 enters the nitrogen cycle not only through the fixation of N_2 to ammonia carried out by microorganisms but also in the form of nitrogen oxides from physical events such as lightning strikes (totalling about the 20% of global nitrogen fixed). Nitrate can also come from mineral sources.

Several biological systems are then able to convert between the various oxidation states of nitrogen shown in **Figure 1.1** with high specificity using a handful of generic classes of enzymes, effectively allowing any oxidation state of nitrogen to be accessed. Where a single enzyme cannot carry out the desired transformation, sequences of enzymes can be used.

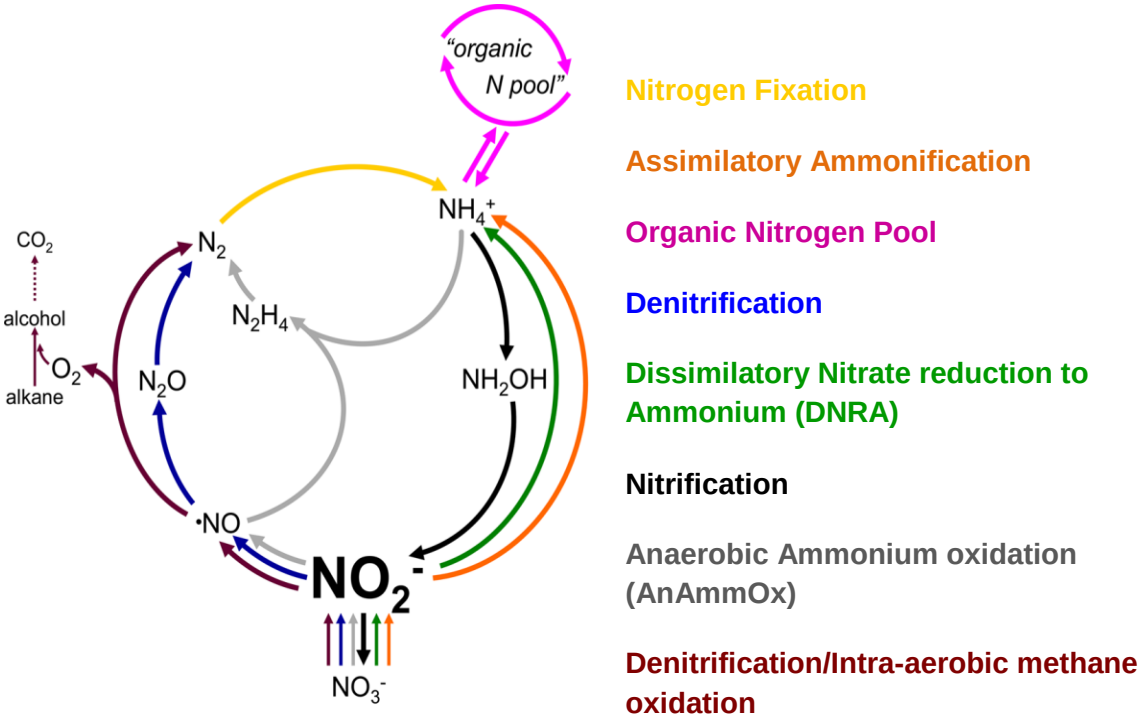

***Figure 1.1**: Scheme for the reactions of the Nitrogen Cycle. Adapted from Chem. Rev, **2014**, 114 (10), pp 5273 with permission of American Chemical Society.*

From **Figure 1.1** we can identify two assimilatory nitrogen pathways: assimilatory ammonification (orange arrow) and nitrogen fixation (yellow arrow), both giving the ammonium essential for biosynthetic purposes.

Ammonification is the direct reduction of N_2 to ammonium and is catalysed by Mo/Fe nitrogenases or by a vanadium nitrogenase [2-5] present in diazotrophs.

Nitrate assimilation is a two steps process where in the first step nitrate is reduced to nitrite by a Mo Nitrate Reductase (NaR)[6-17] then the following reduction to ammonium is promoted by the sirohaem-containing Nitrite reductase (CSNiR).[18-25]

In nature we can find two different kinds of assimilatory CSNiR: both hold the Fe/S sirohaem function but they use a different source of electron depending on whether they are in photosynthetic organisms or heterotrophs organisms. However it is necessary to remember that there are a lot of exceptions in this classification.[26-28]

Indeed in photosynthetic organisms, the source of electrons is photosynthetically reduced ferredoxin and the pyridine nucleotide pool in most of the heterotrophs. The biochemical nitrogen cycle continues with 4 main nitrogen dissimilatory pathways, where nitrogen species are used to derive energy as acceptors or donors of electrons. Nitrate is anaerobically reduced to N_2 via denitrification (blue arrow **Figure 1.1**) or to ammonium (DNRA, green arrow **Figure 1.1**)

Denitrification is found in a wide range of organisms[29-31] from archea to eubacteria and also in some eukaryotes such as fungi, protozoa and benthic Foraminifera and Gromiida.[32-43] It occurs in both autotrophic and heterotrophic organisms.

Denitrification encompasses nitrate reduction to N_2 in an anaerobic environment through four sequential steps involving three oxygen abstractions and one N-N bond formation. These steps are catalysed by metalloenzymes dependent on Mo, Fe and Cu centers.

$$NO_3^- \rightarrow NO_2^- \rightarrow {}^{\cdot}NO \rightarrow N_2O \rightarrow N_2 \qquad (1)$$

DNRA proceeds through a different mechanism since nitrite is reduced directly to ammonium, and is found in organisms living in anaerobic environments. The process is promoted by a multi-c-haem containing enzyme (CcNiR) and the electrons come from the anaerobic oxidation of organic carbon via the membrane quinone pool.[44] In the opposite direction, nitrifiers are organisms that exploit the oxidation of ammonium to nitrate in aerobic condition for the fixation of inorganic carbon.[45,46]

Nitrification is the process of ammonium oxidation to nitrate, a sort of short-circuit in the nitrogen cycle which allows it to bypass (hard to activate) dinitrogen. The ammonium oxidizing bacteria (e.g. Nitrosomonas) exploit ammonium oxidation mainly for respiration. In fact ammonium acts as an electron-donor being then oxidized to hydroxylamine first, then to nitrite. These two processes are respectively catalysed by Ammonium monooxygenase and hydroxylamine oxidoreductase (HAOR). [47-65]

The last part of the nitrification process is carried out by nitrite oxidising bacteria, responsible for the oxidation of nitrite to nitrate. The reaction is catalysed by an enzyme containing Mo (MoNiOR or molybdenum-containing nitriteoxydoreductase). This kind of

bacteria acts in a strictly aerobic environment and is recognised as the main source of nitrate in the cycle.

Indeed, ammonium can also be oxidized following a bio-exothermic pathway in anaerobic conditions. Ammonium is oxidized by nitric oxide to give hydrazine in a reaction promoted by the dihaem-c-containing hydrazine synthase. The hydrazine obtained is then oxidized to dinitrogen by octa-haem-c-containing hydrazine oxidoreductase.

The nitric oxide used in this process comes from nitrite reduction carried out by Cd1NiR one of the enzymes associated with the "classical" nitrification.[66-77]

From **Figure 1.1** we can note that nitrite is a key substrate in all the process described and the reactions involving this molecule as a substrate or product are summarised briefly in **Table 1.1**.

Reaction	Enzyme, Metal and ligands active site	E^{o} red/ox vs. NHE
$NO_3^- + 2e^- + 2H^+ \leftrightharpoons NO_2^- + H_2O$	Nitrate reductase, Mo, 2 dithiolenes per Mo	+0.84 V
$NO_2^- + 6e^- + 8H^+ \leftrightharpoons NH_4^+ + 2H_2O$	Cyt. c nitrite reductase, Fe, porphyrin	+0.90 V
$NO_2^- + 1e^- + 2H^+ \leftrightharpoons NO + H_2O$	Cu nitrite reductase, Cu, 3 histidines per Cu	+1.20 V
$2NO_2^- + 6e^- + 8H^+ \leftrightharpoons N_2 + 4H_2O$	Cyt. cd1 nitrite reductase, Fe, porphyrin	+1.52 V

Table 1.1: *Key biological nitrite conversion reactions and the classes of enzymes responsible*

The fabrication of small inorganic molecules mimicking the active site of an enzyme can be a way to handle nitrite in order to make a wide range of nitrogen-containing compounds by applying a potential, or exploiting chemicals that acts as oxidizing or reducing agents. Some relevant examples of these complexes are described in **Section 1.6**.

As shown in **Figure 1.2** nitrite occupies a central position in the processes mediated by the enzymes described in the previous section.[78]

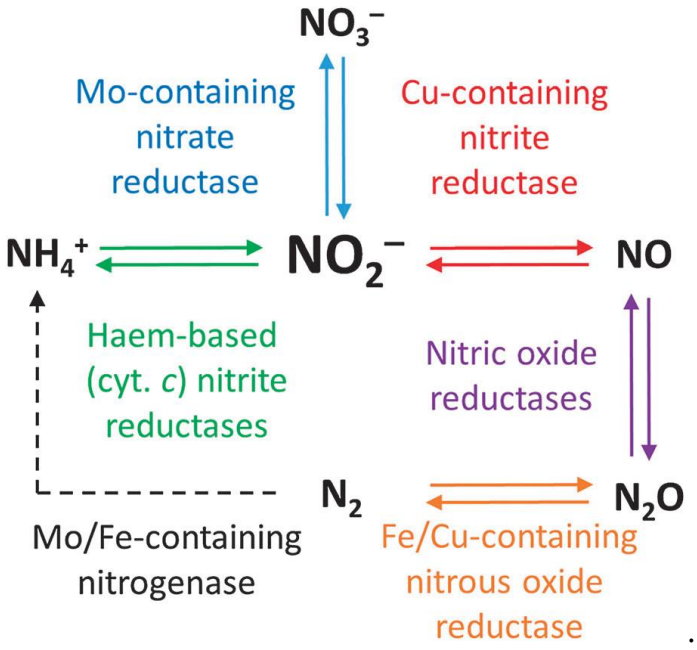

Figure 1.2: *Overview of the nitrogen cycle, showing the central position occupied by nitrite among the different products in the nitrogen cycle. Reproduced from Chem. Soc. Rev,* **2015**, 44, 6708

1.1.2 An overview of various technologies used to fix nitrogen

Following the industrial revolution the uninterrupted growth of the population in Europe required improvements in crop yields and so it was necessary to use more fertilizers. For this reason, we can state that in the XVIII century agriculture became a science. Initially enormous amounts of Chilean saltpetre (sodium nitrate) were used as a fertilizer, but the fact that this kind of material was present only in south-America made it difficult to obtain (especially during times of war).

A method to obtain nitrate was developed in 1903 by Norwegian Kristian Birkeland and Samuel Eyde. It exploits plasma formation via an electric arc formed by two coaxial electrodes and a strong magnetic field (highly analogous to the pathway observed for nitrogen dioxide formation by lighting). The temperature inside the reaction chamber reaches 3000°C and air is blown through the arc; due to the high temperature some of the nitrogen reacts with oxygen to give NO which upon cooling reacts with more oxygen to give gaseous NO_2. This when dissolved in water gives nitric acid. This method is extremely energy intensive since it requires about 15 MWh/Ton of HNO_3 and the yield is around 4%.[(79)]

The great importance of nitrate and nitric acid in agriculture and arms manufacture at the beginning of 20th century was the driving force for this research. Nitric acid production following the method invented by Wilhelm Ostwald started in 1908. This process gives as an intermediate nitric oxide, which is then oxidised to nitric acid in aqueous solution. This process is considered a milestone for the chemical industry since it opened the way to nitric acid production from ammonia using synthetic methods and since ammonia was widely available after the introduction of the Haber-Bosch process (H-B) around the same time. The H-B process allowed to exploits a potentially unlimited source of nitrogen (the atmospheric N_2 stock) to give ammonia as product. This process exploits the ability of (normally Fe-based) catalysts to promote the reaction between dinitrogen and di-hydrogen following **equation 1.2**:

$$N_2 + 3H_2 \rightarrow 2NH_3 \quad (\Delta H° = -45.8\ \text{kJ}\cdot\text{mol}^{-1}) \qquad (2)$$

This was the first process with acceptable efficiency that was exploitable to fix atmospheric nitrogen because it proceeded under relatively mild conditions when compared to the Birkeland-Eyde process and the yield also was better since originally about the 17% of the nitrogen was converted to ammonia by the H-B process. Further developments allow a conversion >97% to be obtained nowadays, but we need to take into account that the exploitation of this process is responsible for about 1% of global energy consumption and also the pollution rising from the Haber-Bosh process is significant (as the H_2 used comes almost entirely from fossil fuels and therefore contributes to the greenhouse effect). The fact that this process is very polluting and energetically non sustainable, requires the development of alternative methods, equally efficient in terms of yield but also effective under milder conditions and with a lower environmental impact.

1.2 Enzymatic catalysis and the Michaelis-Menten model

For most catalysed reactions, it is observed that for a fixed amount of enzyme, at relatively low substrate concentration, the rate of reaction increases linearly with concentration of substrate and tends to reach a limiting value. This trend for the rate of an enzymatic reaction can be described by a simple scheme introduced by Michaelis and Menten in 1913. In their model it is assumed that enzyme (E) and substrate (S) form a complex (ES)

in equilibrium with the reagents and that from this complex we obtain the products (P) and re-generate the enzyme (E) without alteration following **Scheme 1.1**

$$E + S \underset{k_2}{\overset{k_1}{\rightleftharpoons}} ES \xrightarrow{k_3} P + E$$

Scheme 1.1: *The Michaelis-Menten model for enzymatic reactions*

Rate constants k_1 and k_2 are relative to the process of formation of complex E-S and to the reverse reaction. Constant k_3 is relative to the reaction with which the complex E-S gives the products. Applying the steady-state equation it is possible to write:

$$\frac{d[ES]}{dt} = k_1[E][S] - k_2[ES] - k_3[ES] \cong 0 \quad (3)$$

And if we denote the initial concentration of enzyme as $[E_0]$, then at every moment we have that the sum of free enzyme and the [ES] gives $[E]_0$ and on the basis of this and **equation 1.3** it is obtained that:

$$[ES] = \frac{k_1[E]_0[S]}{k_1[S] + k_2 + k_3} \quad (4)$$

Since the rate of product formation is proportional to the concentration of the E-S complex given by **equation 1.3**:

$$v = \frac{d[P]}{dt} = k_3[ES] \quad (5)$$

Considering the form for [ES] given by **equation 1.4** and including this form in **equation 1.5** we have:

$$v = \frac{d[P]}{dt} = \frac{k_1 k_3[E]_0[S]}{k_1[S] + k_2 + k_3} \quad (6)$$

If we divide both numerator and denominator by k_1 and impose $K_M = \frac{k_2 + k_3}{k_1}$, then:

$$v = \frac{k_3[E]_0[S]}{[S] + \frac{k_2 + k_3}{k_1}} = \frac{k_3[E]_0[S]}{[S] + K_M} \quad (7)$$

K_M is the Michaelis-Menten constant and has the dimension of a concentration. It is then possible verify that **equation 1.7** reproduces the experimental trend of reaction rate as a function of substrate concentration.

At lower concentration of substrate (when [S] $\ll K_M$) it is possible to approximate as follows:

$$v = \frac{k_3[E]_0[S]}{K_M} \quad (8)$$

Under this limit we have a linear trend of reaction speed as a function of substrate concentration [S]. Reaction speed is 1st order versus $[E]_0$ and [S]. Under these conditions the ratio k_3/K_M is the second order rate constant for the reaction and its value determines the rate of the process when there is more free enzyme available then [ES] complex. In this limit, the rate determining step is the formation of the [ES] complex. On the other hand, when [S] $\gg K_M$ the previous equation becomes:

$$v = k_3[E]_0 \quad (9)$$

Under these conditions the rate of reaction is independent of the concentration of substrate (the kinetics of the equation are of order 0 versus [S]) and this is the maximum value for the rate of reaction:

$$v_{max} = k_3[E]_0 \quad (10)$$

This value is reached at high substrate concentration. In this limit all the enzyme is present as the [ES] complex and adding more substrate has no effect on the rate of the process. The slowest step of reaction is the decomposition rate of the [ES] complex giving the products. So the **equation 1.7** can be written as follows:

$$v = \frac{v_{max}[S]}{[S] + K_M} \quad (11)$$

In this way the **equation 1.11** allows us to identify K_M as the concentration of substrate $[S]_{1/2}$ at which the rate of reaction is ½ of the maximum value.

$$\frac{v_{max}}{2} = \frac{v_{max}[S]_{1/2}}{[S]_{1/2} + K_M} \quad (12)$$

A large value of K_M indicates that there isn't a strong affinity between enzyme and substrate so [S] has to be relatively large to reach half of the maximum rate of reaction. A small K_M value indicates a strong affinity between enzyme and substrate.

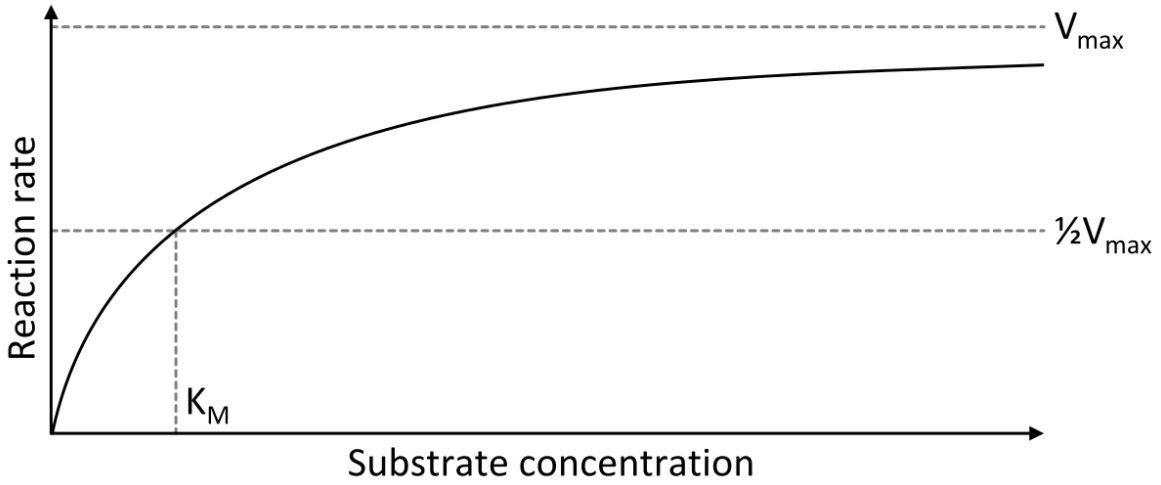

Figure 1.3: *Saturation curve for an enzymatic reaction showing the relation between the substrate concentration and reaction rate*

In the particular case of a redox reaction mediated by a catalyst the behaviour of the voltammetric wave show a dramatic change when the substrate is added in larger amounts. Indeed it is seen that the current increases with the amount of substrate added; so in the presence of this kind of behaviour it is possible to talk about catalytic behaviour, or more commonly, a "catalytic wave". (**Figure 1.4**)

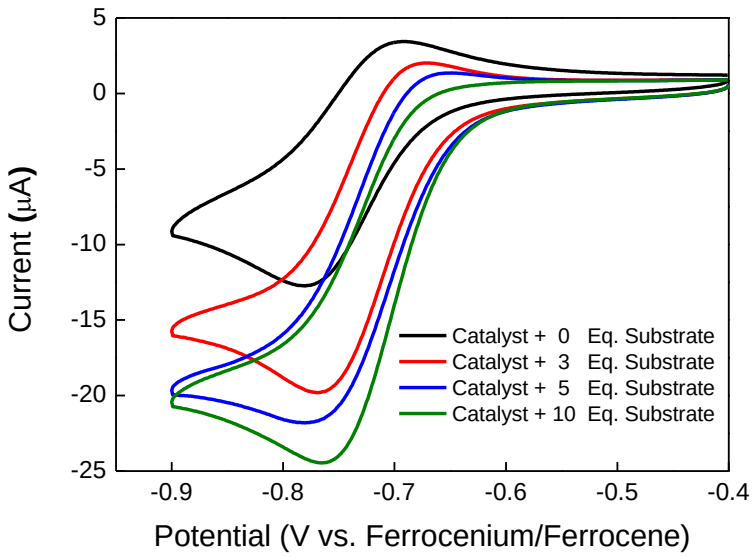

Figure 1.4: *A typical catalytic wave-type response upon adding larger amounts of substrate*

Even if an electron transfer is involved, since it is substantially the same kind of reaction, involving the formation of a [ES] complex, the Michaelis Menten model can be still used

for this system and rearranged to take into account that the source of electrons is represented by an electrode.

This model has the great advantage that it gives us directly a measure of the rate of reaction, since the measured current in a voltammetric wave is the measure of the rate of a redox reaction where the electron transfer is mediated by an electrode.

Equation 1.13 shows that the conversion between the current density and the catalyst concentration at the electrode is straightforward. In fact, when the stoichiometry for the reaction is known, including the number of electrons exchanged and the Faraday Constant, (which gives the charge of 1 mole of electrons) the current density can be transformed directly into a concentration.

$$J_{cat} = \frac{J_{max}[S]}{K_M+[S]} = \frac{v_{max}nF[S]}{K_M+[S]} \quad (13)$$

The use of the current density instead of current is fundamental because (being a reaction happening on the electrode surface) we need to know the amount of species present at the surface.

The quantification of the catalyst concentration at the electrode comes from a voltammogram collected in presence of catalyst alone. The peak concerning the redox process under examination is integrated and the resulting charge, corresponding to the area of the Faradaic peak, gives the concentration of the species at the electrode.

1.3 Proton Coupled Electron Transfer (PCET)

Before discussing mimics of CuNiR it is appropriate to focus our attention on a fundamental point of this thesis the so called "Proton Coupled Electron transfer" (PCET) and the related process of "Concerted Proton Electron Transfer" (CPET).

Since nowadays several of the main challenges for researchers involve the development of better high-performance sensors, better energy conversion systems and the abatement of pollution, knowledge of PCET processes is necessary especially in the case where researchers are trying to mimic the function of natural enzymes, in which PCET processes are commonplace.

As it will be shown in this section**,** pH can profoundly affect the thermodynamic properties and the specific the redox potential, E^0, where a redox process occurs.

Moreover, thermodynamic coupling between proton and electron transfer allows the promotion of electron transfer, for example through films or over long distances in biomolecules exploiting pH changes.[80]

In fact it is known that electron transfer can induce long-range proton transfer through proton channels in biological molecules. The resulting metal-ligand multiple bonds cause large changes in pKa between oxidation states, promoting mechanisms more complex than simple electron transfer.[81,82] When the knowledge of enzymes and biological processes was elucidated at the molecular level it became evident that biology uses PCET extensively since this leads to great advantages from an energetic point of view since thermodynamic coupling between electrons and protons avoids the generation of transition states with high energy.

Over billions of years, complex structures evolved in order to provide suitable structures that integrate electron and proton transfer. These structures are critical to enable PCET since, as well as helping to avoid formation of high-energy intermediates, they also avoid the build-up of electrostatic charge in non-aqueous membrane environments (*e.g*. inside cells). This leads to a levelling of redox potentials and decreases the redox potentials for sequential redox couples since no increase in charge is observed. PCET allows access to higher oxidation states and promotes multiple electron transfer pathways such as in case of hydrogen transfer or O-atom transfer. In biological systems integration of electronic transfer with proton transfer over long distances exploiting a sequence of proton transfers provides a basis for trans-membrane proton equilibration, avoiding local pH gradients.

PCET plays a fundamental role in catalytic processes like water splitting and other enzymatic process like respiration, photosynthesis, and other key reactions in biological and energetic cycles.[83-91] Amongst these reactions, the processes involving nitrogen fixation exploit PCET massively since most of the reactions listed in **Figure 1.2** involve the coupled movement of protons and electrons to and from nitrogen species as shown in **Table 1.1.** The nitrogen species involved in the redox processes are often bound to a single metal centre surrounded by a well-defined ligand environment.

Since one of the main aims of this work is to make coordination compounds that act as electrocatalysts to mimic the behaviour of the CuNiR enzyme, it is necessary to explain the PCET model describing the reaction pathway in presence of a direct source of electrons like an electrode.

For this purpose the model developed by Costentin et al[92,93] explains exhaustively under the mathematical point of view what happens inside the electrochemical cell during a catalytic process promoted by a coordination compound. From the point of view of molecular electrochemistry this specific case is interesting since it couples electron transfer to acid-base chemistry. [94]

Electrochemical approaches to PCET offers several important advantages, firstly because the current is a direct measure of the overall kinetics of reaction, (including diffusion toward and from the electrode) then because the source of electrons is continuous and finally, but not less importantly because voltammetry is easy to run and generally is a non-destructive technique.

Generally reactions involving proton and electron transfer can follow different pathways as summarised graphically in **Figure 1.5**:

- **Electron-Proton transfer (EPT)** where Electron transfer precedes the proton transfer
- **Proton-Electron transfer (PET)** where Proton transfer precedes the electron transfer
- **CPET pathway**, in this case H^+ and e^- transfers are concerted and the high-energy intermediates of the stepwise pathways are bypassed.

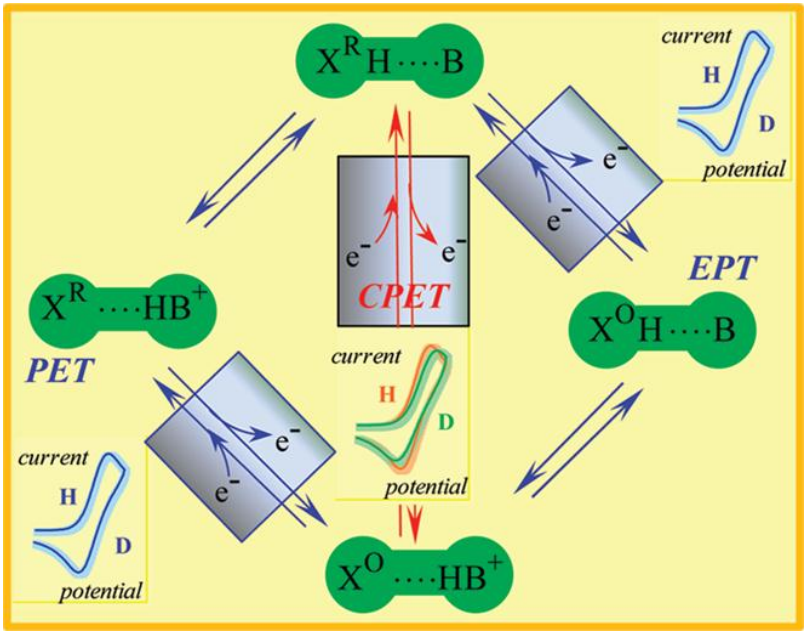

Figure 1.5: *Different Pathways for the Electron and Proton transfer in electrochemical system. Adapted with permission from Acc. Chem. Res.,* ***2010****, 43 (7), 1019. Copyright* ***2010*** *American Chemical Society.*

From an experimental point of view the systematic study of the Redox properties by varying the solution pH allows us to identify the region of pH where the PCET is observed. As shown in **Figure 1.6A**, a plot of the half-wave potential $E^{1/2}$ vs the pH, allows us to create a Pourbaix diagram for the system under study. In fact, as it is possible to observe from the Pourbaix diagram scheme in **Figure 1.6B**, there is a region at intermediate pH values where the potential is influenced by the pH. In the other cases, at lower pH, we find that both the oxidised and reduced species are protonated while at high pH the oxidized and reduced species are both deprotonated.

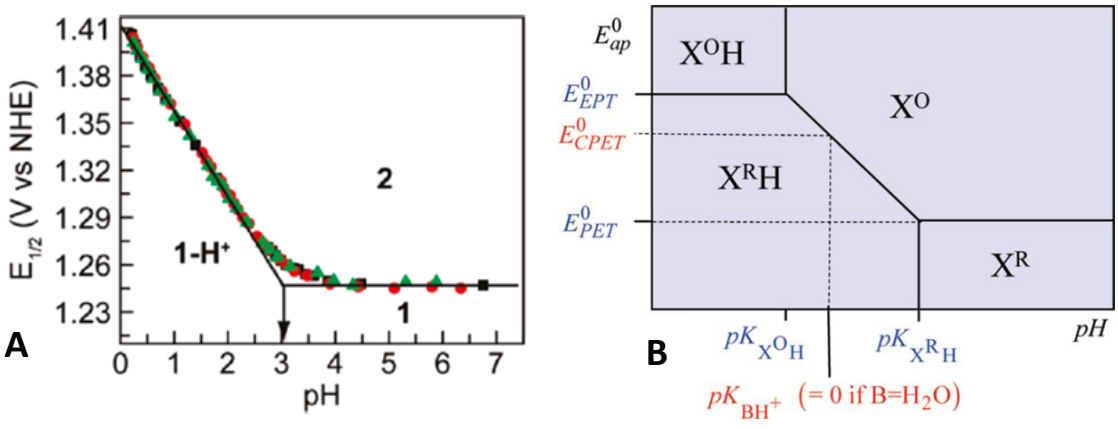

Figure 1.6: *Plot of the $E^{1/2}$ for a generic Oxidation reaction 1⟶ 2 + e^- registered via CV vs pH (**A**). Scheme of a Pourbaix diagram with the species present at different $E^{1/2}$ and pH values (**B**). Adapted with permission from J. Am. Chem. Soc. **2011**, 133, 5174 and Acc. Chem. Res., **2010**, 43 (7), pp 1019. Copyright (**2010,2011**) American Chemical Society.*

More in detail if we consider the generic redox reaction (oxidation) involving the exchange of one proton:

$$+ X^R H + 1e^- \rightarrow X^O + \frac{1}{2} H_2 \qquad (14)$$

From **Figure 1.6B** in the pH region below the $pK_{X^O{}_H}$ both the reduced and oxidised species results to be protonated and is not possible to appreciate a dependence of $E^{1/2}$ for the redox process from the pH. This is the situation where the electron transfer occurs before the proton transfer (EPT). Similar features are observed for pH values greater than $pK_{X^R{}_H}$. Since in this case both the species are deprotonated the proton was transferred before than the eletron (PET). In the region included between $pK_{X^O{}_H}$ and $pK_{X^R{}_H}$ the redox reaction is influenced by pH. In this region there is a point where the two processes are concerted and can be verified the condition for the PCET.

A more practical view is given taking into account some complexes presenting fragments able to promote PCET in a particular reaction of interest. This kind of moiety should increase the performance and the control over the reaction process as for example happens in the case of O-O bond activation[96] or in the case of H_2 generation from weak acids[97] using modified "Hangman" porphiryns in both cases. In **Figure 1.7** is shown the effect of this kind of moiety on the Hydrogen evolution reaction (HER).

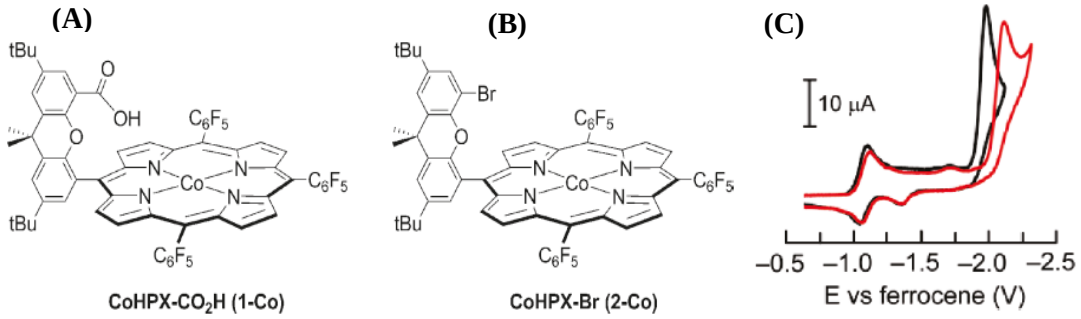

Figure 1.7: *Hangman Porphyrins modified with a carboxylate moiety (**A**) and with a bromine atom (**B**). Effect of the PCET-competent moieties on the overpotential for the hydrogen evolution reaction **(C)**. **A** is the black trace in panel **C** while **B** is the red trace. Reproduced from J. Am. Chem. Soc., **2011**, 133 (23), pp 8775with permission of American Chemical Society.*

Is easy to see that the molecule in **Figure 1.7A** has a moiety able to promote hydrogen bonding with the H coordinated to the cobalt. This ability is absent in the analoguos molecule with the Br shown in **Figure 1.7B** and the effect in the PCET is evident from the voltammograms in **Figure 1.7C** where the overpotential for the HER is about 0.25V lower for the hangman porphirin shown in **Figure 1.7A**. Hydrogen bond between the coordinated substrate and the –COOH moiety can reduce the electron density on the coordinated substrate in order to make more favorable the reduction reaction occurring at the active site. This fact is traduced in a lower overpotential for the reduction reaction as seen in **Figure 1.7C**

Moreover the H bond, if properly oriented, can hold the substrate in the right position, speeding up the reaction process. This is evident in the experimental results detailed in **Chapter 3**, where the in presence of a –COOH fragment makes the reaction studied faster then in the case there this kind of oyety is absent.

1.4 The Cu Nitrite Reductase Enzyme (CuNiR)

Since synthetic mimics of copper containing Nitrite Reductase (CuNiR) is the topic of **Chapter 3**, it is necessary to focus our attention on the structure of the enzyme. The CuNiR class of enzymes catalyses the reduction of nitrite to nitric oxide. As discussed above this is one of the key steps in denitrification and one of the main processes that transforms inorganic nitrogen into biologically available nitrogen. The CuNiR class is organised in homotrimers, where three identical monomers associate together. [98-101] **Figure 1.8** shows the active site of this enzyme. In each monomer there are two slightly structurally different copper sites: type I (T1) and type II (T2). A connection via a cysteine-histidine bridge guarantees rapid electron transfer between T1 and T2.

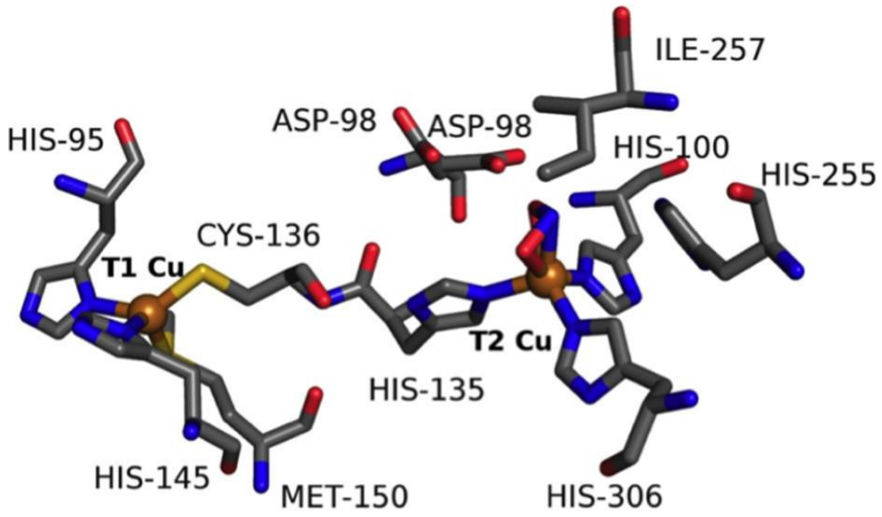

Figure 1.8: *T1 and T2 site in the CuNiR with nearby residues. T2 is the catalytic site while the T1 site transfers an electron from an external source to T2 during the catalytic process. Reproduced from Biochemistry,* ***2015****, 54, 1233*

T2 Cu is the active site of nitrite reduction reaction and it is coordinated by three histidine imidazoles and a molecule of nitrite (or a molecule of H_2O in case the catalytic turnover is concluded) molecule in the remaining coordination site. The catalytic mechanism is a mono-electronic reduction and requires two protons to balance the global reaction.

$$Cu(II) + NO_2^- + 2H^+ + 2e^- \rightarrow Cu(II) + NO + H_2O \qquad \text{(Eq. 15)}$$

The origin of the protons is not well known but, as it is possible to see in **Figure 1.8**, there are two residues that can furnish protons: His255 and Asp98.

Several experiments [102,103] on the enzyme in the presence of excess nitrite have shown that nitrite binds in a bidentate manner, via two oxygen atoms and forms a hydrogen bond with Asp98 which connects to His255 through a solvent-bridged hydrogen bond. The catalytic mechanism of CuNiR has been investigated in crystallographic[103,104-107] spectroscopic,[108-110] kinetic and mutational studies[103,111-114] on enzymes from different species. One important point is that the mutant where the Asp98 and the His255 are not in the optimal positions shows a decrease in the reaction rate constant. This is proof of the importance of these two residues for the enzymatic function of the CuNiR since the Asp98 must be in the right position to hydrogen bond with the nitrite coordinated to the Cu center. X-Ray experiments reveal that Asp98 forms an H-bond to both the nitrite substrate and the nitric oxide product [103-107] suggesting that it promotes the proton transfer happening during the catalysis.

Theoretical studies[101] have shown that only when both Asp98 and His255 are protonated is it possible to have the bidentate coordination of the substrate to the T2 Cu. Another point that needs to be clarified is the electron transfer. There are several theories but experimental data[104,105] and theoretical calculations[101] show that if the nitrite attaches to an already reduced T2 site then bidentate coordination is not possible and the nitrite will attach to the Cu site via a single coordinative interaction through nitrogen. Hence coordination through both oxygens occurs only in the oxidised enzyme. Moreover other experiments [115] show that it is nitrite coordination to T2 that gates the electron transfer since following coordination, the energy of this site decreases and the electron transfer from the T1 to the T2 site. Once these points are clarified the overall mechanism can be summarised as shown in **Figure 1.9**.

The mechanism starts with the displacement of a water molecule from the T2 Cu site by nitrite immediately followed by an electron transfer from T1 that reduces the T2 copper to Cu(I). Then there is nitrite reduction, one oxygen atom is cleaved and forms a water molecule with the protons coming from His255 and Asp98. The H_2O molecule produced forms a hydrogen bond with the Asp98 and the nitric oxide is released. The water molecule then binds to the T2 copper site. Following the protonation of His255 and Asp98 the enzyme is ready for a new catalytic cycle.[101]

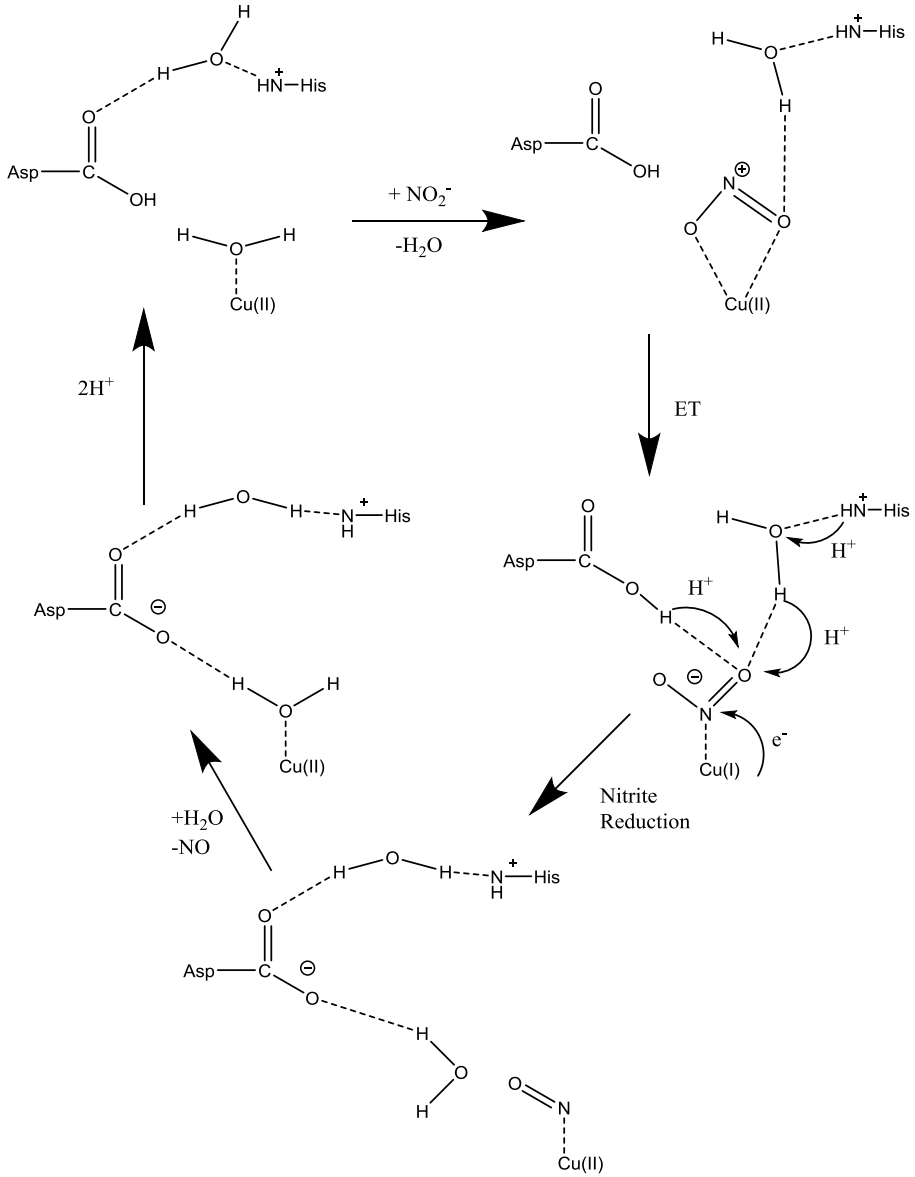

Figure 1.9: *Scheme of the mechanism for the nitrite reduction to nitric oxide promoted by CuNiR*

1.5 Examples of coordination compounds mimicking the active sites of nitrogen oxide-converting enzymes.

1.5.1 Iron porphyrins mimicking Haem-based nitrite reductase

As shown in **table 1.1** (page 6) nitrite reduction to ammonium is a 6 electron reduction and is catalysed by a certain number of nitrite reductases that use haem groups as their active centres. The stoichiometry of this reaction is reported below:

$$NO_2^- + 6e^- + 8H^+ \leftrightharpoons NH_4^+ + 2H_2O \qquad (15)$$

Cytochrome c nitrite reductase is probably the best characterised haem-based enzyme in this class. This enzyme promotes the multi-electron and multi-proton reduction to ammonia without the formation of less reduced by-products like for example nitric oxide. A mechanism describing the nitrite reduction promoted by cytochrome c nitrite reductase was proposed by Neese and co-workers. This is based on the crystal structures of reaction intermediates and DFT calculations,[116] as shown in **Figure 1.10.**

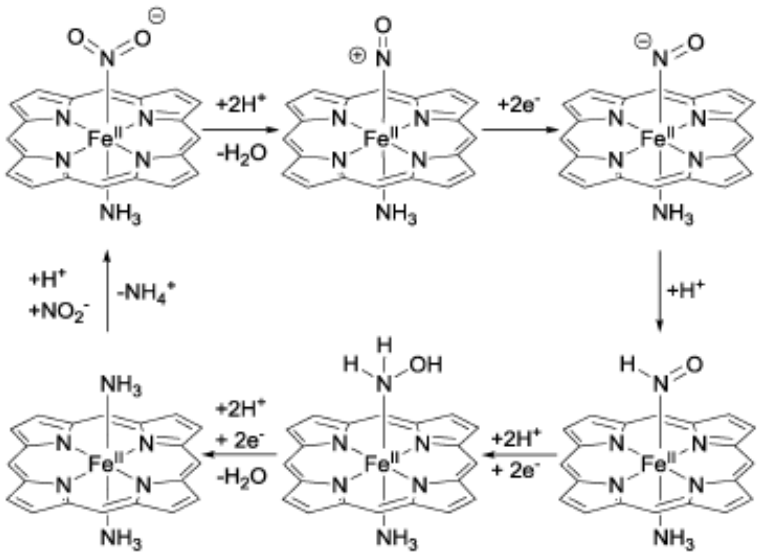

Figure 1.10: *Scheme of the reaction mechanism for the 6 electron reduction of nitrite to ammonia catalysed by Fe-haem enzymes.Reproduced from Chem. Soc. Rev,* ***2015****, 44, 6708 with the permission of The Royal Society of Chemistry.*

Nitrite is coordinated to the Fe(II) centre and heterolysis of the N–O bond occurs to generate a haem-nitrosyl ({Fe–NO}) complex. The high degree of back-bonding from the d_{xz} orbital of the Fe(II) to an empty orbital with π^* character on nitrite facilitates the process since back-bonding makes the Fe–N bond stronger and at the same time weakens the N–O bonds, promoting heterolysis.[116] Formation of hydrogen bonds between protonated histidine or arginine residues and the oxygen atoms of the nitrite molecule also contribute to the heterolysis of the N-O bond in a similar way to that seen in the case of CuNiR. The particular coordination environment provided by the protein matrix makes the local pH at the active site below 3 and that promotes protonation of the oxygen atoms of coordinated nitrite.

A second concerted electron and proton transfer leads to the formation of the {Fe–NH(O)} adduct, where the nitrogen coordinated to iron is preferentially protonated.

A further electron-proton concerted transfer leads to the formation of an iron–hydroxylamine complex ({Fe–NH_2OH}. This complex is then protonated and reduced to

break the final N–O bond, releasing water and giving the {Fe–NH_3} intermediate. Due to the high pH in the active site, ammonia is protonated and the resulting ammonium is released. This allows a second molecule of nitrite to coordinate to the Fe(II) center and permits the enzyme to enter the next catalytic cycle.[1,116] Several examples of mimics of this enzyme are reported in the literature [117-119] exploiting Fe-porphyrins to promote the breakage of the N-O bond.

Chi and coworkers exploited iron meso-tetrakis(4-N-methylpyridiniumyl)porphyrin ([Fe(III)(TMPyP)]$^{5+}$) (**1**) to generate electrochemically nitric oxide from nitrite in aqueous solutions at pH neutral. The mechanism starts with the reduction of the original complex to the analoguos Fe(II) porphyrin complex with two molecules of nitrite coordinated. This species then disproportionates to give the starting compound and the mono nitrosyl complex Fe(II)(NO)(TMPyP)$^{4+}$ that is electrochemically oxidised to the starting Fe(III) complex releasing a further molecule of nitric oxide.[119]

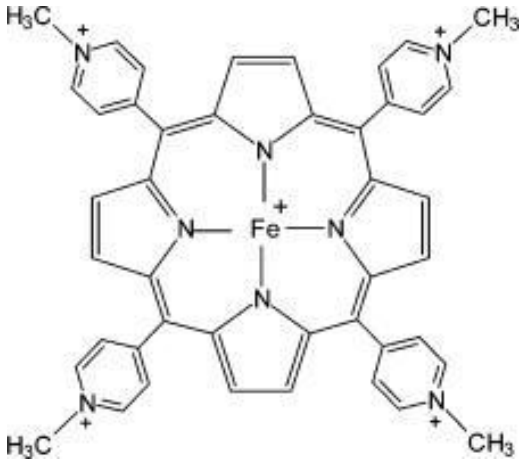

Figure 1.11: *Representation of the water soluble compound (**1**) complex studied by Chi et al.*[119] *Reproduced from Inorg. Chem.*, **2004**, 43 (26), pp 8437 *with permission of American Chemical Society.*

Ford and co-workers report that using a water soluble Fe(III) porphyrin they were able to observe the formation of the nitrosyl complex Fe(II)(TPPS)(NO) with the transfer of an oxygen atom to a sulphur-containing molecule (i.e. cysteine). At slightly acidic pH (≈ 6) they also observed spontaneous redox reactions leading to formation of N_2O and HNO with the regeneration of the starting Fe(III) complex. However, the mechanism at pH 6 remains unclear since the Fe(II)-nitrosyl complexes are not inert as usually assumed[118]

In 1986 Meyer and co-workers reported that in aqueous solution, at acidic pH values (4.5 and 6.7) the water-soluble porphyrin [Fe(III)(H_2O)(TPPS)]$^{3-}$ (H_2TPPS^{4-} = tetraanionic

form of meso(-tetrakisb-sulfonatopheny1)porphyrin) is able to catalyse efficiently the electrochemical reduction of the nitrite ion to ammonia.[117]

However the selectivity of the process is not excellent since products like hydroxylamine or N_2O also appear in significant amounts, depending upon the reaction conditions because their relative concentration increases with the pH. This fact is expected because nitrous oxide and hydroxylamine are intermediate products in this multielectronic process, as confirmed by theory for the cytochrome C nitrite reductase enzyme.

The reductions proceed via the Fe-nitrosyl complex at pH <3 by a reaction between the Fe(III) porphyrin and NO arising from disproportionation of HONO. For pHs between 4.0 and 7.0, following reduction of Fe(III) to Fe(II) ($E^{1/2}$ = -0.23 V vs. SCE) via an acid-base reaction, the electrochemical reduction of the Fe-nitrosyl complex occurs by a sequence of monoelectronic steps at $E^{1/2}$ = +0.35 and -0.63 V vs. SCE, the second of which at pH <2.6 becomes pH-dependent and leads to the intermediate product before then leading to ammonia.

1.5.2 Structural analogues of Molybdenum Nitrate Oxidoreductase (MoNiOR) for the electrochemical reduction of nitrate

Enzymes containing molybdenum or tungsten in their active sites appear to be present in all forms of life, from ancient archaea to man. About 50 enzymes of this type are known and they catalyse a wide range of reactions in metabolism of elements like carbon, sulfur and nitrogen. [120,121] The development of synthetic structures that mimic dynamic aspects of these biological systems is a major focus nowadays; in fact no structure for MoNiOR enzyme has yet been obtained, even if the structure of the active site of MoNiOR has been extrapolated from comparison with analogous Mo-enzymes such as the DMSO reductases.[122]

Hence it is thought that two thiolate-bearing pyranopterin cofactors enforce a distorted Trigonal Prismatic Geometry on the Mo centre, with the thiolates defining one rectangular face of the prism. Model complexes of DMSO reductases with dithiolene ligand sets have been synthesised.[123,124] The coordination sphere around the Mo includes four thiol ligands from 2 molibdopterin groups (**Figure 1.12**), one sulfur ligand from a cysteine fragment and one oxygen atom.

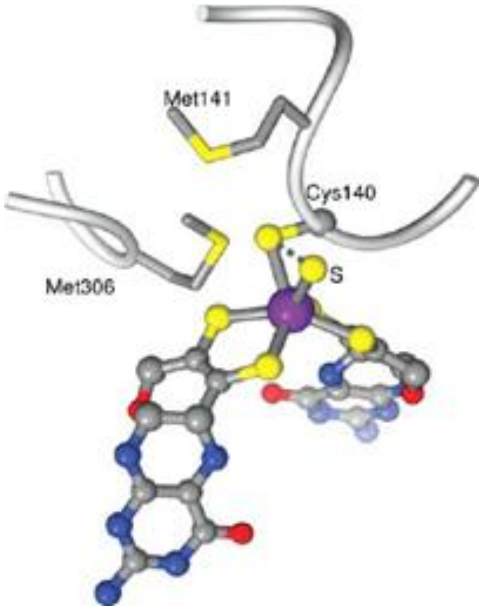

Figure 1.12: *The Mo active site of D. desulfuricans periplasmic nitrate reductase. Adapted from Dalton Trans., 2009, 4053 with permission of The Royal Society of Chemistry*

In *E. coli NapA* for example the Mo-O bond length is 2.6 Å and suggestive of H_2O ligation, whilst in *D. desulfuricans NapA* it is 2.1 Å, indicative of OH^- ligation. The involvement of a Mo^{6+}=O species in an oxo-transfer mechanism is widely expected for nitrate reductases and other molybdenum analogues such as the DMSO-reductase.(125)
The stoichiometry of the reaction (listed in **Table 1.1**) is reported below:

$$NO_3^- + 2e^- + 2H^+ \leftrightharpoons NO_2^- + H_2O \qquad (16)$$

On the basis of this assertion a hypothesis concerning the catalytic cycle can be proposed. In the proposed mechanism, a water molecule is lost on reduction from Mo^{6+} to Mo^{5+}, vacating a coordination site and allowing NO_3^- binding (**Figure 1.13,** State 2).
The formation of a bond between NO_3^- and the Mo^{5+} (**Figure 1.13,** State 3) promotes reduction of Mo^{5+}/NO_3^- by an electron. The resulting Mo^{4+}-NO_3^- now has the two electrons required for reduction of nitrate to nitrite (**Figure 1.13**, State 4), which will yield a Mo^{6+}=O species (**Figure 1.13,** State 5) through an oxo-transfer reaction. This species then will be protonated to give the stable Mo^{6+}-OH or Mo^{6+}-OH_2 (**Figure 1.13,** State 1) states resolved in the crystal structures of the E. Coli and D. desulfuricans NapA Mo enzymes. (125)

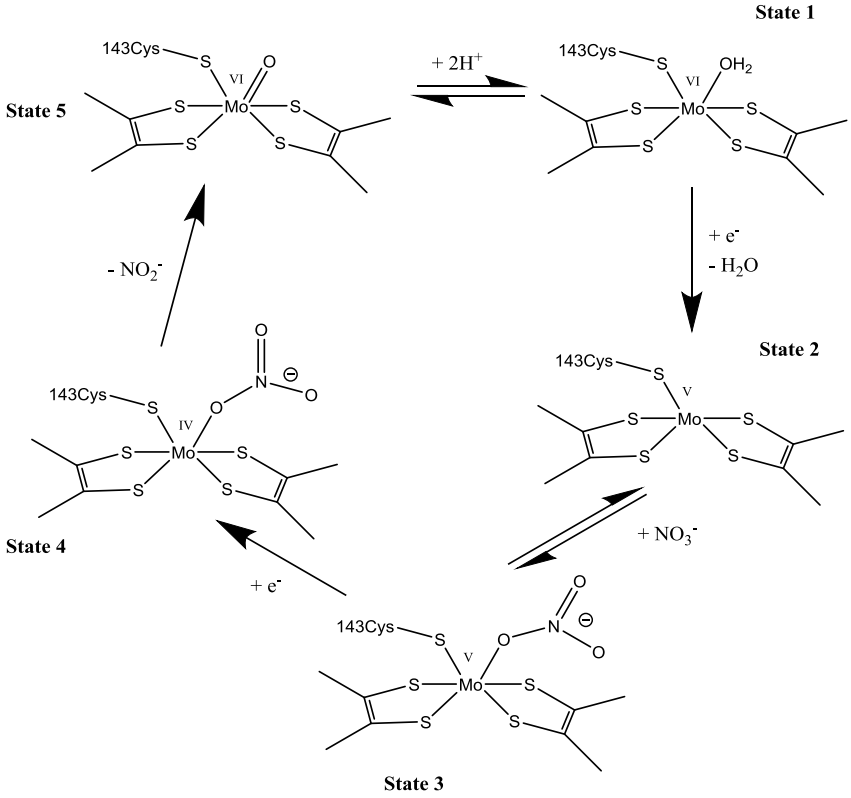

***Figure 1.13**: Scheme of the proposed catalytic cycle for the Molybdenum Nitrate Oxidoretuctase*

Moreover reaction centres containing Mo and W are often unstable when separated from their native protein matrices and so simple and robust active site mimics are extremely useful to establish possible structures and mechanisms of action for these enzymes since many of them remain only poorly understood,[124] and from this point of view dithiolene ligands form the basis for much of the coordination chemistry of Mo and W in the mimics of Mo and W-containing enzymes. The active sites of these tungstoenzymes for which there is compositional information contain two pyranopterindithiolates per metal atom, similarly to Mo analogues. (**Figure 1.12**) In general terms, tungsten-mediated oxo transfer and related synthetic chemistry are far less developed than for molybdenum.[126-127]

Concerning mimics of MoNiOR, the first research was done by Holm and co-workers in 1989 when they reported for the first time the reduction of nitrate to nitrite mediated by a bis-molybdenum compound.[128] This compound was not similar to the structure of MoNiOR since it was synthesised before the structure of this class of molecules was discovered. However in following studies Holm and co-workers synthesised a wide range of molybdenum (and tungsten) coordination compounds modeled on the active site of MoNiOR and some of these compounds are able to promote oxygen atom transfer reaction from nitrate as shown in **Figure 1.14**.[129]

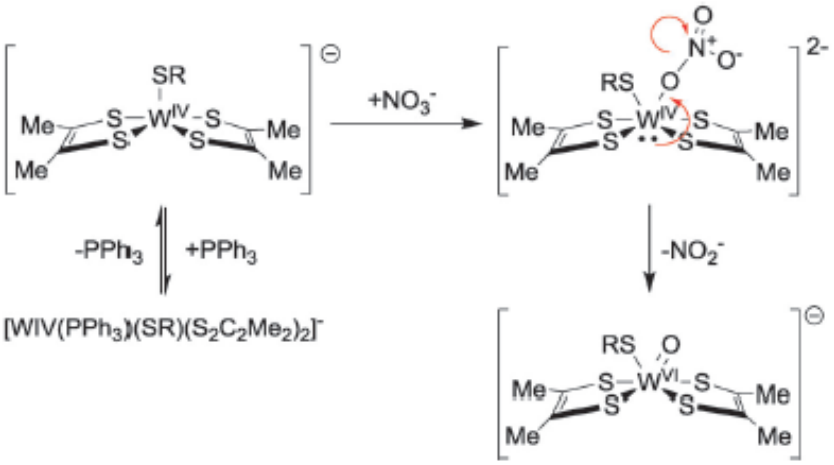

Figure 1.14: *Mechanism of nitrate reduction to nitrite with Holm's tungsten centred Class of catalyst.* [129] *Reproduced from Chem. Soc. Rev,* ***2015****, 44, 6708 with the permission of The Royal Society of Chemistry.*

Also Sarkar and coworkers reported the catalytic nitrate reduction to nitrite mediated by $[Et_4N][Mo^{IV}(SPh)(PPh_3)(mnt)_2$ (**2**) compound bearing in the coordination environment two dithiolene ligands, a benzenethiol and a molecule of triphenylphosphine (PPh_3).[130,131]

The catalytic cycle, shown in **Figure 1.15**, begins with the dissociation of the TPP ligand and the formation of a pentacoordinated Mo species that undergoes reaction with nitrate. During this reaction an oxygen atom is passed from the nitrate to the Mo center, which becomes oxidised from Mo(IV) to Mo(VI) (making an Mo=O complex) and a molecule of nitrite is formed. The catalytic cycle is ccompleted by using PPh_3, which becomes oxidised to triphenylphosphine oxide ($O=PPh_3$) with concomitant formation of the active pentacoordinated species ready to react again. PPh_3 can also coordinate to the Mo center re-generating the initial (non-catalytically active) complex.

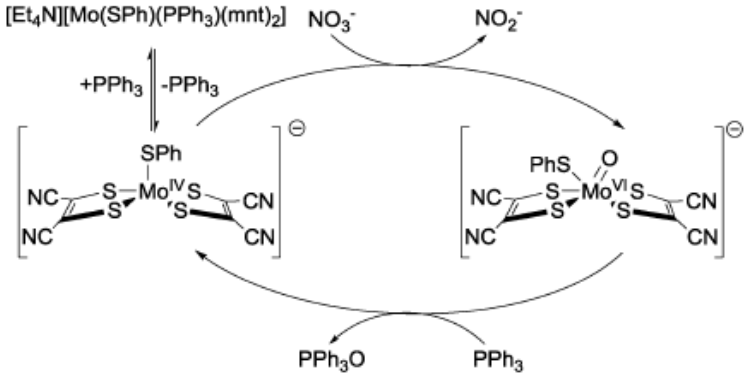

Figure 1.15: *The catalytic cycle for the nitrate reduction mediated by compound (**2**) reduction reported by Sarkar and co-workers.*[130] *Reproduced from Chem. Soc. Rev,* ***2015****, 44, 6708 with the permission of The Royal Society of Chemistry.*

1.5.3 Copper tripod coordination complexes mimicking Cu nitrite reductase

In order to promote the monoelectronic reduction of nitrite to nitric oxide a great number of copper coordination complexes have been developed during the last few decades as mimics of CuNiR according to **equation 15** (page 17).[132,133] The mechanism proposed for all the presented complexes is the one shown in **Section 1.4** and it is briefly summarised in **Figure 1.16a**. Nitrite coordinates to transition metal complexes in various modes and the most common are Z1-NO_2 (N-nitro), Z1-ONO (O-nitrito), and Z2-O–N–O (O,O-bidentate). Theoretical [134] and experimental[135] works show that the interconversion in solution between the different forms of coordinated nitrite is facile. A graphic for these coordination modes is shown in **Figure 1.16b**.

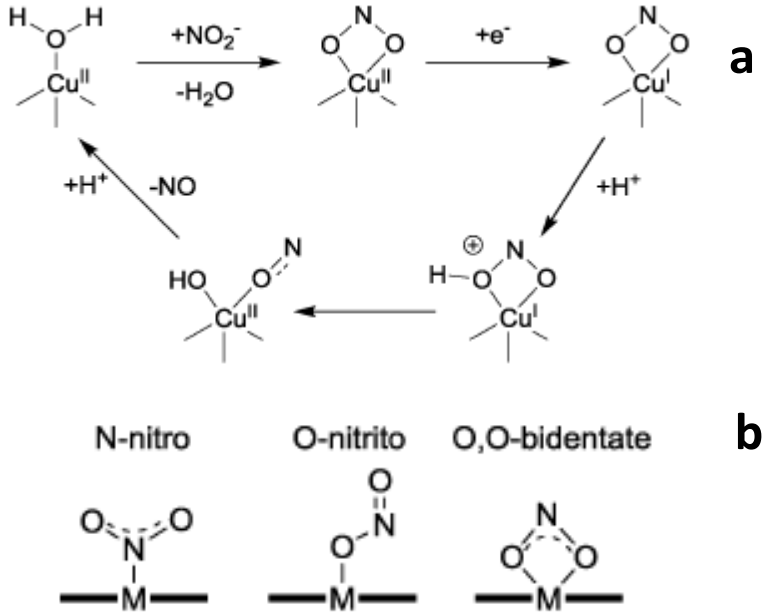

Figure 1.16: ***(a)*** *Simplified scheme for nitrite reduction at the CuNiR active site.* ***(b)****: scheme of the most common modes of coordination of nitrite to the metal center. Readapted from Chem. Soc. Rev,* ***2015****, 44, 6708 with the permission of The Royal Society of Chemistry.*

The first example of a coordination complex that mimics the CuNiR active site was reported in 1995 by Tolman and co-workers. They reported a functional, mononuclear model complex containing a Cu(I) centre coordinated by a sterically hindered tripodal ligand that creates a coordination environment similar to the active site of the enzyme.[136] Nitrite was bound to the metal in an N-nitro coordination mode, producing a distorted tetrahedral geometry at the copper atom. After the addition of acetic acid to this Cu(I)–nitrite adduct, NO evolution is observed according to **Equation 15** (page 17) accompanied by the simultaneous formation of the corresponding Cu(II)–di-acetate complex.

Since 1995, several other Cu complexes coordinated by tripodal ligands have been shown to catalyse the monoelectronic reduction of nitrite to NO and here are reported some of these complexes.

Firstly, in 2008 Kujime and co-workers studied several copper complexes with a wide variety of tridentate ligands in order to determine the steric and electronic effects of the ligands on the catalytic promotion of the monoelectronic reduction of nitrite to NO.[137]

In their work, Kujime and co-workers observed that there is a great difference in the catalytic properties of the Cu-tripodal complexes with the change in the steric and electronic factors. Specifically, they found that in terms of electronic factors, catalytic activity increases with the increase of electron donation from the ligand. Hence nitrite coordinated to the copper centre can accept an electron into its empty π^* antibonding orbital via a back donation mechanism. The effect of an electron-donating ligand is that increasing the electron density on the Cu centre increases the back-bonding contribution and therefore increases the electron density on the nitrite bound to the Cu site. Thus by controlling the electron density on the ligand it is then possible to control the electronic density on the metal centre and hence that on the coordinated nitite.[78]

For both the (TIC)Cu(NO_2) (TIC = hydrotris(3,5-dimethylpyrazolyl)methane (**3**), **Figure 1.17** left) and (TPM)Cu(NO_2)-type (TPM = tris(3,5-dimethylpyrazolyl)methane (**4**), **Figure 1.17** right) complexes reported by Kujime, the HOMO is formed by a combination of the unoccupied 4s-orbital of the Cu atom and the occupied ps-orbital of the bound nitrite. The HOMO of the Cu complex then interacts with the protons during the reaction and this allows one of the N-O bonds to be broken and the release of an oxygen atom as a water molecule.

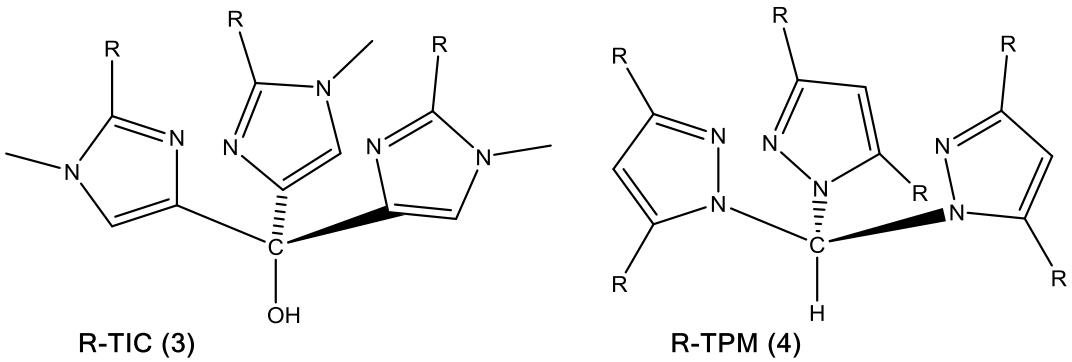

Figure 1.17: *On the left scheme of hydrotris(3,5-dimethylpyrazolyl)methane (**3**) R = iPr, Et. On the right side scheme of tris(3,5-dimethylpyrazolyl)methane (**4**) R = iPr, Et, Me. Both ligands are studied by Kujime and co-workers.[136] Readapted from Chem. Soc. Rev, **2015**, 44, 6708 with the permission of The Royal Society of Chemistry.*

The mechanism proposed for protonation of bound nitrite is stepwise, with formation of a protonated Cu-NO_2H as the intermediate. The protonation of the copper-bound nitrite is the rate determining step.[137] The HOMO of the (**3**)Cu(NO_2) complexes is about 0.5 eV higher than that of the (**4**)Cu(NO_2) analogues, suggesting enhanced reactivity for the TIC–Cu complexes. The calculated stabilization energy for the protonation of the Cu(I)–nitrite complexes was around 40 kJ·mol^{-1} larger than for the (**4**)Cu(NO_2) analogues. This value is comparable to the difference in energies between the HOMO orbitals of the two complexes. Hence it was postulated that the higher the energy of the HOMO then the faster the initial protonation of the nitrite, and hence the greater the reactivity observed.

Steric effects also have a large influence on reactivity, since when more bulky ligands are used it was observed that bond length for the Cu-N increases. This reduced electron donation from the ligand to Cu centre and consequentially decreased the overall electronic density on the coordinated nitrite since the back-donation process observed became less efficient. Hence a less bulky ligand should show better catalytic performance.

Another set of Cu-tripodal coordination complexes, this time based on Cu(II), that mimics the CuNiR active site was developed by Holland and co-workers[138] Some of the structures presented by Holland et al are shown in **Figure 1.18-20**. The generic formula is indicated as ([Cu(NO_2)-(L)][PF_6]) (**5**) where L = Tris(2-aminoethyl)amine (Tren) (complex **5 Figure 1.18**) and Tris-[(benzimidazol-2-yl)methyl]amine (complex **6 Figure 1.19**). X-ray crystallography revealed that the nitrite coordinates both complex **5** and complex **6** with similar features. Both the complexes after exposure to nitrite, give a mixture of two coordination isomers: η^1-NO_2 (Isomers **5a** and **6a**) and μ^1-ONO (Isomers **5b** and **6b**).

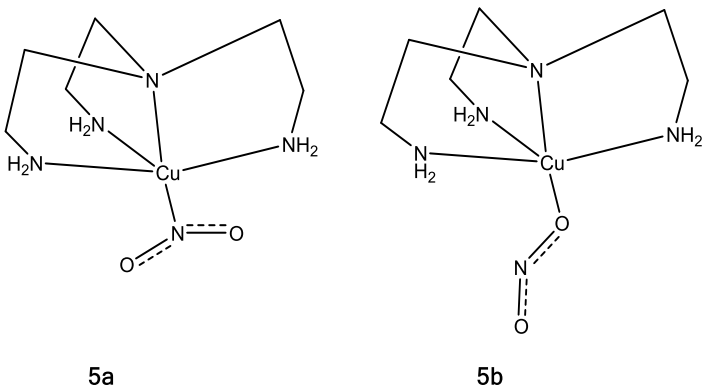

***Figure 1.18**: Chemical structures of the complexes **5** [Cu(NO_2)-(Tren)][PF_6])with the possible coordination of nitrite observed. Readapted from Chem. Soc. Rev,* **2015**, 44, 6708 *with the permission of The Royal Society of Chemistry.*

In the η^1-ONO isomers **5b** and **6b** the N-O1 (O1 is the oxygen coordinated to Cu site) bond is shorter than the N-O2 bond. The difference in bond length is expected in the isomers presenting O-nitrito coordination. Moreover the difference in length observed for the N-O bond length in complex **6** but not in complex **5** suggests that there is some difference in the electronic distribution between Cu center and NO_2^- due to the different ligand environments.(138)

The two d_{xz} or d_{yz} orbitals of Cu(II) ion in complex **5a** and **6a** are involved in the bond between Cu and nitrogen. In fact, due to back-bonding contribution they can delocalise electron density into the empty π^* orbitals of nitrite. From **Figure 1.19** is possible to see that Compound **6** shows an extended aromatic structure where electron density can be delocalised, absent in compound **5**. This fact leads to an overall lower electron density on the Cu^{2+} ion in complex **6a** than in complex **5a**. This fact appears evident since it is possible to observe a difference in the position of the Cu(I)/Cu(II) redox couples. Complex **6a** show a less cathodic $E^{1/2}$ for the reduction from Cu^{2+} to Cu^{+} if compared with the complex **5a** because of this nephelauxetic effect.(138)

The Cu-ONO isomer **6b** showed the elongation of the r(N–O1) bond (1.361 Å) with contraction of the r(N–O2) bond (1.210 Å) typical of the μ-ONO bound mode. Moreover, DFT calculations showed that the Cu-NO_2 isomers were lower in energy than the Cu-ONO isomers by 5.2 kJ mol^{-1} and by 3.8 kJ·mol^{-1} for complexes **5** and **6** respectively in the gas phase.

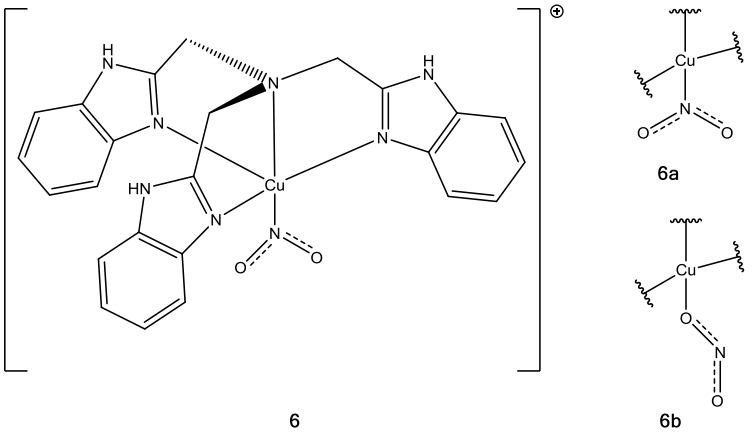

***Figure 1.19**: Chemical structures of the complexes **6** ([Cu(NO₂)(Tris-[(benzimidazol-2-yl)methyl]-amine)][NO₂]) with the possible coordination of nitrite observed. Readapted from Chem. Soc. Rev, **2015**, 44, 6708 with the permission of The Royal Society of Chemistry.*

This small ΔE can explain why both the Cu-ONO and Cu-NO_2 linkage isomers were observed both in solution and in the crystal phase. Catalysis of nitrite reduction was investigated via GC-MS analysis with the result that complex **6** shows better performance

toward monoelectronic reduction of nitrite to nitric oxide then the other molecules prepared by Holland and co-workers [138]

In case of the complex [Cu(ONO)$_2$(Tris-(2-pyridyl)phosphine)] (compound **7** shown in **Figure 1.20**) both the nono and bidentate coordination mode are observed when nitrite is coordinated to the copper centre. A comparison of the bond lengths, based on crystallographic data, suggests that nitrite in the O-nitrito mode is bound more strongly than that in the bidentate O-nitrite mode.

Complex **7** shows great selectivity for the reduction of nitrate since the 88% of the substrate is converted to NO without any trace of other by-products like nitrous oxide (N_2O) present in quite all the other cases. [138]

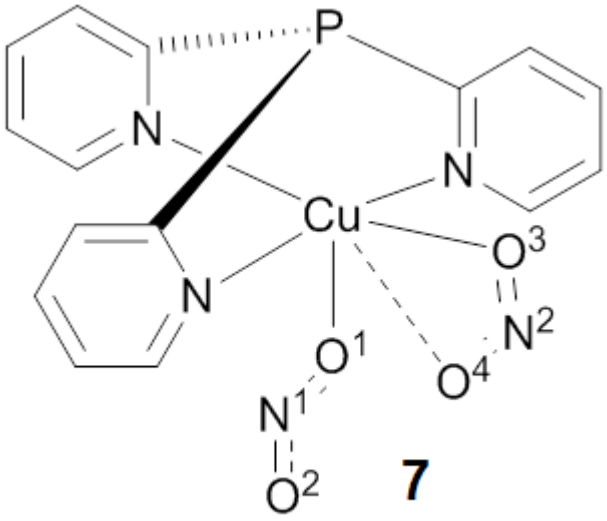

***Figure 1.20**: Chemical structure of the complex (**7**) with the possible coordination of nitrite observed. Readapted from Chem. Soc. Rev,* **2015**, 44, 6708

Tanaka and coworkers[139-140] developed a Cu(II)tripodal coordination complex that can promote the reduction of nitrite electrochemically. They found that the tripodal ligand tris[(2-pyridyl)-methyl]amine (or TPA) creates an environment similar to the active site of the CuNiR enzyme and that nitrite coordinates in different modes to the Cu center (compound **8**).

The main product of reduction is not nitric oxide but nitrous oxide (N_2O). Traces of nitric oxide are however observed. This fact is not surprising since the electrolysis is carried at neutral conditions (pH = 7.0). The crystal structure of the catalyst described is reported in **Figure 1.21**.

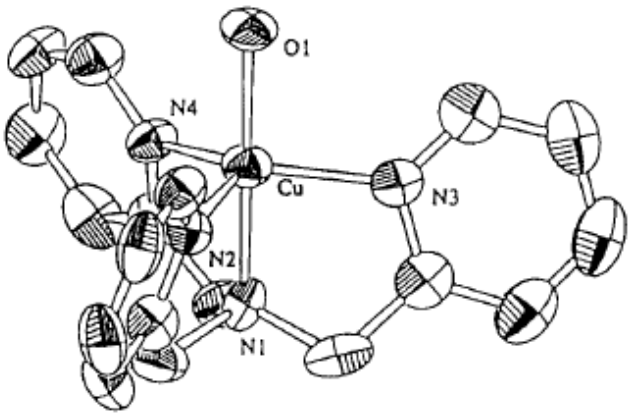

Figure 1.21: *Molecular structures for: (**8**) with heteroatoms labelled. Reproduced from Inorg. Chem. **1996**, 35, 6809with the permission of American Chemical Society.*

However it remained unexplained as to what the active coordination form for the reduction was and if there was a relationship between the coordination mode and the reactivity. Research linking the coordination mode to activity towards monoelectronic nitrite reduction to NO, is an intriguing topic and several studies on this were done in the recent past. Indeed, such a study was carried out in our research group,[(135)] where a Cu(II) tripod coordination complex (Cu[6-methyl-tris(2-pyridyl)methoxide]$(NO_2)_2$ indicated as **9**(NO_2)) , showing all the three modes of coordination for the nitrite molecule at the same time, was synthesised. The structure for this compound is shown in **Figure 1.22**.

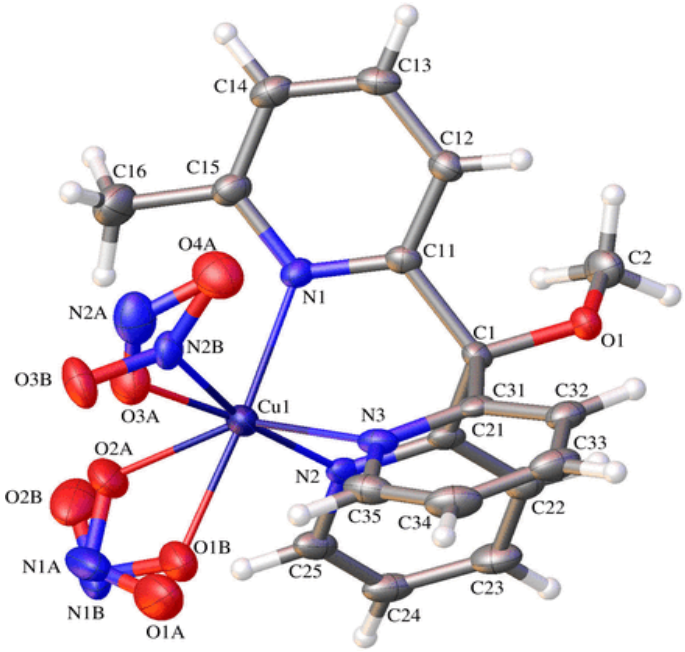

Figure 1.22: *Crystal structure of complex **9**(NO_2). This structure results to be a mixture of (**9**)(η^1-ONO)(η^2-NO_2) and (**9**)(η^1-NO_2)(η^2-NO_2) and the unexpected heptacoordinated structure is due to this fact. The colour scheme is: C grey, N blue, O red, Cu purple and H white. Reproduced from R. Soc. open sci. **2017**, 4, 170593.Copyright 2017.*

From the disorder in the disposition of the 2 nitrite molecules bonded to the Cu centre, it appears evident that the structure is a mixture of two different isomers. Subsequent DFT calculations showed that the resulting structure is a mixture of two different diasteroisomers, both showing one nitrite molecule coordinated in the bidentate κ^2-ONO mode and the other one in the κ^1-NO2 or κ^1-ONO mode.

The isomer showing the κ^1-ONO κ^2-ONO coordination for the two nitrites is slightly more stable ($\Delta G \approx 1$kJ/mol) than the other one. This small energy difference justifies the presence of both the species in equal proportion and the resulting disorder upon the coordination of nitrite. An optimised structure of the two isomers, based on DFT calculation is shown in **Figure 1.23**.

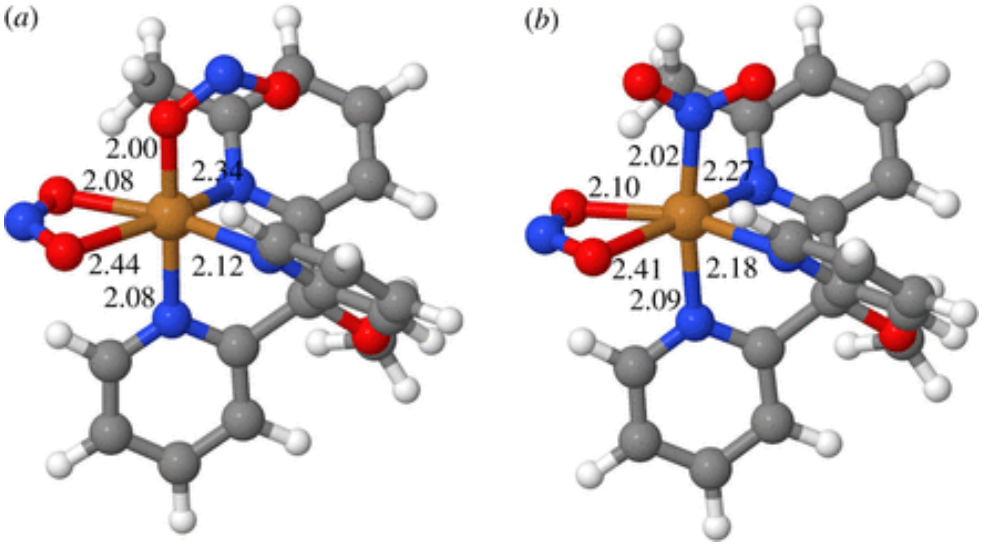

Figure 1.23: *DFT-optimised structures of the two linkage isomers for* ***(9)****$(NO_2)_2$ with the metal-ligand bond lengths in the coordination environment expressed in Angstrom.*[(135)] ***(a)****:* ***(9)****(η^1-ONO)(η^2-NO_2).* ***(b)****:* ***(9)****(η^1-NO_2)(η^2-NO_2). Reproduced from R. Soc. open sci.* ***2017****, 4, 170593 with permission of Royal Society of Chemistry. Copyright 2017*

These Cu-tripod compounds are good candidates to be used on modified electrode surfaces to create heterogeneous catalysts that promote the reduction of nitrite to nitric oxide.

An example of this application is the work of Yamaguchi and co-workers where an electrochemical approach to reducing nitrite using copper complexes covalently attached to the electrode surface was explored. Specifically, these authors used the tripodal N,N,N ligand bis(6-methyl-2 pyridylmethyl)amine ethyl sulfide complex with Cu(I) (indicated as **10**) attached to the surface of gold electrodes exploiting the particular affinity of sulfur to make strong covalent bonds with gold surfaces.[(141)]

Under acidic conditions (pH 5.3) they observed an electrocatalytic wave corresponding to the electrochemical reduction of nitrite to nitric oxide. The fact that no such wave was observed in the presence of nitrite at higher pH suggests the importance of having protons immediately available in the reduction reaction. These protons are then delivered to the substrate in a PCET process (in **Figure 1.24**).

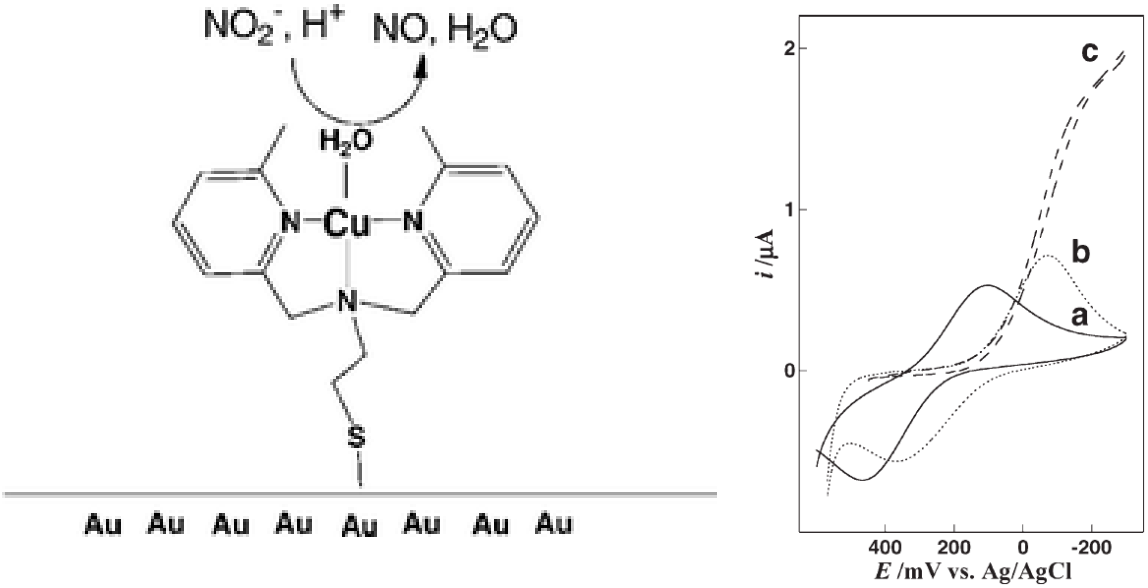

Figure 1.24: *On the left scheme of the gold electrode modified with the compound **10**, on the right side a comparison between (**a**) Au-**10** working electrode (**b**) after addition of 500 mM $NaNO_2$ to the electrolyte solution a, and (**c**) after addition of $HClO_4$ to b for adjustment of pH to 5.3. The reaction environment was 100 mM $NaClO_4$ (aqueous solution) and a scan rate of 10 mV/sec was used. Counter electrode: Au wire, reference electrode: Ag/AgCl. Adapted from Chem. Commun.* **2005**, 4534. *with permission of The Royal Society of Chemistry.*

Similarly Orain and coworkers have covalently attached $[CuII(6\text{-}eTMPA)(H_2O)]^{2+}$ (indicated as **11**) to gold electrodes and have also observed the necessity to have an acidic environment in order to observe evolution of nitric oxide from nitrite solutions(**Figure 1.25**).[142] By analogy with the case presented above [141] no catalytic current for nitrite reduction was evident at pH 8.9. The only process visible was the reversible wave due to the Cu(II)/Cu(I) reduction process. However, after the addition of nitric acid (pH = 4.6), it was possible to appreciate a dramatic increase in the current corresponding to the catalytic reduction of nitrite to NO.

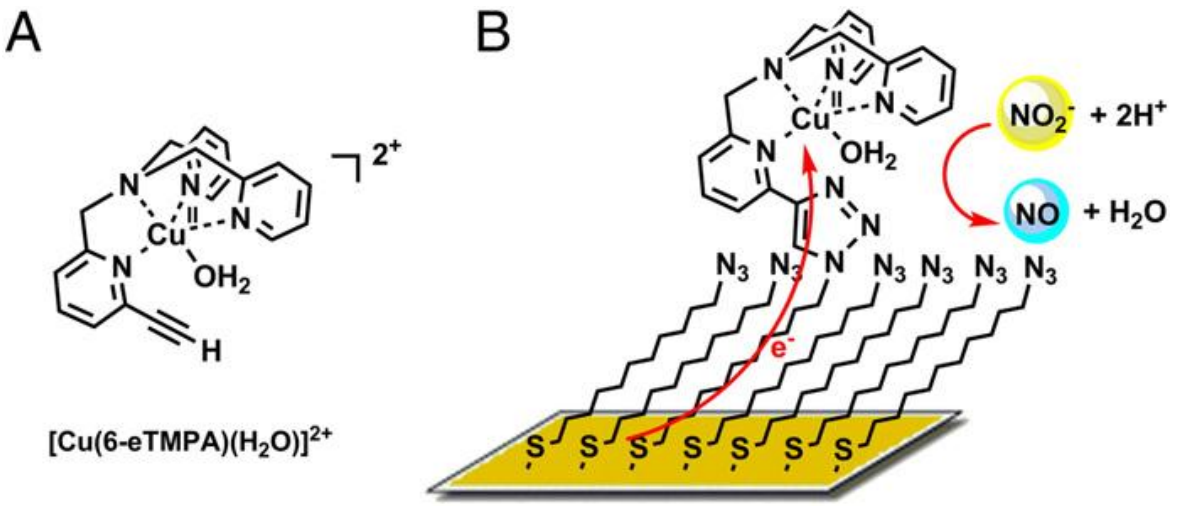

Figure 1.25: *Schematic representation of compound **11** (**A**) and Au-**11** modified electrode (**B**) reported by Le Poul et al. attached via S-Au interactions, which is competent for the electrocatalytic reduction of nitrite.*[(141)] *"Reproduced from Electrochem. Commun. **2013**, 34, 204, with permission from Elsevier Copyright (2013)*

Although it is known that protons are necessary to reduce nitrite to nitric oxide, no one until now investigated the effect of a ligand including a group able to promote the correct alignment of the species involved during electrocatalytic PCET in order to try to mimic more closely the behaviour of the enzyme. In recent years several research groups started to investigate the properties of ligands with fragments able to promote the proton transfer by the inclusion of groups able to undergo hydrogen bonding with the substrate coordinated to the metal centre.[(134,143,144)]

Fout and co-workers reported the synthesis of a Fe(II) non-haem coordination compound (**12**) capable to promote hydrogen bonding. After the exposure of this compound to $TBANO_2$ they observe the oxidation of the Fe(II) to Fe(III) and the evolution of 1 equivalent of NO.

A crystal structure on the species obtained showed the presence of an Fe(III) oxo-compound (**12A**) where the O atom was coordinated by three hydrogen bonds as shown in **Figure 1.26A**. Comparison with an analogous compound obtained by exposing the **12** to NO shows completely different features since the NO in this instance is bonded via the N (**Figure 1.26B**). Moreover the H bond-promoting groups are oriented towards the outside in this second molecule. This fact confirms that H-bond properly orientated promotes the transfer of an oxygen atom from the substrate to the catalyst.

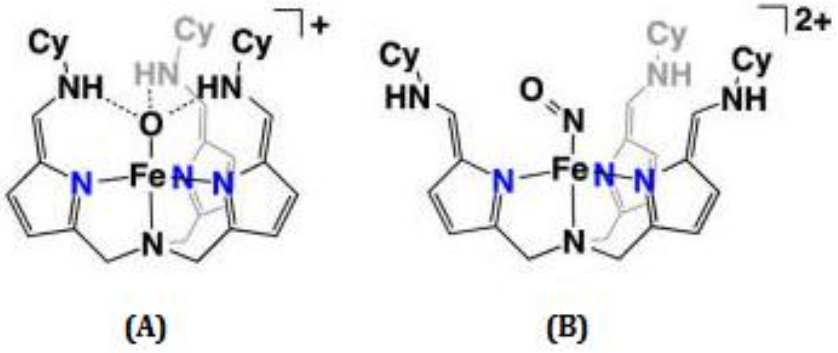

Figure 1.26: *Scheme of the product coming from nitrite reduction of* ***12*** *(**A**) and from exposure of 12 to NO (**B**)*[142] *Aadapted with permission from J. Am. Chem. Soc.* ***2014****, 136 (50), 17398. Copyright (2014) American Chemical Society.*

Szymczak and co-workers reported a Cu-tripodal coordination (**13**) compound with analogous behaviour to the molecule reported by Fout.[134,143] Although the compound shows a coordination environment similar to the environment present in the T2 site of CuNiR, it does not show catalytic activity since there is no external source of electrons reaction terminates when the Cu(II) is fully reduced to Cu(I) and no electrochemical analysis have been performed.

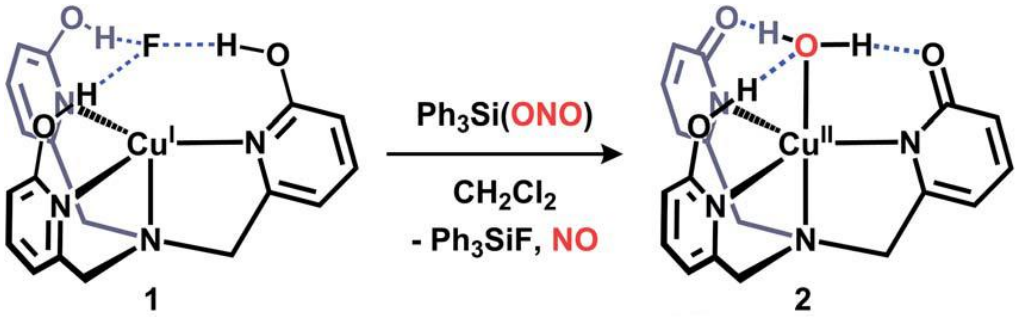

Figure 1.27: *Synthesis of Cu(OH$_2$)(Hhpa) (**13**) reported by Szymczak et al.*[134] *Readapted from Chem. Sci.* ***2015****, 6, 3373 with permission of the Royal Society of Chemistry.*

Gilbertson and co-workers report a similar case where a proton-responsive pyridinediimine ligand is used in a coordination compound with an Fe atom (**14**).[144] They observe the formation of a product with two NO molecules coordinated as shown in **Figure 1.28**.

The study of the examples described in this section allowed us to prepare electrocatalysts based on the active site of CuNiR. In **Chapter 3** the synthesis and characterization of two new copper complexes (indicated in **Chapter 3** as **17** and **18)** is detailed, which allow to address for the first time the role of PCET in the electrocatalytic reduction of nitrite to NO with synthetic, small-molecule platforms.

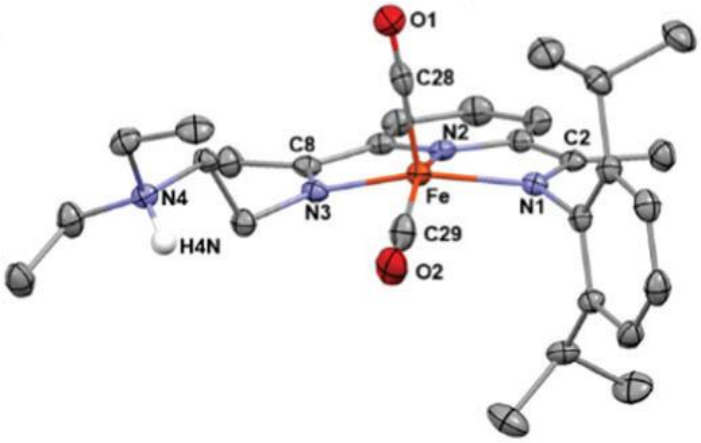

Figure 1.28: *Solid state structure at 30% probability of* $[Fe(HDEAPDI)(CO)_2]^+$ ***(14)*** *prepared by Gilbertson et al.*[143] *Adapted from Chem. Commun.* ***2016****, 52, 11016 with permission of The Royal Society of Chemistry.*

Both complexes contain a copper center coordinated by a tetradentate tris(2-methylpyridyl)amine (TMPA) ligand (highly analogue to compound **8** reported in **Figure 1.21**)[139,140] and both are competent for the electrocatalytic reduction of nitrite to NO. However, complex **18** (in which a carboxylate group is positioned in close proximity to nitrite bound to the copper center), is roughly twice as effective a catalyst for this transformation as complex **17**, which lacks any such proton-relaying groups.

These results suggest that the incorporation of PCET-competent groups in the secondary coordination sphere of the metal center gives rise to a considerable enhancement in the rate of electrocatalytic nitrite reduction, and hence give insights into the workings of the natural CuNiR enzymes and suggest new avenues for the development of biomimetic catalysts for applications such as the removal of NO_2^- from waste-water streams[145] and NO-release systems for biomedical applications[146-147] since NO plays an important role in neurotransmission and vasodilation[148-150]

1.6 Synthesis of compound 19, 20, 21 and 24

Before to engage in the synthesis of the compounds **17** and **18** was tried the synthesis of Molybdenum and Tungsten bis dithiolene coordination compounds in order to mimic the active site of the MoNiOR enzyme class shown in **Figure 1.12** (page 23). This synthesis followed two different pathways: in the first one was synthesised a ligand based on 1,2-benzenedithiolene where we tried to add a substituent able to promote PCET.

In the second pathway we tried to introduct the PCET promoting fragment in a ligand that was not going to coordinates the atom via sulphur atoms. These reactions will no be

described in this thesis work but is necessary to mention it in order to introduce the reason because we started investigating the chemistry of these cobalt compounds.

Infact during the investigation of MoNiOR chemistry we tried to study chemistry of bis dithiolene ligands with other metals, in the specific we tried Cobalt and Nikel. For what concern Ni no results will be detailed in the next chapters but for what concerns cobalt we will describe a certain number of complexes never reported before and with interesting properties. We investigated the solvatochromic properties of compounds **19**-**21**[151] (detailed in **Chapter 4**) and the interesting redox and coordinative properties of compound **24**[152] in **Chapter 5**.

1.7 References:

[1] L.B. Maia, J.J.G. Moura, *Chem. Rev*. **2014**, 114, 5273

[2] R.D. Joerger, P.E. Bishop, *Crit. Rev. Microbiol*. **1988**, 16, 1.

[3] P.S. Kessler, J. Mclarnan, J.A. Leigh, *J. Bacteriol*. **1997**, 179, 541.

[4] S.E. McGlynn, E.S. Boyd, J.W. Peters, V.J. Orphan, *Front. Microbiol*. **2013**, 3, 419.

[5] J. Simon, M. G. Klotz, *Biochimica et Biophysica Acta*, **2013**, 1827, 114–135

[6] P.G. González, C. Correia, I. Moura, C.D. Brondino, J.J.G. Moura, *J. Inorg. Biochem*. **2006**, 100, 1015.

[7] H. Dobbek, *Coord. Chem. Rev*. **2011**, 255, 1104.

[8] M.J. Pushie, G.N. George, *Coord. Chem. Rev*. **2011**, 255, 1055.

[9] S. Grimaldi, B. Schoepp-Cothenet, P. Ceccaldi, B. Guigliarelli, A. Magalon, *Biochim. Biophys. Acta*, **2013**, 1827, 1048.

[10] M. Jormakka, D. Richardson, B. Byrne, S. Iwata, *Structure*, **2004**, 12, 95.

[11] P. Arnoux, M. Sabaty, J. Alric, B. Frangioni, B. Guigliarelli, J.M. Adriano, D. Pignol, *Nat. Struct. Biol*. **2003**, 10, 928.

[12] C. Coelho, P.J. Gonzalez, J. Trincão, A.L. Carvalho, S. Najmudin, T. Hettman, S. Dieckman, J.J.G. Moura, I. Moura, M.J. Romão, *Acta Crystallogr. Sect. F*, **2007**, 63, 516.

[12] B.J.N. Jepson, S. Mohan, T.A. Clarke, A.J. Gates, J.A. Cole, C.S. Butler, J.N. Butt, A.M. Hemmings, D.J Richardson, *J. Biol. Chem*. **2007**, 282, 6425.

[13] S. Najmudin, P.J. Gonzalez, J. Trincão, C. Coelho, A. Mukhopadhyay, C.C. Romão, I. Moura, J.J.G. Moura, C.D. Brondino, M.J. Romão, *J. Biol. Inorg. Chem*. **2008**, 13, 737

[14] M. Cerqueira, P.J. Gonzalez, C.D. Brondino, M.J. Romão, C.C Romão, I. Moura, J.J.G. Moura, *J. Comput. Chem*. **2009**, 30, 2466.

[15] B.J.N. Jepson, L.J. Anderson, L.M. Rubio, C.J. Taylor, C.S. Butler, E. Flores, A. Herrero, J.N. Butt, D.J. Richardson, *J. Biol. Chem*. **2004**, 279, 32212.

[16] M.G. Bertero, R.A. Rothery, M. Palak, C. Hou, D. Lim, F. Blasco, J.H. Weiner, N.C. Strynadka, *J. Nat. Struct. Biol*. **2003**, 10, 681.

[17] R.M. Martinez-Espinosa, E.J. Dridge, M.J. Bonete, J.N. Butt, C.S. Butler, F. Sargent, D.J. Richardson, *FEMS Microbiol. Lett*. **2007**, 276, 129.

[18] E.J. Hewitt, *Ann. Rev. Plant Physiol*. **1975**, 26, 73.

[19] M.G. Guerrero, J.M. Vega, M. Losada, *Ann. Rev. Plant Physiol*. **1981**, 32, 169.

[20] B.D. Knaff, M. Hirasawa, *Biochim. Biophys. Acta*, **1991**, 1056, 93.

[21] J.T. Lin, V. Stewart, *Adv. Microb. Physiol*. **1997**, 39, 1.

[22] K. Fischer, G.G. Barbier, H.J. Hecht, R.R. Mendel, W.H. Campbell, G. Schwarz, *Plant Cell*, **2005**, 17, 1167.

[23] E. Flores, J.E. Frias, L.M. Rubio, A. Herrero, *Photosynth. Res*. **2005**, 83, 117.

[24] C. Moreno-Vivián, E. Flores, *Biology of the Nitrogen Cycle*; **2007**, Elsevier: Amsterdam, p 263.

[25] A.J. Gates, V.M. Luque-Almagro, A.D. Goddard, S.J. Ferguson, D. Roldán, D.J. Richardson, D. J. *Biochem. J*. **2011**, 435, 743.

[26] M. Hirasawa, K. Fukushima, G. Tamura, D.B. Knaff, *Biochim. Biophys. Acta*, **1984**, 791, 145.

[27] M.F. Olmo-Mira, P. Cabello, C. Pino, M. Martínez-Luque, D.J. Richardson, F. Castillo, M.D. Roldán, C. Moreno-Vivián, *Arch. Microbiol*. **2006**, 186, 339.

[28] C. Pino, F. Olmo-Mira, P. Cabello, M. Martínez-Luque, F. Castillo, M.D. Roldán, C. Moreno-Vivián, *Biochem. Soc. Trans*. **2006**, 34, 127.

[29] W.G. Zumft, *Microbiol. Mol. Biol. Rev*. **1997**, 61, 533.

[30] I. Moura, J.J.G Moura, *Curr. Opin. Chem. Biol*. **2001**, 5, 168.

[31] O. Einsle, P.M. Kroneck, *Biol. Chem*. **2004**, 385, 875.

[32] M. Kobayashi, H. Shoun, *J. Biol. Chem*. **1995**, 270, 4146.

[33] M. Kobayashi, Y. Matsuo, A. Takimoto, S. Suzuki, F. Maruo, H. Shoun, *J. Biol. Chem*. **1996**, 271, 16263.

[34] N. Takaya, S. Kuwazaki, Y. Adachi, S. Suzuki, T. Kikuchi, H. Nakamura, Y.Shiro, H. Shoun, J. *Biochem*. **2003**, 133, 461.

[35] S.W. Kim, S. Fushinobu, S. Zhou, T. Wakagi, H. Shoun, *Biosci. Biotechnol. Biochem*. **2010**, 74, 1403.

[36] Y. Nakanishi, S. Zhou, S.W. Kim, S. Fushinobu, J. Maruyama, K. Kitamoto, T. Wakagi, H. Shoun, *Biosci. Biotechnol. Biochem*. **2010**, 74, 984.

[37] E. Piña-Ochoa, S. Høgslund, E. Geslin, T. Cedhagen, N. Peter Revsbech, K.P. Nielsen, M. Schweizer, F. Jorissen, S. Rysgaard, N. Risgaard-Petersen, *PNAS*, **2010**, 107, 1148.

[38] H. Shoun, S. Fushinobu, L. Jiang, S.W. Kim, T. Wakagi, T. *Philos. Trans. R. Soc B,* **2012**, 367, 1186.

[39] S.W. Kim, S. Fushinobu, S. Zhou, T. Wakagi, H. Shoun, *Appl. Environ. Microbiol*, **2009**, 75, 2652.

[40] N.J. Takaya, *Biosci. Bioeng*, **2002**, 94, 506.

[41] Risgaard-Petersen, N.; Langezaal, A. M.; Ingvardsen, S.; Schmid, M. C.; Jetten, M. S. M.; H.J.M. Op den Camp, J.W.M. Derksen, E. Piña-Ochoa, S.P. Eriksson, L.P. Nielsen, N.P. Revsbech, T. Cedhagen, G.J. van der Zwaan, *Nature* **2006**, 443, 93.

[42] T. Fujii, N. Takaya, *Biosci. Biotechnol. Biochem*. **2008**, 72, 412.

[43] S. Demaneche, L. Philippot, M.M. David, E. Navarro, T.M. Vogel, P. Simonet, *Appl. Environ. Microbiol*. **2009**, 75, 534.

[44] J. Simon, *FEMS Microbiol. Rev*. **2002**, 26, 285.

[45] H.P. Koops, A. Pommerening-Roser, *FEMS Microbiol. Ecol.* **2001**, 37, 1.

[46] S.E. Vlaeminck, A.G. Hay, L. Maignien, W. Verstraete, *Environ. Microbiol*. **2011**, 13, 283.

[47] G.A. Ritchie, D.J. Nicholas, *Biochem. J*. **1974**, 138, 471.

[48] AA. DiSpirito, L.R. Taaffe, J.D. Lipscomb, A.B. Hooper, *Biochim. Biophys. Acta*, **1985**, 827, 320.

[49] H.J. Beaumont, N.G. Hommes, L.A. Sayavedra-Soto, D.J. Arp, D.M. Arciero, A.B. Hooper, H.V. Westerhoff, R.J.M. van Spanning, *J. Bacteriol.* **2002**, 184, 2557.

[50] P. Chain, J. Lamerdin, F. Larimer, W. Regala, V. Lao, M. Land, L. Hauser, A. Hooper, M. Klotz, J. Norton, L. Sayavedra-Soto, D. Arciero, N. Hommes, M. Whittaker, M.; D. Arp, *J. Bacteriol*. **2003**, 185, 2759.

[51] H.J.E. Beaumont, S.I. Lens, W.N.M. Reijnders, H.V. Westerhoff, R.J.M. van Spanning, *Mol. Microbiol*. **2004**, 54, 148.

[52] I. Schmidt, R.J.M. van Spanning, M.S.M. Jetten, *Microbiology* **2004**, 150, 4107.

[53] H.J.E. Beaumont, S.I. Lens, H.V. Westerhoff, R.J.M. van Spanning, *Bacteriol*. **2005**, 187, 6849.

[54] J.J. Cantera, L.Y. Stein, *Arch. Microbiol*. **2007**, 188, 349.

[55] J.J. Cantera, L.Y. Stein, *Environ. Microbiol*. **2007**, 9, 765.

[56] I. Schmidt, *Curr. Microbiol*. **2009**, 59, 130.

[57] R. Yu, K. Chandran, *BMC Microbiol*. **2010**, 10, 70.

[58] K. Kondo, K. Yoshimatsu, T. Fujiwara, *Microbes Environ*. **2012**, 27, 407.

[59] L.Y. Stein, D.J. Arp, *Appl. Environ. Microb*. **1998**, 64, 4098.

[60] T.J. Goreau, W.A. Kaplan, S.C. Wofsy, M.B. McElroy, F.W. Valois, S.W. Watson, *Appl. Environ. Microbiol*. **1980**, 40, 526.

[61] F. Lipschultz, O.C. Zafiriou, S.C. Wofsy, *Nature* **1981**, 294, 641.

[62] M. Poth, D.D. Focht, *Appl. Environ. Microbio*l. **1985**, 49, 1134.

[63] N. Yoshida, H. Morimoto, M. Hirano, I. Koike, S. Matsuo, E. Wada, T. Saino, A. Hattori, *Nature* **1989**, 342, 895.

[64] N.K. Shrestha, S. Hadano, T. Kamachi, I. Okura, Appl. *Biochem. Biotechnol*. **2001**, 90, 221.

[65] N.C.G. Tan, M.J. Kampschreur, W. Wanders, W.L. van der Pol, J. van de Vossenberg, R. Kleerebezem, M.C. van Loosdrecht, M.S.M. Jetten, *Syst. Appl. Microbiol*. **2008**, 31, 114.

[66] M.S.M. Jetten, M. Strous, K.T. van de Pas-Schoonen, J. Schalk, U.G. van Dongen, A.A. van de Graaf, S. Logemann, G. Muyzer, M.C. van Loosdrecht, J.G. Kuenen, *FEMS Microbiol. Rev.* **1998**, 22, 421.

[67] M. Strous, J.A. Fuerst, E.H.M. Kramer, S. Logemann, G. Muyzer, K.T. van de Pas-Schoonen, R. Webb, J.G. Kuenen, M.S.M. Jetten, *Nature* **1999**, 400, 446.

[68] M. Strous, E. Pelletier, S. Mangenot, T. Rattei, A. Lehner, M.W. Taylor, M. Horn, H. Daims, D. Bartol-Mavel, P. Wincker, V. Barbe, N. Fonknechten, D. Vallenet, B. Segurens, C. Schenowitz-Truong, C. Medigue, A. Collingro, B. Snel, B.E. Dutilh, H.J.M. Op den Camp, C. van der Drift, I. Cirpus, K.T. van de Pas-Schoonen, H.R. Harhangi, L. van Niftrik, M. Schmid, J. Keltjens, J. van de Vossenberg, B. Kartal, H. Meier, D. Frishman, M.A. Huynen, H.W. Mewes, J. Weissenbach, M.S.M. Jetten, M. Wagner, D. Le Paslier, *Nature*, **2006**, 440, 790.

[69] M.G. Klotz, L.Y. Stein, *FEMS Microbiol. Lett.* **2008**, 278, 146.

[70] J.G. Kuenen, *Nat. Rev. Microbiol*. **2008**, 6, 320.

[71] M.S.M. Jetten, L. van Niftrik, M. Strous, B. Kartal, J.T. Keltjens, H.J.M. Op den Camp, *Crit. Rev. Biochem. Mol. Biol*. **2009**, 44, 65.

[72] N.M. de Almeida, W.J. Maalcke, J.T. Keltjens, M.S.M. Jetten, B. Kartal, *Biochem. Soc. Trans.* **2011**, 39, 303.

[73] B. Kartal, W.J. Maalcke, N.M. de Almeida, I. Cirpus, J. Gloerich, W. Geerts, H.J.M. Op den Camp, H.R. Harhangi, E.M. Janssen-Megens, K.J. Francoijs, H.G. Stunnenberg, J.T. Keltjens, M.S.M. Jetten, M. Strous, *Nature* **2011**, 479, 127.

[74] B. Kartal, L. van Niftrik, J.T. Keltjens, H.J.M. Op den Camp, M.S. Jetten, *Adv. Microb. Physiol.* **2012**, 60, 211.

[75] J. van de Vossenberg, D. Woebken, W.J. Maalcke, H.J.C.T. Wessels, B.E. Dutilh, B. Kartal, E.M. Janssen-Megens, G. Roeselers, J. Yan, D. Speth, J. Gloerich, W. Geerts, E. van der Biezen, W. Pluk, K.J. Francoijs, L. Russ, P. Lam, S.A. Malfatti, S.G. Tringe, S.C.M. Haaijer, H.J.M. Op den Camp, H.G. Stunnenberg, R. Amann, M.M. Kuypers, M. M..S.M. Jetten, *Environ. Microbiol.* **2013**, 15, 1275.

[76] M. Shimamura, T. Nishiyama, H. Shigetomo, T. Toyomoto, Y. Kawahara, K. Furukawa, T. Fujii, *Appl. Environ. Microbiol.* **2007**, 73, 1065.

[77] M. Li, T. Ford, X. Li, J.D. Gu, *Environ. Sci. Technol*. **2011**, 45, 3547.

[78] A.J. Timmons, M.D. Symes, *Chem. Soc. Rev.*, **2015**, 44, 6708

[79] S. Eyde, *Journal of the Royal Society of Arts*, **1909**,57, 568

[80] M.H.V. Huynh, T.J. Meyer, *Chem. Rev*. **2007**, 107, 5004-5064

[81] T.J. Meyer, M.V.H Huynh, *Inorg. Chem.* **2003**, 42, 8140

[82] T.J. Meyer, M. Tsutsui, R. Ugo, *Fundamental Research in Homogeneous Catalysis; Plenum Press: New York*, **1977**, p 169.

[83] R.J.P.J. Williams, *Theor. Biol*. **2002**, 219, 389.

[84] S. Cukierman, *Frontiers Biosci*. **2003**, 8, S1118.

[85] T.E. Decoursey, *Physiol. Rev*. **2003**, 83, 475.

[86] P. Brzezinski, G. Larsson, *Biochim. Biophys. Acta Bioenerg*. **2003**, 1605, 1.

[87] C. Tommos, G.T. Babcock, *Acc. Chem. Res*. **1998**, 31, 18.

[88] C.W Hoganson, G.T. Babcock, *Science* **1997**, 277, 1953

[89] A. Remy, K. Gerwert, *Nature Struct. Biol*. **2003**, 10, 637.

[90] G.T. Babcock, M. Espe, C. Hoganson, N. LydakisSimantiris, J. McCracken, W.J. Shi, S. Styring, C. Tommos, K. Warncke, *Acta Chim. Scand.* **1997**, 51, 533.

[91] Proshlyakov, D. A.; Pressler, M. A.; Babcock, G. T. *PNAS* **1998**, 95, 8020

[92] C. Costentin, M. Robert, J.M. Savéant, A.N. Teillout *PNAS*, **2009**, 106, 11829

[93] C. Costentin, M.Robert & J.M. Saveant *Acc. Chem. Res.* **2010** 43, 1019

[94] J.M. Savéant, *Elements of Molecular and Biomolecular Electrochemistry* (WileyInterscience, New York), **2006**, pp 140

[95] M.D. Symes, Y. Surendranath, D.A. Lutterman, D.G. Nocera. *J. Am. Chem. Soc.* **2011**, 133, 5174

[96] J. Rosenthal, D.G. Nocera, *Acc. Chem. Res*. **2007**, 40, 543

[97] C.H. Lee, D.K. Dogutan, D.G. Nocera, *J. Am. Chem. Soc*. **2011**, 133, 8775

[98] E. Libby, B. Averill, *Biochem. Biophys. Res. Commun*, **1992**, 187, 1529

[99] Z. Abraham, D. Lowe, B. Smith, *Biochem. J*. **1993**, 295, 587.

[100] M. Kukimoto, M. Nishiyama, M. Murphy, S. Turley, E. Adman, S. Horinouchi, T. Beppu, *Biochemistry* **1994**, 33, 5246−5252.

[101] Y. Li, M.Hodak, J. Bernholc, *Biochemistry*, **2015**, 54, 1233.

[102] Murphy, M., Turley, S., and Adman, E. *J. Biol. Chem*, **1997**, 272, 28455.

[103] M. Boulanger, M. Murphy, *Biochemistry*, **2001**, 40, 9132.

[104] E.I. Tocheva, F.I. Rosell, A.G. Mauk, M.E.P. Murphy, *Science*, **2004**, 304, 867.

[105] S.V. Antonyuk, R.W. Strange, G. Sawers, R.R Eady, S.S Hasnain, *PNAS*, **2005**, 102, 12041.

[106] E.I. Tocheva, F.I. Rosell, A.G. Mauk, M.E.P Murphy, *Biochemistry*, **2007**, 46, 12366.

[107] F. Jacobson, A. Pistorius, D. Farkas, W. De Grip, O. Hansson, L. Sjölin, R. Neutze, *J. Biol. Chem*, **2007**, 282, 6347.

[108] H. Yokoyama., K. Yamaguchi, M. Sugimoto, S. Suzuki, *Eur. J. Inorg. Chem*. **2005**, 1435.

[109] O. Usov, Y. Sun, V. Grigoryants, J. Shapleigh, C. Scholes, *J. Am. Chem. Soc.* **2006** 128, 13102.

[110] N. Lehnert, U. Cornelissen, F. Neese, T. Ono, Y. Noguchi, K. Okamoto, K. Fujisawa, *Inorg. Chem*, **2007**, 46, 3916.

[111] M. Boulanger, M. Kukimoto, M. Nishiyama, S. Horinouchi, M. Murphy, *J. Biol. Chem.* **2000**, 275, 23957

[112] K. Kataoka, H. Furusawa, K. Takagi, K. Yamaguchi, S. Suzuki, *J. Biochem.* **2000** 127, 345

[113] M. Prudêncio., R. Eady, G. Sawers, *J. Bacteriol.* **1999**, 181, 2323

[114] H. Zhang, M. Boulanger, A. Mauk, M. Murphy, *J. Phys. Chem.* B **2000**, 104, 10738

[115] M.A. Hough, S.V.Antonyuk, R.W. Strange, R.R. Eady, S.S. Hasnain, *J. Mol. Biol*. **2008**, 378, 353.

[116] O. Einsle, A. Messerschmidt, R. Huber, P.M. H. Kroneck, F. Neese, *J. Am. Chem. Soc.* **2002**, 124, 11737.

[117] M.H. Barley, K.J. Takeuchi, T.J. Meyer, *J. Am. Chem. Soc.* **1986**, 108, 5876

[118] J. L. Heinecke, C. Khin, J.C.M. Pereira, S.A. Suarez, A.V. Iretskii, F. Doctorovich, P.C. Ford, *J. Am. Chem. Soc.* **2013**, 135, 4007.

[119] Y. Chi, J. Chen and K. Aoki, *Inorg. Chem*. **2004**, 43, 8437.

[120] R. Hille, *Chem. Rev.* **1996**, 96, 2757.

[121] R. Hille, *Trends Biochem. Sci.* **2002**, 27, 360.

[122] P.M.H. Kroneck, J.A. Abt, *Met. Ions Biol. Syst*. **2002**, 39, 369.

[123] H. Enemark, J.J. A. Cooney, J.J. Wang, R.H. Holm, *Chem. Rev.* **2004**, 104, 1175.

[124] H. Sugimoto, H. Tsukube, *Chem. Soc. Rev.* **2008**, 37, 2609.

[125] J.M. Dias, M.E. Than, A. Humm, R. Huber, G.P. Bourenkov, H.D. Bartunik, S. Bursakov J. Calvete, J. Caldeira, C. Carneiro, J.J.Moura, I. Moura, M.J. Romao, *Structure*, **1999**, 7, 65

[126] R.H. Holm, *Chem. Rev.* **1987**, 87, 1401

[127] G.C. Tucci, J.P. Donahue, R.H. Holm, *Inorg. Chem.* **1998**, 37, 1602.

[128] J. A. Craig, R.H. Holm, *J. Am. Chem. Soc.* **1989**, 111, 2111.

[129] J. Jiang, R.H. Holm, *Inorg. Chem.* **2005**, 44, 1068.

[130] A. Majumdar, K. Pal and S. Sarkar, *J. Am. Chem. Soc*, **2006**, 128, 4196.

[131] A. Majumdar, K. Pal and S. Sarkar, *Inorg. Chem*. **2008**, 47, 3393.

[132] I.M. Wasser, S. de Vries, P. Moenne-Loccoz, I. Schroder and K.D. Karlin, *Chem. Rev*. **2002**, 102, 1201

[133] A. C. Merkle and N. Lehnert, *Dalton Trans*. **2012**, 41, 3355.

[134] C.M. Moore, N.K. Szymczak, *Chem. Sci*. **2015**, 6, 3373

[135] I. Roger, C. Wilson, H.M. Senn, S. Sproules, M.D. Symes, *R. Soc. open sci*. **2017**, 4, 170593

[136] J.A. Halfen, S. Mahapatra, E.C. Wilkinson, A.J. Gengenbach, V.G. Young Jr, L. Que Jr, W.B. Tolman, *J. Am. Chem. Soc*. **1996**, 118, 763.

[137] M. Kujime, C. Izumi, M. Tomura, M. Hada and H. Fujii, *J. Am. Chem. Soc*. **2008**, 130, 6088.

[138] J.G. Woollard-Shore, J.P. Holland, M.W. Jones , J. R. Dilworth, *Dalton Trans*. **2010**, 39, 1576.

[139] N. Komeda, H. Nagao, Y. Kushi, G. Adachi, M. Suzuki, A. Uehara, K. Tanaka, *Bull. Chem. Soc. Jpn*. **1995**, 68, 581

[140] H. Nagao, N. Komeda, M. Mukaida, M. Suzuki, K. Tanaka, *Inorg. Chem. **1996**, 35, 6809*

[141] T. Hiratsu, S. Suzuki and K. Yamaguchi, *Chem. Commun*. **2005**, 4534.

[142] C. Orain, A.G. Porras-Gutierrez, F. Evoung Evoung, C. Charles, N. Cosquer, A. Gomila, F. Conan, Y. Le Mest and N. Le Poul, *Electrochem. Commun*. **2013**, 34, 204.

[143] E.M. Matson, Y.J. Park, A.R. Fout, *J. Am. Chem. Soc*. **2014**, 136, 17398

[144] Y.M. Kwon, M. Delgado, L.N. Zakharov, T. Sedac and J. D. Gilbertson, *Chem. Commun*. **2016**, 52, 11016

[145] F.J. Cervantes, D.A. De la Rosa, J. Gómez, *Bioresour. Technol.* **2001**, *79*, 165-170.

[146] H. Ren, J. Wu, C. Xi, N. Lehnert, T. Major, R.H. Bartlett, M.E. Meyerhoff, *ACS Appl. Mater. Interfaces*, **2014**, *6*, 3779.

[147] K. Cosby, K.S. Partovi, J.H. Crawford, R.P. Patel, C.D. Reiter, S. Martyr, B.K. Yang, M.A. Waclawiw, G. Zalos, X. Xu, K.T. Huang, H. Shields, D.B. Kim-Shapiro, A.N. Schechter, R.O. Cannon III; M.T. Gladwin, *Nat. Med.* **2003**, *9*, 1498.

[148] V. Calabrese, C. Mancuso, M. Calvani, E. Rizzarelli, D.A. Butterfield, A.M. Giuffrida Stella, *Nat. Rev. Neurosci.* **2007**, *8*, 766–775.

[149] S.A. Omar, A.J. Webb, A. J. *J. Mol. Cell. Cardiol.* **2014**, *73*, 57-69.

[150] J. Heinecke, P.C. Ford, Mechanistic Studies of Nitrite Reactions with Metalloproteins and Models Relevant to Mammalian Physiology. *Coord. Chem. Rev.* **2010**, *254*, 235.

[151] G.Cioncoloni, H. M. Senn, S. Sproules, C. Wilson and M. D. Symes, *Dalton Trans.*, **2016**,45, 15575.

[152] G. Cioncoloni, S. Sproules, C. Wilson and M. D. Symes, *Eur. J. Inorg. Chem.* ***2017****, 3707.*

Overview of The Techniques used and practical experimental details

Synopsis:

In this chapter are briefly explained the main experimental techniques used in **Chapters 3** to **6** so as to have a theoretical background prior to encountering them later in the text. This way it will be clear why a particular technique was chosen and how they complement each other for different applications. At the end of the chapter are showed the practical experimental details concerning the work done.

2.1 Electrochemical techniques

It is possible to divide electrochemical techniques into three different classes depending on whether (I) the potential is controlled or (II) the charge is controlled with (III) impedance spectroscopy being the third class. In the following section the electrochemical techniques used throughout this thesis are briefly explained with particular attention to the information we can obtain from them and in which cases it is better to use one technique rather than another one.

2.1.1 Linear sweep and cyclic voltammetry

A preliminary overview of the redox aptitude of a species can be easily obtained by varying with the time the potential applied to the working electrode (when this is immersed in a solution of the species under study) and recording the curve obtained by plotting the current measured as a function of the potential applied. The curve obtained is called voltammogram.

In a linear sweep voltammetry experiment the potential is linearly swept at a constant rate from an initial value E_1 (at which the current is ideally zero) to a final value of potential E_2. Linear sweep voltammetry experiments can be used to obtain Tafel slopes, which are useful when it is necessary to assign the number of electrons exchanged during a redox process.[(1)]

If after the scan from E_1 to E_2 the potential is reversed back to E_1 at the same scan rate, the potential scan makes a complete cycle and the technique resulting from this procedure is called cyclic voltammetry. Without any doubt this is the most popular electrochemical technique used in inorganic chemistry since it can give easily useful information on redox states and potentials. However cyclic voltammetry needs to be used along with other techniques to obtain full information concerning a particular electrochemical process.
The profile of potential versus time is shown in **Figure 2.1**. For the case of LSV (**Figure 2.1a**) the curve describes a straight line. For what concern cyclic voltammetry the E vs time profile is shown in **Figure 2.1b** and it can be described as a series of LSV with different directions. It is also interesting to note that the slope of the curve gives the scan-rate of the experiment.[(1)]

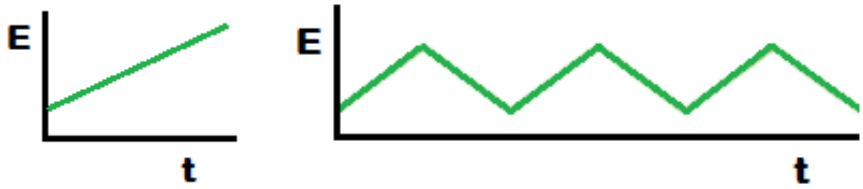

***Figure 2.1**: Trend of the potential change with the time for (**left**) Linear sweep voltammetry and (**right**) cyclic voltammetry. Note that the slope of each line represents the scan rate.*

For an electrode reaction we need to use at least two electrodes: a working electrode (W.E), where the redox process of interest occurs and a counter electrode (C.E), which operates to maintain the electro-neutrality of the solution through a half-reaction of the opposite sign.

Although the circuit can be closed with just the two of them, we normally use a third one, called the reference electrode (R.E), to compare the potential we apply to the working electrode.

It is possible to work without the reference electrode in a two-electrode configuration, but in this case what we apply/measure is the difference of potential between W.E and C.E.

This set up is used to analyze the performance of the whole electrochemical cell rather than to test a catalyst for one of the half-reactions. In this manner we are able to control accurately the reaction rate at the W.E. In all the experiments presented in this thesis a three electrode configuration was used, the scheme of which is shown in **Figure 2.2**.[(2)]

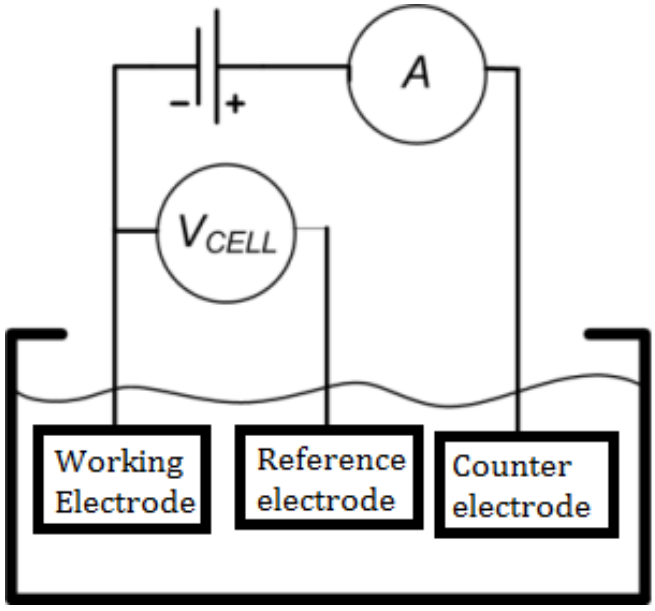

***Figure 2.2**: Scheme of a three electrode electrochemical cell.*

2.1.2 Chemical and electrochemical reversibility of a redox process

In the study of mechanisms that characterises an electrochemical process it is necessary to know the difference between chemical and electrochemical reversibility of a redox process. Consider the generic redox half reaction:

$$Ox \quad + ne^- \rightarrow Red$$

This process is defined as being chemically reversible if the species Ox is reduced to Red accepting n electrons and this reduced species is stable. This implies that Red, losing n electrons, forms Ox. If this event is prevented (for example if the reduced species decomposes) then the process will be defined as chemically irreversible.(1)

Concerning the classification of a process as electrochemically reversible or irreversible, it is necessary to consider both charge transfer from the electrode to the active specie and the mass transport from the bulk of solution to the electrode surface (and vice-versa)

So it is necessary to analyse the ratio between the rate constants of the following processes:

$$Ox_{\text{bulk sol.}} \rightarrow Ox_{\text{electrode surface}}$$

$$Ox_{\text{electrode surface}} + ne^- \underset{k_{ox}}{\overset{k_{red}}{\rightleftarrows}} Red_{\text{electrode surface}}$$

If k_{red} and k_{ox} are both large, and larger than the mass transport rate constants, then the second reaction remains constantly at the equilibrium and the process is defined as electrochemically reversible. When k_{red} and k_{ox} are both small, the second reaction cannot remain at equilibrium and only one process preferentially happens, depending which constant out of k_{ox} and k_{red} is higher. In this case we talk about electrochemical irreversibility.

Regarding electrochemical reversibility, there exists also a third case, intermediate between the two just described and which takes the name of an electrochemically quasi-reversible process. This happens when the rate for charge transfer is comparable with the rate of the mass transfer.(1) An example of cyclic voltammogram is shown in **Figure 2.3**

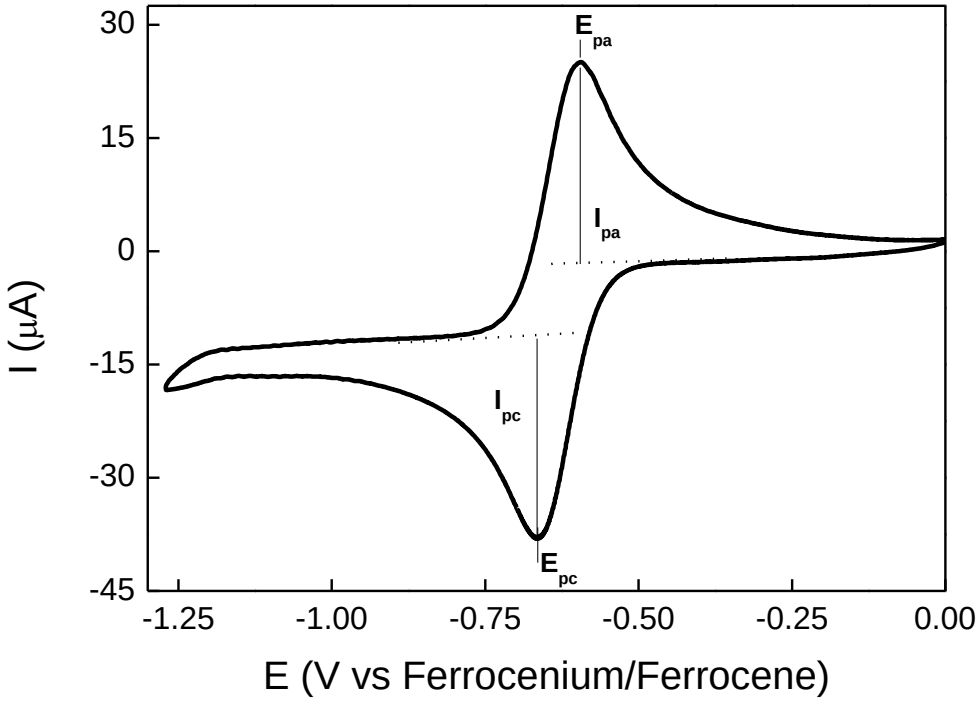

Figure 2.3:*Example of a Cyclic Voltammetry with features of reversibility*

Figure 2.3 shows the typical trend of a cyclic voltammogram with features of reversibility and the most important points to consider in a voltammogram. E_{pc} and E_{pa} are respectively the cathodic and anodic peak potential and the value of potential for which the current reaches respectively the minimum and the maximum. From the peak potentials it is possible to extrapolate the peak-peak separation that is important since it indicates the number of electrons involved and also can indicate the occurrence of internal rearrangements after the electronic transfer. The current is indicative of the reaction rate.[(1)] The ratio between the forward current peak and the return current peak is also a fundamental parameter since it indicates the reversibility of a process. If the ratio is close to 1 the process is considered to be reversible; otherwise this serves as evidence that some of the electrogenerated specie decomposes and doesn't undergo the return redox process.

2.1.3 Bulk electrolysis under controlled potential

During bulk electrolysis experiments a specific potential is maintained over time and the current vs. the time of electrolysis is recorded. The integration of the current with respect to time gives the charge passed during the process and from this we can obtain further

information; this kind of experiment is called chronocoulometry and is based on Faraday's law:

$$Q = nFM$$

Where:

Q = Amount of Charge passed (in coulomb)
F = Faraday's constant (96.485 coulomb/mol)
M = number of moles of active material present

Bulk electrolysis in this thesis is used mainly for two different purposes: the first one is to know the number of electrons involved in a redox process (as happens in **Chapter 4** and **Chapter 5**) and the second is to test the catalytic properties of different catalysts toward the promotion of a redox reaction and to determine turnover number (as happens in **Chapter 3**).

In the first case, a known amount of material is introduced into the cell and by applying an overpotential of between 0.1 and 0.2V bigger than the E_p for the process of interest, the amount of charge necessary to drive the reaction to completion can be determined. Since the current decreases asynptotically, the experiment is considered ended when current reaches $1/100^{th}$ of the initial current. Moreover if the redox process under examination is chemically reversible and the electro-generated species is, bulk electrolysis on the return wave should give the same value of charge passed. This is a proof of the reversibility of the process.[(2)]

In the second case, the important point of the bulk electrolysis experiment is the current. In fact, if we want to compare the performances of two different catalysts, the comparison of the resulting current recorded under the same experimental condition is a definitive proof of the efficiency of an electrocatalyst since the current recorded is a direct expression of the rate of reaction.

2.1.4 Reference electrodes

In order to compare the electrochemical potentials of different redox active species all the redox process are recorded versus a reference electrode. Conventionally the half reaction of the reduction of protons to give molecular hydrogen is taken as reference point (defined as 0V) and all the other redox process are referenced to it.

The standard electrode based on this reaction exists and is called Normal Hydrogen Electrode (NHE), but it is quite cumbersome and difficult to use in the lab. Hence reference electrodes based on other electrochemical systems are used instead and then referenced the potential of the NHE system, and indeed we often report the potential versus these secondary references.

The important thing for a reference electrode is that it needs to be non-polarizable. This means that the reference electrode needs to be able to maintain constant the potential during the experiment so that the potential for the working electrode can be referred to it at every moment.

In all the cases reported in the following chapters of this thesis all the measurements were carried in organic solvents and an $Ag/AgNO_3$ pseudo-reference electrode consisting of Ag wire immersed in a 0.1M solution of $AgNO_3$ in MeCN was used and all the measurements were then reported versus the Ferrocene/Ferrocenium couple.[2]

2.2 Optical spectroscopic techniques

2.2.1 Ultraviolet-Visible spectroscopy

Ultraviolet-Visible spectroscopy is also called electronic spectroscopy since it involves transitions of electrons from the ground state to an excited state following the interaction with a photon with an energy that usually falls in the visible region of the spectrum or in the UV region. When the transition involves electrons in the highest energy occupied orbital (i.e. HOMO-LUMO transitions) the energy involved will usually fall in the visible region or in the near UV region. In the visible region is common to find d-d transitions, recurrent in the coordination compounds treated in this thesis and also $\pi \rightarrow \pi^*$ transitions of molecules with extended π conjugated systems. A scheme for the electronic transition observable in the UV-Visible region of the spectrum is shown in **Figure 2.4.**[3,4]

From **Figure 2.4** it is easy to understand that transition between orbitals with a smaller energy gap will fall at lower energies than transitions involving a larger energy. Exploiting this spectroscopic technique it is possible to carry out both quantitative and qualitative analysis and it is also possible to conduct kinetic studies.

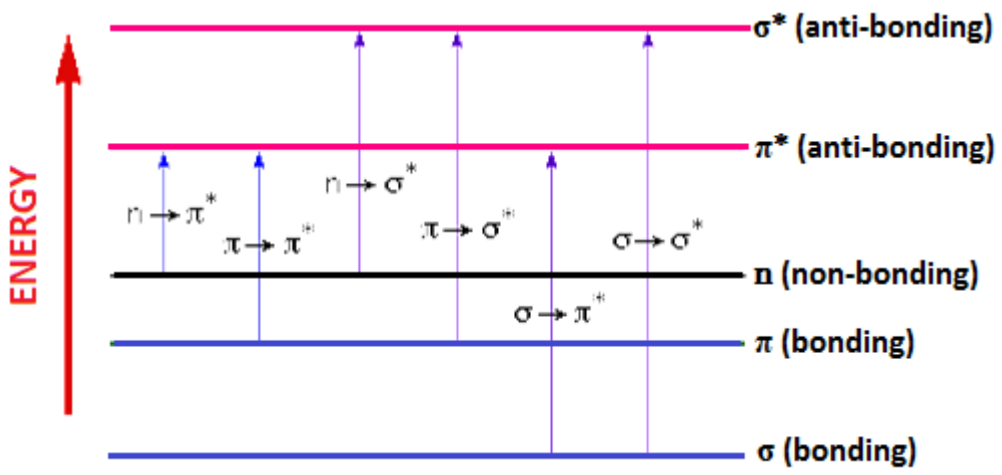

Figure 2.4: *Scheme illustrating the transitions observable in the UV-Vis region*

The absorption recorded following the interaction between a chromophore and a photon with the correct energy in a certain range of concentrations and in presence of monochromatic radiation follows the Lambert-Beer law. This law can be expressed as follows:

$$A = \varepsilon_\lambda l C \qquad (1)$$

This equation relates directly the absorbance A with the concentration C of a species presenting a maximum of absorbance at a specific wavelength λ. The coefficient ε is called the molar extinction coefficient and is a parameter that is specific to the species under examination. Via the preparation of a calibration curve it is possible to obtain directly the concentration of a species in a sample just plotting the value of absorbance and extrapolating the concentration of the sample from the Lambert-Beer law.[3,4] This method is directly used in **Chapter 6** and indirectly in **Chapter 3.**

The UV-Vis spectrometer can be schematically divided into the followings components:

- A source of radiation in the UV-Visible region, usually consisting of a deuterium lamp or a Xenon lamp. These two kinds of lamps allow one to cover effectively both the visible and the UV region.
- A monochromator, which allows the use a restricted interval of emitted radiation focused on the λ of interest. This in the past used to be a concave mirror but the use of reflectings diffraction gratings allows one to reach a precision in the wavelength selection of about 0.1nm.

- A receptacle for the sample also called cuvette, made with a material that is transparent to the UV-Vis radiation. This container usually has a length of 1cm in order to make immediate the application of Lambert-Beer law. Quartz is the best material for a cuvette since it transparent over a wide region (until 200 nm). Plastic materials are good for visible analysis but they absorb at wavelengths <350 nm making them useless in the UV region.
- A detector. It is a photosensitive device that exploits the photoelectric effect.

2.2.2 Infrared Spectroscopy

Infrared (IR) spectroscopy is a technique involving the interaction of a molecule with a photon of wavelength in the infrared region. The IR region of the spectrum extends from the nominal red edge of the visible spectrum at 700 nanometers (frequency 430 THz), to 1 millimeter (300 GHz).

Usually an IR spectrum can be visualized in a graph of infrared light transmittance on the vertical axis vs. frequency or wavelength on the horizontal axis. The typical units of frequency used in IR spectra are reciprocal centimeters with the symbol cm^{-1} (also called wave numbers).

The infrared region of the electromagnetic spectrum is usually divided into three sub-regions: near-IR, mid-IR and far-IR, named for their relation to the visible spectrum.

The higher-energy near-IR, approximately 14000–4000 cm^{-1} can excite overtone or harmonic vibrations. In this region is also possible to observe some electronic transitions.

The mid-infrared, approximately 4000–400 cm^{-1} may be used to study the fundamental vibrations and associated rotational-vibrational structure. [3,4]

The far-infrared, approximately 400–10 cm^{-1}, lying adjacent to the microwave region, has low energy and may be used for rotational spectroscopy. Classification of the IR regions in these sub-regions is a convention and these are only loosely based on the relative molecular or electromagnetic properties.

IR spectroscopy exploits the fact that molecules absorb frequencies that are characteristic of their structure. These absorptions occur at specific frequencies. When the frequency of the incident radiation matches the energy of the vibrational transition we can observe the absorption at that frequency.

The theoretical model for IR adsorption considers that a simple molecule formed of 2 different atoms behaves like a harmonic oscillator (even if there exists always a certain degree of anharmonicity) for which Hooke's Law is applicable.

If the Schrodinger equation is applied to this system the result is:

$$-\frac{\hbar^2}{2\mu}\frac{d^2\Psi}{dx^2}+\frac{1}{2}kx^2\Psi=E\Psi$$

Where: $\mu=\frac{m_Am_B}{m_A+m_B}$ is the reduced mass for the system and k is the strength constant for the bond.(4)

The solution of the Schrodinger equation gives the allowed vibrational energetic levels the energies of which can described by:

$$E_\mu=(\nu+\tfrac{1}{2})\frac{h}{2\pi}\omega \qquad (2)$$

Where ν is the vibrational quantum number and ω is the vibrational frequency given by the following relationship:

$$\omega=\sqrt{\frac{k}{\mu}} \qquad (3)$$

Introducing the term G it is possible to describe the energies in terms of wave number:

$$G(\nu)=\left(\nu+\tfrac{1}{2}\right)\frac{1}{2\pi c}\sqrt{\frac{k}{\mu}} \qquad (4)$$

From the foregoing it is easily verified that the greater is the strength of the bond the greater will be the frequency for a given vibrational level (and indeed the heavier the atoms are then the smaller will be the vibrational frequency). This fact can be proven by experiments with isotopes.(3)

In order to have a vibrational transition the necessary condition necessary is that a change of electric dipole moment needs to happen following the change of the atoms' relative positions.

Hence homo-atomic molecules like N_2 or O_2 are IR inactive. Indeed, non-polar molecules like CO_2 can resonate with radiation only because they can undergo asymmetric vibrations

producing an instantaneous dipole. The selection rule states that to observe absorption or emission, the following relationship needs to hold:

$$\Delta v = \pm 1$$

Despite this rule, it is possible also to observe the overtone bands related to superior harmonics that are in contrast with this selection rule. These particular bands are due to the anharmonicity of the chemical bond.(3)

The energy involved in vibrational transitions is smaller than the energy involved in electronic transitions by about one or two orders of magnitude. This is relevant since electronic transitions (treated in the previous section) are always accompanied by vibrational transitions since they occur at lower energy and they allow some otherwise forbidden electronic transitions to occur (for example the case of an asymmetric vibration). A scheme of this is shown in **Figure 2.5**

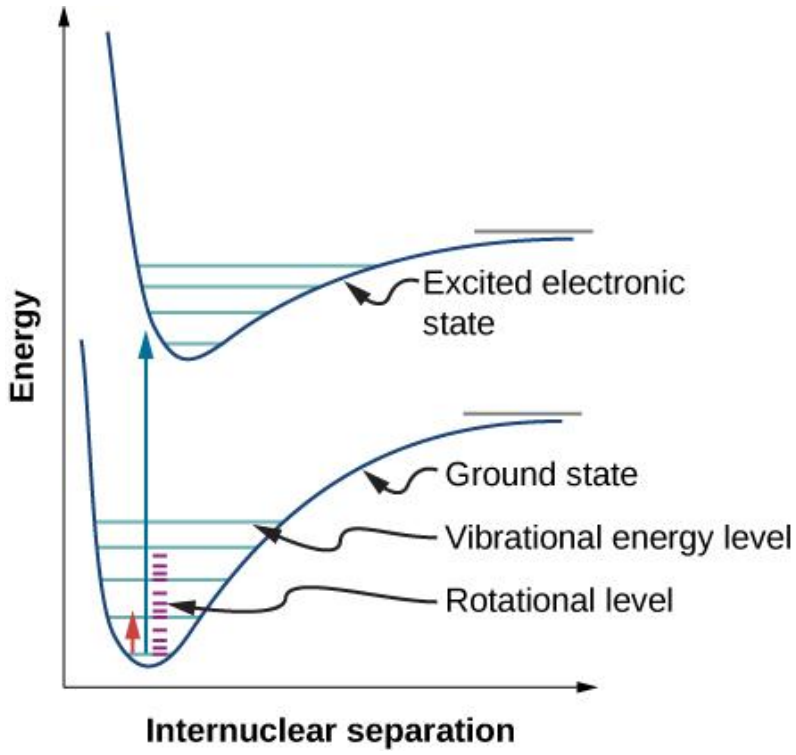

Figure 2.5: *Graph showing the energy difference between vibrational levels and electronic levels. Image used with permission (CC BY 3.0; OpenStax)*

Generally IR spectrometers work in Fourier transform mode, more commonly known as FT-IR. This kind of machine exploits the presence of an interferometer that allows

scanning of all the frequencies in the IR radiation generated by the source. A system of mobile mirrors allows one to collect an interferogram which represents the intensity in the temporal domain.[4]

Applying the Fourier transform, the IR spectrum that is obtained consists of the representation of the intensity in the frequencies domain. In this kind of instrument there is also a laser that emits red light (632.8nm) necessary to measure the exact position of the mirror. This is also useful for signal sampling.

FTIR allows better performance in terms of noise/signal ratio and the time of analysis of results is smaller compared with non FT-IR spectroscopy.

2.3 Single Crystal X-Ray diffraction

It is known that electromagnetic radiation can interact with matter by scattering as well as by absorption, as already seen for UV-Vis and IR spectroscopy. In this case radiation will be diffracted by matter and the electromagnetic waves involved change their direction of propagation. It is the electrons in the atoms which scatter the radiation. These particles give rise to secondary spherical waves and this phenomenon takes the name of elastic scattering when there is no absorption of energy from the electron. In the case when an exchange of energy is observed, then the energy of the scattered wave will be different and the process is called inelastic scattering.[5] This phenomenon is observed not only for light but also for particles like neutrons and muons for example. In this section only the diffraction due to the interaction of ligh and atoms is described.

X-Ray crystallography is a technique that exploits the interaction of X-Rays with a crystalline lattice producing a scattered beam. When these beams land on the detector they make a pattern of spots called diffraction pattern; each of these spots is called a reflection. The strengths and angles of these beams are recorded as the crystal is gradually rotated.

Every reflection corresponds to the reflection from one set of evenly spaced planes within the crystal.

Crystals are regular arrays of atoms and a regular array of scatterers produces a regular array of spherical waves and although these waves cancel one another out in most directions through destructive interference, in a few specific directions they add constructively. This is determined by Bragg's law:

$$2d \sin\theta = n\lambda$$

Where: *d* is the spacing between diffracting planes, θ is the incident angle, *n* is any integer, and λ is the wavelength of the scattered beam. These specific directions appear as reflections on the diffraction pattern. This is shown in **Figure 2.6.**

This resulting pattern is analysed and the results coming from this analysis lead to the atomic structure of a molecule. For single crystals of sufficient purity and regularity, X-ray diffraction data can determine the mean chemical bond lengths and angles to within a small confidence interval.[5,6]

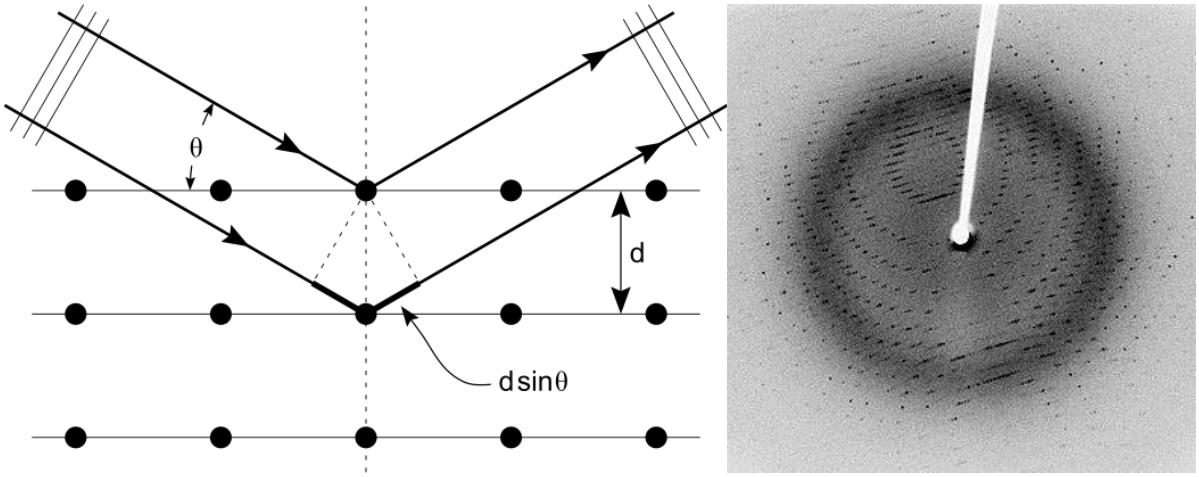

Figure 2.6: *On the right side is shown an image of a diffraction pattern. On the left side is shown a scheme for the elastic scattering of the incident radiation with the parameter given by Bragg's law.* ***Readapted from*** *https://en.wikipedia.org/wiki/X-ray_crystallography Copyright 2011.*

X-rays are used to produce diffraction patterns because their wavelength is typically the same order of magnitude (1–100 angstroms) as the spacing distance between planes in the crystal. This is a necessary condition to observe significant diffraction since spacing between the scatterers and the wavelength of the impinging wave should be similar in size.

It is possible to recognise, in the technique of X-rays single-crystal diffraction, three basic steps: the first step consists in obtaining suitable crystals of the desired compound. These crystals should be sufficiently large and pure in composition. Ideally crystals need to be larger than 0.1 mm in each dimension. Moreover it is necessary that these crystals show no significant imperfections such as cracks for example.

In the second step, the crystal is placed in an intense beam of monochromatic X-rays, producing the regular pattern of reflections. Since the crystal is gradually rotated, previous reflections disappear and new ones appear. The intensity of every reflection is recorded for every orientation of the crystal.

In the third step, these data are combined computationally with complementary chemical information to produce and refine a model of the arrangement of atoms within the crystal. The final, refined model of the atomic arrangement now called a crystal structure and is stored in a public database (e.g. the Cambridge Crystallographic Database).

The instrument used to carry out this kind of experiment is called diffractometer and it is composed of a source of high energy and monochromatic radiation, some apparatus with the scope to focus the radiation, a compartment for the sample, and a detector. The scheme of a diffractometer is shown in **Figure 2.7**

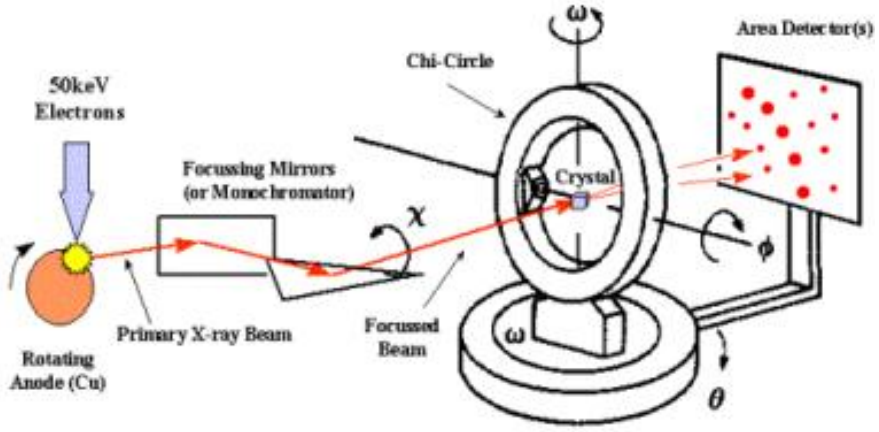

Figure 2.7: *Scheme of a diffractometer for single crystal X-ray diffraction. Reproduced fromhttp://pruffle.mit.edu/atomiccontrol/education/xray/xray_diff.php*

Electrons with high energy are shot toward a metallic anode, usually made of copper or molybdenum. This metallic anode releases monochromatic X-rays of typical wavelength via photoelectric effect. X-rays arrive at the sample, located in a goniometer that allows the sample to rotate in all directions. A detector collects the diffraction pattern and the structure is refined via specific software.

2.4 Nuclear Magnetic Resonance spectroscopy (NMR)

2.4.1 Physical Fundamentals of NMR

Nuclear magnetic resonance (NMR) spectroscopy is a technique that allows one to obtain detailed information about the structure of a molecule by studying the behaviour of the magnetically active atomic nuclei in presence of a magnetic field.[7]

After immersing the sample in a strong magnetic field the absorption of a radiofrequency (100-1000 MHz that causes nuclear spin transition in some of the nuclei) is measured. Hence using NMR it is possible to observe only nuclei that possess a nuclear magnetic

moment of spin. This magnetic moment shows the same behaviour as a needle in a compass and can be re-orientated when a magnetic field is applied. The nuclear magnetic moment is given by the relationship:

$$\mu = I\gamma\frac{h}{2\pi}$$

Where *I* is the quantum number for the nuclear spin, γ is the gyromagnetic ratio, and *h* is the Planck constant. Nuclear spin arises from the protons and neutrons forming the nucleus. These particles behave like they are rotating around their axis and both show spin ½.

Like the electrons in an orbital protons and neutrons can also couple. In some atoms, protons and neutrons are present in even number, so all the spins are coupled and the resulting *I* is 0. In other atoms like ^{1}H and ^{13}C, protons or neutrons are present in odd number and show an *I* is different to zero.(7)

It is possible to distinguish three different cases:

The first case is where both protons and neutrons are present in even number and $I = 0$ so the atom is silent with respect to NMR spectroscopy. The second case is where both protons and neutrons are odd, in this case *I* is an integer and it is possible to study these nuclei with NMR even if the study is difficult.

In the third case (where *I = ½, 3/2, 5/2* etc.) it is possible to study the system with NMR more easily then in the previous case.

When a nucleus with spin is immersed in a magnetic field it is subjected to two different forces that have the effect of rotating the nuclear spin in order to align with the external magnetic field, B_0.

The possible orientations are governed by the quantum number *m*, it can assume values going from +l to –l with an increment of 1 unit. Globally it can take $(2l + 1)$ different values.

For ^{1}H there are only two possible orientations, one with m = - ½ and another one with m = +½.

These two states have slightly different energies. The energy aligned with B_0 has a slightly lower energy than the state with m = - ½ (aligned opposite to B_0).

Nuclear magnetic moment does not remain stationary but it oscillates around the direction of B_0 with a precession movement similar to a spinning top.

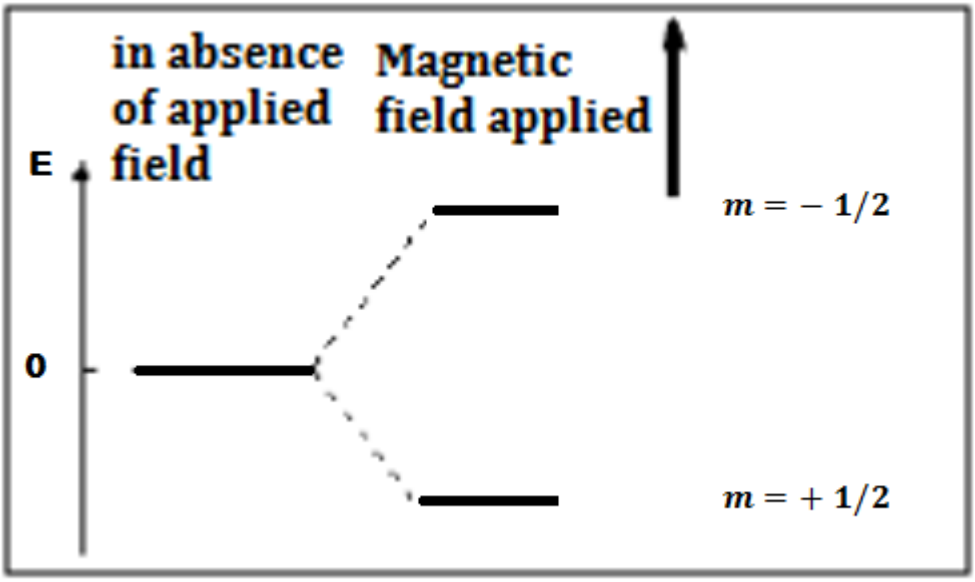

Figure 2.8: *The representation of the two spin states for a particle with I = ½. Readapted with permission from http://www.pianetachimica.it*

In the case of ^1H, the precession motion of nuclear magnetic moments occurs with a frequency proportional to the ΔE between the two levels. This frequency is called Larmor freuency and is given by the formula:

$$\nu = B_0 \frac{\gamma}{2\pi}$$

Increasing the value of B_0 also increases the value of the Larmor frequency and then the ΔE between the two levels also increases. Since the difference is on the order of $10^{-5}/10^{-6}$ kcal/mol, the population in the two states is practically identical, with a small prevalence for the lower energy state.(7)

If the sample is irradiated with a radiation of frequency comparable with the Larmor Frequency then an interaction of the magnetic component of the radiation with nuclear magnetic moments (also oscillating at Larmor's frequency) is observed. In this way the energy from radiation can be transferred to the nuclei.

Every adsorption involves a change in the orientation of nuclear spin that rotates from aligned with the field to be aligned opposite to the field. When this spin transition occurs

nuclei are in resonance with the radiofrequency and the name Nuclear Magnetic Resonance comes from this.

In the first NMR instruments, the sample was irradiated with increasing radiofrequencies in order to excite in sequence all the nuclei and then recorded the absorbed energy. This technique was very slow and nowadays does not find application. In modern instruments, the signal is generated with a pulsed method and subjected to a subsequent Fourier Transform. With this technique all the nuclei from one species are excited at the same time using a pulse of radiofrequencies containing the appropriate frequency range. Data are then elaborated with Fourier transforms.

In order to understand how radiofrequencies interact with the nuclei under examination it is necessary to introduce the macroscopic magnetization vector M_o that is the result of all the nuclear magnetic moments.

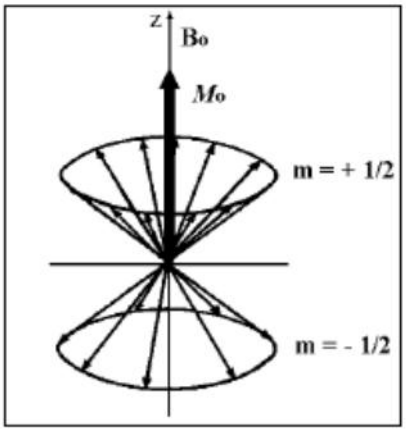

Figure 2.9: *Visualization of the Mo vector resulting from the oriented spins of singles particles. Readapted with permission from http://www.pianetachimica.it.*

This is not zero since there is a small excess of population in the state with the spin aligned with B_0. This vector will be orientated along a dimension indicated as z (direction of the magnetic field) and the radiofrequency pulse is irradiated along the x direction. Following the adsorption of energy, nuclei undergo the spin transition that macroscopically is represented by the M_o vector rotating and moving away from z axis to approach the x-y plane and a precession starts around the z axis as shown in **Figure 2.10**

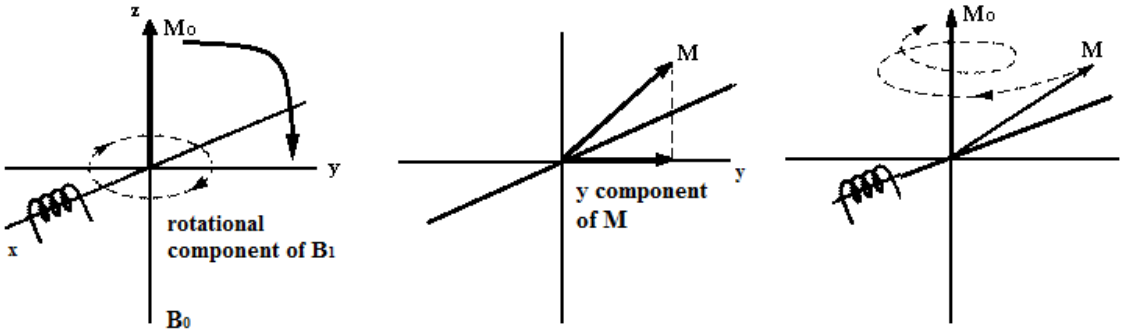

Figure 2.10: *Graphic description of the excitation of M_0 and the subsequent relaxation. Readapted with permission from http://www.pianetachimica.it.*

At this point, the radiofrequency pulse stops. The nuclei then emit a signal in the radiofrequency range that decays with time. This can be seen as an echo of the adsorbed signal. To record this signal a receiving circuit, B_2, orientated along y axis, is used to measure the oscillation of the y-component of M. Absorbed energy is slowly released via two different mechanisms: one called spin-lattice relaxation (which involves interaction of the spin with the dipoles of surrounding molecules) and the other called spin-spin relaxation, which involves the interaction with the spin of surrounding H atoms.

The M vector, due to this dissipation of energy, returns to the Mo value by doing precession spirals around z axis, to a position where M_y is zero. The time necessary to recuperate 66% of the magnetization is called the T1 relaxation time and is usually around 1 second. The relaxation time spin-lattice T1 is used in medicine as it is indicative of tissue where the hydrogens under examination are immersed. The interval of the radiofrequency pulse t(i) needs to be determined with absolute precision to produce a strong NMR signal. If t(i) is enough to bend M_o by 90° then the maximum M_y is obtained. Usually t(i) is on the order of microseconds.

The recorded signal is oscillates and decays with the time. It is called FID (Free Induction Decay). The FID for CH_3I is shown in **Figure 2.11.**

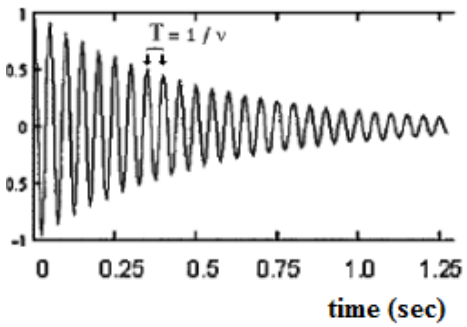

Figure 2.11*:FID of CH_3I for hydrogen nuclei. Readapted with permission from http://www.pianetachimica.it.*

Since CH_3I has three equivalent hydrogens, they have the same frequency of resonance. In the graph this frequency is easy to distinguish since it is the wavelength between two successive crests and represents period T of the wave. The frequency is then obtained from:

$$\nu = \frac{1}{T}$$

Starting from a graph in the time domain, the FID, it is possible to obtain a new graph as a function of the frequency by exploiting the Fourier transform. This is the NMR spectrum showing the adsorbed frequency and that then re-emitted by the atoms of the molecule.(7)

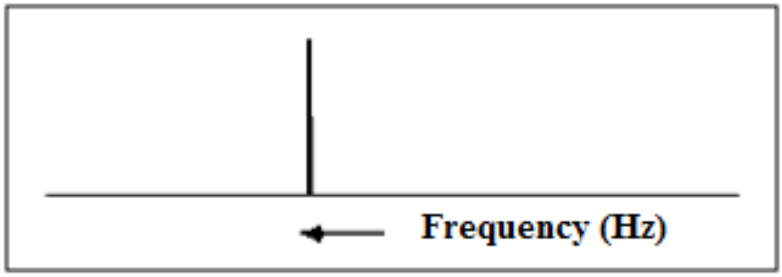

***Figure 2.12**: ^1H NMR spectrum of CH_3I Readapted with permission from http://www.pianetachimica.it*

2.4.2 The Chemical Shift

Since all the hydrogen atoms have the same magnetic moment μ it is obvious to think that they all resonate at the same frequency if a specific B_0 is applied. However if this was the case then NMR spectroscopy would be useless since in the spectrum there would be only one signal for all the hydrogens in all the molecules.

Luckily for us in nature, the chemical environment influences the frequency of the resonating nucleus and the consequence is that the frequency of resonance of nuclei in different chemical environments is different.

Depending the electronegativity of the atom to which it is bonded, a proton can experience a greater or lesser effective electron density than might otherwise be expected. Electrons are charged particles and when an external magnetic field is applied they undergo a small electronic circulation that generates a small induced magnetic field B_i. This induced magnetic field is opposite in sign to B_0 but is much smaller than it.

If the hydrogen is bound to an atom that is not very electronegative it experiences an increase in electron density and feels an induced magnetic field less intense than the case where is bound to a more electronegative atom. In the first case the hydrogen adsorbs at lower frequencies then in the case where it is bound to an electronegative atom.

The variation of the absorption frequency is called the chemical shift. To be quantified, it is necessary to assign one of the hydrogen signals as a reference and assign to it the value of zero on the chemical shift scale.

For convention, zero is attributed to the hydrogens in tetramethyl-sylane ($Si(CH_3)_4$ since they are more shielded because of the low electronegativity of silicon atom. For this reason the chemical shifts of most hydrogens are positive.

Moreover chemical shift is proportional to the B_0 applied since it is generated from the shielding effect of the electrons which are induced from the same B_0. Hence instruments working with different applied fields will generate different chemical shifts and to avoid confusion, the chemical shift is defined as follow:

$$\boldsymbol{Chemical\ shift} = \frac{Hz_{under\ exam} - Hz_{TMS}}{MHz_{H\ TMS}}$$

The chemical shift is in this way the same for all instruments independent of the intensity of the magnetic fields applied.

The common scale for the chemical shift is usually between 0-12 ppm for ^{1}H NMR and between 0-220 ppm for the ^{13}C NMR.(7)

2.5 Electronic Paramagnetic Resonance Spectroscopy (EPR)

Electronic Paramagnetic Resonance, also called Electronic Spin Resonance (ESR) is a spectroscopic technique where the magnetic component of the radiation is absorbed by atoms or molecules that have an unpaired electron. For this reason it finds application in the study of species like organic radicals, transition metal compounds and solids with local defects.(8)

EPR spectroscopy presents some similarities with NMR but also a number of differences. For example, in NMR the transition between the two states (when I = ½) derives from the alignment of the nuclear magnetic moments with the applied field and the transition happens when the correct radiofrequency is applied. In EPR the different energy state

derives from the interaction of electronic spin moments with the magnetic field (the electronic Zeeman effect) and transitions are observed when a frequency in the microwave region is applied.

Another difference is that electron has an intrinsic angular moment (spin) and an orbital angular moment. Both of these factors, in the presence of an external magnetic field, generate a corresponding magnetic moment that needs to be taken into account to describe properly the EPR phenomenon.[7,8]

It is known from classical physics that the angular momentum (L) of a particle with mass m describing an orbit with radius *r* at a specific speed (*v*) is as follows:

$$L = mrv \tag{5}$$

Since the electron in the orbital does not follow a circular orbital but it follows quantum mechanical rules, this equation is not the correct mode to describe the orbital moment. From the Schrodinger equation for the wave-function describing the hydrogen atom one can obtain the orbital quantum number *l* that determines the value of the orbital angular momentum L:

$$L = \sqrt{l(l+1)\,{}^{h}/_{2\pi}} \tag{6}$$

The component of the angular momentum vector on the z axis is quantized and it can assume only the allowed values for the magnetic quantum number m_l that assumes integer values between $+l$ and $-l$. For example if $l = 2$ (as in the case of a d orbital) then $m_l = +2, +1, 0, -1, -2$.

Associated with the orbital angular momentum there is the magnetic orbital momentum μ_l which it is possible to describe by classical physics: $\mu = IA$ where I is the current and A is the orbital area.[8]

Since $I = \frac{q}{T}$ (where T is the period of the orbit) $T = \frac{v}{2\pi r}$ and q = -e is obtained that:

$$I = -\frac{ev}{2\pi r} \tag{7}$$

If the numerator and denominator are multiplied by $m_e r$ (m_e is the mass of an electron), the equation becomes:

$$I = -\frac{em_e vr}{2\pi m_e r^2} \quad (8)$$

So taking $A = \pi r^2$ the equation for μ becomes:

$$\mu = IA = \frac{em_e vr}{2m_e} \quad (9)$$

Substituting equation 5 for L into the equation 9 we have:

$$\mu_l = -\frac{e}{2m_e} L \quad (10)$$

Since orbital angular momentum is quantized, so also the orbital magnetic moment associated is quantized and:

$$\mu_l = -\frac{e}{2m_e} \sqrt{l(l+1)\frac{h}{2\pi}} \quad (11)$$

Combining all the constants as the Bohr magneton β_e, for an electron: $\beta_e = \frac{eh}{4\pi m_e}$

The expression for μ_l becomes:

$$\mu_l = \sqrt{l(l+1)}\,\beta_e \quad (12)$$

From this relationship it is evident that the orbital magnetic momentum on the z axis is also quantized and can assume only values corresponding to m_l. Then:

$$\mu_z = -m_l \beta_e \quad (13)$$

Concerning the spin, electrons have half integer spin like neutrons and protons and so they obey to the same quantum mechanical laws and (similarly to the case of NMR spectroscopy) the spin component is represented as:

$$S = \sqrt{s(s+1)}\,{}^{h}/_{2\pi} \qquad (14)$$

This equation represents the component of the vector representing the spin angular moment on the z direction and it can assume only values allowed by the quantum number, m_s (= ±1/2).[8]

If the same considerations used for the orbital momentum are applied to the spin, one can obtain an expression analogous to the previous one apart from the coefficient g:

$$\mu_{ls} = \sqrt{s(s+1)}\,g\beta_e \qquad \text{and consequentially:} \qquad \mu_z = -m_s g \beta e$$

As in NMR spectroscopy, also in EPR spectroscopy is present g parameter that links the μ to the quantum number of the angular momentum. In EPR g parameter is not constant. In fact in NMR spectroscopy g for nuclei is considered constant and is introduced the screen constant σ to take into account the difference between nuclei in different chemical environments. The measured g-value for the free electron is 2.0023 (approximately). Spin angular momentum and orbital angular momentum can be considered separately in EPR apart from the case where it is necessary to take into account spin-orbit interactions (as in the case of a transition metal coordination complex). In this case the g coefficient will assume a value that is sensibly different from g of the free electron. Indeed for organic radicals this interaction is negligible.[7,8]

When a molecule with a $\mu_e \neq 0$ is introduced into a magnetic field, it behaves like a magnetic dipole and will show a potential energy depending on the orientation of the magnetic field applied. This potential energy is given by the scalar product between μ and the applied field as shown in **Figure 2.13.**

$$E = -\mu_z B = m_s g \beta_e B$$

As appears evident the energy is at the minimum when the dipole is aligned with the applied field (ϑ = 0°) and when the equation for μ_z is:

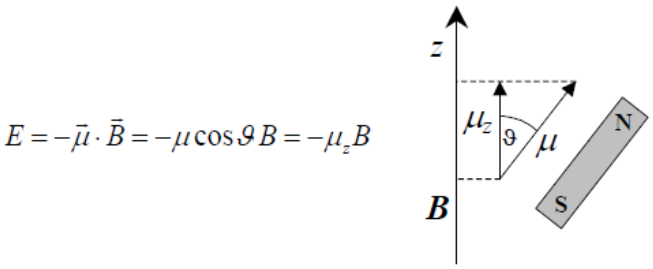

Figure 2.13: *Potential energy of a dipole in a magnetic field Readapted with permission from http://www.pianetachimica.it*

The energy of the electrons depends on the spin magnetic quantum number and on the intensity of the applied field. **Figure 2.14** represents this situation.[8]

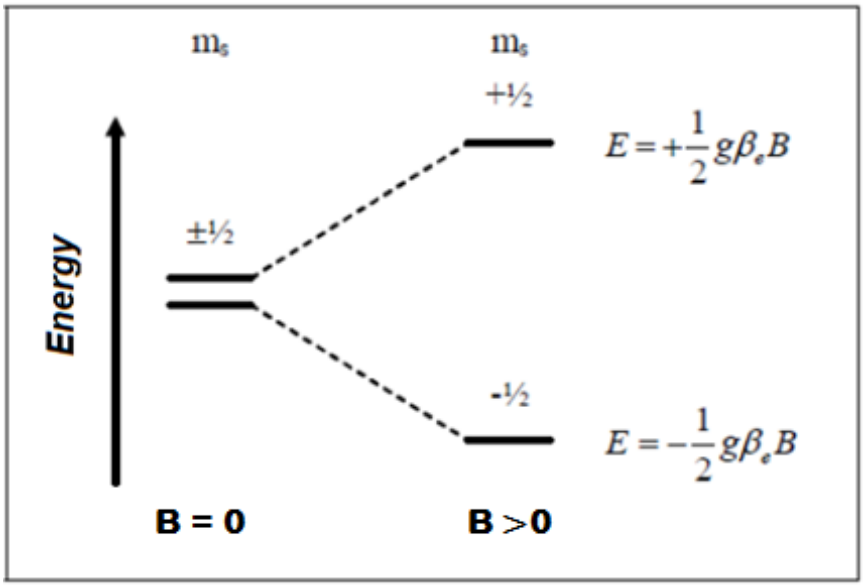

Figure 2.14: *Energies for electrons immersed in a magnetic field. Readapted with permission from http://www.pianetachimica.it*

When the applied field is 0 the two levels are isoenergetic, but the presence of an external field removes the degeneracy between the levels, and the ΔE between the two values, called Zeeman levels, increases with the increasing applied field. The expression for this energy difference is:

$$\Delta E = +\frac{1}{2} g\beta_e B - \left(-\frac{1}{2} g\beta_e B\right) = g\beta_e B$$

Transition between two energy levels is observed when the sample is irradiated with a radiation of frequency ν that is resonant with ΔE: $h\nu = g\beta_e B$

When these conditions are met one molecule is excited from the ground state to the excited state, changing the alignment of the spin towards the applied magnetic field. The g value for the species under examination can be calculated from the known terms (h, ν, β_e) using the value of B at the maximum of the curve of absorption:

$$g = \frac{h\nu}{\beta_e B_r}$$

When the electronic spin momentum interacts with the momentum μ_n of other nuclei with nuclear spin *I*, the single EPR signal is split into 2*I* +1 equidistant lines and this interaction is called the hyperfine interaction. This phenomenon can be explained via the Fermi contact interaction. However the unpaired electron is not only located in a specific atom but sometimes can be shared in a wider molecular orbital. For this reason the unpaired electron can interact also with nearby nuclei, and even if the probability to be in contact with these atoms is smaller, sometimes it is possible to distinguish between the interaction of the electronic spin with the nucleus around which the electron is orbiting and the interaction of the electronic spin with the nuclei surrounding the atom around which the uncoupled electron is orbiting. Sometimes this contribution is detectable and is very useful since it gives precious information, for example concerning the coordination sphere of a metal coordination complex.[8]

When these two kinds of interaction are taken in account the equation for the Hamiltonian operator will be:

$$\hat{H} = \hat{H}_e + \hat{H}_N + \hat{H}_{hyperfine} = g\beta_e B\hat{S}_z - g_N\beta_N B\hat{I}_z + A\hat{S}_z\hat{I}_z$$

Energetic modifications caused by the nuclear Zeeman are smaller than the effect due to the electronic Zeeman effect. Moreover the Hyperfine interaction involves smaller energies, however the resulting spectrum can give more information. A scheme of this is shown in **Figure 2.15**

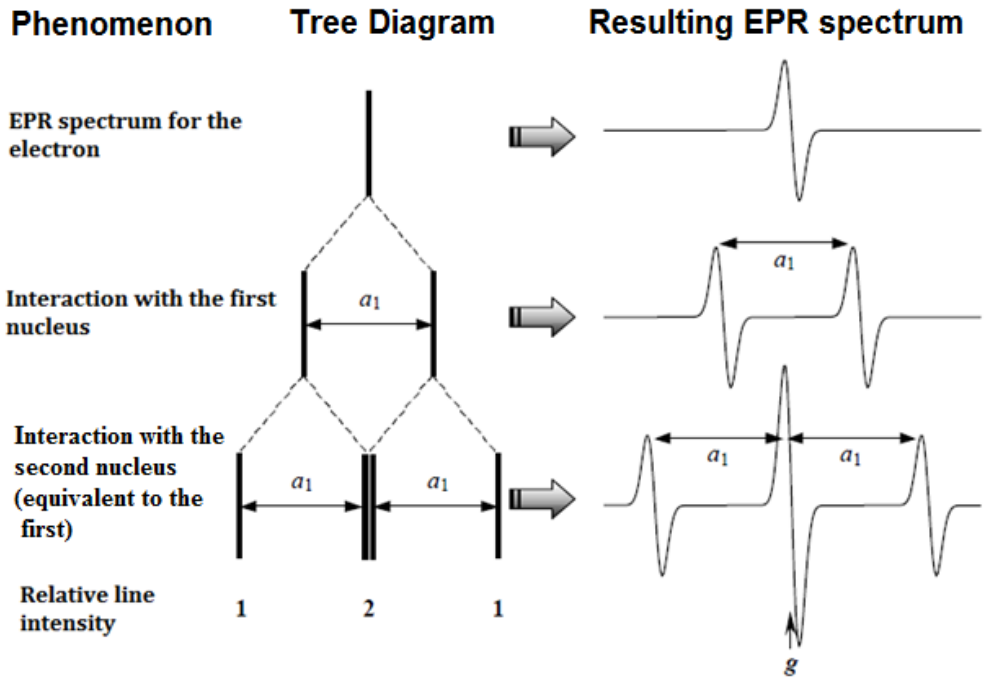

Figure 2.15: *Scheme for the interpretation of an EPR spectrum. In this specific case the spectrum is that of the hydroxymethyl radical*

2.6 Practical experimental details

2.6.1 General Experimental Remarks

Tetrabutylammonium hexafluorophosphate (TBA-PF_6 >98%) was supplied by TCI. Bis(2-pyridylmethyl)amine (97%), benzoic acid (99.5%), $Cu(ClO_4)_2 \cdot 6H_2O$ (98%), sodium nitrite (min. 99.0%) and tetrabutylammonium nitrite were purchased from Sigma Aldrich. 2,2′-bipyridine (≥99%), 5,5′-dimethyl-2,2′-bipyridine (98%), catechol (1,2-dihydroxybenzene, ≥99%), $Co(NO_3)_2 \cdot 6H_2O$ (98%) and $CoCl_2 \cdot 6H_2O$ (98%) were supplied by Sigma Aldrich. 1,2-benzenedithiol (96%) was obtained by Alfa Aesar. All chemical reagents and solvents were used as purchased.

Electronic spectra were collected on a JASCO V-670 spectrophotometer using 1 cm pathlength cuvettes. Solid state IR spectra were collected on Thermo scientific Nicolet iS5. Solution-phase IR spectra were collected with a Shimadzu FTIR-8400S.

X-band EPR spectra were recorded on a Bruker ELEXSYS E500 spectrometer, and simulations performed with Bruker's Xsophe software package.[97]

All ^{1}H and ^{13}C NMR spectra were recorded on a Bruker AV 400 instrument, at a constant temperature of 300 K. Chemical shifts are reported in parts per million from low to high field. Coupling constants (*J*) are reported in hertz (Hz). Standard abbreviations indicating

multiplicity were used as follows: m = multiplet, t = triplet, d = doublet, s = singlet. Assignments of signals to specific protons are based on 2D (COSY) spectra.

CHN analyses were collected by the services facility at the School of Chemistry, University of Glasgow, as were FAB mass spectra (positive mode) and LM-MS mass spectra (ESI, positive mode, Bruker micrOTOF-Q machine).

TGA analyses were collected by the services facility at the School of Chemistry, University of Glasgow on a TA Instruments SDT Q600 machine. All the experiments were carried out under Argon at a flow rate of 100 mL/min and the temperature ramp rate was 10 °C per minute.

CHN analyses were collected by the services facility at the School of Chemistry, University of Glasgow, as were LM-MS mass spectra (ESI, positive mode, Bruker micrOTOF-Q machine). Experiments performed at "room temperature" were carried out at 20 °C.

Electrochemical experiments were performed as below. Experiments performed at "room temperature" were carried out at 20 °C.

2.6.2 Electrochemical Methods

Electrochemical studies were performed in a three-electrode configuration using CH Instruments CHI760D potentiostats. For cyclic voltammetry, a Pt wire was used as the counter electrode, along with an $Ag/AgNO_3$ pseudo reference electrode (CH Instruments). Potentials are reported relative to the ferrocenium/ferrocene couple, the position of which was judged by adding ferrocene to the samples analyzed. Working electrodes were washed with acetone and deionized water prior to use.

Cyclic voltammograms were collected at room temperature under an atmosphere of Ar at a scan rate of 100 mV s^{-1}, unless otherwise noted. A glassy carbon button electrode (area = 0.071 cm^2, CH Instruments) was used as the working electrode for cyclic voltammetry. The supporting electrolyte was 0.1 M TBA-PF_6 in acetonitrile, unless otherwise noted. Measurements were conducted without stirring and with *i*R compensation enabled. The *i*R test function available on the CH potentiostats uses the general method developed by He and Faulkner.[9]

Bulk electrolyses were carried out in 0.2 M TBA-PF_6 in acetonitrile (15 mL) in a sealed single-chamber cell (headspace volume = 97 mL), using an $Ag/AgNO_3$ pseudo reference electrode, a Pt wire counter electrode and a large area glassy carbon (Carbon-Vitreous 3000C (C) foil, 1.0 mm thickness, GoodFellow) foil electrode of area 4.6 cm^2. Solutions

were stirred during bulk electrolyses, which were conducted without considering any resistive losses; solution resistances were measured using the *i*R test function (as for cyclic voltammetry) and were found to be on the order of 10–30 Ω. At the currents typically passing in these experiments, the voltage drops caused by this uncompensated resistance were thus generally under 1 mV, and could be neglected.

2.6.3 Crystallography

Crystallographic data were collected at the University of Glasgow on a Bruker APEX-II CCD diffractometer for [**17**-CH_3CN]$(ClO_4)_2$, and using a Bruker D8Venture with PhotonII detector and dual Imus 3.0 micro-source for [**18**-NO_2].

Crystallographic data for compound **20** and **24** were collected at the EPSRC UK National Crystallography Service at the University of Southampton using a rotating anode radiation source,[10]

For [**17**-CH_3CN]$^{2+}$, a blue, block-shaped crystal of dimensions 0.42 × 0.4 × 0.31 mm was used for single crystal X-ray diffraction data collection. $C_{22}H_{23}CuN_5O_2 \cdot 2(ClO_4)$ crystallized in the triclinic space group *P*-1 (space group No. 2), with unit cell dimensions a = 8.4706(7), b = 8.8319(8), c = 17.982(2) Å, α = 95.471(2)°, β = 99.637(2)°, γ = 102.415(2)° and V = 1283.2(2) Å^3, T = 100 K. 15864 reflections were measured by ω scans, 5798 independent reflections with R_{int} = 0.068, θ_{max} = 27.4°, θ_{min} = 1.2° using Mo *Kα* radiation, λ = 0.71073 Å. The structure was solved using Superflip[11-13] and refined using SHELXL[14] within OLEX2[15] which was also used for molecular graphics and to prepare material for publication. CCDC entry 1588602 contains the supplementary crystallographic data for this compound.

For [**18**-NO_2], a green block-shaped crystal of dimensions 0.39 × 0.33 × 0.16 mm was used for single crystal X-ray diffraction data collection. $C_{19}H_{17}CuN_5O_4 \cdot 0.5(C_2H_3N)$ crystallized in the orthorhombic space group *Pbcn*, with unit cell dimensions a = 14.817(8), b = 19.01(1), c = 15.569(9) Å and V = 4386(4) Å^3, T = 298 K. 8296 reflections were measured by ω scans, 5403 independent reflections with R_{int} = 0.037, θ_{max} = 28.3°, θ_{min} = 2.2° using Mo *Kα* radiation, λ = 0.71073 Å. The structure was solved using XT[16] and refined using SHELXL[17] within OLEX2, which was again used for molecular graphics and to prepare material for publication. The nitrite nitrogen atom is well-ordered; however, the oxygen atoms show disorder and were modelled as follows: O1N was modelled as fully-occupied and common to both partially-occupied orientations of O2N and O3N, each of which was modelled as 0.5-occupied. All oxygen atoms show large atomic displacements. Distance

similarity restraints were applied to the N1N–O2N and N1N–O3N distances. CCDC entry 1588603 contains the supplementary crystallographic data for this compound. More details on the crystallographic data and its collection can be found in the **Appendix A**.

For compound **20**: $C_{30}H_{28}CoN_4O_2 \cdot 1(NO_3)$, M = 597.50, trigonal, a = 21.2619 (15), c = 14.3882 (10) Å, U = 5633.0 (7) Å^3, T = 100 K, space group P-3c1 (no.165), Z = 6, 40590 reflections measured, 3339 unique (R_1 = 0.24), which were used in all calculations. The final w$R(F^2)$ was 0.126 (1325 reflections with $I > 2\sigma(I)$).

SQUEEZE[18] was used to calculate the solvent-accessible volume and the electron density within it; 1149 Å3 containing 214 electrons. This equates to ~20% of the total crystal volume being occupied by disordered solvent, which accounts (at least partially) for the sub-optimal R-value. CCDC 1452332 contains the supplementary crystallographic data for this chapter. More details on the crystallographic data and its collection can be found in the **Appendix A**

For compound **24**, dark blue/green opaque crystal of dimensions 0.10 × 0.09 × 0.02 mm was used for single crystal X-ray diffraction data collection. $C_{48}H_{44}Co_2N_6S_4 \cdot 2(NO_3) \cdot 1.25(H_2O) \cdot 0.25(CH_3OH)$ crystallised in the monoclinic space group $P2_1/n$ (space group No. 14), with unit cell dimensions a = 12.6021 (3), b = 22.7893 (5), c = 17.1872 (6) Å, β = 103.500 (3)° and V = 4799.7 (2) Å^3, T = 100 K. 59216 reflections were measured by ω scans, 11002 independent reflections with R_{int} = 0.053, θ_{max} = 27.5°, θ_{min} = 2.4° using Mo $K\alpha$ radiation, λ = 0.71073 Å, on a Rigaku FRE+ equipped with VHF Varimax confocal mirrors and an AFC10 goniometer and HG Saturn 724+ detector diffractometer. Data were integrated using *CrysAlis PRO* 1.171.38.43 (Rigaku OD, 2015), with Lorentz and polarization corrections made. A multi-scan correction for absorption was applied T_{min} = 0.538, T_{max} = 1.000, μ = 0.93 mm^{-1}, Mr = 1105.54, F(000) = 2284, ρ_{calcd} = 1.530 Mg m^{-3}.

The structure was solved using ShelXT.[16] All 11002 reflections were used in the refinement and positions and anisotropic atomic displacement parameters (adps) were refined for all fully occupied non-hydrogen atoms using SHELXL within OLEX2.[14,15] A region of lattice solvent was modelled as 0.75 H_2O with two further 0.25-occupied H_2O molecules and a 0.25-occupied molecule of MeOH. One nitrate anion was modelled with the oxygen atoms over two partially occupied (0.9/0.1) sites. The 0.75-occupied H_2O hydrogen atoms were located in difference Fourier maps and refined with O-H distance restraints, hydrogen atoms for the 0.25-H_2O and MeOH were not included in the model but were included in the unit cell contents and values derived from them, otherwise hydrogen

atoms were placed in calculated positions and refined as part of a riding model or as a rigid rotor for Me hydrogens. Final $wR(F^2)$ = 0.097, $R[F^2 > 2\sigma(F^2)]$ = 0.043 (8780 reflections with $I > 2\sigma(I)$) for 670 parameters, $\Delta\rho_{max}$ = 0.50 e Å^{-3} and $\Delta\rho_{min}$ = −0.39 e Å^{-3} maximum and minimum residual electron density. CCDC 1537318 and **Appendix A** contain the supplementary crystallographic data for this chapter.

2.6.4 Calculations

Calculations concerning compounds **17**, **18** and **24** are made using the program package ORCA.[19] Calculation for compound **20** and **21** were performed with the Gaussian 09 program.[20] The input geometry for all molecules were generated using ArgusLab. The geometries of all molecules were fully optimized by a spin-unrestricted DFT method employing the BP86 functional with acetonitrile as solvent.[21,22]

For compounds **17**, **18**, **24**, split-valence basis sets with one set of polarization functions (def2-SVP) were used for all atoms.[23,24] A scalar relativistic correction was applied using the zeroth-order regular approximation (ZORA) method.[25-27] The RIJCOSX approximation combined with the appropriate Ahlrichs auxiliary basis set was used to speed up the calculations.[28-30] The conductor like screening model (COSMO) was used for all calculations.[31] The self-consistent field calculations were tightly converged (1×10^{-8} E_h in energy, 1×10^{-7} E_h in the charge density, and 1×10^{-7} in the maximum element of the DIIS[32,33] error vector). The geometry was converged with the following convergence criteria: change in energy $<10^{-5}$ E_h, average force $<5 \times 10^{-4}$ E_h Bohr^{-1}, and the maximum force 10^{-4} E_h Bohr^{-1}. The geometry search for all complexes was carried out in redundant internal coordinates without imposing geometry constraints. The stability of all solutions was checked by performing frequency calculations: no negative frequencies were observed. Single point calculations were performed on optimized coordinates using the PBE0 functional[34,35] and triple-ζ-quality basis sets with one set of polarization functions (def2-TZVP) for all atoms.[22]

The structures of the complexes **20** and **21** were optimized at the TPSS[36] -D3[37] /def2-TZVP[24,38], level in vacuum. We tested several other functionals (PBE-D3, M06-L, M06, ωB97-XD), both in vacuum and in water (using PCM), and found that TPSS-D3 gave the best agreement with experiment (metal–ligand bond lengths within 0.01 Å) and that solvation had a negligible effect on the structure (changes in metal–ligand bond lengths of ≤ 0.01 Å). We therefore used the TPSS-D3/def2-TZVP/vacuum structure in all subsequent calculations. TD-DFT was used to calculate vertical singlet excitation energies at the

ωB97-XD[39] /def2-TZVP/PCM level. The default IEF-PCM solvation model was used, which only includes electrostatic solvation effects; non-equilibrium solvation was used for excited states. NTO analyses[40] were performed with Gaussian.

Structures and orbitals were visualized with the program ChemCraft.[41] The calculated S_1 excitation energies in various solvents were found to be significantly overestimated (by ~0.6 eV) compared to the experimental band maxima. It is well known[42] that the positions of ligand-field excitations, particularly in first transition row complexes, are not predicted reliably by TD-DFT and are highly dependent on the chosen functional. Moreover, many such excitations have a certain amount of charge-transfer character, which is also problematic for TD-DFT. The latter problem is alleviated by using a long-range corrected functional like ωB97-XD. We did not attempt to identify the optimal functional for the systems under investigation as the deviations are systematic and constant for a given excitation and functional. Therefore, the shifts due to solvation and the nature of the excitations, which are the focus of the present work, can still be considered reliable.

2.6.5 Colorimetric NO determination

The NO generated during bulk electrolysis was quantified in an airtight cell (headspace volume = 97 mL) in 0.2 M TBA-PF_6 in acetonitrile (15 mL) using an $Ag/AgNO_3$ pseudo reference electrode, a Pt wire counter electrode and a large area glassy carbon foil working electrode (area 4.6 cm^2). The concentration of compound **17** or compound **18** employed was 7×10^{-6} M. The electrolyte also contained 120 equivalents of benzoic acid and 120 equivalents of TBA-NO_2 relative to compound **17** or **18**. A control reaction was also performed containing these amounts of benzoic acid and TBA-NO_2 but in the absence of any catalyst. A 14 mL vial was glued to the internal wall of the airtight cell above the level of the electrolyte solution, into which was placed 5 mL of an 8×10^{-5} M Co-TPP solution in dichloromethane, the concentration of which was cross-checked using the molar extinction coefficient reported by Berry and co-workers.[43] The vial was left open at the top, so that NO in the headspace could diffuse into the Co-TPP solution, but the Co-TPP solution and the electrolyte could not mix. The electrolyte and headspace of the cell were thoroughly degassed with Ar for 30 minutes before initiation of electrolysis. Bulk electrolyses were then conducted at –0.91 V (*vs.* ferrocenium/ferrocene) with stirring. At the end of electrolysis, the solution continued to be stirred and the cell was left sealed for a further two hours, in order to allow time for NO in the headspace to diffuse fully into the Co-TPP solution. An aliquot of the Co-TPP solution was then withdrawn from the 14 mL

vial, and its electronic spectrum measured. Given a Henry's Law coefficient for the solubility of NO in CH_3CN at room temperature of 1.35×10^8 Pa,[44] the amount of NO dissolved in solution was calculated to be negligible under these conditions and was thus ignored.

A calibration curve equating the shift in the position of the Co-TPP absorbance band at $\lambda_{max} \approx 530$ nm was constructed (see **Figure 3.15**), using a similar sealed cell configuration to that described above with a dichloromethane/Co-TPP solution in an open vial attached to the inner wall of the cell, but where the Co-TPP solution was not in contact with the liquid in the main cell. The main body of the cell was then purged with Ar and filled with 20 mL of a 50 mM solution of ascorbic acid in glacial acetic acid/H_2O (respectively 18 mL/2 mL), which is known to generate NO stoichiometrically from nitrite.[45] Known aliquots of sodium nitrite (as a solution in water) were then added to this solution, which was then stirred in the sealed cell for 2 hours. After this time, an aliquot of the Co-TPP solution was withdrawn from the 14 mL vial, and its electronic spectrum measured. From this, a graph of shift in λ_{max} *vs.* amount of NO generated was constructed.

2.6.6 Quantification of nitric oxide release by chemiluminescence

Bulk electrolysis was conducted as for the colorimetric tests for NO in identical sealed cells. NO release measurements by chemiluminescence were then performed using a Sievers NOA 280i chemiluminescence nitric oxide analyzer. The instrument was calibrated by passing air through a zero filter (Sievers, <1 ppb NO) and 89.8 ppm NO gas (BOC, balance nitrogen). The flow rate was set to 200 mL min^{-1} with a cell pressure of 6.5 Torr and an oxygen pressure of 6.1 psig. To measure NO production, nitrogen gas was flushed through the electrochemical cell, the resultant gas directed into the analyzer, and the concentration of NO recorded. The limit of detection of this analyzer is 0.5 ppb.

2.7 References:

[1] P. Zanello, *Inorganic Electrochemistry, Theory, Practice and Application*, The Royal Society of Chemistry, Cambridge, **2003**.

[2] J. O'M. Bockris, A. K.N. Reddy, *Modern Electrochemistry Volume 1*, Springer US, **1998.**

[3] P. Atkins, J. De Paula, *Physical Chemistry*, Oxford University Press, **2006** (8th ed.)

[4] J. M. Hollas, *Modern Spectroscopy*, John Wiley & sons, **2004** (4th edition)

[5] C. Giacovazzo, *Fundamentals of Crystallography*, Oxford University Press, **2002**

[6] D. Schwarzenbach *Crystallography*, John Wiley, **1996**, New York

[7] J. Keeler, *Understanding NMR Spectroscopy*, John Wiley & Sons Ltd, **2005**, Chichester

[8] E. Talsi, K. Bryliakov, *Applications of EPR and NMR Spectroscopy in Homogeneous Catalysis*, CRC Press, Taylor & Francis Group, **2017**, Boca Raton

[9] P. He, L. R. Faulkner, *Anal. Chem*, **1986**, 58, 517-523.

[10] S. J. Coles and P. A. Gale, *Chem. Sci.* **2012**, 3, 683.

[11] L. Palatinus, G. Chapuis, *J. Appl. Cryst*. **2007**, 40, 786.

[12] L. Palatinus, A. van der Lee, *J. Appl. Cryst*. **2008**, 41, 975.

[13] L. Palatinus, S. J. Prathapa, J. van Smaalen, *J. Appl. Cryst.* **2012**, 45, 575.

[14] G. M. Sheldrick, Acta Cryst. C, **2015**, 71, 3.

[15] O. V. Dolomanov, L. J. Bourhis, R. J. Gildea, J. A. K. Howard, H. Puschmann, J. Appl. Cryst. **2009**, 42, 339.

[16] G. M. Sheldrick, *Acta Cryst. A*, **2015**, 71, 3.

[17] G. M. Sheldrick, *Acta Cryst. A*, **2008**, 64, 112.

[18] A. L. Spek, Acta Cryst. C, **2015**, 71, 9.

[19] F. Neese, *WIREs Comput. Mol. Sci.* **2012**, 2, 73.

[20] M. J. Frisch, G. W. Trucks, H. B. Schlegel, G. E. Scuseria, M. A. Robb, J. R. Cheeseman, G. Scalmani, V. Barone, B. Mennucci, G. A. Petersson, H. Nakatsuji, M. Caricato, X. Li, H. P. Hratchian, A. F. Izmaylov, J. Bloino, G. Zheng, J. L. Sonnenberg, M. Hada, M. Ehara, K. Toyota, R. Fukuda, J. Hasegawa, M. Ishida, T. Nakajima, Y. Honda, O. Kitao, H. Nakai, T. Vreven, J. A. Montgomery, Jr., J. E. Peralta, F. Ogliaro, M. Bearpark, J. J. Heyd, E. Brothers, K. N. Kudin, V. N. Staroverov, R. Kobayashi, J. Normand, K. Raghavachari, A. Rendell, J. C. Burant, S. S. Iyengar, J. Tomasi, M. Cossi, N. Rega, N. J. Millam, M. Klene, J. E. Knox, J. B. Cross, V. Bakken, C. Adamo, J. Jaramillo, R. Gomperts, R. E. Stratmann, O. Yazyev, A. J. Austin, R. Cammi, C. Pomelli, J. W. Ochterski, R. L. Martin, K. Morokuma, V. G. Zakrzewski, G. A. Voth, P. Salvador, J. J. Dannenberg, S. Dapprich, A. D. Daniels, Ö. Farkas, J. B. Foresman, J. V. Ortiz, J. Cioslowski and D. J. Fox, Gaussian 09, Revision D.01, Gaussian, Inc., Wallingford, CT, **2013**.

[21] A. D. Becke, *Phys. Rev. A* **1988**, 38, 3098.

[22] J. P. Perdew, *Phys. Rev.* B **1986**, 33, 8822.

[23] R. Ahlrichs, K. May, *Phys. Chem. Chem. Phys*. **2000**, 2, 943.

[24] F. Weigend, R. Ahlrichs, *Phys. Chem. Chem. Phys*. **2005**, 7, 3297.

[25] E. van Lenthe, J. G. Snijders, E. J. Baerends, *J. Chem. Phys.* **1996**, 105, 6505.

[26] E. van Lenthe, S. Faas, J. G. Snijders, *Chem. Phys. Lett*. **2000**, 328, 107.

[27] E. van Lenthe, A. van der Avoird, P. E. S. Wormer, *J. Chem. Phys.* **1998**, 108, 4783-4796.

[28] F. Neese, F. Wennmohs, A. Hansen, U. Becker, *Chem. Phys.* **2009**, 356, 98. 116

[29] K. Eichkorn, O. Treutler, H. Öhm, M. Häser, R. Ahlrichs, *Chem. Phys. Lett*. **1995**, 242, 652.

[30] K. Eichkorn, F. Weigend, O. Treutler, R. Ahlrichs, *Theor. Chem. Acc*. **1997**, 97, 119.

[31] A. Klamt, G. Schüürmann, *J. Chem. Soc., Perkin Trans.* **1993**, 2, 799.

[32] P. Pulay, *Phys. Lett.* **1980**, 73, 393.

[33] P. Pulay, *J. Comput. Chem*. **1982**, 3, 556.

[34] J. P. Perdew, K. Burke, M. Ernzerhof, *Phys. Rev. Lett*. **1996**, 77, 3865.

[35] C. Adamo, V. Barone, *J. Chem. Phys*. **1999**, 110, 6158.

[36] J. M. Tao, J. P. Perdew, V. N. Staroverov and G. E. Scuseria, *Phys. Rev. Lett*. **2003**, 91, 146401.

[37] S. Grimme, J. Antony, S. Ehrlich and H. Krieg, *J. Chem. Phys.* **2010**, 132, 154104.

[38] F. Weigend, *Phys. Chem. Chem. Phys*. **2006**, 8, 1057.

[39] J. D. Chai and M. Head-Gordon, *Phys. Chem. Chem. Phys*. **2008**, 10, 6615.

[40] R. L. Martin, *J. Chem. Phys*. **2003**, 118, 4775.

[41] G. A. Andrienko, ChemCraft, v. 1.8(445), www.chemcraftprog.com (accessed, July **2016**).

[42] M. Rudolph, T. Ziegler and J. Autschbach, *Chem. Phys*. **2011**, 391, 92.

[43] S. A, Yao, C. B. Hansen, J. F. Berry, *Polyhedron*, **2013**, 58, 2.

[44] A. W. Shaw, A. J. Vosper, J. *Chem. Soc., Faraday Trans*. 1, **1977**, 73, 1239.

[45] E. Nagababu, J. M. Rifkind, *Methods Mol. Biol.* **2010**, 610, 41.

Proton-Coupled-Electron Transfer Enhances the Electrocatalytic Reduction of Nitrite to NO in a Bioinspired Copper Complex

Published as "*Proton-Coupled-Electron Transfer Enhances the Electrocatalytic Reduction of Nitrite to NO in a Bioinspired Copper Complex*"

Giacomo Cioncoloni, Isolda Roger, Paul S. Wheatley, Claire Wilson, Russell E. Morris, Stephen Sproules, and Mark D. Symes

ACS Catal. **2018**, 8, 5070−5084

Acknowledgments and declaration

Me and Isolda Roger performed the synthesis and characterization of the compounds, and undertook the electrochemical and spectroscopic NO quantification studies. Me, Isolda Roger and Paul S. Wheatley performed NO quantification studies using the Sievers NO analysis system. Claire Wilson collected and refined the single crystal X-ray diffraction data. Stephen Sproules performed the EPR experiments, the EPR data analysis and the DFT calculations. Mark D. Symes conceived the idea and planned the required experiments, and Mark D. Symes and Russell E. Morris supervised the work.

Synopsis

The selective and efficient electrocatalytic reduction of nitrite to nitric oxide (NO) is of tremendous importance, both for the development of NO-release systems for biomedical applications and for the removal of nitrogen oxide pollutants from the environment. In nature, this transformation is mediated by (amongst others) enzymes known as the copper-containing nitrite reductases. The development of synthetic copper complexes that can reduce nitrite to NO has therefore attracted considerable interest. However, there are no studies describing the crucial role of proton-coupled-electron transfer during nitrite reduction when using such synthetic complexes. Herein, we describe the synthesis and characterization of two previously unreported Cu complexes (**17** and **18**) for the electrocatalytic reduction of nitrite to NO, in which the role of proton-relaying units in the secondary coordination sphere of the metal can be probed. Complex **18** bears a pendant carboxylate group in close proximity to the copper center, whilst complex **17** lacks such functionality. Our results suggest that complex **18** is twice as effective an electrocatalyst for nitrite reduction than is complex **17**, and that complex **18** is the best copper-based molecular electrocatalyst for this reaction yet discovered. The differences in reactivity between **17** and **18** are probed using a range of electrochemical, spectroscopic and computational methods, which shed light on the possible catalytic mechanism of **18** and implicate the proton-relaying ability of its pendant carboxylate group in the enhanced reactivity that this complex displays. These results highlight the critical role of proton-coupled-electron transfer in the reduction of nitrite to NO and have important implications for the design of biomimetic catalysts for the selective interconversions of the nitrogen oxides.

3.1 Introduction

The mono-electronic reduction of nitrite (NO_2^-) to nitric oxide (NO) is a potential source of NO in physiological environment[1-4] and a key step in the natural nitrogen cycle, being part of the process of bacterial denitrification.[5] As widely discuss in **Chapter 1** there are a number of classes of enzyme that perform this transformation, including those using haem, molybdenum and copper center in the active site. In the case of copper-containing nitrite reductases (CuNiR) the reaction mediated is summarized in **Equation 1**[6]

$$Cu(I) + NO_2^- + 2H^+ \rightarrow Cu(II) + NO + H_2O \qquad \text{(Eq. 1)}$$

The crystal structure of a CuNIR-type enzyme was determined in 1991.[7] The active site for the reduction of NO_2^- consists of a Cu(II) ion coordinated by three histidine ligands and a single water molecule, giving a distorted tetrahedral geometry at the copper center (see **Figure 1.8** page 17 for the structure). These results have been supported by subsequent studies, which have also given insight into the nature of nitrite binding during catalysis.[8,10]

On account of the comparatively simple active site structure of CuNiR suggested by the crystallographic studies, a number of groups have developed simplified analogues of this enzyme based on tripodal N-donor ligands coordinated to a Cu center.[11-45]

In many cases was found that these analogues can mediate the reduction of nitrite to NO with the use of stoichiometric sacrificial electron donors but there is also a distinct subset of such Cu-N donor complexes that can mediate the electrocatalytic reduction of nitrite to NO.[46-51]

A critical role is played by a proton sources since acidic regimes are essential for catalytic reduction of nitrite to NO and this appears evident also from the stoichiometry showed in **Equation 1** and the reaction mechanism detailed in **Chapter 1** (page 18 **Figure 1.9**)

Considering that protons are required for this reduction, was surprising the relative dearth of studies on the role of proton-relay units that might mediate proton-coupled-electron transfer (PCET)[52-56] during catalytic nitrite reduction in these systems.

In the natural CuNiR class of enzymes, Asp-98 residue sits in close proximity to the bound nitrite and helps to mediate proton transfer to one of the nitrite oxygens, which is lost as water.[5,10] Crystallographic[57] and site-directed mutagenesis[58] studies on the relevant enzymes highlighted the importance of this fragment in the reaction mechanism.

In recent years three papers were published showing the importance of hydrogen bonding in the secondary coordination sphere of synthetic systems for nitrite reduction based on both iron[59,60] and copper,[61] although none of these systems was able to demonstrate catalytic turnover (see at this purpose compounds **12, 13, 14**, pages 34-35)

As was shown in **Section 1.5.3**, a lot of small molecules mimicking the Cu-NiR active site were synthesized, however, to the best of our knowledge, there exist no examples of synthetic, small-molecule platforms for the catalytic reduction of nitrite to NO where the role of proton relays has been addressed explicitly, as it has been, for example, with synthetic platforms for catalytic proton reduction,[62-67] water oxidation[68-70] and CO_2 reduction.[71,72]

In this chapter is detailed the synthesis and characterization of two new copper complexes (**17** and **18**) which allow to understand and rationalize the role of PCET in the electrocatalytic reduction of nitrite to NO with synthetic, small-molecule platforms.

We probe and rationalize these differences in reactivity using a range of electrochemical, spectroscopic and computational methods, which together shed light on the possible mechanism of reaction.

3.2 Results and discussion

3.2.1 Synthesis and Crystallography.

The general synthetic route for the formation of complexes **17** and **18** is shown in **Scheme 3.1**. Hence, 6-chloromethylpyridine-2-carboxylic acid methyl ester was prepared *via* the procedure of Mato-Iglesias *et al*.[73] The synthesis of compound **15** (see **Figure 3.24** page 111) was then achieved by reaction of this methyl ester with bis(2-pyridylmethyl)amine according to the procedure used by Kotani *et al.* for the preparation of the allied ethyl ester.[74] Compound **15** could then be hydrolyzed to yield the known acid (compound **16**)[74,75] by treatment with NaOH. Metallation of the acid and ester ligands was then achieved accordingly to adapted literature procedures,[46,76] generating the new complexes [**17**-H_2O]$^{2+}$ and [**18**-H_2O]$^{+}$ (see Synthetic section at the end of this chapter).

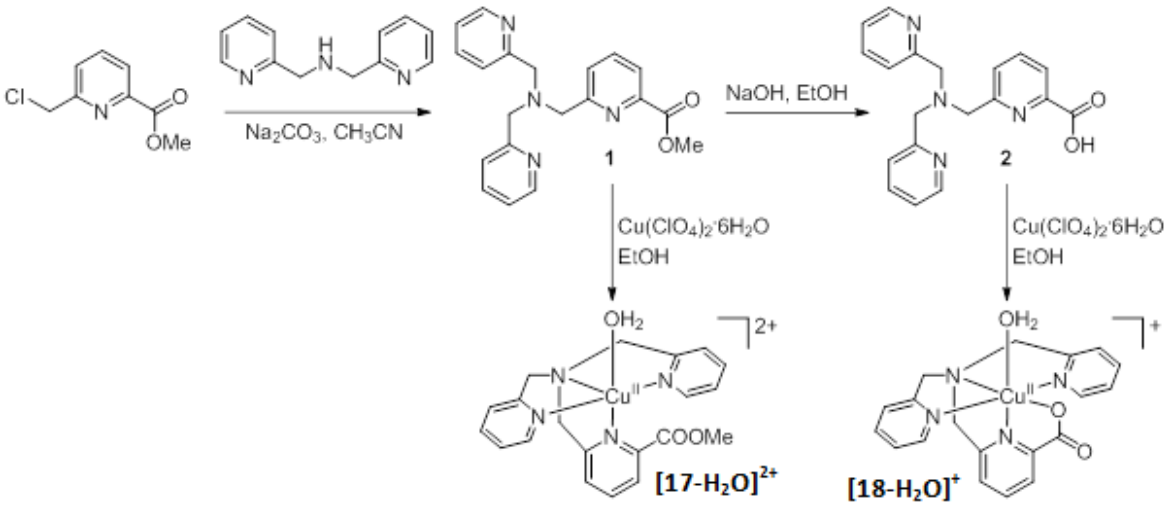

Scheme 3.1. *The synthetic route to obtain complexes [**17**-H_2O]$^{2+}$ and [**18**-H_2O]$^{+}$. Reproduced from ACS Catal. **2018**, 8, 5070 with permission of American Chemical Society. Copyright 2018*

After dissolution in CH_3CN, dark blue crystals of the acetonitrile adduct of complex **17** [**17**-CH_3CN]$(ClO_4)_2$ were obtained after standing at room temperature for 3 weeks. These crystals proved to be of suitable quality for X-ray diffraction, allowing the structure shown in **Figure 3.1** to be obtained.

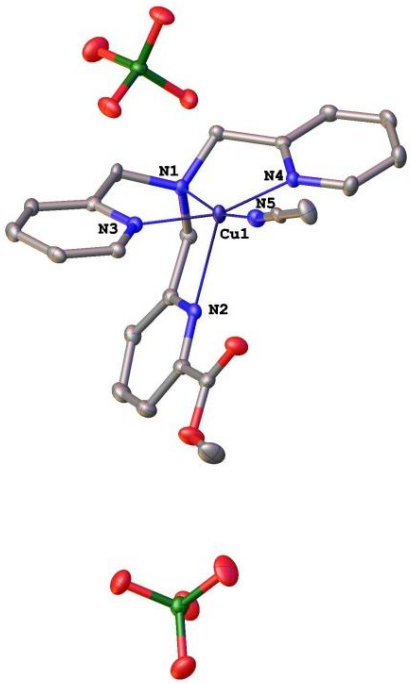

Figure 3.1: *The molecular structure of [**17**-CH_3CN]$(ClO_4)_2$. Further crystallographic details can be found in **Appendix A1**. Ellipsoids are drawn at 50% probability level. Color scheme: C = grey, N = blue, O = red, Cl = green, Cu = purple. For selected bond lengths and angles, see **Table 3.1**. Reproduced from ACS Catal. **2018**, 8, 5070 with permission of American Chemical Society. Copyright 2018*

The presence of two perchlorate anions per Cu complex indicated that the copper center remained in the +II oxidation state. Typically, Cu(II) complexes with tris(2-methylpyridyl)amine (TMPA) ligands adopt a distorted trigonal bipyramidal geometry, whereby the Cu–$N_{(pyridyl)TMPA}$ bonds define the triangular plane (with typical lengths between 2.0 and 2.1 Å) and the apices of the bipyramid consist of a rather short Cu–$N_{acetonitrile}$ distance (~2.0 Å) and a comparatively longer Cu–$N_{(alkyl)TMPA}$ interaction (~2.4 Å).[43,77-79] However, the geometry of [**17**-CH_3CN]$^{2+}$ is more akin to a square-based pyramid (τ value ≈ 0.1 on the scale of Addison and Reedijk[80]), with N2 as its apex (see selected bond lengths and angles in **Table 3.1**). This gives Cu–N bond lengths in the square plane of between 2.045(2) and 1.972(2) Å, whilst the Cu–N2 interaction appears to be only very weak (Cu1–N2 = 2.473(2) Å). That said, **Figure 3.1** shows that the lone pair on the N2 nitrogen is clearly directed towards the Cu(II) center. It is noteworthy that this elongation in the Cu–N2 distance occurs for the pyridine which bears the methyl ester substituent adjacent to the N-donor. This arrangement is typical of complex presented in **Section 1.5.3** and was also previously observed by Tanaka and co-workers for the complex [CuCl(Me_1TMPA)]$^+$ (structure similar to compound **8** shown in **Figure 1.21** at page 30) where the TMPA pyridine bearing the methyl group exhibited a much longer Cu–N interaction than the unsubstituted pyridines (2.337 Å *vs.* ~1.99 Å) presents comparable features.[46] On account of the differing electronic properties of methyl and methyl ester substituents, it therefore seems likely that this common bond elongation effect is the result of steric crowding brought about by the close proximity of the substituents to the N-donor atom.[81] Similarly long Cu–N interactions have also been noted before in Cu(II)-tris(2-methylpyridyl)amine complexes bearing bulky substituents next to the N-donors (albeit where the ligands were more symmetrically-substituted) by Reinaud and co-workers.[82]

Table 3.1: *Experimental Bond Distances (Å) and Angles (°) in [**17**-CH_3CN]$^{2+}$ Reproduced from ACS Catal. **2018**, 8, 5070 with permission of American Chemical Society. Copyright 2018*

Cu1–N1	2.045(2)	N1–Cu1–N2	77.49(9)
Cu1–N2	2.473(2)	N3–Cu1–N1	84.5(1)
Cu1–N3	1.972(2)	N3–Cu1–N2	79.14(9)
Cu1–N4	1.981(2)	N3–Cu1–N4	161.9(1)
Cu1–N5	1.984(3)	N3–Cu1–N5	96.6(1)
		N4–Cu1–N1	82.6(1)
		N4–Cu1–N2	110.26(9)
		N4–Cu1–N5	92.9(1)
		N5–Cu1–N1	166.0(1)
		N5–Cu1–N2	116.45(9)

When tetrabutylammonium nitrite (TBA-NO_2) is added to solutions of complexes **17** and **18** in acetonitrile, the initially blue solutions immediately turned green (see **Figure 3.2**), indicating coordination of the Cu(II) center to nitrite in both cases.[42]

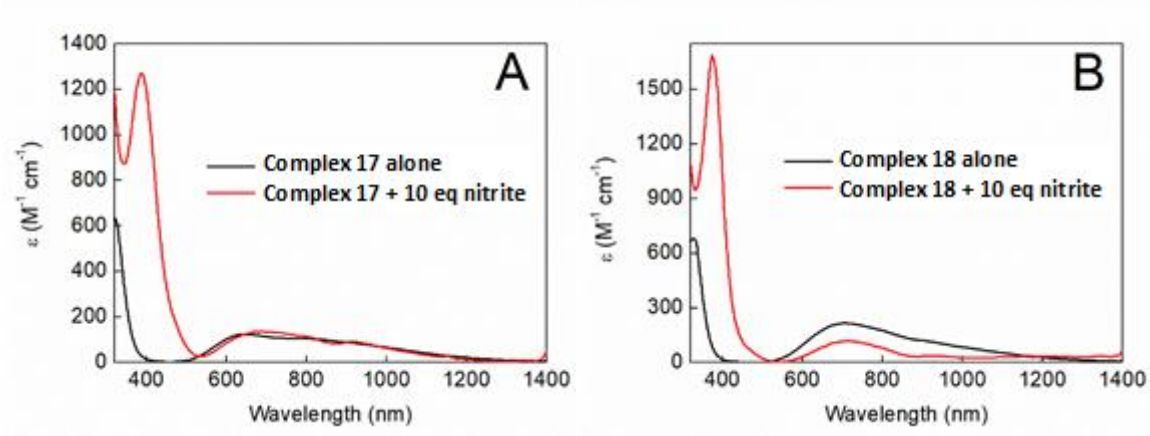

Figure 3.2: A: *Overlay of the electronic spectra of complex **17** in acetonitrile (black line) and of this complex after the addition of 10 equivalents of TBA-NO_2 (also in acetonitrile, red line).* ***B:*** *Overlay of the electronic spectra of complex **18** in acetonitrile (black line) and of this complex after the addition of 10 equivalents of TBA-NO_2 (also in acetonitrile, red line). Reproduced from ACS Catal. **2018**, 8, 5070 with permission of American Chemical Society. Copyright 2018*

Green crystals of complex **18** bound to nitrite were isolated from an acetonitrile solution of this complex in the presence of 5 equivalents of TBA-NO_2 and one equivalent of benzoic acid. X-ray diffraction on these crystals revealed a structure in which nitrite is bound to the copper center through nitrogen, whilst the carboxylate group remains coordinated to Cu, giving an overall neutral species (with no further counterions present), which we formulate as [**18**-NO_2] (see **Figure 3.3**). Hence, although acid was added to the crystallization medium, there is no evidence that the complex is protonated under these conditions. We note that Kojima and co-workers have previously noted the tendency for this carboxylate group to coordinate to the metal center in their allied Ru and Cr complexes,[74,75] and Lonnon *et al.* have similarly reported a Co(III) complex of ligand **16** in which the carboxylate group also coordinates to the metal center, giving a distorted octahedral geometry at the metal.[83]

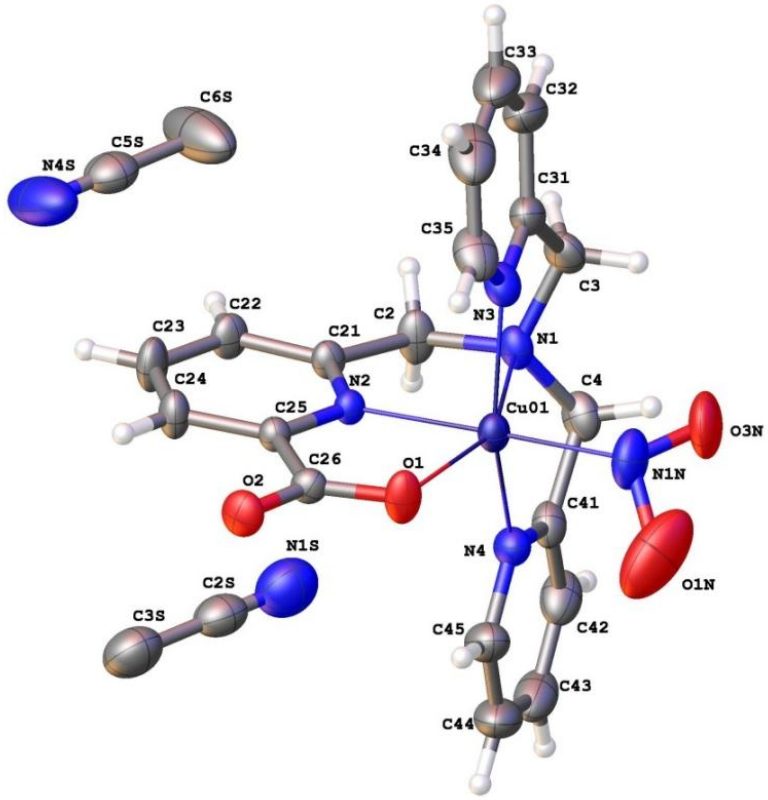

Figure 3.3: *The molecular structure of [**18**-NO_2]. Further crystallographic details can be found in the **Appendix A1**. Ellipsoids are drawn at 30% probability level. Color scheme: C = grey, H = white, N = blue, O = red, Cu = purple. A minor disorder component for bound NO_2^- has been omitted. For selected bond lengths and angles, see **Table 3.2**. Reproduced from ACS Catal. **2018**, 8, 5070 with permission of American Chemical Society. Copyright 2018*

The geometry around the copper center in [**18**-NO_2] is probably best described as distorted octahedral, with a Jahn-Teller elongation along the N1–Cu–O1 axis. This leads to a rather long Cu–N1 distance (2.384(2) Å), whilst the Cu-$N_{pyridyl}$ lengths are all significantly shorter (2.047(2) – 2.031(2) Å) and more similar to the Cu-N1N distance between the copper center and the bound nitrite (1.983(3) Å). It is these Cu-$N_{pyridyl}$ and Cu-N1N interactions that define the equator of the distorted octahedron (with roughly 90° angles between them, see **Table 3.2**), whilst the second axial position is occupied by O1 (Cu–O1 = 2.205(2) Å). However, as the bond angles in **Table 3.2** show, O1 does not sit directly over the center of the equatorial plane, but rather is skewed towards N2.

Two somewhat related Cu(II) complexes that incorporate a TMPA ligand bearing a carboxylate group that binds to the metal center have been reported by Suzuki and co-workers,[84,85] although in both of these structures the metal has only five coordination interactions (*i.e.* there is no coordinated nitrite, or similar small molecule) and so the Cu(II) adopts square pyramidal geometry. Meanwhile, Comba and co-workers have reported a

number of structures in which Cu(II) is supported by a TMPA-like ligand (which also bears a carboxylate group which coordinates to the metal),[86,87] but where the linkage between the pyridine groups is a bispidine unit. This then affords structures in which the metal center forms six coordinative interactions (one to each of the three pyridines, one to the carboxylate oxygen and one to each of the two amines in the bispidine system), giving distorted octahedral geometries. Again, however, there is no interaction between the metal center and any small molecules (such as the nitrite in **Figure 3.3**). Hence the structure reported here for [**18**-NO_2] appears to be unique in showing a Cu(II) center ligated by a TMPA-derived ligand, and which is also coordinated to both nitrite and carboxylate.

Table 3.2: *Experimental Bond Distances (Å) and Angles (°) in [**18**-NO_2] Reproduced from ACS Catal. **2018**, 8, 5070 with permission of American Chemical Society. Copyright 2018*

Cu01–O1	2.205(2)	O1–Cu01–N1	154.03(7)
Cu01–N1	2.384(2)	N2–Cu01–O1	76.67(7)
Cu01–N2	2.031(2)	N2–Cu01–N1	77.37(8)
Cu01–N3	2.047(2)	N2–Cu01–N3	88.49(7)
Cu01–N4	2.039(2)	N2–Cu01–N4	92.37(7)
Cu01–N1N	1.983(3)	N3–Cu01–O1	101.32(8)
		N3–Cu01–N1	77.29(8)
		N4–Cu01–O1	105.68(8)
		N4–Cu01–N1	76.05(8)
		N4–Cu01–N3	152.5(1)
		N1N–Cu01–O1	98.8(1)
		N1N–Cu01–N1	107.1(1)
		N1N–Cu01–N2	175.2(1)
		N1N–Cu01–N3	90.9(1)
		N1N–Cu01–N4	90.3(1)

3.2.2 EPR Spectroscopy of Complexes 3 and 4.

Complexes **17** and **18** are paramagnetic with an $S = {}^1/_2$ ground state. Their EPR spectra recorded in CH_3CN solution at room temperature are very similar (**Figure 3.4a** both panels), exhibiting the hallmark four-line pattern resulting from the hyperfine coupling of the Cu(II) electron spin with the $I = {}^3/_2$ nuclear spin of the ^{63,65}Cu isotopes (100% natural abundance). Their similarity is underscored by the near identical spin-Hamiltonian parameters obtained from spectral simulation, with $g_{iso} = 2.122$ and $A_{iso} = 57 \times 10^{-4}$ cm^{-1} for **17**, and $g_{iso} = 2.123$, $A_{iso} = 55 \times 10^{-4}$ cm^{-1} for **18**.

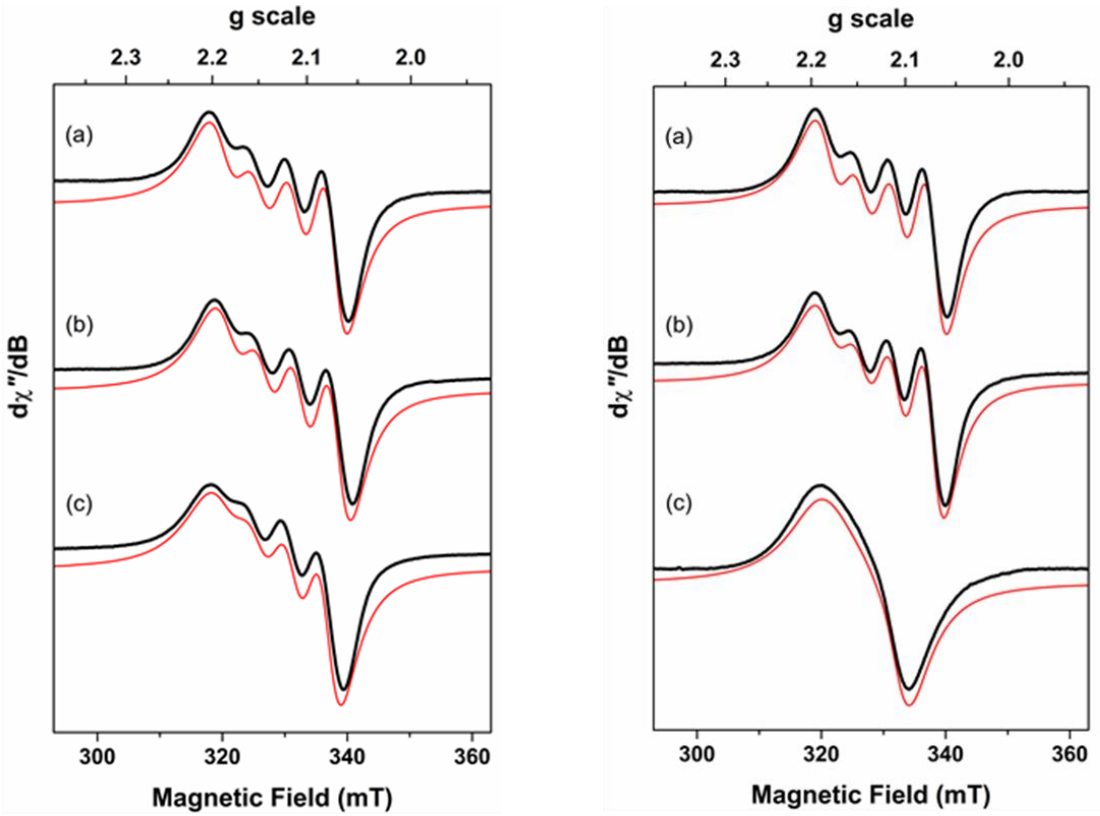

Figure 3.4 Left: *X-band EPR spectra of* ***(a)*** *[**17**-NCCH3]$^{2+,}$* ***(b)*** *[**17**-NCCH3]2^{+} treated with benzoic acid, and* ***(c)*** *[**17**-NO2]$^{+}$ in MeCN solution at 293 K (experimental conditions: frequency, 9.802 GHz; power, 20.0 mW; modulation, 0.5 mT). Experimental data are represented by the black lines; simulation is depicted by the red trace:* ***(a)*** *g_{iso} = 2.122, A_{iso} = 57 × 10^{-4} cm^{-1};* ***(b)*** *g_{iso} = 2.122, A_{iso} = 56 × 10^{-4} cm^{-1};* ***(c)*** *g_{iso} = 2.130, A_{iso} = 53 × 10^{-4} cm^{-1}.* ***Right:*** *X-band EPR spectra of* ***(a)*** *[**18**-$NCCH_3$]$^{+}$,* ***(b)*** *[**18**-$NCCH_3$]$^{+}$ treated with benzoic acid, and* ***(c)*** *[**18**-NO_2] in MeCN solution at 293 K (experimental conditions: frequency, 9.802 GHz; power, 20.0 mW; modulation, 0.5 mT). Experimental data are represented by the black lines; simulation is depicted by the red trace:* ***(a)*** *g_{iso} = 2.123, A_{iso} = 55 × 10^{-4} cm^{-1};* ***(b)*** *g_{iso} = 2.124, A_{iso} = 54 × 10^{-4} cm^{-1};* ***(c)*** *g_{iso} = 2.142, A_{iso} = 34 × 10^{-4} cm^{-1}. Reproduced from ACS Catal.* ***2018****, 8, 5070 with permission of American Chemical Society. Copyright 2018*

The large linewidth obscures any additional splitting from the spin-active ^{14}N (I = 1, 99.7% natural abundance) atoms in the ligands, and derives from the rates of tumbling of the molecules in solution. Given the presence of a coordinated acetonitrile in the crystal structure (**Figure 3.1** page 83), we assign these species as being [**17**-$NCCH_3$]$^{2+}$ and [**18**-$NCCH_3$]$^{+}$ complex ions in solution, though there will likely be species without the solvent ligand that will have similar parameters that contribute to the linewidth. Interestingly, treating these samples with an excess of benzoic acid (**Figure 3.4b** both panels) does not alter the spectral profile, confirming that the carboxylate group in complex **18** does not

become protonated under these conditions (*i.e.* the bulk of the sample is the carboxylate-bound version of complex **18**).

Upon treating solutions of [**17**-$NCCH_3$]$^{2+}$ and [**18**-$NCCH_3$]$^{+}$ with excess TBA-NO_2, the resulting EPR spectra exhibit rather different profiles (**Figure 3.4c** both panels). In the case of complex **17**, the EPR spectrum that is obtained shows only a slight change from that of [**17**-$NCCH_3$]$^{2+}$ (g_{iso} = 2.130 and A_{iso} = 53 × 10^{-4} cm^{-1}), with the increase in *g*-value being commensurate with replacement of CH_3CN by NO_2^-. Hence the EPR data suggest that nitrite is bound to give a species of the form [**17**-NO_2]$^{+}$. In contrast, when [**18**-$NCCH_3$]$^{+}$ is treated with excess TBA-NO_2, the resulting spectrum of [**18**-NO_2] is featureless with rampant line broadening that drowns out the hyperfine features (**Figure 3.4c** right panel). This is either the result of attenuated molecular tumbling in this solvent medium or overlapping spectra from various isomers and conformations of two or more species.

To gain more information on the nature of complexes **17** and **18** in solution in the presence of acid and nitrite, dichloromethane was added to the solution samples of [**17**-$NCCH_3$]$^{2+}$ and [**18**-$NCCH_3$]$^{+}$ to produce a homogeneous frozen glasses for measurements at 150 K. The spectrum of [**17**-$NCCH_3$]$^{2+}$ is quintessentially that of a Cu(II) species with an unpaired electron in the $d_{x^2-y^2}$ orbital (**Figure 3.5a**). The spectrum yielded axial spin-Hamiltonian parameters, *g* = (2.054, 2.083, 2.226) and A_{Cu} = (-6, -6, 180) × 10^{-4} cm^{-1}, where the average values, $\langle g \rangle$ = 2.121 and $\langle A \rangle$ = 56 × 10^{-4} cm^{-1}, nicely match the isotropic parameters and so confirm that a single dominant species is present at both 150 K and room temperature. The benzoic acid-treated sample of [**17**-$NCCH_3$]$^{2+}$ reveals some differences in the frozen solution spectrum which we ascribe to the presence of a minor second species and aggregation effects common in Cu(II) EPR spectra (**Figure 3.5b**).

The frozen glass EPR spectrum of [**17**-NO_2]$^{+}$ is shown in **Figure 3.5c** and is dominated by a signal with *g* = (2.044, 2.102, 2.247) and A_{Cu} = (10, 14, 144) × 10^{-4} cm^{-1}. These values are consistent with nitrite binding to copper through oxygen in a quasi-bidentate manner (*i.e.* as [**17**(κ^2-ONO)]). The spectrum in **Figure 3.5c** also has a 5% contribution from a species containing two nitrites [**17**(κ^1-NO_2)(κ^2-ONO)]. This second spectrum has *g* = (2.053, 2.059, 2.312); A_{Cu} = (0, 24, 162) × 10^{-4} cm^{-1}; A_N = (0, 20, 0) × 10^{-4} cm^{-1}; A_N = (0, 18, 0) × 10^{-4} cm^{-1}. These data are nearly identical to those previously reported for the complex **9** shown in **Chapter 1** at page 31-32 (**Figures 1.22-23**).[42] The occurrence of a similar species in the current case is readily apparent due to its narrow lines in the frozen glass that is indicative of anisotropic coupling to two different ^{14}N nuclei, one for the N-bound NO_2^- ligand and the other for the pyridyl-N *trans* to the nitrite. **Figure 3.5d** shows that when

benzoic acid is added to this sample, very little change is observed in the EPR signal, suggesting that the coordination geometry remains unchanged.

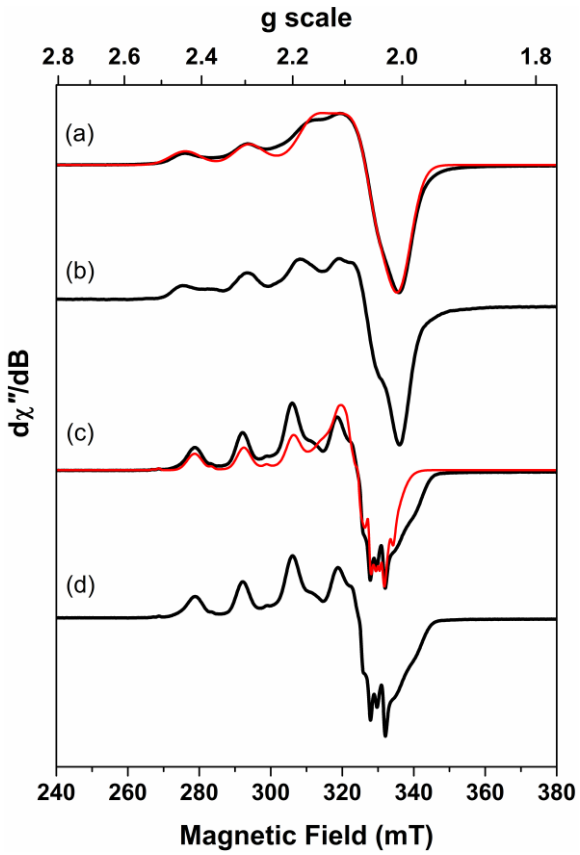

Figure 3.5. *Comparison of the X-band EPR spectra of* ***(a)*** *[**17**-$NCCH_3$]$^{2+}$,* ***(b)*** *[**17**-$NCCH_3$]$^{2+}$ treated with benzoic acid,* ***(c)*** *[**17**-NO_2]$^+$, and* ***(d)*** *[**17**-NO_2]$^+$ treated with benzoic acid, recorded in 5:1 CH_3CN/CH_2Cl_2 solution at 150 K (experimental conditions: frequency, 9.418 GHz; power, 6.3 mW; modulation, 0.1 mT). Experimental data are represented by the black lines. Simulations are shown by the red trace:* ***(a)*** *g = (2.054, 2.083, 2.226), A_{Cu} = (-6, -6, 180) × 10^{-4} cm^{-1};* ***(c)*** *subspectrum 1: g = (2.044, 2.102, 2.247); A_{Cu} = (10, 14, 142) × 10^{-4} cm^{-1} (wt. 95%); subspectrum 2: g = (2.053, 2.059, 2.311); A_{Cu} = (0, 27, 162) × 10^{-4} cm^{-1}; A_N = (0, 20, 0) × 10^{-4} cm^{-1}; A_N = (0, 18, 0) × 10^{-4} cm^{-1} (wt. 5%). Reproduced from ACS Catal.* ***2018****, 8, 5070 with permission of American Chemical Society. Copyright 2018*

The frozen solution spectrum of [**18**-$NCCH_3$]$^+$ in CH_3CN/CH_2Cl_2 is more elaborate and consists of a least two different monocopper species present in the sample in addition to aggregation of these complexes in the frozen glass (**Figure 3.6a**). This is confirmed by using DMF as a glassing solvent (**Figure 3.6b**), which leads to an almost featureless spectrum as this more basic solvent mixture promotes greater aggregation of the Cu(II) species. The absence of a half-field signal rules out dimerization of this complex, for example through the pendant carboxylate group of the TMPA ligand. Treating [**18**-$NCCH_3$]$^+$ with excess benzoic acid (**Figures 3.6c and 3.6d**) shows that one of the two monocopper species is favoured over the other and also diminishes the effects of

aggregation. Furthermore, these frozen solution spectra suggest that slow tumbling (rather than multiple overlapping signals) produces the broad line observed in the room temperature spectrum of [**18**-$NCCH_3$]$^+$ treated with benzoic acid.

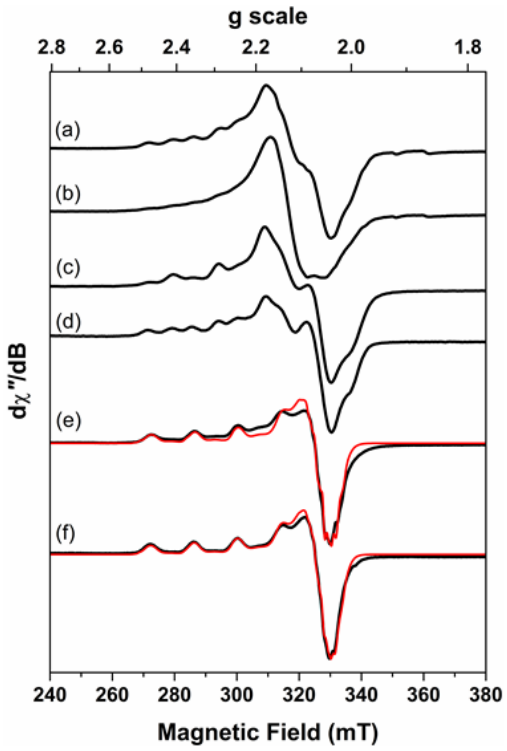

Figure 3.6: *Comparison of the X-band EPR spectra of* ***(a)*** *[**18**-$NCCH_3$]$^+$ in 5:1 CH_3CN/CH_2Cl_2,* ***(b)*** *[**18**-$NCCH_3$]$^+$ in CH_3CN/DMF, (c) [**18**-$NCCH_3$]$^+$ treated with benzoic acid in 5:1 CH_3CN/CH_2Cl_2,* ***(d)*** *[**18**-$NCCH_3$]$^+$ treated with benzoic acid in CH_3CN/DMF,* ***(e)*** *[**18**-NO_2], and* ***(f)*** *[**18**-NO_2] treated with benzoic acid in 5:1 CH_3CN/CH_2Cl_2 solution at 150 K (experimental conditions: frequency, 9.430 GHz; power, 6.3 mW; modulation, 0.1 mT). Experimental data are represented by the black lines. Simulations are shown by the red trace:* ***(e)*** *subspectrum 1: g = (2.058, 2.081, 2.295), A_{Cu} = (10, 10, 147) × 10^{-4} cm^{-1} (82%); subspectrum 2: g = (2.044, 2.102, 2.247); A_{Cu} = (10, 14, 144) × 10^{-4} cm^{-1} (wt. 15%); subspectrum 3: g = (2.053, 2.059, 2.312); A_{Cu} = (0, 24, 162) × 10^{-4} cm^{-1}; A_N = (0, 20, 0) × 10^{-4} cm^{-1}; A_N = (0, 18, 0) × 10^{-4} cm^{-1} (wt. 3%);* ***(f)*** *same spin-Hamiltonian parameters with subspectrum ratio of 88 : 10 : 2.] Reproduced from ACS Catal.* ***2018****, 8, 5070 with permission of American Chemical Society. Copyright 2018*

The spectrum of [**18**-NO_2] recorded in a CH_3CN/CH_2Cl_2 frozen glass is shown in **Figure 3.7 and Figure 3.6e**. Simulation of this spectrum reveals that it is composed of three subspectra (lower panels in **Figure 3.7**). Hence the major species (82% of the spectrum, orange line in **Figure 3.7**) has been simulated with g = (2.058, 2.081, 2.295) and A_{Cu} = (10, 10, 147) × 10^{-4} cm^{-1}, where the average g-value, $\langle g \rangle$ = 2.145, matches that from the fluid solution spectrum, g_{iso} = 2.142, suggesting that the nitrite is bound to the copper center through nitrogen. The two minor species have been included in the fit as their features are clearly observed, and they are very similar to the spectra observed for [**17**-NO_2]$^+$ (**Figure 3.5c**).

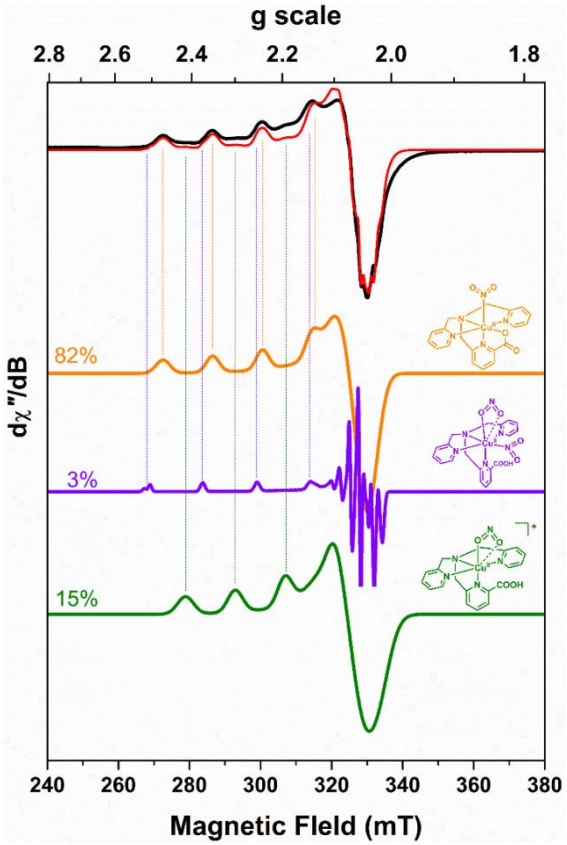

Figure 3.7: *X-band EPR spectrum of [**18**-NO_2] recorded in 5:1 CH_3CN/CH_2Cl_2 solution at 150 K (experimental conditions: frequency, 9.430 GHz; power, 6.3 mW; modulation, 0.1 mT). Experimental data are represented by the black line. The simulation is composed of three subspectra with relevant weighting shown in orange, violet and green lines; the sum is given by the red trace overlaid on the experimental spectrum. Guidelines map the contribution of each subspectrum to the $A_{//}$ features of the experimental spectrum. Reproduced from ACS Catal.* ***2018****, 8, 5070 with permission of American Chemical Society. Copyright 2018*

Hence there is a component accounting for 15% of the spectrum with g = (2.044, 2.102, 2.247) and A_{Cu} = (10, 14, 144) × 10^{-4} cm^{-1}, which we assign to a quasi-bidentate *O*-bound species, [**18**(κ^2-ONO)] (green trace in **Figure 3.7**). Meanwhile, by analogy to **Figure S4c**, the smallest of the simulated components corresponds to [**18**(κ^1-NO_2)(κ^2-ONO)] (purple trace in **Figure 3.7**). Isomerization to the weaker nitrito ligand will account for the lower $g_{||}$-value, and is corroborated by calculations that show the κ^1-NO_2 and κ^2-ONO structures are isoenergetic (*vide infra*).

The spectrum of [**18**-NO_2] treated with excess benzoic acid (**Figure 3.6f**) is almost identical to that for [**18**-NO_2], except that it has a slightly different ratio of 88:10:2 of the three subspectra under discussion. The dominant species is thus again assigned as [**18**-NO_2], where the carboxylate remains bound to the Cu ion in a six-coordinate complex. Despite the lack of an observable hyperfine splitting, we nevertheless assign this complex with an *N*-bound nitrite ligand based on computational analysis (*vide infra*). The second

subspectrum has features that closely resemble those of the frozen solution spectrum of [**17**-NO_2]$^+$ (**Figure 3.5c**), suggesting that there is a 10% component from [Cu(κ^2-ONO)(TMPA-CO_2H)] and a 2% component from [**18**(κ^1-NO_2)(κ^2-ONO)].

Hence these EPR data support the assumption that nitrite binds to complex **18** in solution primarily through nitrogen, in a similar fashion to that observed in the solid state (**Figure 3.3**), although with significant minority species where the nitrite is bound through oxygen. Furthermore, the data suggest that protonation of [**18**-NO_2] does not lead to a significant change in the coordination geometry at the copper center, implying that species where the carboxylate group remains bound to the metal dominate in solution.

3.2.3 Infrared spectroscopy

The infrared spectrum of complex [**17**-NO_2]$^+$ in acetonitrile solution is shown in **Figure 3.8**. There is an intense band at 1097 cm^{-1} which is characteristic of the antisymmetric N-O stretch previously observed for nitrite bound to Cu(II) centers in a κ^2-ONO fashion.[30,46] This solution-phase IR spectrum is therefore in agreement with the EPR data, which also suggest that nitrite binds to copper through both its oxygens in a quasi-bidentate manner in complex **17**. The corresponding symmetrical stretch is expected to come between 1450 and 1400 cm^{-1},[43] but this is obscured by signals arising from acetonitrile in the same region. Meanwhile, a band at 1736 cm^{-1} can be assigned to the C=O stretch in the methyl ester.[88]

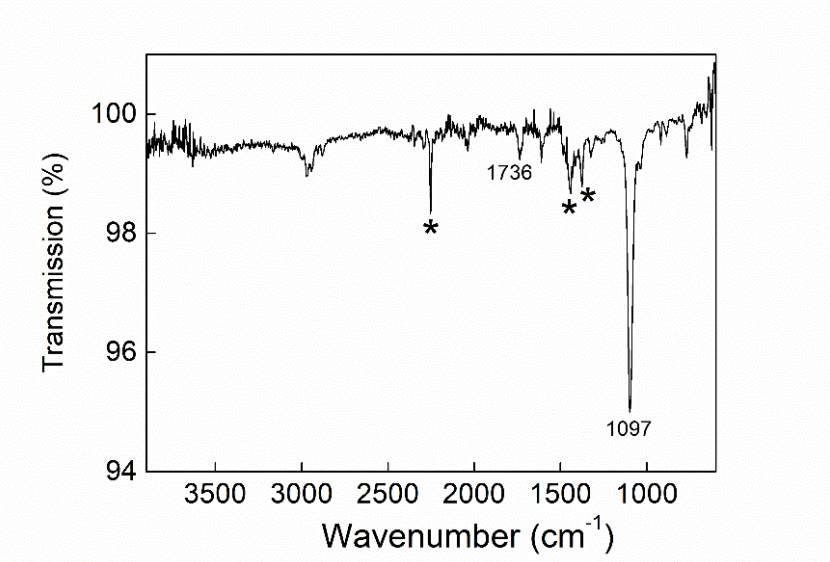

Figure 3.8: *Infrared spectrum of a 1.6 mM solution of [**17**-NO_2]$^+$ in acetonitrile. Bands indicated with asterisks are attributable to acetonitrile. Labelled stretches are discussed in the main text. Reproduced from ACS Catal.* ***2018****, 8, 5070 with permission of American Chemical Society. Copyright 2018*

The solid state infrared spectrum of complex [**18**-NO_2] is shown in **Figure 3.9**. This spectrum shows strong absorbances at 1362 and 1328 cm^{-1}, which are assigned to the $\nu_{asym}(NO_2)$ and $\nu_{sym}(NO_2)$ bands of *N*-bound nitrite respectively by comparison with the literature.[27,30,43] Hence the IR data are consistent with the EPR spectra and solid state structures in suggesting that nitrite is predominantly *O*-bound in complex [**17**-NO_2]$^+$ and predominantly *N*-bound in complex [**18**-NO_2].

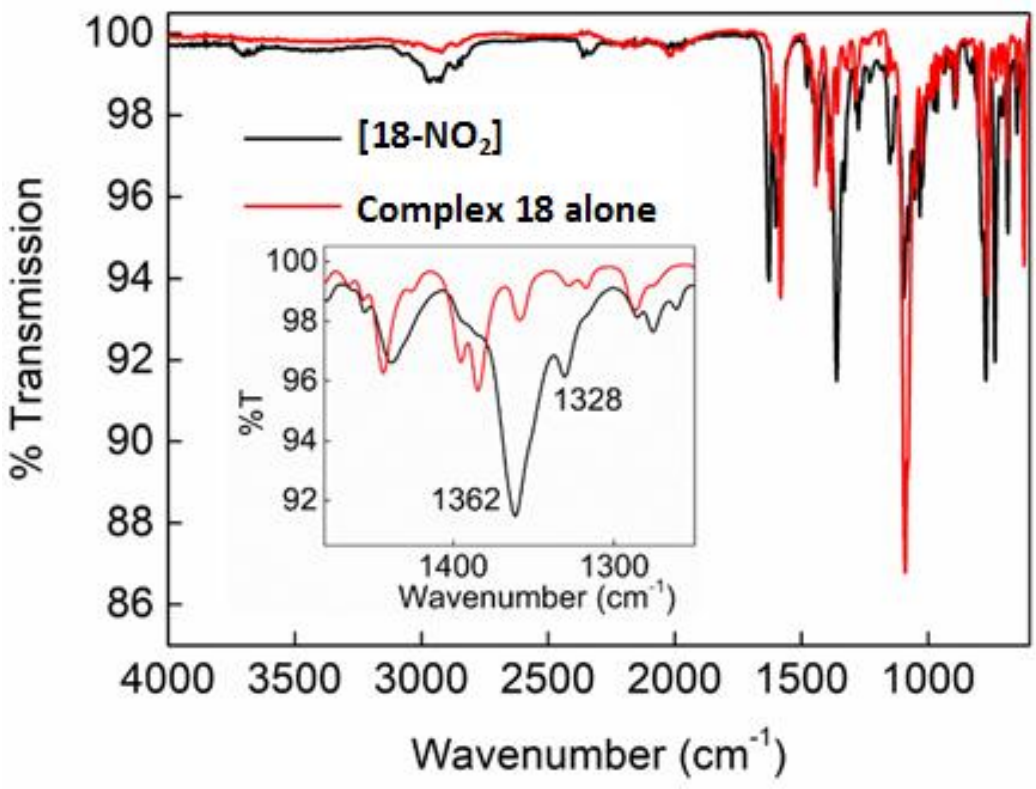

Figure3.9: *Infrared spectrum of [**18**-NO_2] (black) and complex **18** without nitrite for comparison (red). Labelled stretches in the inset are discussed in the main text. Reproduced from ACS Catal.* ***2018****, 8, 5070 with permission of American Chemical Society. Copyright 2018*

3.2.4 Electrocatalysis of nitrite reduction.

The potential electrocatalytic activity of complexes **17** and **18** for the reduction of nitrite to NO was then explored by cyclic voltammetry. **Figure 3.10A** (black trace) shows the behavior of complex **17** in acetonitrile containing 0.1 M tetrabutylammonium hexafluorophosphate (TBA-PF_6). A reversible redox wave is evident at $E_{1/2} \approx -0.29$ V (*vs.* ferrocenium/ferrocene), which we assign as the Cu(II)/Cu(I) couple.

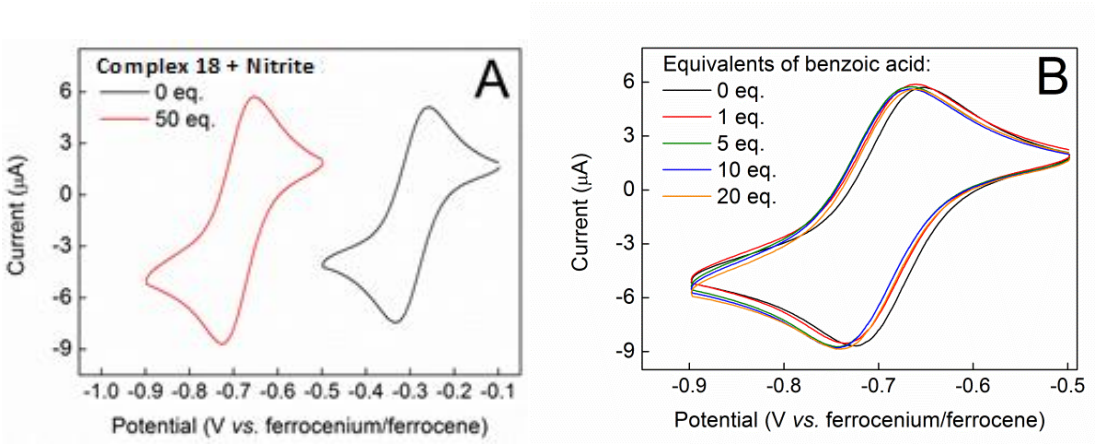

Figure 3.10: *(**A**) Cyclic voltammograms of a 0.6 mM acetonitrile solution of complex **17** containing 0.1 M TBA-PF_6 run under the conditions detailed in **Section 2.6.2**. The black trace shows the behavior of the complex on its own, and the red trace shows the behavior in the presence of 50 equivalents of tetrabutylammonium nitrite. (**B**) Overlay of the cyclic voltammograms of a 0.6 mM acetonitrile solution of complex **17** containing 0.1 M TBA-PF_6 in the presence of 50 equivalents of tetrabutylammonium nitrite, and adding benzoic acid as indicated: 0 equivalents (black line), 1 equivalent (red line), 5 equivalents (green line), 10 equivalents (blue line) and 20 equivalents (orange line). Reproduced from ACS Catal. **2018**, 8, 5070 with permission of American Chemical Society. Copyright 2018*

This wave shifts to significantly more cathodic potentials ($E_{1/2}$ = –0.69 V) upon the addition of tetrabutylammonium nitrite (red trace; see also **Figure 3.11** for a comparison over a larger voltage window).

The solution also turns green as nitrite is added. Both the color change and the shift in the position of the reversible redox wave are consistent with nitrite binding to the Cu(II) center and displacing the coordinated acetonitrile found in the crystal structure (**Figure 3.1**); the replacement of a neutral CH_3CN ligand by a more electron-rich NO_2^- ligand would be expected to make the reduction of the Cu(II) center more difficult. There is, however, no catalytic wave that would suggest electro-reduction of nitrite mediated by the complex under these conditions.

Figure 3.10B then shows the effect of adding the proton source benzoic acid to a solution of complex **17** containing 50 equivalents of tetrabutylammonium nitrite. Hence it is apparent that even at 20 equivalents of protons added to the solution of complex **17**, the only effect on the wave is a slight cathodic shift to $E_{1/2}$ = –0.71 V, with no catalytic wave for nitrite reduction evident.

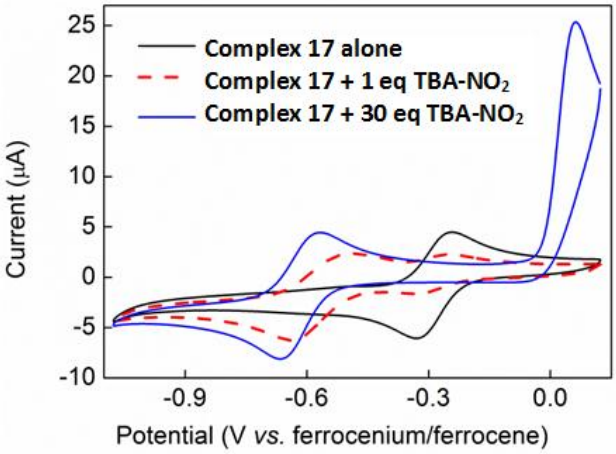

Figure 3.11: *Cyclic voltammograms of a 0.6 mM acetonitrile solution of complex* ***17*** *containing 0.1 M TBA-PF_6 run under the conditions detailed in the Experimental Section, but using a scan rate of 50 mV s^{-1}. The black trace shows the behavior of the complex on its own, the red dashed trace shows the behaviour in the presence of 1 equivalent of tetrabutylammonium nitrite, and the blue solid trace shows the behaviour in the presence of 5 equivalents of tetrabutylammonium nitrite. The large oxidative wave at 0 V in the latter voltammogram corresponds to the oxidation of free nitrite in this solvent/electrolyte system, as previously reported.* [(42)] *Reproduced from ACS Catal.* ***2018****, 8, 5070 with permission of American Chemical Society. Copyright 2018*

However, the situation changes when the methyl ester on complex **17** is deprotected to give complex **18**. In **Figure 3.12A**, the CV of complex **18** in acetonitrile containing 0.1 M tetrabutylammonium hexafluorophosphate is shown (black trace in **Figure 3.12A**, and see also **Figure 3.13** for cyclic voltammograms of [**17**-NO_2]$^+$ and [**18**-NO_2]).).

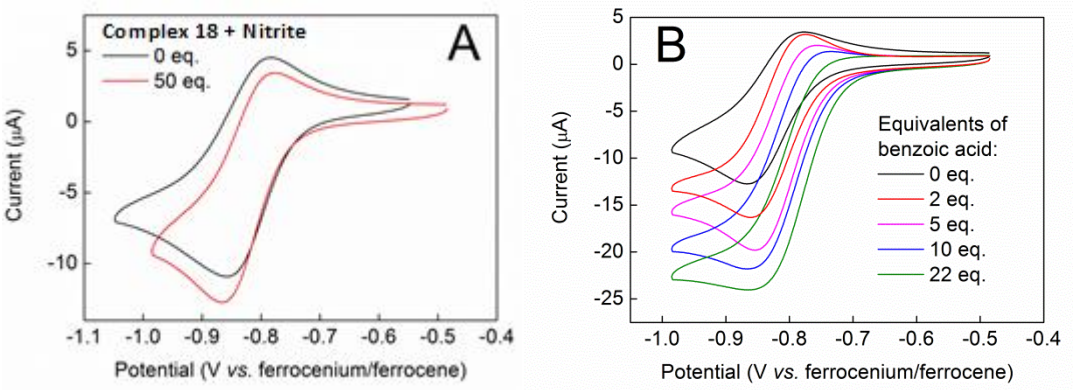

Figure 3.12: ***(A)*** *Cyclic voltammograms of a 1 mM acetonitrile solution of complex* ***18*** *containing 0.1 M TBA-PF_6 run under the conditions detailed in the Experimental Section. The black trace shows the behavior of the complex on its own, and the red trace shows the behaviour in the presence of 50 equivalents of tetrabutylammonium nitrite.* ***(B)*** *Cyclic voltammograms of a 1 mM acetonitrile solution of complex* ***18*** *containing 0.1 M TBA-PF_6 in the presence of 50 equivalents of tetrabutylammonium nitrite, and adding benzoic acid as indicated: 0 equivalents (black line), 2 equivalents (red line), 5 equivalents (purple line), 10 equivalents (blue line) and 20 equivalents (green line). Reproduced from ACS Catal.* ***2018****, 8, 5070 with permission of American Chemical Society. Copyright 2018*

This presents a reversible redox wave for the Cu(II)/Cu(I) redox couple at $E_{1/2}$ = –0.82 V, the position of which changes very little upon addition of nitrite (red trace). The much more cathodic position of the Cu(II)/Cu(I) redox wave in comparison to that seen in complex **17** is further evidence that the deprotonated carboxylic acid group remains coordinated to the copper center in solution (increasing the effective electron density at the metal and making reduction harder), as seen in the solid state (**Figure 3.3**), and also as suggested by EPR, mass spectrometry and CHN analysis (shown in support of the synthetic procedure (page 111). In contrast to the case for complex **17**, it is, therefore, very difficult to gauge nitrite binding by observing the shift in the Cu(II)/Cu(I) redox wave for complex **18**.

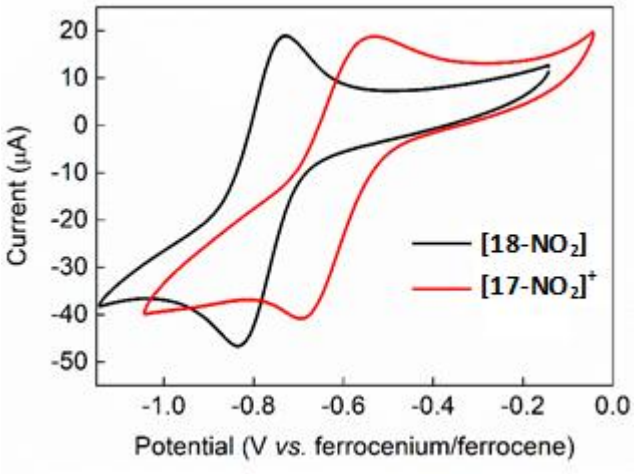

Figure 3.13: *Cyclic voltammograms of [**17**-NO_2]$^+$ (1.6 mM, red trace) and [**18**-NO_2] (1.8 mM, black trace) in acetonitrile solution containing 0.2 M TBA-PF_6 run under the conditions detailed in the Experimental Section, at a scan rate of 100 mV s^{-1}. Reproduced from ACS Catal.* ***2018****, 8, 5070 with permission of American Chemical Society. Copyright 2018*

However, the color change of the solution from blue to green suggests that nitrite is indeed bound, as do the EPR and crystallographic data. Further evidence for this comes in the shape of the red trace in **Figure 3.12A**, which now shows some of the features characteristic of a catalytic wave.

Intrigued by this wave-shape, we added benzoic acid to solutions of **18** in the presence of 50 equivalents of tetrabutylammonium nitrite, as shown in **Figure 3.12B**. A clear trend was apparent, in which adding larger amounts of the proton source gave rise to a more and more pronounced catalytic wave at the potential of the Cu(II)/Cu(I) redox couple. There was also a slight anodic shift in the position of the peak current for this wave with increasing acid concentration.

In order to determine the product(s) of this electrocatalytic activity, we conducted bulk electrolyses in sealed electrochemical cells at a fixed potential –0.91 V *vs.* ferrocenium/ferrocene under a variety of conditions. Representative current density *vs.* time curves are shown in **Figure 3.14** for electrolyses using 5 mM benzoic acid, 5 mM TBA-NO_2 and complex **17** (blue line), 5 mM benzoic acid, 5 mM TBA-NO_2 and complex **18** (red line), and a control containing just 5 mM benzoic acid and 5 mM TBA-NO_2 (black line). Hence it is apparent that considerably more current flows when complex **18** is employed compared to when complex **17** is used, or compared to the background reaction. In order to determine if any NO was produced during these bulk electrolyses, we used the known NO-complexation agent *meso*-tetraphenylporphyrin cobalt(II) (Co-TPP),[89-92] which undergoes a highly characteristic shift in the position of its visible absorption band ($\lambda_{max} \approx 530$ nm) upon NO binding.[29,93]

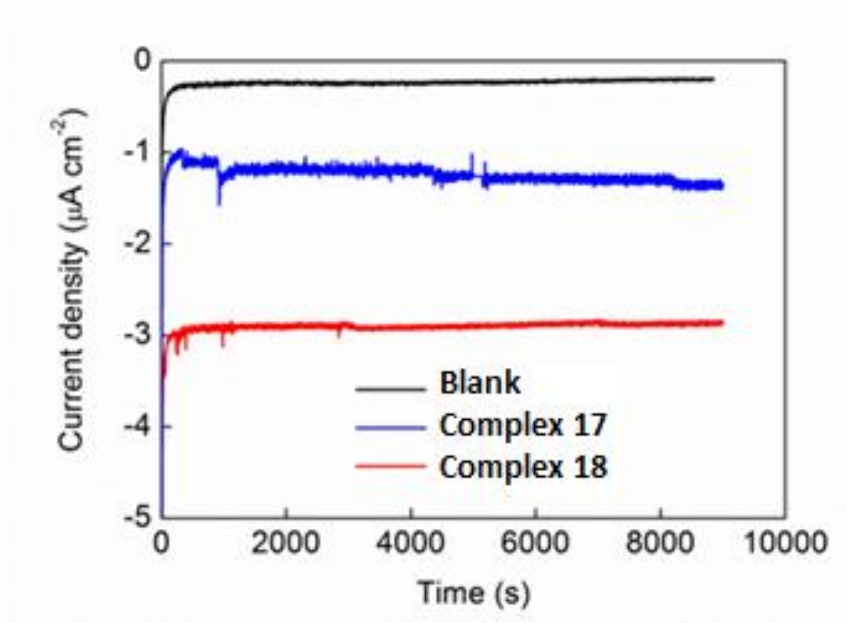

Figure 3.14: *Bulk electrolysis in 0.2 M TBA-PF_6 in acetonitrile of a 7 μM solution of complex* ***17*** *(blue line) a 7 μM solution of complex* ***18*** *(red line) and in the absence of any catalyst (black line) at a fixed potential of –0.91 V vs. ferrocenium/ferrocene. The working electrode was a glassy carbon foil electrode (area ~4.6 cm^2). An Ag/$AgNO_3$ pseudo reference electrode and a Pt wire counter electrode were used. In each case, the electrolyte also contained 5 mM benzoic acid and 5 mM TBA-NO_2. Reproduced from ACS Catal.* ***2018****, 8, 5070 with permission of American Chemical Society. Copyright 2018*

A calibration curve (**Figure 3.15**) was constructed, which allowed the amount of NO in the reaction vessel headspace to be determined on the basis of the position of the Co-TPP absorption band (see **Section 2.6.5**). By assessing the shifts produced in the Co-TPP

absorption band in bulk electrolyses that passed various amounts of charge, a Faradaic yield for the production of NO by complex **18** of 97.3 ± 3.6% was obtained.

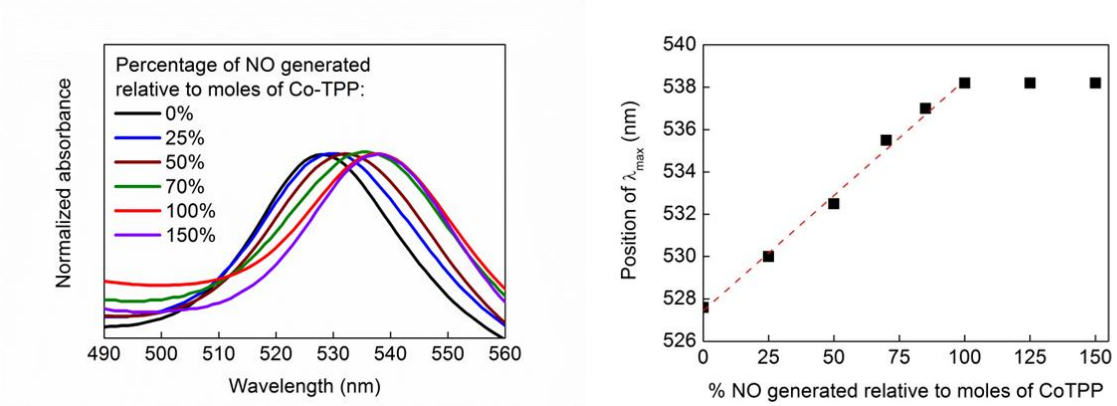

Figure 3.15: *(**a**) Normalized UV-vis spectra showing the shift in absorbance band of Co-TPP with increasing level of complexation to NO. For experimental details, see the Experimental Section of the main paper. (**b**) Calibration curve extracted from the peak maxima in (**a**), showing the linear trend in absorption maximum shift with % complexation to NO. Reproduced from ACS Catal.* ***2018****, 8, 5070 with permission of American Chemical Society. Copyright 2018*

In an extended-run bulk electrolysis with complex **18** (**Figure 3.16**), 0.225 C of charge were passed for the reduction of nitrite to NO over 22000 s, without any apparent diminution of the current density. Given a concentration of catalyst of 7 μM in 15 mL of solution, this corresponds to around 22 turnovers of the catalyst, thus proving that complex **18** is functioning as a genuine catalyst for this reaction.

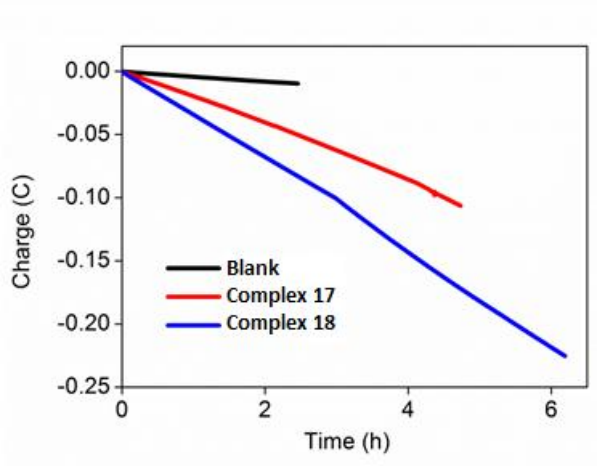

Figure 3.16. *Bulk electrolysis in 0.2 M TBA-PF_6 in acetonitrile of a 7 μM solution of complex* ***17*** *(red line) a 7 μM solution of complex* ***18*** *(blue line) and in the absence of any catalyst (black line) at a fixed potential of –0.91 V vs. ferrocenium/ferrocene. The working electrode was a glassy carbon foil electrode (area ~4.6 cm^2). An Ag/$AgNO_3$ pseudo reference electrode and a Pt wire counter electrode were used. In each case, the electrolyte also contained 5 mM benzoic acid and 5 mM TBA-NO_2. Reproduced from ACS Catal.* ***2018****, 8, 5070 with permission of American Chemical Society. Copyright 2018*

Inspection of **Figure 3.14** suggests that current appreciably above the background level is also observed with complex **17** in the presence of benzoic acid and TBA-NO_2. Moreover, Co-TPP-based colorimetric NO determination assays revealed that this current was associated with NO formation (Faradaic yield = 88.2 ± 7.3%).

Given the apparent absence of electrocatalytic activity evident in **Figure 3.10**, this was initially surprising to us. We therefore conducted further cyclic voltammetry experiments with complex **17** in the presence of benzoic acid and TBA-NO_2 at the slower scan-rate of 10 mV s^{-1}, as shown in **Figure 3.17**. This indicated that a catalytic wave is evident when the scan-rate is slowed.

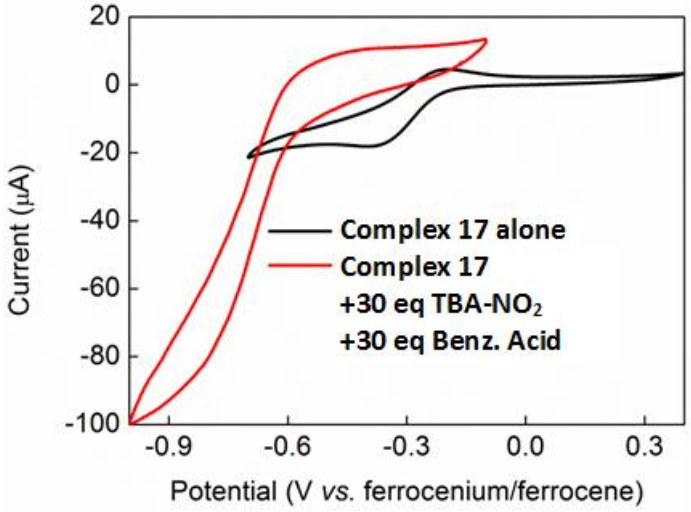

Figure 3.17: *Cyclic voltammograms of a 0.6 mM acetonitrile solution of complex **17** containing 0.1 M TBA-PF_6 run under the conditions detailed in the Experimental Section, but at a scan-rate of 10 mV/s. The black trace shows the behavior of the complex on its own, and the red trace shows the behaviour in the presence of 30 equivalents of tetrabutylammonium nitrite and 30 equivalents of benzoic acid. Reproduced from ACS Catal. **2018**, 8, 5070 with permission of American Chemical Society. Copyright 2018*

Coupled with the above-background currents observed by bulk electrolysis (and the associated detection of NO), this suggests that complex **17** is indeed competent for nitrite reduction electrocatalysis, but that the catalysis with complex **17** is less effective than it is with complex **18**. Indeed, in an extended-run bulk electrolysis, complex **17** could be induced to turn over 10 times in a 17000 s time period (see **Figure 3.16**).

To further confirm the production of NO during bulk electrolysis, NO release profiles were obtained using a Sievers NOA 280i chemiluminescence nitric oxide analyzer (**Section 2.6.6**). **Figure 3.18** shows one such experiment with complex **18** in which a bulk electrolysis was performed for an hour at a fixed potential of –0.91 V *vs.* ferrocenium/ferrocene in a sealed cell (**Figure 3.18A**), after which time the contents of the headspace were flushed into the detector of the Sievers instrument using a stream of nitrogen. The main panel in **Figure**

3.18B then shows the total (cumulative) amount of NO measured by the detector after termination of the electrolysis, whilst the inset shows the instantaneous level of NO detected.

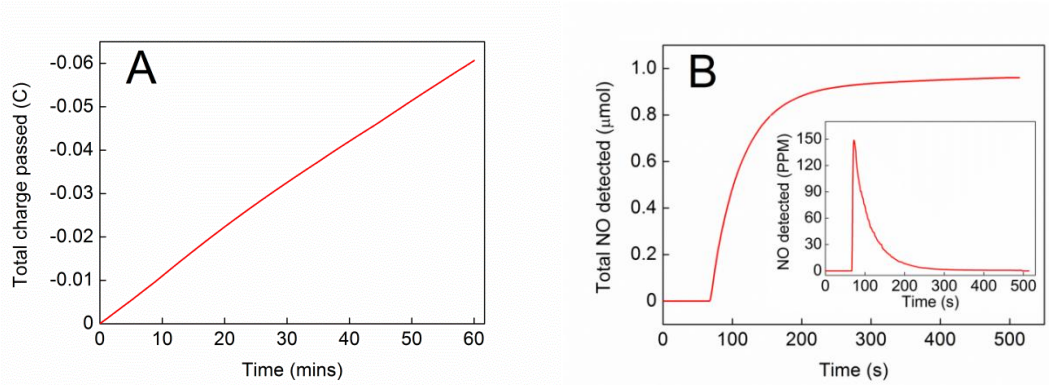

Figure 3.18 *(**A**) Charge vs. time curve for the bulk electrolysis of complex **18** at a fixed potential of –0.91 V vs. ferrocenium/ferrocene in acetonitrile/0.2 M TBA-PF_6 as per the conditions detailed in the Experimental Section.(**B**) (main panel) total NO measured upon flushing cell headspace into the NO detector after termination of electrolysis and (inset) instantaneous NO detection. Reproduced from ACS Catal.* ***2018****, 8, 5070 with permission of American Chemical Society. Copyright 2018*

On the basis of this instantaneous data, one can conclude that after about 300 s, the level of NO detected has decayed back to basal levels. The slope of the graph in the main panel after 300 s therefore allows the rate of background NO production due to spontaneous processes to be calculated. Subtracting this value from the overall amount of NO produced gives a Faradaic yield for NO production by complex **18** using this method of 100 ± 1%, in good agreement with the values obtained by colorimetric tests. As expected, electrolysis under the same conditions but in the absence of any catalyst produces significantly less NO (see **Figure 3.19**).

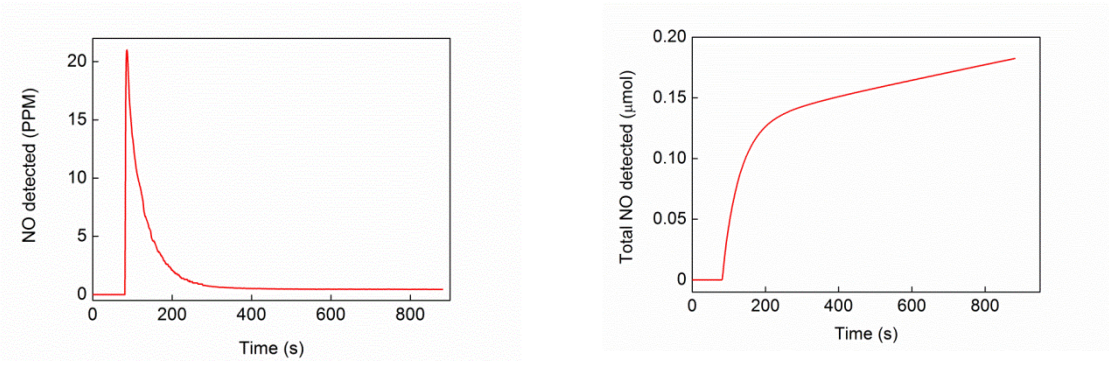

Figure 3.19: Left *instantaneous NO detection measured after bulk electrolysis of 0.84 mM benzoic acid and 0.84 mM TBA-NO_2 at a fixed potential of –0.91 V vs. ferrocenium/ferrocene in acetonitrile/0.2 M TBA-PF_6.* ***Right:*** *total NO measured upon flushing cell headspace into the NO detector after termination of electrolysis. Reproduced from ACS Catal.* ***2018****, 8, 5070 with permission of American Chemical Society. Copyright 2018*

The above tests serve to establish that both complexes **17** and **18** are competent for electrocatalytic nitrite reduction to NO with essentially full Faradaic efficiency, but that complex **18** appears to be the more effective of the two. In order to gain insight into these apparent differences in catalytic activity, further electrochemical investigations were undertaken. Firstly, Tafel analysis of **17** and **18** in 0.1 M TBA-PF_6/acetonitrile in the presence of 30 equivalents of both TBA-NO_2 and benzoic acid was found to give slopes of 138 and 128 mV decade^{-1} respectively if a transfer coefficient of 0.5 was assumed (**Figure 3.20**). These are close to the theoretical value for a rate-limiting one-electron process (120 mV decade^{-1}), in agreement with a reaction such as that given in **Equation 1** (page 81) for the one-electron reduction of nitrite to NO.

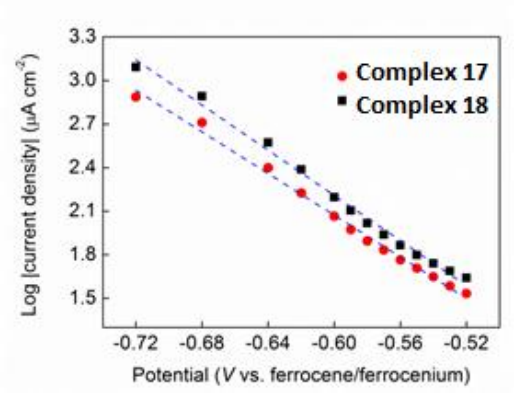

Figure 3.20: *Tafel analysis of compounds **3** and **4** in 0.1 M TBA-PF_6/acetonitrile in the presence of 30 equivalents of both TBA-NO_2 and benzoic acid. Tafel data were collected by linear sweep voltammetry (with stirring) at a scan rate of 1 mV/s. Both complexes were used at a concentration of 5 mM. A glassy carbon button working electrode (area = 0.071 cm^2, CH Instruments), Pt wire and Ag/$AgNO_3$ were used as the working, counter and pseudo reference electrodes respectively. The Tafel plot was constructed using the modulus of the current density. The blue dashed lines are guides to the eye. Reproduced from ACS Catal. **2018**, 8, 5070 with permission of American Chemical Society. Copyright 2018*

Next, we investigated the kinetics of the nitrite reduction reaction by cyclic voltammetry. Hence the peak current for electrocatalytic nitrite reduction by both complex **17** and complex **18** was measured as a function of nitrite concentration in the presence of a large excess (300 equivalents relative to the catalyst complexes) of benzoic acid at a scan-rate of 10 mV s^{-1} (at which scan-rate there is evidence of an electrocatalytic wave with both complexes; see above).

As the Faradaic yield for NO production is essentially unity, and as the reduction of nitrite to NO is a one-electron process, these current densities can be converted to a rate of nitric oxide production per unit area of electrode ($V_{[NO]}$) by dividing the current density by

Faraday's constant. This data (**Figures 3.21**, **3.22**), can then be fitted to Michaelis-Menten-type kinetics as per **Equation 2**:

$$V_{[NO]} = V_{max}[NO_2^-]/(K_M + [NO_2^-]) \quad \text{(Eq. 2)}$$

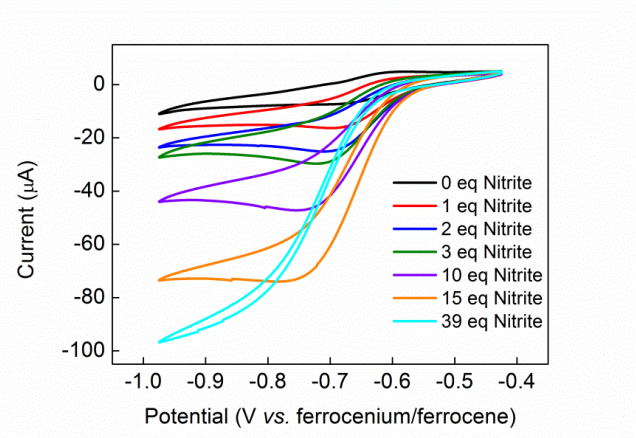

Figure 3.21: *Cyclic voltammograms of a 1 mM acetonitrile solution of complex* ***18*** *containing 0.2 M TBA-PF_6 and 300 equivalents of benzoic acid run under the conditions detailed in the Experimental Section, but at a scan-rate of 10 mV/s. TBA-NO_2 was then added as a solution from a 0.2 M stock solution in acetonitrile, so as to produce a minimal volume change. The black trace shows the behavior of the complex on its own in the presence of 300 equivalents of benzoic acid. Subsequent additions of TBA-NO_2 were as follows: 1 equivalent (red line), 2 equivalents (blue line), 3 equivalents (green line), 10 equivalents (purple line), 15 equivalents (orange line) and 39 equivalents (cyan line). Reproduced from ACS Catal.* ***2018****, 8, 5070 with permission of American Chemical Society. Copyright 2018*

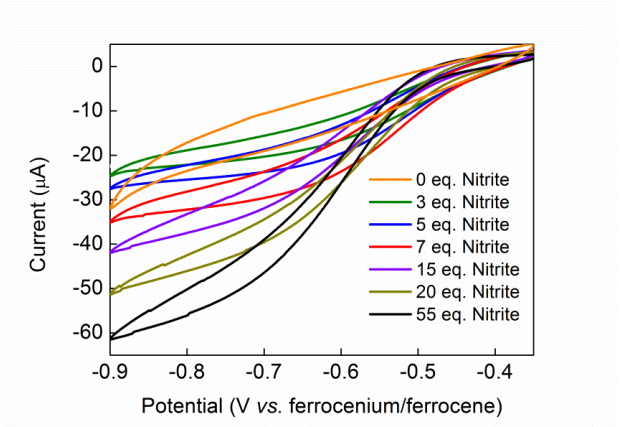

Figure 3.22: *Cyclic voltammograms of a 1 mM acetonitrile solution of complex* ***3*** *containing 0.2 M TBA-PF_6 and 300 equivalents of benzoic acid run under the conditions detailed in the Experimental Section, but at a scan-rate of 10 mV/s. TBA-NO_2 was then added as a solution from a 0.2 M stock solution in acetonitrile, so as to produce a minimal volume change. The orange trace shows the behavior of the complex on its own in the presence of 300 equivalents of benzoic acid. Subsequent additions of TBA-NO_2 were as follows: 3 equivalents (green line), 5 equivalents (blue line), 7 equivalents (red line), 15 equivalents (purple line), 20 equivalents (olive line) and 55 equivalents (black line). Reproduced from ACS Catal.* ***2018****, 8, 5070 with permission of American Chemical Society. Copyright 2018*

which allows the maximal rate of reaction (V_{max}) for complex **18** to be estimated as being 14.7 ± 1.5 nmol s^{-1} cm^{-2}, with a Michaelis constant (K_M) of 11 ± 3 mM as shown in **Figure 3.23**. The value of V_{max} can be de-convoluted to yield the Michaelis-Menten k_{cat} (the turnover frequency) by dividing V_{max} by the concentration of catalyst molecules. In our case, this concentration corresponds to the number of catalyst molecules participating in the electrochemical reaction, which (given that the reaction medium is not stirred in these CV measurements) can be determined by integrating the charge passed in the reversible Cu(II)/Cu(I) redox wave in the absence of substrate. When this integration is performed, an electrochemically-active surface concentration of catalyst molecules of 1.1×10^{-9} mol cm^{-2} is obtained, which in turn gives a value for k_{cat} (the turnover frequency) for complex **18** of 13.4 ± 1.4 s^{-1}. From this value, the catalytic efficiency of the catalyst can be expressed by the ratio k_{cat}/K_M, which gives a value of around 1200 M^{-1} s^{-1}.

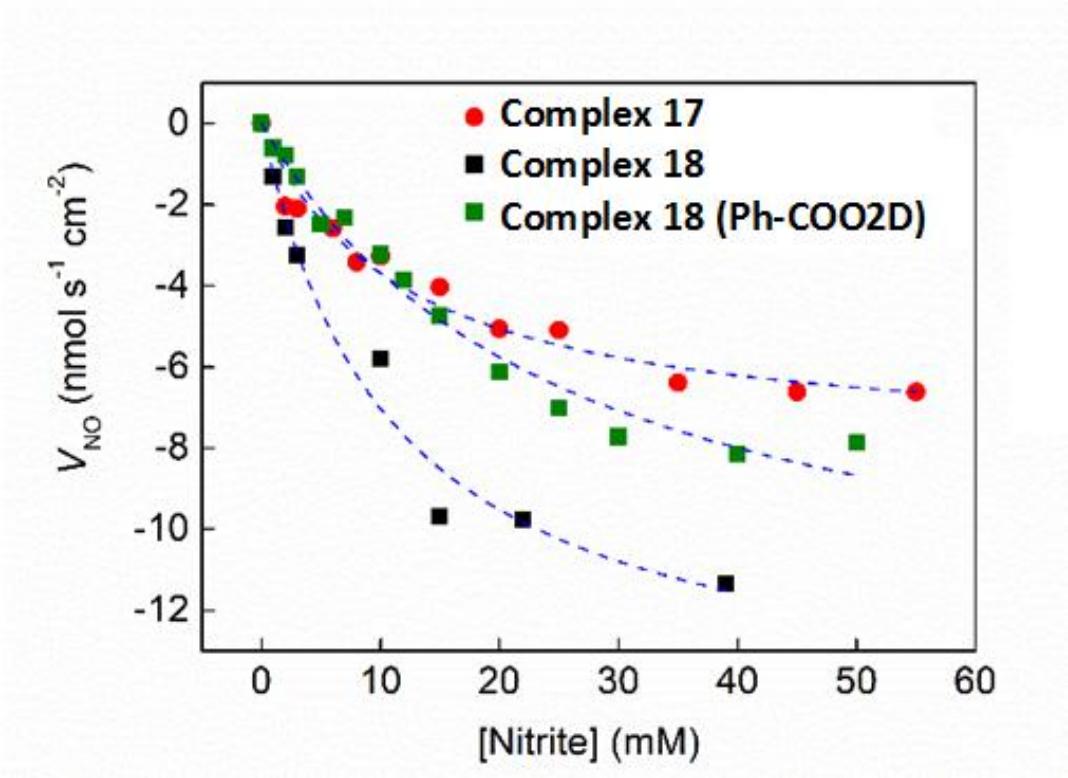

Figure 3.23: *The dependence of the rate of electrochemical NO generation on [NO_2^-] for complexes **17** (red circles) and **18** (black squares) in the presence of 300 equivalents of benzoic acid (Ph-CO_2H) in acetonitrile/0.2 M TBA-PF_6 as per the conditions detailed in the bulk text. The green squares show analogous data for complex **18** but in deuterated acetonitrile/0.2 M TBA-PF_6 in the presence of 300 equivalents of deuterated benzoic acid (Ph-CO_2D). The blue dashed lines show fits to the Michaelis-Menten equation. Reproduced from ACS Catal. **2018**, 8, 5070 with permission of American Chemical Society. Copyright 2018*

These values can be compared to those previously reported by Orain and co-workers (compound **11** described at page 34)[78] and Yamaguchi and co-workers (page 33 compound **10**)[48] for Cu-TMPA complexes without any pendant acid/base units immobilized on the surface of an electrode and performing the reduction of nitrite to NO in aqueous solution.[47,50] Hence, the best metrics achieved by Orain and co-workers were k_{cat} = 1.39 s^{-1} with K_M = 70 mM (giving k_{cat}/K_M = 17.4 M^{-1} s^{-1}), whilst Yamaguchi and co-workers reported k_{cat} = 0.11 s^{-1} with K_M = 15.8 mM (giving k_{cat}/K_M = 7.0 M^{-1} s^{-1}). Thus our system is the most effective small molecule Cu-based platform for electrocatalysis of NO_2^- reduction to NO yet reported. For comparison, the CuNIR enzyme from *Alcaligenes faecalis* has been estimated to have a turnover frequency of around 2000 s^{-1} and a K_M of around 100 μM, giving $k_{cat}/K_M \approx 2 \times 10^7$ M^{-1} s^{-1}.[94]

To discriminate between the effects of the pendant acid/base group and the change in solvent and reaction conditions in this apparent improvement in catalytic efficiency relative to the previous studies with TMPA-based Cu complexes, we also performed a similar Michaelis-Menten analysis on complex **17** (which lacks any the pendant acid/base groups) under analogous conditions (**Figures 3.2** and **3.23**). The resulting Michaelis-Menten plot allowed the maximal rate of reaction (V_{max}) to be estimated as 8.0 ± 0.5 nmol s^{-1} cm^{-2}, with a Michaelis constant (K_M) of 12 ± 2 mM. Taking the electrochemically-active surface concentration of catalyst molecules to be 1.1×10^{-9} mol cm^{-2}, the value of k_{cat} is then 7.3 ± 0.5 s^{-1}, giving $k_{cat}/K_M \approx 600$ M^{-1} s^{-1}. Hence there is a demonstrable enhancement in the catalytic performance of complex **18** compared to complex **17** over and above that attributable to the change in solvent medium relative to the previous studies.[47,50]

The nature of the proton-coupled-electron transfer event occurring during nitrite reduction with complex **18** was then probed by comparing the kinetics in a protic environment with those observed under deuterated conditions. Hence the solvent medium was switched to CD_3CN and a deuterated benzoic acid source (Ph-CO_2D) was used. **Figure3.23** (green squares) shows the results of this deuteration. V_{max} remains largely unaltered with respect to protic conditions, at 13.1 ± 1.1 nmol s^{-1} cm^{-2} (giving k_{cat} = 11.9 ± 1.0 s^{-1}). However, K_M increases significantly to 25 ± 4 mM, suggesting that higher concentrations of substrate are required to reach this maximal turnover frequency. This in turn gives a value for the catalytic efficiency of complex **18** under deuterated conditions of around 470 M^{-1} s^{-1}, implying a significant kinetic isotope effect of ~2.5. The fact that such a pronounced effect

can be seen upon moving to deuterated solvents suggests that the proton and electron transfers are concerted.[95]

3.2.5 Calculations.

Based on the experimental observations derived from spectroscopic and electrochemical data, a mechanism for the catalytic reduction of nitrite to nitric oxide was developed using DFT calculations. Optimizations were performed at the BP86 level of theory using the def2-SVP basis set for all atoms and acetonitrile as the solvent continuum. Single-point calculations were performed on the optimized coordinates at the PBE0 level of theory with triple-ζ basis sets.

In these simulations, we found that nitrite readily displaces a coordinated solvent molecule (H_2O or CH_3CN) from complexes **17** and **18** to give [**17**-NO_2]$^+$ and [**18**-NO_2]. The coordination mode of the nitrite ligand in [**18**-NO_2] favors the N-bound (nitro) linkage isomer by 2.9 kcal mol^{-1} over that of the nitrito (O-bound) variant. Although this is very close to the limit of energies distinguishable by DFT, it does match the solid state structure (**Figure 3.3**), and the major solution-phase species suggested by EPR (**Figure 3.7**). Additionally, no optimized complex retained a chelating κ^2-ONO ligand when combined with **18**. For **17**, the absence of the pendant acid/base group gave isoenergetic complexes with nitro or chelating nitrito ligands (1.4 kcal mol^{-1} in favor of the latter). The latter is proposed to be the complex that provides the largest contribution to the EPR spectrum of [**17**-NO_2]$^+$ on account of the sizeable *g*-shift compared with [**18**-NO_2] (see EPR discussion in the previous section and **Figure 3.5**). These isomers were 5.6 kcal mol^{-1} more favorable energetically than the complex with a monodentate nitrito ligand.

Having established the most likely entry point into the catalytic cycle as being [**18**-NO_2], further computational analysis (**Scheme 2**) reveals that protonation of [**18**-NO_2] to give [**18**H-NO_2]$^+$ would afford a 17.2 kcal mol^{-1} increase in stability, but (as discussed above in relation to the EPR data) there is no evidence to support protonation of the carboxylate group in [**18**-NO_2] in the presence of excess benzoic acid. On the other hand, reduction of [**18**-NO_2] by one electron (to give the Cu(I) species [**18**-NO_2]$^-$) leads to a decrease in stability of 32.7 kcal mol^{-1}. This is unsurprising as six-coordinate species are not favored by Cu(I). However, subsequent protonation of the carboxylate in [**18**-NO_2]$^-$ to give [**18**H-NO_2] (in which the carboxylate unit is no longer coordinated to copper), affords a 26.9 kcal

mol^{-1} increase in stability relative to [**18**-NO_2]$^-$. This DFT-modelled PCET is therefore consistent with the experimental observation of concerted proton and electron transfer, in which the reduction of the Cu(II) complex is concomitant with the release and protonation of the carboxylate, leading directly from [**18**-NO_2] to [**4**H-NO_2] and avoiding the high energy [**18**-NO_2]$^-$ intermediate.

Computational optimization of [**18**H-NO_2] then leads spontaneously to a structure where the carboxylate proton had migrated to the adjacent nitro ligand to give a coordinated nitrous acid group, [**18**-HNO_2] (**Scheme 2**). This underscores the key role played by the proton-relaying group in nitrite reduction, as the *in silico* process follows an analogous path to that observed experimentally. This is not the case for the nitrito isomers of this Cu(I) complex, which are less stable than the nitro isomer. This further corroborates our assignment of the nitro isomer as the catalytically competent species in complex **18**. Meanwhile, complex **17** is found to be a less effective electrocatalyst for this process than complex **18**, which can be attributed both to its lack of any proton-relaying units and to the different nature of the dominant nitrite coordination mode in complex **17** (*i.e.* predominantly through oxygen), which will also impact upon the N-O bond cleavage pathway that is followed with this complex (probably by making the nitrite more difficult to protonate in complex **17)**.

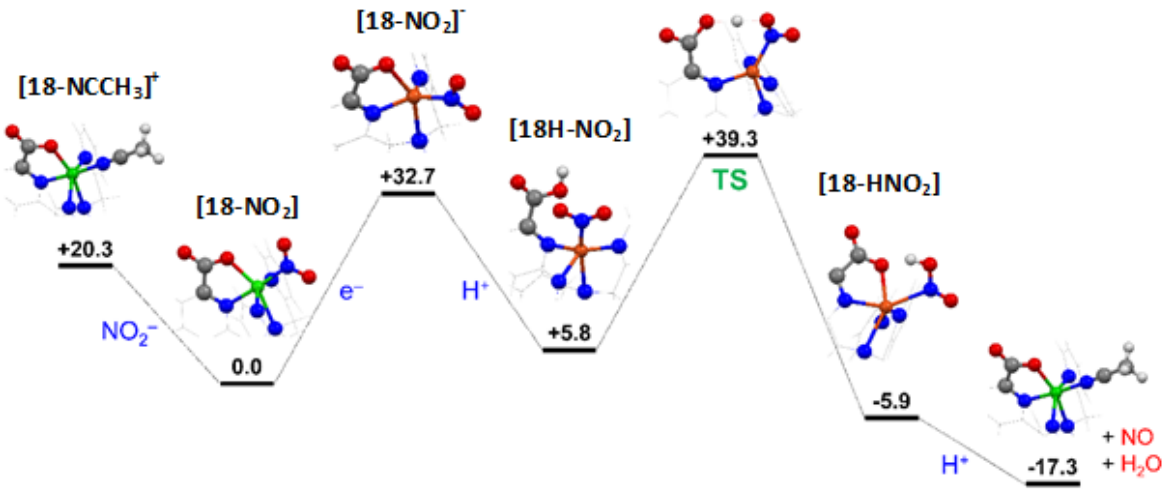

Scheme 2: *Proposed pathway of the electrocatalytic reduction of NO_2^- to NO and H_2O using the [**18**-$NCCH_3$]$^+$ pre-catalyst, showing optimized structures (color palette: Cu(II) = green, Cu(I) = bronze, O = red, N = blue, C = pewter, H = white). Relative energies at the PBE0/ZORA/def2-TZVP + COSMO-RS[CH_3CN] level are in kcal mol^{-1}. Reproduced from ACS Catal.* ***2018****, 8, 5070 with permission of American Chemical Society. Copyright 2018*

Following the PCET to generate [**18**H-NO_2], the proton undergoes intramolecular proton transfer from the pendant carboxylic group to the bound nitrite, to give [**18**-HNO_2]. This process was modelled by creating fixed-structure complexes where the proton was incrementally shifted from the carboxylate to the adjacent nitrite ligand. A transition state ("TS" in Scheme 2) where the H^+ resides midway between these donor/acceptor ligands presents a 33.5 kcal mol^{-1} barrier in this process. Plotting the same reaction pathway with a sequence of Cu(II) species (*i.e.* without the electron transfer process), presents a demanding 50.7 kcal mol^{-1} barrier to the intramolecular proton transfer step. Furthermore, optimization of a Cu(II) species with a coordinated nitrous acid ligand, [**18**-HNO_2]$^+$, sees the proton migrate back toward the pendant carboxylate. In **Scheme 2**, there are then further energy gains leading to a Cu(I) center with an *N*-coordinated nitrous acid and finally an electron transfer from the Cu(I) to the nitrous acid giving the reaction products nitric oxide and water, and regenerating the pre-catalyst.

3.3 Conclusions

In summary, we have developed two new catalysts (**17** and **18**) for the selective electro-reduction of nitrite to NO that function with essentially full Faradaic efficiency for NO production, as indicated by NO-trapping and chemiluminescence tests. Compared to literature reports for electrocatalytic nitrite reduction with Cu-complexes, **17** and **18** are the most efficient catalysts for this transformation yet reported by over an order of magnitude.

This huge increase in catalytic power also in compound **17** can be explained in first instance by the different coordination environment around the Cu site.

In the case of compound[48] the coordination environment is different since the Cu atom is coordinated by only three atoms of nitrogen, and the resulting k_{cat}/K_M is two times lower then the case studied by Orian and co-workers and this will lead to a smaller match with the enzyme. For what concerns compound[78] although it looks more similar to our compound the thread used to bond the complex may influence the electronic factors involved in the catalytic process that we analised in **Chapter 1**.

Another point to take in account is the fact that the catalysts in the cases detailed above are covalently bounded to the electrode. This of course influences the concentration of catalyst at the electrode as well as bringing some kind of steric constraint around the active site that may influences the catalytic power.

The last point to take in account in order to explain the great difference in catalytic power is the reaction envinment. In both the references the experiments are carried in aqueous solutions indeed in our case we did the experiment in acetonitrile in order to have hydrogen bond coming only from a source of protons added in known quantity. Moreover this environment results to be more similar to the hydrophobic pocket where the T2 site is located (see for more information references in **Section 1.4** pp. 17-19). In order to see if in aqueous environment catalytic power of our catalyst is comparable with the previous references, kinetic studies in aqueous solutions will be an interesting further development of this project.

Moreover, we have shown that incorporation of a proton-relaying moiety into the secondary coordination sphere of one of these complexes (**18**) enhances the electrocatalytic nitrite reduction activity displayed by this complex by a factor of two when compared to the analogous complex that lacks this functionality (complex **17**). Using DFT calculations, the possible role of the pendant carboxylate unit in facilitating protonation of the bound nitrite can be discerned. This study therefore constitutes the first report in which the role of proton-coupled-electron transfer in the reduction of nitrite to NO with synthetic molecular catalysts has been addressed. Our results serve to highlight the central role of proton-coupled-electron transfer in the reduction of nitrite to NO (and in the activation of small molecules in general) and could have important implications for the development of new catalysts for the selective interconversions of the nitrogen oxides and other substrates.

3.4 Synthetic procedures

3.4.1 Synthesis of Compound 15

To a solution of 6-chloromethylpyridine-2-carboxylic acid methyl ester[(75)] (270 mg, 1.45 mmol, 1 equiv.) in CH_3CN (14 mL) was added 848 mg of Na_2CO_3 (8 mmol, 5.5 equiv.), giving a yellowish suspension. To this mixture, a solution of bis(2-pyridylmethyl)amine (319 mg, 1.6 mmol, 1.1 equiv.) in CH_3CN (8 mL) was added, and the resulting mixture heated to reflux for 24 h. No change of color was seen when the amine was added, but as the reaction mixture was heated up it turned orange. After 24 h reflux, the mixture was allowed to cool to room temperature, and then filtered to remove the Na_2CO_3. The filtrate was then concentrated *in vacuo*, affording crude compound **15** as a tan solid. This solid was then triturated with ethyl acetate/hexane (4:1), yielding an off-white solid and an orange liquid. Isolation of the solid and a further round of trituration in ethyl

acetate/hexane (4:1) then yielded pure compound **15** (380 mg, 1.09 mmol, 75%). ^{1}H NMR (MeOD, 400 MHz), δ = 8.44 – 8.42 (m, 2H, H_a), 7.98 (dd, J_1 = 8, J_2 = 1, 1H, $H_{g\ or}\ H_i$), 7.92 (t, J = 8, 1H, H_h), 7.86 (dd, J_1 = 8, J_2 = 1, 1H, $H_{g\ or}\ H_i$), 7.78 (dt, J_1 = 8, J_2 = 2, 2H, $H_{b\ or}\ H_c$), 7.68 (d, J = 8, 2H, H_d), 7.29 – 7.24 (m, 2H, $H_{b\ or}\ H_c$), 3.96 (s, 3H, H_j), 3.94 (s, 2H, H_f), 3.88 (s, 4H, H_e). Letter codes correspond to those shown on the ^{1}H NMR spectrum of this compound in **Figure 3.24**. ^{13}C NMR (MeOD, 400 MHz), δ = 166.7, 161.0, 159.8, 149.5, 148.0, 139.1, 138.5, 127.9, 124.8, 124.6, 123.7, 61.1, 60.6, 53.0. ESI-LMMS (methanol): m/z = 371.1464 $[M^{+}Na]^{+}$ (calcd. for $C_{20}H_{20}N_4NaO_2$; 371.1484).

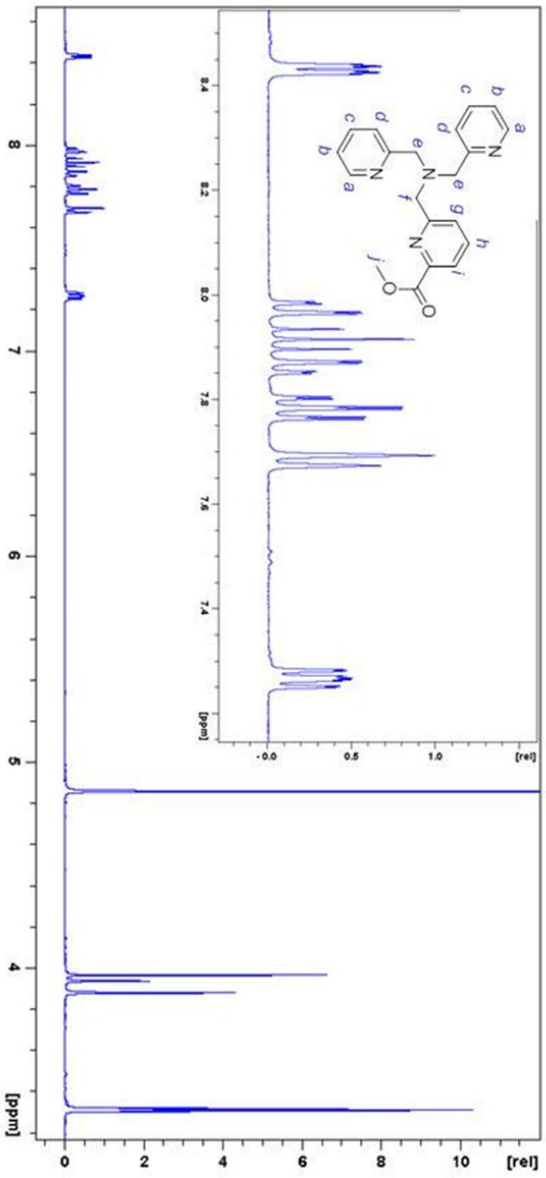

Figure 3.24: *^{1}H NMR spectrum (MeOD, 400 MHz) of compound **15**. An expansion of the aromatic region shown as an inset. Lettering corresponds to the signal assignments in the bulk text. Reproduced from ACS Catal. **2018**, 8, 5070 with permission of American Chemical Society. Copyright 2018*

3.4.2 Synthesis of Compound 16

498 mg (1.43 mmol) of compound **15** were dissolved in 5 mL of ethanol with the aid of ultrasonication. To this solution, 20 mL 0.5 M NaOH was then added and the mixture heated to reflux for 20 h. After this time, the reaction mixture was allowed to cool to room temperature and concentrated *in vacuo* to remove the ethanol. The resulting reaction mixture was then acidified to pH 4 with aqueous HCl and then extracted with $CHCl_3$ (2 × 100 mL). The combined organic extracts were then dried over $MgSO_4$ and concentrated under reduced pressure to yield compound **16** as a yellow oil (200 mg, 0.598 mmol, 42%). The compound gave spectra in agreement with those previously reported for this compound.[76]

3.4.3 Synthesis of Complex 17-H_2O

95 mg (0.273 mmol, 1 equiv.) of compound **15** was dissolved in 3.5 mL of ethanol, giving a bright yellow solution. This solution was then added (with stirring) to a solution of 104 mg (0.273 mmol, 1 equiv.) of $Cu(ClO_4)_2 \cdot 6H_2O$ in 3.5 mL EtOH, leading to the immediate formation of a dark blue precipitate. The reaction mixture was stirred for a further 10 minutes, after which it was filtered, yielding complex **17**-H_2O as a dark blue solid (160 mg, 0.254 mmol, 93%). Anal. calcd. for $C_{20}H_{22}Cl_2CuN_4O_{11}$: C, 38.20; H, 3.53; N, 8.91. Found: C, 38.13; H, 3.16; N, 8.89. ESI-LMMS (methanol): m/z = 411.0517 $[M\text{-}H_2O]^+$ (calcd. for $C_{20}H_{20}CuN_4O_2$; 411.0882).

3.4.4 Synthesis of Complex 18-H_2O

82 mg (0.24 mmol, 1.1 equiv.) of $Cu(ClO_4)_2 \cdot 6H_2O$ were dissolved in the 3 mL of EtOH, giving a light blue solution. Meanwhile, 74 mg (0.22 mmol, 1 equiv.) of compound **16** were dissolved 3 mL of ethanol, giving a dark yellow-orange solution, and this solution then added to the blue copper solution. A greenish-blue precipitate immediately formed, which was filtered off and dried, giving complex **18**-H_2O (0.074 g, 0.144 mmol, 60%). Anal. calcd. for $C_{19}H_{19}ClCuN_4O_7$: C, 44.37; H, 3.72; N, 10.89. Found: C, 44.68; H, 3.37; N, 10.73. MS-FAB/NOVA (low resolution): m/z = 396 ($[M]^+$–H_2O); ESI-LMMS (methanol): 396.0624 ($[M]^+$–H_2O) (calcd. for $C_{19}H_{17}CuN_4O_2$; 396.0648).

3.5 References

[1] Cosby, K.; Partovi, K. S.; Crawford, J. H.; Patel, R. P.; Reiter, C. D.; Martyr, S.; Yang, B. K.; Waclawiw, M. A.; Zalos, G.; Xu, X.; Huang, K. T.; Shields, H.; Kim-Shapiro, D. B.; Schechter, A. N.; Cannon, R. O., III; Gladwin, M. T. Nitrite Reduction to Nitric Oxide by Deoxyhemoglobin Vasodilates the Human Circulation. *Nat. Med.* **2003**, *9*, 1498-1505.

[2] Calabrese, V.; Mancuso, C.; Calvani, M.; Rizzarelli, E.; Butterfield, D. A.; Giuffrida Stella, A. M. Nitric Oxide in the Central Nervous System: Neuroprotection Versus Neurotoxicity. *Nat. Rev. Neurosci.* **2007**, *8*, 766–775.

[3] Omar, S. A.; Webb, A. J. Nitrite Reduction and Cardiovascular Protection. *J. Mol. Cell. Cardiol.* **2014**, *73*, 57-69.

[4] Heinecke, J.; Ford, P. C. Mechanistic Studies of Nitrite Reactions with Metalloproteins and Models Relevant to Mammalian Physiology. *Coord. Chem. Rev.* **2010**, *254*, 235-247.

[5] Maia, L. B.; Moura, J. J. G. How Biology Handles Nitrite. *Chem. Rev.* **2014**, *114*, 5273–5357.

[6] Averill, B. A. Dissimilatory Nitrite and Nitric Oxide Reductases. *Chem. Rev.* **1996**, *96*, 2951-2964.

[7] Godden, J.W.; Turley, S.; Teller, D. C.; Adman, E. T.; Liu, M. Y.; Payne, W. J.; LeGall, J. The 2.3 Angstrom X-Ray Structure of Nitrite Reductase from Achromobacter Cycloclastes. *Science*, **1991**, *253*, 438-442.

[8] Tocheva, E. I.; Rosell, F. I.; Mauk, A. G.; Murphy, M. E. P. Side-On Copper-Nitrosyl Coordination by Nitrite Reductase. *Science*, **2004**, *304*, 867-870.

[9] Halsted, T. P.; Yamashita, K.; Hirata, K.; Ago, H.; Ueno, G.; Tosha, T.; Eady, R. R.; Antonyuk, S. V.; Yamamoto, M.; Hasnain, S. S. An Unprecedented Dioxygen Species Revealed by Serial Femtosecond Rotation Crystallography in Copper Nitrite Reductase. *IUCrJ*, **2018,** *5*, 22-31.

[10] Ghosh, S.; Dey, A.; Sun, Y.; Scholes, C. P.; Solomon, E. I. Spectroscopic and Computational Studies of Nitrite Reductase: Proton Induced Electron Transfer and Backbonding Contributions to Reactivity. *J. Am. Chem. Soc.* **2009**, *131*, 277-288.

[11] Wasser, I. M.; de Vries, S.; Moënne-Loccoz, P.; Schröder, I.; Karlin, K. D. Nitric Oxide in Biological Denitrification: Fe/Cu Metalloenzyme and Metal Complex NO_x Redox Chemistry. *Chem. Rev.* **2002**, *102*, 1201–1234.

[12] Merkle, A. C.; Lehnert, N. Binding and Activation of Nitrite and Nitric Oxide by Copper Nitrite Reductase and Corresponding Model Complexes. *Dalton Trans.* **2012**, *41*, 3355-3368.

[13] Timmons, A. J.; Symes, M. D. Converting between the Oxides of Nitrogen Using Metal–Ligand Coordination Complexes. *Chem. Soc. Rev.* **2015**, *44*, 6708-6722.

[14] Rosca, V.; Duca, M.; de Groot, M. T.; Koper, M. T. M. Nitrogen Cycle Electrocatalysis. *Chem. Rev.* **2009**, *109*, 2209-2244.

[15] Tolman, W. B. A Model for the Substrate Adduct of Copper Nitrite Reductase and its Conversion to a Novel Tetrahedral Copper(II) Triflate Complex. *Inorg. Chem.* **1991**, *30*, 4877–4880.

[16] Casella, L.; Carugo, O.; Gullotti, M.; Doldi, S.; Frassoni, M. Synthesis, Structure, and Reactivity of Model Complexes of Copper Nitrite Reductase. *Inorg. Chem.* **1996**, *35*, 1101–1113.

[17] Ruggiero, C. E.; Carrier, S. M.; Tolman, W. B. Reductive Disproportionation of NO Mediated by Copper Complexes: Modeling N_2O Generation by Copper Proteins and Heterogeneous Catalysts. *Angew. Chem., Int. Ed. Engl.* **1994**, *33*, 895–897.

[18] Paul, P. P.; Tyeklar, Z.; Farooq, A.; Karlin, K. D.; Liu, S.; Zubieta, J. Isolation and X-Ray Structure of a Dinuclear Copper-Nitrosyl Complex. *J. Am. Chem. Soc.* **1990**, *112*, 2430–2432.

[19] Paul, P. P.; Karlin, K. D. Functional Modeling of copper Nitrite Reductases: Reactions of NO_2^- or Nitric Oxide with Copper(I) Complexes. *J. Am. Chem. Soc.* **1991**, *113*, 6331–6332.

[20] Carrier, S. M.; Ruggiero, C. E.; Tolman, W. B.; Jameson, G. B. Synthesis and Structural Characterization of a Mononuclear Copper Nitrosyl Complex. *J. Am. Chem. Soc.* **1992**, *114*, 4407–4408.

[21] Schneider, J. L.; Carrier, S. M.; Ruggiero, C. E.; Young, V. G., Jr.; Tolman, W. B. Influences of Ligand Environment on the Spectroscopic Properties and Disproportionation Reactivity of Copper−Nitrosyl Complexes. *J. Am. Chem. Soc.* **1998**, *120*, 11408–11418.

[22] Halfen, J. A.; Mahapatra, S.; Olmstead, M. M.; Tolman, W. B. Synthetic Analogs of Nitrite Adducts of Copper Proteins: Characterization and Interconversion of Dicopper(II) and -(I,II) Complexes Bridged only by NO_2^-. *J. Am. Chem. Soc.* **1994**, *116*, 2173–2174.

[23] Halfen, J. A.; Mahapatra, S.; Wilkinson, E. C.; Gengenbach, A. J.; Young, V. G., Jr.; Que, L., Jr.; Tolman, W. B. Synthetic Modeling of Nitrite Binding and Activation by Reduced Copper Proteins. Characterization of Copper(I)−Nitrite Complexes that Evolve Nitric Oxide. *J. Am. Chem. Soc.* **1996**, *118*, 763–776.

[24] Kujime, M.; Fujii, H. Spectroscopic Characterization of Reaction Intermediates in a Model for Copper Nitrite Reductase. *Angew. Chem. Int. Ed.* **2006**, *45*, 1089–1092.

[25] Kujime, M.; Izumi, C.; Tomura, M.; Hada, M.; Fujii, H. Effect of a Tridentate Ligand on the Structure, Electronic Structure, and Reactivity of the Copper(I) Nitrite Complex: Role of the Conserved Three-Histidine Ligand Environment of the Type-2 Copper Site in Copper-Containing Nitrite Reductases. *J. Am. Chem. Soc.* **2008**, *130*, 6088–6098.

[26] Hsu, S. C. N.; Chang, Y.-L.; Chuang, W.-J.; Chen, H.-Y.; Lin, I.-J.; Chiang, M. Y.; Kao, C.-L.; Chen, H.-Y. Copper(I) Nitro Complex with an Anionic $[HB(3,5\text{-}Me_2Pz)_3]^-$ Ligand: A Synthetic Model for the Copper Nitrite Reductase Active Site. *Inorg. Chem.* **2012**, *51*, 9297–9308.

[27] Woollard-Shore, J. G.; Holland, J. P.; Jones, M. W.; Dilworth, J. R. Nitrite Reduction by Copper Complexes. *Dalton Trans.* **2010**, *39*, 1576-1585.

[28] Maji, R. C.; Barman, S. K.; Roy, S.; Chatterjee, S. K.; Bowles, F. L.; Olmstead, M. M.; Patra, A. K. Copper Complexes Relevant to the Catalytic Cycle of Copper Nitrite Reductase: Electrochemical Detection of NO(g) Evolution and Flipping of NO_2 Binding Mode upon $Cu^{II} \rightarrow Cu^{I}$ Reduction. *Inorg. Chem.* **2013**, *52*, 11084–11095.

[29] Kumar, M.; Dixon, N. A.; Merkle, A. C.; Zeller, M.; Lehnert, N.; Papish, E. T. Hydrotris(triazolyl)borate Complexes as Functional Models for Cu Nitrite Reductase: The Electronic Influence of Distal Nitrogens. *Inorg. Chem.* **2012**, *51*, 7004−7006.

[30] Lehnert, N.; Cornelissen, U.; Neese, F.; Ono, T.; Noguchi, Y.; Okamoto, K.-i.; Fujisawa, K. Synthesis and Spectroscopic Characterization of Copper(II)−Nitrito Complexes with Hydrotris(pyrazolyl)borate and Related Coligands. *Inorg. Chem.* **2007**, *46*, 3916–3933.

[31] Hematian, S.; Siegler, M. A.; Karlin, K. D. Heme/Copper Assembly Mediated Nitrite and Nitric Oxide Interconversion. *J. Am. Chem. Soc.* **2012**, *134*, 18912-18915.

[32] Sakhaei, Z.; Kundu, S.; Donnelly, J. M.; Bertke, J. A.; Kim, W. K.; Warren, T. H. Nitric Oxide Release via Oxygen Atom Transfer from Nitrite at Copper(II). *Chem. Commun*. **2017**, *53*, 549-552.

[33] Scarpellini, M.; Neves, A.; Castellano, E. E.; de Almeida Neves, E. F.; Franco, D. W. A Structural Model for Oxidized Type II Copper Nitrite Reductase with a Polyimidazole Tripodal Ligand. *Polyhedron*, **2004**, *23*, 511–518.

[34] Burg, A.; Lozinsky, E.; Cohen, H.; Meyerstein, D. Mechanism of Reduction of the Nitrite Ion by Cu^{I} Complexes. *Eur. J. Inorg. Chem.* **2004**, 3675-3680.

[35] Fujisawa, K.; Tateda, A.; Miyashita, Y.; Okamoto, K.-i.; Paulat, F.; Praneeth, V. K. K.; Merkle, A.; Lehnert, N. Structural and Spectroscopic Characterization of Mononuclear Copper(I) Nitrosyl Complexes: End-On versus Side-On Coordination of NO to Copper(I). *J. Am. Chem. Soc.* **2008**, *130*, 1205-1213.

[36] Kundu, S.; Kim, W. Y.; Bertke, J. A.; Warren, T. H. Copper(II) Activation of Nitrite: Nitrosation of Nucleophiles and Generation of NO by Thiols. *J. Am. Chem. Soc.* **2017**, *139*, 1045−1048.

[37] Chen, C.-S.; Dai, H.-F.; Chen, C.-H.; Yeh, W.-Y. Synthesis, Characterization and Protonation Reaction of Copper and Palladium Complexes Bearing Nitrite Ligands in *O,O*-bidentate and *N*-monodentate Bonding Fashions. *Inorg. Chim. Acta*, **2011**, *376*, 396–400.

[38] Monzani, E.; Koolhaas, G. J. A. A.; Spandre, A.; Leggieri, E.; Casella, L.; Gullotti, M.; Nardin, G.; Randaccio, L.; Fontani, M.; Zanello, P.; Reedijk, J. Binding of Nitrite and its Reductive Activation to Nitric Oxide at Biomimetic Copper Centers. *J. Biol. Inorg. Chem.* **2000**, *5*, 251-261.

[39] Beretta, M.; Bouwman, E.; Casella, L.; Douziech, B.; Driessen, W. L.; Gutierrez-Soto, L.; Monzani, E.; Reedijk, J. Copper Complexes of a new Tridentate Imidazole-Containing Ligand: Spectroscopy, Structures and Nitrite Reductase Reactivity: The Molecular Structures of $[Cu(biap)(NO_2)_2]$ and $[Cu(biap)Br_2]$. *Inorg. Chim. Acta*, **2000**, *310*, 41–50.

[40] Chuang, W.-J.; Lin, I.-J.; Chen, H.-Y.; Chang, Y.-L.; Hsu, S. C. N. Characterization of a New Copper(I)−Nitrito Complex that Evolves Nitric Oxide. *Inorg. Chem.* **2010**, *49*, 5377–5384.

[41] Chen, C.-S.; Yeh, W.-Y. Coordination of NO_2^- Ligand to Cu(I) Ion in an *O,O*-Bidentate Fashion that Evolves NO Gas upon Protonation: A Model Reaction Relevant to the Denitrification Process. *Chem. Commun.* **2010**, *46*, 3098–3100.

[42] Roger, I.; Wilson, C.; Senn, H. M.; Sproules, S.; Symes, M. D. An Investigation into the Unusual Linkage Isomerization and Nitrite Reduction Activity of a Novel Tris(2-pyridyl) Copper Complex. *R. Soc. open sci.* **2017**, *4*, 170593.

[43] Komeda, N.; Nagao, H.; Kushi, Y.; Adachi, G.-y.; Suzuki, M.; Uehara, A.; Tanaka, K. Molecular Structure of Nitro- and Nitrito-Copper Complexes as Reaction Intermediates in Electrochemical Reduction of Nitrite to Dinitrogen Oxide. *Bull. Chem. Soc. Jpn.* **1995**, *68*, 581-589.

[44] Tegoni, M.; Yu, F.; Bersellini, M.; Penner-Hahn, J. E.; Pecoraro, V. L. Designing a Functional Type 2 Copper Center that has Nitrite Reductase Activity within α-Helical Coiled Coils. *Proc. Natl. Acad. Sci. USA*, **2012**, *109*, 21234–21239.

[45] Koebke, K. J.; Yu, F.; Salerno, E.; Stappen, C. V.; Tebo, A. G.; Penner-Hahn, J. E.; Pecoraro, V. L. Modifying the Steric Properties in the Second Coordination Sphere of Designed Peptides Leads to Enhancement of Nitrite Reductase Activity. *Angew. Chem. Int. Ed.* **2018**, DOI: 10.1002/anie.201712757

[46] Nagao, H.; Komeda, N.; Mukaida, M.; Suzuki, M.; Tanaka, K. Structural and Electrochemical Comparison of Copper(II) Complexes with Tripodal Ligands. *Inorg. Chem.* **1996**, *35*, 6809-6815.

[47] Orain, C.; Porras-Gutiérrez, A. G.; Evoung Evoung, F.; Charles, C.; Cosquer, N.; Gomila, A.; Conan, F.; Le Mest, Y.; Le Poul, N. Electrocatalytic Reduction of Nitrite Ions by a Copper Complex Attached as SAMs on Gold by "Self-Induced Electroclick": Enhancement of the Catalytic Rate by Surface Coverage Decrease. *Electrochem. Commun.* **2013**, *34*, 204-207.

[48] Hiratsu, T.; Suzuki, S.; Yamaguchi, K. Electroreduction of Nitrite on Gold Electrodemodified with Cu-Containing Nitrite Reductase Model Complex. *Chem. Commun.* **2005**, 4534-4535.

[49] Isoda, N.; Yokoyama, H.; Nojiri, M.; Suzuki, S.; Yamaguchi, K. Electroreduction of Nitrite to Nitrogen Oxide by a Copper-Containing Nitrite Reductase Model Complex Incorporated into Collagen Film. *Bioelectrochemistry*, **2010**, *77*, 82–88.

[50] Migita, Y.; Yokoyama, H.; Minami, A.; Mori, T.; Nojiri, M.; Suzuki, S.; Yamaguchi, K. Electrocatalytic Nitrite Reduction to Nitrogen Oxide by a Synthetic

Analogue of the Active Site of Cu-Containing Nitrite Reductase Incorporated in Nafion Film. *Electroanalysis*, **2009**, *21*, 2441 – 2446.

[51] Siek, S.; Dixon, N. A.; Papish, E. T. Electrochemical reduction of Ttz copper(II) complexes in the presence and absence of protons: Processes Relevant to Enzymatic Nitrite Reduction (TtzR,R′=tris(3-R, 5-R′-1, 2, 4-triazolyl)borate). *Inorg. Chim. Acta*, **2017**, *459*, 80–86.

[52] Weinberg, D. R.; Gagliardi, C. J.; Hull, J. F.; Murphy, C. F.; Kent, C. A.; Westlake, B. C.; Paul, A.; Ess, D. H.; McCafferty, D. G.; Meyer, T. J. Proton-Coupled Electron Transfer. *Chem. Rev.* **2012**, *112*, 4016-4093.

[53] Reece, S. Y.; Nocera, D. G. Proton-Coupled Electron Transfer in Biology: Results from Synergistic Studies in Natural and Model Systems. *Annu. Rev. Biochem.* **2009**, *78*, 673-699.

[54] Koper, M. T. M. Theory of Multiple Proton–Electron Transfer Reactions and its Implications for Electrocatalysis. *Chem. Sci.* **2013**, *4*, 2710-2723.

[55] Hammes-Schiffer, S. Proton-Coupled Electron Transfer: Moving Together and Charging Forward. *J. Am. Chem. Soc.* **2015**, *137*, 8860-8871.

[56] Gentry, E. C.; Knowles, R. R. Synthetic Applications of Proton-Coupled Electron Transfer. *Acc. Chem. Res.* **2016**, *49*, 1546-1556.

[57] Fukuda, Y.; Tse, K. M.; Nakane, T.; Nakatsu, T.; Suzuki, M.; Sugahara, M.; Inoue, S.; Masuda, T.; Yumoto, F.; Matsugaki, N.; Nango, E.; Tono, K.; Joti, Y.; Kameshima, T.; Song, C.; Hatsui, T.; Yabashi, M.; Nureki, O.; Murphy, M. E. P.; Inoue, T.; Iwata, S.; Mizohata, E. Redox-Coupled Proton Transfer Mechanism in Nitrite Reductase Revealed by Femtosecond Crystallography. *Proc. Natl. Acad. Sci. USA*, **2016**, *113*, 2928-2933.

[58] Berry, S. M.; Strange, J. N.; Bladholm, E. L.; Khatiwada, B.; Hedstrom, C. G.; Sauer, A. M. Nitrite Reductase Activity in Engineered Azurin Variants. *Inorg. Chem.* **2016**, *55*, 4233−4247.

[59] Matson, E. M.; Park, Y. J.; Fout, A. R. Facile Nitrite Reduction in a Non-Heme Iron System: Formation of an Iron(III)-Oxo. *J. Am. Chem. Soc.* **2014**, *136*, 17398-17401.

[60] Kwon, Y. M.; Delgado, M.; Zakharov, L. N.; Seda, T.; Gilbertson, J. D. Nitrite Reduction by a Pyridinediimine Complex with a Proton-Responsive Secondary Coordination Sphere. *Chem.Commun.* **2016**, *52*, 11016-11019.

[61] Moore, C. M.; Szymczak, N. K. Nitrite Reduction by Copper Through Ligand-Mediated Proton and Electron Transfer. *Chem. Sci.* **2015**, *6*, 3373-3377.

[62] Koshiba, K.; Yamauchi, K.; Sakai, K. A Nickel Dithiolate Water Reduction Catalyst Providing Ligand-Based Proton-Coupled Electron-Transfer Pathways. *Angew. Chem. Int. Ed.* **2017**, *56*, 4247-4251.

[63] Horvath, S.; Fernandez, L. E.; Appel, A. M.; Hammes-Schiffer, S. pH-Dependent Reduction Potentials and Proton-Coupled Electron Transfer Mechanisms in Hydrogen-Producing Nickel Molecular Electrocatalysts. *Inorg. Chem.* **2013**, *52*, 3643−3652.

[64] Helm, M. L.; Stewart, M. P.; Bullock, R. M.; Rakowski DuBois, M.; DuBois, D. L. A Synthetic Nickel Electrocatalyst with a Turnover Frequency above 100,000 s^{-1} for H_2 Production. *Science*, **2011**, *333*, 863-866.

[65] O'Hagan, M.; Shaw, W. J.; Raugei, S.; Chen, S.; Yang, J. Y.; Kilgore, U. J.; DuBois, D. L.; Bullock, R. M. Moving Protons with Pendant Amines: Proton Mobility in a Nickel Catalyst for Oxidation of Hydrogen. *J. Am. Chem. Soc.* **2011**, *133*, 14301–14312.

[66] Berning, D. E.; Noll, B. C.; DuBois, D. L. Relative Hydride, Proton, and Hydrogen Atom Transfer Abilities of $[HM(diphosphine)_2]PF_6$ Complexes (M = Pt, Ni). *J. Am. Chem. Soc.* **1999**, *121*, 11432–11447.

[67] Lee, C. H.; Dogutan, D. K.; Nocera, D. G. Hydrogen Generation by Hangman Metalloporphyrins. *J. Am. Chem. Soc.* **2011**, *133*, 8775-8777.

[68] Dogutan, D. K.; McGuire, R., Jr.; Nocera, D. G. Electocatalytic Water Oxidation by Cobalt(III) Hangman β-Octafluoro Corroles. *J. Am. Chem. Soc.* **2011**, *133*, 9178-9180.

[69] Gagliardi, C. J.; Vannucci, A. K.; Concepcion, J. J.; Chen, Z.; Meyer, T. J. The Role of Proton Coupled Electron Transfer in Water Oxidation. *Energy Environ. Sci.* **2012**, *5*, 7704-7717.

[70] Symes, M. D.; Surendranath, Y.; Lutterman, D. A.; Nocera, D. G. Bidirectional and Unidirectional PCET in a Molecular Model of a Cobalt-Based Oxygen-Evolving Catalyst. *J. Am. Chem. Soc.* **2011**, *133*, 5174-5177.

[71] Costentin, C.; Drouet, S.; Robert, M.; Savéant, J.-M. A Local Proton Source Enhances CO_2 Electroreduction to CO by a Molecular Fe Catalyst. *Science*, **2012**, *338*, 90-94.

[72] Costentin, C.; Passard, G.; Robert, M.; Savéant, J.-M. Pendant Acid–Base Groups in Molecular Catalysts: H-Bond Promoters or Proton Relays? Mechanisms of the Conversion of CO_2 to CO by Electrogenerated Iron(0)Porphyrins Bearing Prepositioned Phenol Functionalities. *J. Am. Chem. Soc.* **2014**, *136*, 11821–11829.

[73] Mato-Iglesias, M.; Roca-Sabio, A.; Pálinkás, Z.; Esteban-Gómez, D.; Platas-Iglesias, C.; Tóth, E.; de Blas, A.; Rodríguez-Blas, T. Lanthanide Complexes Based on a 1,7-Diaza-12-Crown-4 Platform Containing Picolinate Pendants: A new Structural Entry for the Design of Magnetic Resonance Imaging Contrast Agents. *Inorg. Chem.* **2008**, *47*, 7840–7851.

[74] Kotani, H.; Kaida, S.; Ishizuka, T.; Sakaguchi, M.; Ogura, T.; Shiota, Y.; Yoshizawa, K.; Kojima, T. Formation and Characterization of a Reactive Chromium(V)–Oxo Complex: Mechanistic Insight into Hydrogen-Atom Transfer Reactions. *Chem. Sci.* **2015**, *6*, 945-955.

[75] Kojima, T.; Hirai, Y.; Ishizuka, T.; Shiota, Y.; Yoshizawa, K.; Ikemura, K.; Ogura, T.; Fukuzumi, S. A Low-Spin Ruthenium(IV)–Oxo Complex: Does the Spin State Have an Impact on the Reactivity? *Angew. Chem. Int. Ed.* **2010**, *49*, 8449–8453.

[76] Jacobson, R. R.; Tyeklar, Z.; Karlin, K. D.; Zubieta, J. Fluoride as a Terminal and Bridging Ligand for Copper: Isolation and X-Ray Crystallographic Characterization of Copper Monomeric and Dimeric Complexes $[Cu^{II}(TMPA)F]_n^{n+}$ (n = 1 or 2; TMPA = Tris[(2-pyridyl)methyl]amine). *Inorg. Chem.* **1991**, *30*, 2035-2040.

[77] Tyeklár, Z.; Jacobson, R. R.; Wei, N.; Murthy, N. N.; Zubieta, J.; Karlin, K. D. Reversible Reaction of Dioxygen (and Carbon Monoxide) with a Copper(I) Complex. X-Ray Structures of Relevant Mononuclear Cu(I) Precursor Adducts and the *Trans*-(μ-1,2-peroxo)dicopper(II) Product. *J. Am. Chem. Soc.* **1993**, *115*, 2677–2689.

[78] Le Poul, N.; Douziech, B.; Zeitouny, J.; Thiabaud, G.; Colas, H.; Conan, F.; Cosquer, N.; Jabin, I.; Lagrost, C.; Hapiot, P.; Reinaud, O.; Le Mest, Y. Mimicking the Protein Access Channel to a Metal Center: Effect of a Funnel Complex on Dissociative versus Associative Copper Redox Chemistry. *J. Am. Chem. Soc.* **2009**, *131*, 17800–17807.

[79] Karlin, K. D.; Hayes, J. C.; Juen, S.; Hutchinson, J. P.; Zubieta, J. Tetragonal vs. Trigonal Coordination in Copper(II) Complexes with Tripod Ligands: Structures

and Properties of $[Cu(C_{21}H_{24}N_4)Cl]PF_6$ and $[Cu(C_{18}H_{18}N_4)Cl]PF_6$. *Inorg. Chem.* **1982**, *21*, 4106–4108.

[80] Addison, A. W.; Rao, T. N.; Reedijk, J.; van Rijn, J.; Verschoor, G. C. Synthesis, Structure, and Spectroscopic Properties of Copper(II) Compounds Containing Nitrogen–Sulphur Donor Ligands; the Crystal and Molecular Structure of Aqua[1,7-bis(*N*-methylbenzimidazol-2′-yl)-2,6-dithiaheptane]Copper(II) Perchlorate. *J. Chem. Soc., Dalton Trans.* **1984**, 1349-1356.

[81] Symes, M. D.; Wilson, C. Probing the Effects of Steric Bulk on the Solution-Phase Behaviour and Redox Chemistry of Cobalt-Diimine Complexes. *Supramol. Chem.* **2017**, DOI: 10.1080/10610278.2017.1373195

[82] Izzet, G.; Zeng, X.; Akdas, H.; Marrot, J.; Reinaud, O. Drastic Effects of the Second Coordination Sphere on Neutral *vs.* Anionic Guest Binding to a Biomimetic Cu(II) Center Embedded in a Calix[6]aza-Cryptand. *Chem. Commun.* **2007**, 810–812.

[83] Lonnon, D. G.; Craig, D. C.; Colbran, S. B. An Unusual but Informative Synthesis and the Crystal Structure of $[Co(tpaCO_2)Cl](ClO_4)$ ($tpaCO_2^-$ = 6-carboxylato-2-(pyridylmethyl)-bis(2-pyridylmethyl)amine). *Inorg. Chem. Commun.* **2003**, *6*, 1351–1353.

[84] Hayashi, H.; Uozumi, K.; Fujinami, S.; Nagatomo, S.; Shiren, K.; Furutachi, H.; Suzuki, M.; Uehara, A.; Kitagawa, T. Modulation of the Copper-Dioxygen Reactivity by Stereochemical Effect of Tetradentate Tripodal Ligands. *Chem. Lett.* **2002**, 416-417.

[85] Mizuno, M.; Honda, K.; Cho, J.; Furutachi, H.; Tosha, T.; Matsumoto, T.; Fujinami, S.; Kitagawa, T.; Suzuki, M. A Mononuclear Alkylperoxocopper(II) Complex as a Reaction Intermediate in the Oxidation of the Methyl Group of the Supporting Ligand. *Angew. Chem. Int. Ed.* **2006**, *45*, 6911–6914.

[86] Comba, P.; Grimm, L.; Orvig, C.; Rück, K.; Wadepohl, H. Synthesis and Coordination Chemistry of Hexadentate Picolinic Acid Based Bispidine Ligands. *Inorg. Chem.* **2016**, *55*, 12531−12543.

[87] Comba, P.; Jakob, M.; Rück, K.; Wadepohl, H. Tuning of the Properties of a Picolinic Acid-Based Bispidine Ligand for Stable Copper(II) Complexation. *Inorg. Chim. Acta*, **2017**, DOI: 10.1016/j.ica.2017.08.022

[88] G. Socrates, *Infrared and Raman Characteristic Group Frequencies: Tables and Charts*, John Wiley & sons, **2004** (3^{th} edition)

[89] Adler, A. D.; Longo, F. R.; Finarelli, J. D.; Goldmacher, J.; Assour, J.; Korsakoff, L. A Simplified Synthesis for Meso-Tetraphenylporphine. *J. Org. Chem.* **1967**, *32*, 476–476.

[90] Anderson, C. E.; Vagin, S. I.; Xia, W.; Jin, H.; Rieger, B. Cobaltoporphyrin-Catalyzed CO_2/Epoxide Copolymerization: Selectivity Control by Molecular Design. *Macromolecules*, **2012**, *45*, 6840-6849.

[91] Mori, S.; Ishii, K.; Hirakawa, Y.; Nakamura, R.; Hashimoto, K. In Vivo Participation of Artificial Porphyrins in Electron-Transport Chains: Electrochemical and Spectroscopic Analyses of Microbial Metabolism. *Inorg. Chem.* **2011**, *50*, 2037-2039.

[92] Zheng, L.; Ye, D.; Xiong, L.; Xu, J.; Tao, K.; Zou, Z.; Huang, D.; Kang, X.; Yang, S.; Xia, J. Preparation of Cobalt-Tetraphenylporphyrin/Reduced Graphene Oxide Nanocomposite and its Application on Hydrogen Peroxide Biosensor. *Anal. Chim. Acta*, **2013**, *768*, 69–75.

[93] Richter-Addo, G. B.; Hodge, S. J.; Yi, G.-B.; Khan, M. A.; Ma, T.; Van Caemelbecke, E.; Guo, N.; Kadish, K. M. Synthesis, Characterization, and Spectroelectrochemistry of Cobalt Porphyrins Containing Axially Bound Nitric Oxide. *Inorg. Chem.* **1996**, *35*, 6530-6538.

[94] Wijma, H. J.; Jeuken, L. J. C.; Verbeet, M. P.; Armstrong, F. A.; Canters, G. W. A Random-Sequential Mechanism for Nitrite Binding and Active Site Reduction in Copper-Containing Nitrite Reductase. *J. Biol. Chem.* **2006**, *281*, 16340–16346.

[95] Warren, J. J.; Tronic, T. A.; Mayer, J. M. Thermochemistry of Proton-Coupled Electron Transfer Reagents and its Implications. *Chem. Rev.* **2010**, *110*, 6961–7001.

CHAPTER 4

The Electronic and Solvatochromic Properties of $[Co(L)(bipyridine)_2]^+$ (L = o-catecholato, o-benzenedithiolato) Species: a Combined Experimental and Computational Study

Published as "*The Electronic and Solvatochromic Properties of $[Co(L)(bipyridine)_2]^+$ (L = o-catecholato, o-benzenedithiolato) Species: a Combined Experimental and Computational Study*"

Giacomo Cioncoloni, Hans M. Senn, Stephen Sproules, Claire Wilson and Mark D. Symes, *Dalton Trans.*, **2016**,45, 15575-15585

Acknowledgments and declaration

The project covered in this chapter was a collaboration with several researchers from other groups at University of Glasgow. I performed all the synthesis work presented in this chapter as well as the UV-Vis. Solvatochromic, IR and all the electrochemical studies.
Dr. Stephen Sproules performed the EPR study, Dr. Hans M. Senn performed all the theoretical studies and Dr. Claire Wilson performed the crystallographic study.

Synopsis

Complexes of Co(III) containing mixed chelating diimine and *o*-quinone ligand sets are of fundamental interest on account of their interesting magnetic and electronic properties. Whilst complexes of this type containing one diimine and two *o*-quinone ligands have been studied extensively, those with the reverse stoichiometry (two diimines and one *o*-quinone) are much rarer. Herein, we describe a ready route to the synthesis of the complex $[Co^{III}$(*o*-catecholate) (2,2'-bipyridine$)_2]^+$ (**19**), and also report the synthesis of $[Co^{III}$(*o*-catecholate)(5,5′-dimethyl-2,2′-bipyridine$)_2]^+$ (**20**) and $[Co^{III}$(*o*-benezenedithiolate)(5,5′-dimethyl-2,2′-bipyridine$)_2]^+$ (**21**) for the first time. The electronic properties of complexes **20** and **21** were studied in some detail, by both experimental and theoretical methods. Spectroscopic studies show that complex **20** displays intriguing solvatochromic behaviour as a function of solvent polarity and hydrogen bond donation ability, a property of this type of complex which has hitherto not been reported. Using time-dependent density function theory (TD-DFT), we show that this effect arises as a result of hydrogen bonding between the solvent and the oxygen atoms of the catecholate ligand. In contrast, the sulfur atoms in the benzenedithiolate analogue **21** are much weaker acceptors of hydrogen bonds from the solvent, meaning that complex **21** is only very weakly solvatochromic. Furthermore, we show that complex **20** has some potential as a molecular probe that can report on the composition of mixed solvent systems as a function of its absorbance spectrum.

4.1 Introduction

Complexes of Co(III) containing both chelating diimines (e.g. 2,2′-bipyridyl) and either o-catecholate or o-benzenedithiolate ligands are attractive targets as these compounds frequently display interesting electronic and magnetic properties on account of the redox activity of the catecholate/benzenedithiolate ligands.[1-11] Within this class of complexes, those containing two o-catecholate and one diimine ligand tend to be more common, with only a few examples existing of complexes of the type $[CoIII(o\text{-catecholate})(bipyridyl)_2]^+$ (where the metal centre is attached to only one o-catecholate ligand and two chelating diimines).[1-6] Moreover, to the best of our knowledge, the solvatochromic properties of this class of complexes has not been studied in any great detail before, nor have any analogues of these compounds bearing o-benezenedithiolate ligands in place of the o-catecholate moieties been reported. Herein, we report the synthesis and characterization of the complexes $[Co^{III}(o\text{-catecholate})(2,2'\text{-bipyridine})_2]^+$ (**19**), $[Co^{III}(o\text{-catecholate})(5,5'\text{-dimethyl-}2,2'\text{-bipyridine})_2]^+$ (**20**) and $[Co^{III}(o\text{-benezenedithiolate})(5,5'\text{-dimethyl-}2,2'\text{-bipyridine})_2]^+$ (**21**), where complexes **20** and **21** are both previously unreported. We then undertake an in-depth analysis of the solvatochromism displayed by complexes **20** and **21** using both experimental and computational methods. Synthetic procedure for complex **21** gives as main product a dicobalt coordination compound detailed in **Chapter 5** as compound **24.**

Given its apparent simplicity, it was surprising to us at the outset of our studies that no detailed synthesis or characterization of the parent compound $[CoIII(o\text{-catecholate})(2,2'\text{-bipyridine})_2]^+$ (**19**) exists (although this compound has been reported previously, experimental and characterization particulars are very brief[12]). With a view to investigating the electronic properties of this complex, we therefore adapted synthetic methods reported by Panja[3] to obtain this compound (compound **19**) in almost quantitative yield using a straightforward and quick one-pot synthesis (note, however, that high yields are only obtained if the order of addition of the components is controlled – see below). As the solubility of compound **19** was rather low in common laboratory solvents, we used the same general procedure to obtain the analogous (and previously unreported) 5,5′-dimethylbipyridyl complex (**20**, also in near-quantitative yield), which is much more soluble. Furthermore, we were able to extend this methodology to synthesize the novel complex $[Co^{III}(o\text{-}$

benezenedithiolate)(5,5′-dimethyl-2,2′-bipyridine)$_2$]$^+$ (**21**). Complex **21** is a rare example of a Co-bipyridine-dithiolene complex that can be prepared without isolation of any intermediate species and that contains only one benzenedithiolate ligand in the isolated compound.[13-16]

Both complexes **20** and **21** proved sufficiently soluble to allow us to probe their electronic properties by electrochemistry and EPR. These studies revealed that complexes **20** and **21** tend to decompose when their o-catecholate and o-benzenedithiolate ligands are oxidized, rendering these complexes of limited use for studying the effects of any redox non-innocence that may be exhibited by their ligands. However, our investigations did reveal some intriguing differences between the complexes regarding their solution-phase UV-vis spectra, with complex **20** exhibiting a strong negative solvatochromic shift in its visible absorbance band as a function of solvent polarity and hydrogen bond donor ability. Meanwhile, complex **21** was much less affected by these factors (indeed, it showed no perturbation in absorbance as a function of hydrogen bonding at all). In the following, we rationalize these effects using time-dependent density function theory (TD-DFT) and suggest that the differences in behaviour between these two complexes are attributable to hydrogen bonding between the oxygen atoms of the catecholate ligand of complex **20** and the solvent (an interaction which is switched off in complex **21** on account of sulfur being a weaker hydrogen bond-acceptor than oxygen). Finally, we show that complexes of this type may hold some promise as molecular probes that can report on the composition of mixed solvent systems as a function of their absorbance spectra.

4.2 Results and discussion

4.2.1 Synthesis and structures of compounds 19 and 20

A general route to the synthesis of compounds **19** and **20** is given in **Scheme 4.1**. Taking the example of compound **20**, addition of one equivalent of $Co(NO_3)_2 \cdot 6H_2O$ to two equivalents of 5,5′-dimethyl-2,2′-bipyridine resulted in the formation of an orange solution, the colour of which remained unchanged (to the eye) upon the addition of one equivalent of catechol. However, subsequent addition of the base triethylamine produced an instantaneous darkening of the reaction mixture to red/brown. If the reaction was carried

out under inert atmosphere, the reaction remained red/brown and a red precipitate formed within a few minutes. However, if the addition reaction was performed under air, the red colour disappeared and a bottle-green solution was obtained around 10 minutes after addition of the triethylamine. Stirring of this solution under air for up to 2 hours produced no further colour or solubility changes. Precipitation of a green/grey solid from this solution, followed by drying yielded a brown powder in near-quantitative yield. Subsequent recrystallization from DMF/diethylether then afforded brown crystals of **20** suitable for X-ray diffraction (**Figure 4.1**). The same pathway could be followed to obtain the 2,2′-bipyridine analogue, **19**, but the product was considerably less soluble in solvents such as methanol, acetonitrile and dichloromethane than complex **20** and so complex **20** was selected for further study on account of being the more tractable of the two.

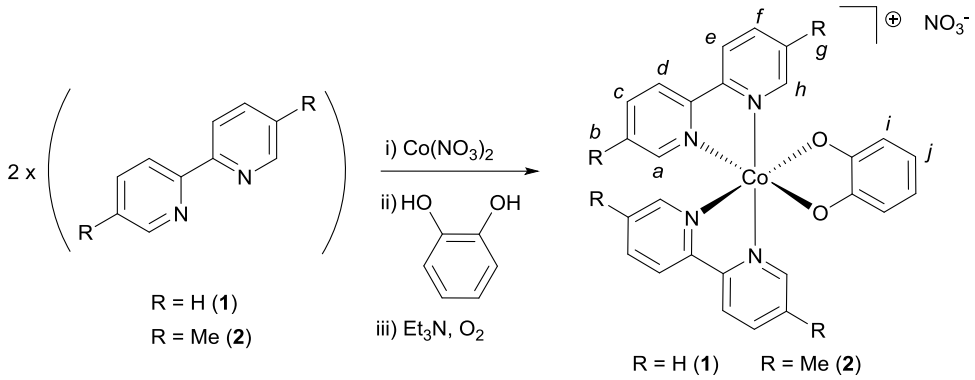

Scheme 4.1: *The general synthetic route followed to synthesize compounds **19** and **20**. Italic letters on the product structure correspond to the ^{1}H NMR signal assignments in the **Section 4.4** Reproduced from Dalton Trans.,* **2016**,45, 15575 *with permission of Royal Society of Chemistry. Copyright 2016*

The connectivity of **20** is evident from **Figure 4.1a**, which shows the two bipyridine moieties to be coordinated in a cis¬ ¬fashion around the metal, with the octahedral geometry of the cobalt centre completed by bidentate coordination to the catecholate ligand. The Co–O and Co–N bond lengths in **Figure 4.1a** are: Co–O1 = 1.889(6), Co–N1 = 1.951(8) and Co–N2 = 1.926(8) Å, which are typical of Co(III) according to a search of the Cambridge Structural Database.[17,18] Whilst there is precedent for using the bond lengths in the chelate rings of various catecholate-metal complexes in order to gauge the oxidation state of the metal[19], the overall quality of the crystallographic data only allows us to comment with confidence on the bond lengths around the Co centre and the general connectivity/packing of the molecule.

In regard to the latter, **Figure 4.1b** shows the suggested packing of **20** in the solid state, evincing large (~20%) solvent-accessible voids of ~1150 Å3 per unit cell.

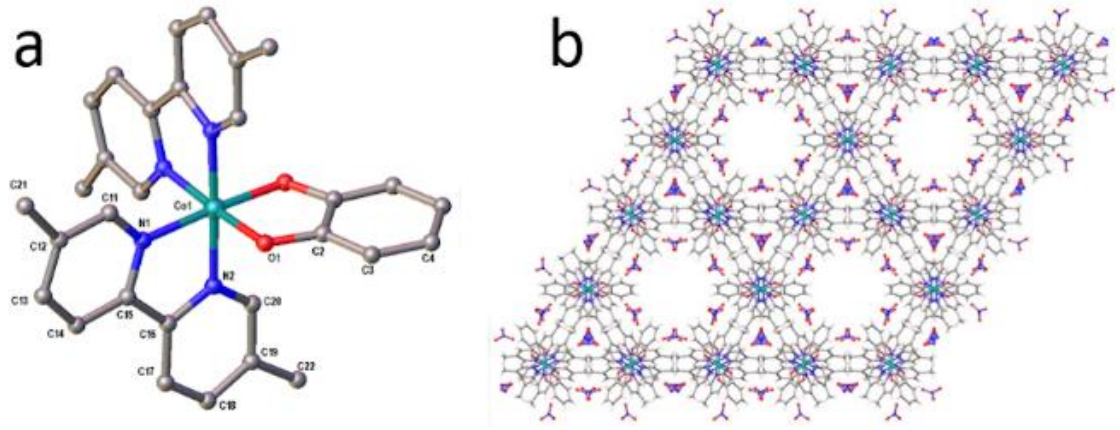

Figure 4.1: *(**a**) The crystal structure of compound **20** showing the connectivity of the complex. Hydrogen atoms, solvent and counterions have been omitted from the structure. Crystallographic details can be found in the ESI. (**b**) The packing structure of complex **20** in the solid state, viewed along the crystallographic c-axis. Colour scheme for both panels: C = grey, N = blue, O = red, Co = cyan. Reproduced from Dalton Trans.,* **2016**,45, 15575 *with permission of Royal Society of Chemistry. Copyright 2016*

The assignment of the cobalt oxidation state in compound **20** as +3 was reinforced by the ^{1}H NMR of this complex (see **Figures 4.2**) which implied that the compound was diamagnetic.

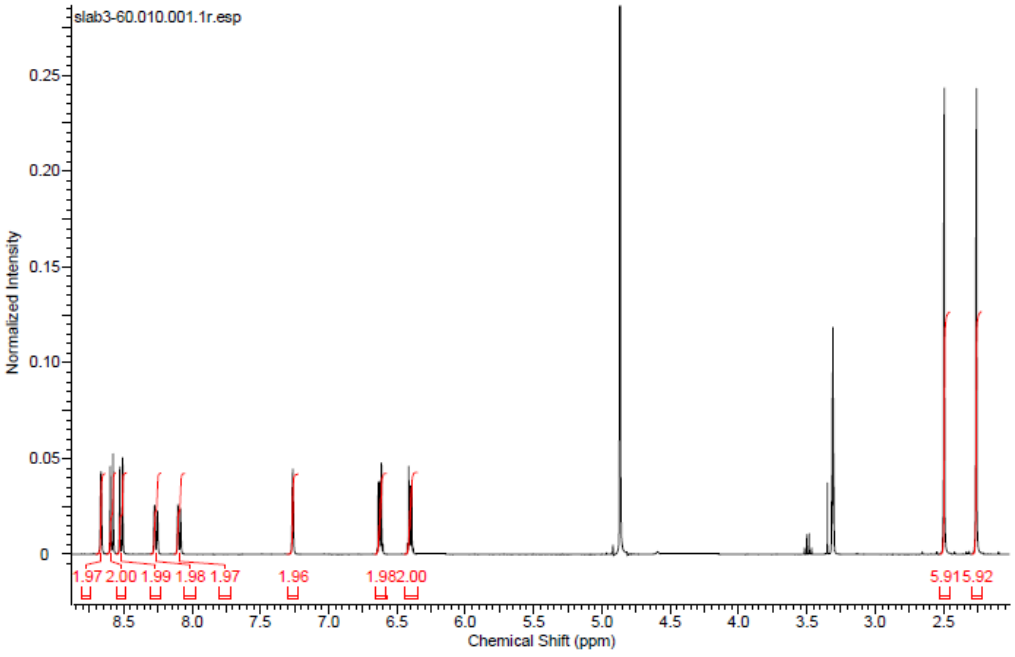

Figure 4.2: *^{1}H NMR spectrum of compound **20** in MeOD. Reproduced from Dalton Trans.,* **2016**,45, 15575 *with permission of Royal Society of Chemistry. Copyright 2016.*

Moreover, compound **20** as isolated was found to be EPR-silent, which further supports this conclusion. The similarity of the ^{1}H NMR spectrum of complex **19** to that of complex **20** (**Figure 4.3**) indicates that these complexes share a common basic geometry and that the cobalt is in the +III oxidation state in both of these compounds.

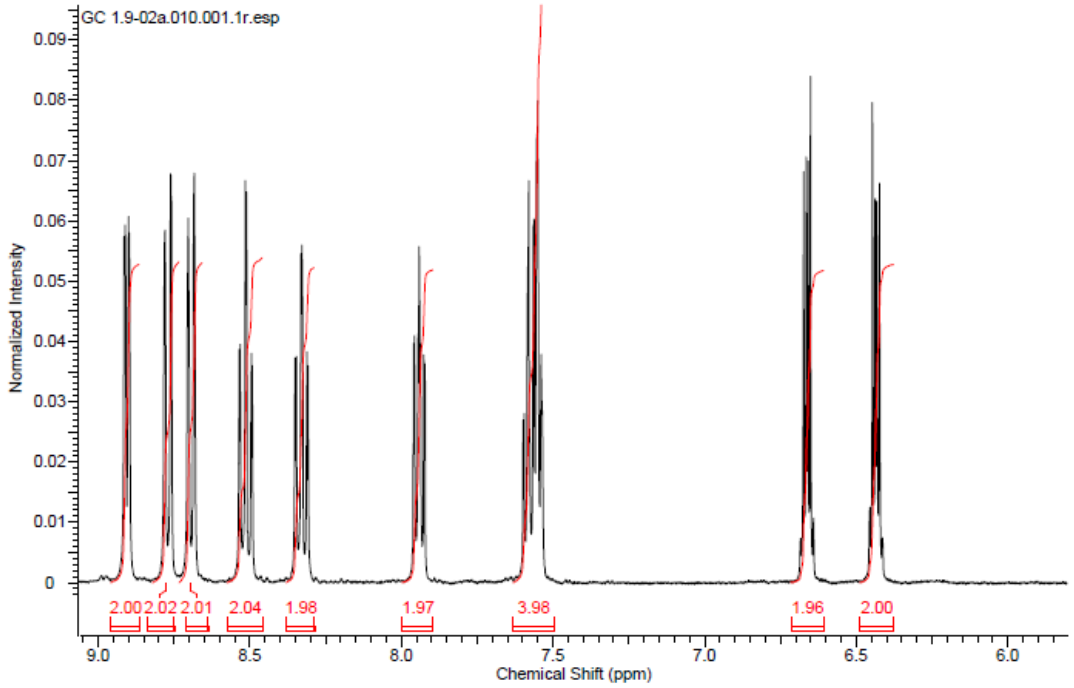

Figure 4.3: *^{1}H NMR spectrum of compound **19** in MeOD. Reproduced from Dalton Trans.,* **2016**,45, 15575 *with permission of Royal Society of Chemistry. Copyright 2016*

The order of addition of the components to the reaction mixture was found to be crucial for the isolation of complexes **19** and **20** in high yield. For example, if one equivalent of catechol is added to one equivalent of $Co(NO_3)_2 \cdot 6H_2O$ in methanol the solution remains dark pink in colour. Addition of triethylamine to this turns the solution dark blue/green. If two equivalents of 5,5′-dimethyl-2,2′-bipyridine are then added under air, the reaction mixture becomes an intense dark green (distinct from the bottle green colour observed with the order of addition given in **Scheme 4.1**). Upon stirring of this dark green solution under air for 2 hours, a dark yellow slurry forms in the otherwise green solution. Analysis of the green solution by NMR suggests that some compound **20** is present in here (along with other unidentified paramagnetic species), but after isolation the yield of complex **20** is only 25%. The dark yellow solid on the other hand (which is the main product of this reaction) is insoluble in common laboratory solvents such as methanol and chloroform.

4.2.2 Redox chemistry of compound 20

If the red/brown reaction mixture formed upon triethylamine addition under inert atmosphere (during the synthesis of compound **20** according to the order of addition of reactants shown in **Scheme 4.1**) is allowed to equilibrate with air, then any precipitated solids soon re-dissolve and the mixture turns green, giving clean and quantitative conversion to **20**. This suggested that aereobic oxidation was a key step in the formation of these complexes, causing oxidation of Co(II) to Co(III). However, attempts to reduce complex **20** back to this red/brown material were not successful. For example, addition of zinc dust to a green solution of **20** in methanol evinced no colour changes, implying no reduction of the complex. Similarly, electrochemical methods failed to show any redox waves that might correspond to the reduction of complex **20** (**Figure 4.4a**). Instead, all that was observed in these experiments were two closely-spaced and quasi-reversible redox events with oxidation waves between –0.1 and +0.2 V (vs. ferrocene/ferrocenium), which we attribute to oxidation of the catecholate ligands by analogy both to other Co-catecholate complexes[4] and to complexes of other metals containing catecholate ligands.[20]

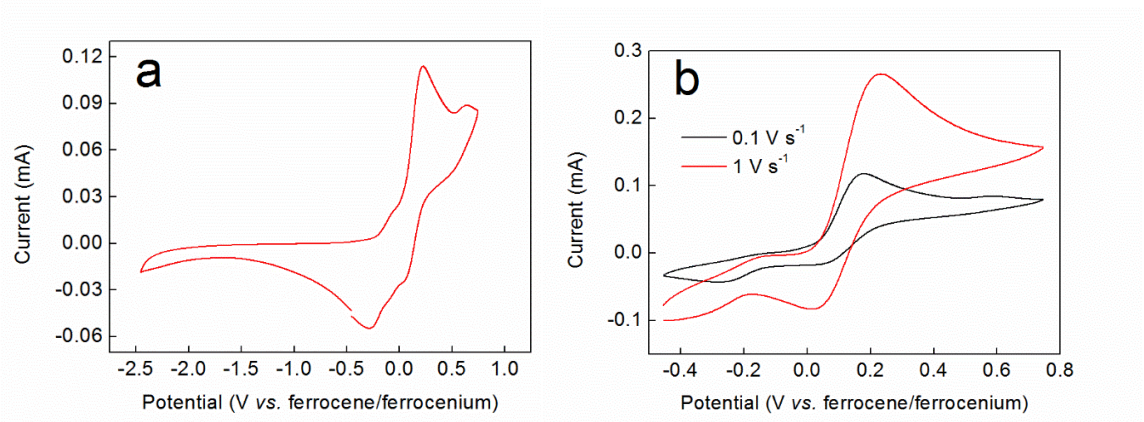

Figure 4.4: *(**a**) Cyclic voltammogram of a 12 mM solution of the nitrate salt of complex **20** in 0.1 M TBA-PF_6 / acetonitrile run under the conditions detailed in the Experimental Section. (**b**) Cyclic voltammograms as in panel (**a**), but over a narrower potential range and showing the effect of variation in the scan rate as indicated. The ferrocene/ferrocenium couple is not shown for clarity. Reproduced from Dalton Trans., **2016**,45, 15575 with permission of Royal Society of Chemistry. Copyright 2016*

Support for assigning the locus of the redox activity to the catecholate ligand was supplied by EPR spectroscopy. Chemical oxidation, which occurs on a faster timescale than its

electrochemical equivalent, was achieved by treating a 3 mM solution of complex **20** in acetonitrile with 1 equivalent of $NOBF_4$. However, the one electron-oxidized species thus generated proved to be unstable (as suggested also by the electrochemical data in **Figure 4.4**). Hence the resulting solution EPR spectrum recorded at X-band frequency revealed an elegant 15-line profile, consistent with coupling to two ^{59}Co (I = 7/2, 100% abundant) nuclei (**Figure 4.5**) rather than the expected 8-line spectrum for a benzosemiquinone radical bound to a single Co(III) centre[21–31]. The signal was very weak considering the concentration of the sample, suggesting the rapid decomposition of complex **20** upon oxidation. This is in agreement with the cyclic voltammetry, which suggests that the more rapidly the sample is re-reduced following oxidation, the lesser the extent of decomposition (as evinced by the greater reversibility of the redox wave at higher scan rates in **Figure 4.4b**). Spectral simulation gave giso = 2.0007 and Aiso = 3.4×10^{-4} cm^{-1}, which are hallmark values for a benzosemiquinone radical bound to two Co(III) ions. [32–34] The extremities of the experimental spectrum in **Figure 4.5** show additional hyperfine lines that are not associated with the dominant 15-line signal.

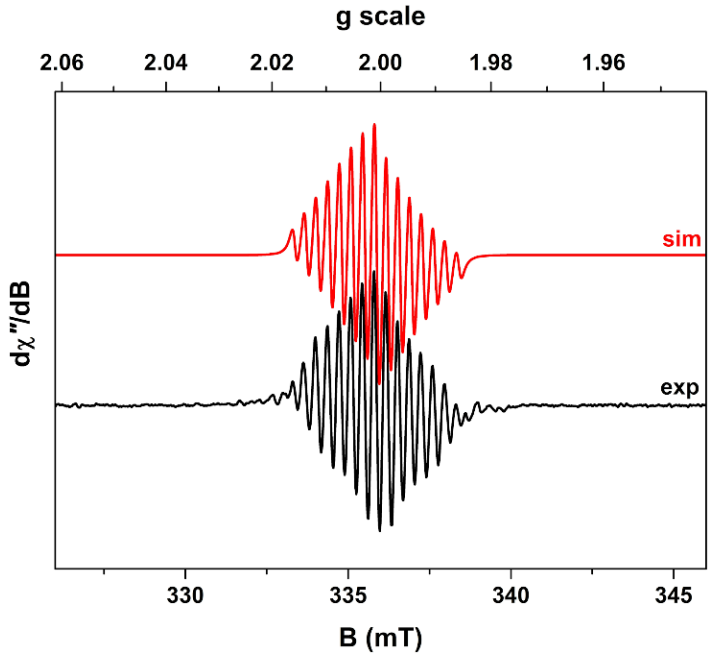

Figure 4.5: *X-band EPR spectrum of paramagnetic species generated from the reaction of complex* ***20*** *with $NOBF_4$, recorded in acetonitrile solution at 293 K (experimental conditions: frequency, 9.4053 GHz; power, 9.5 mW; modulation, 0.1 mT). Experimental data are represented by the black line; a simulation is depicted by the red trace. Reproduced from Dalton Trans.*, **2016**,45, 15575 *with permission of Royal Society of Chemistry. Copyright 2016*

These presumably arise from other decomposition products or intermediates, but are not present at sufficient concentrations to be diagnosed. Interestingly, examination of the

spectrum by varying the temperature incrementally to just above the solvent freezing point (–45 °C), showed no change in the number of lines, nor any deviation from binomially-distributed intensity.[35] This suggests a symmetrical disposition of the two Co(III) ions attached to a bridging benzosemiquinone radical, such that the hyperfine interaction is not biased towards a particular Co nucleus as noted in more elaborate dicobalt complexes.[34] The corresponding frozen solution EPR spectrum recorded at 150 K possesses very little *g* anisotropy (*g* = 2.0094, 2.0024, 1.9899), synonymous with an organic-based unpaired electron (**Figure 4.6**). The line-shape is reproduced well by including coupling from both 59Co nuclei, A = (3.1, 4.6, 1.5) × 10^{-4} cm^{-1}, whose average matches the isotropic value. These EPR and electrochemical measurements suggest that oxidation of complex **20** is ligand-based, leading to the formation of a dicobalt decomposition species with a bridging benzosemiquinone radical which is sufficiently long-lived to be detected by EPR.

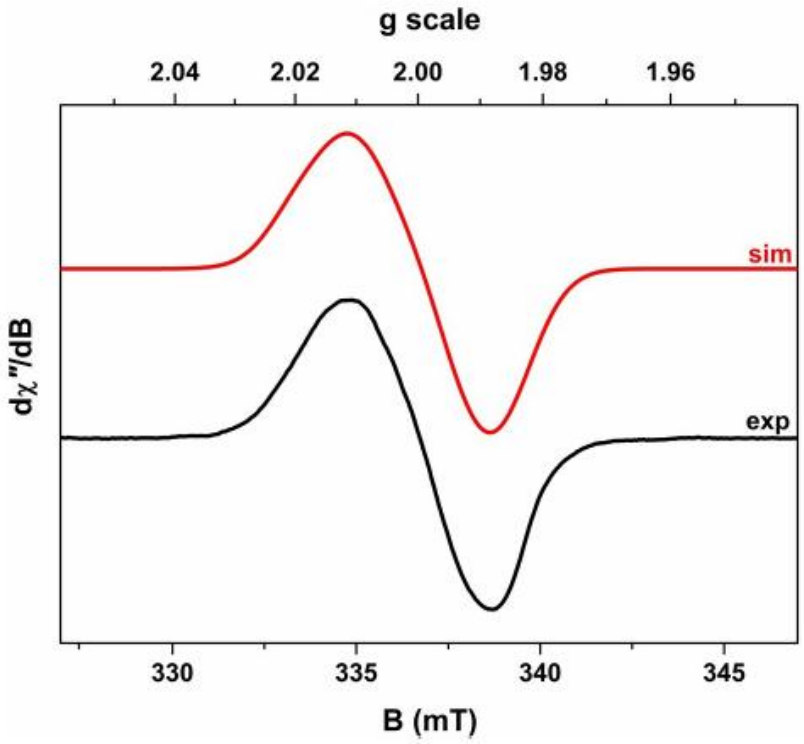

Figure 4.6: *X-band EPR spectrum of paramagnetic species generated from the reaction of complex* ***20*** *with* $NOBF_4$*, recorded in acetonitrile/THF solution at 150 K (experimental conditions: frequency, 9.4243 GHz; power, 0.63 mW; modulation, 0.3 mT). Experimental data are represented by the black line; simulation is depicted by the red trace. Reproduced from Dalton Trans.,* **2016**,45, 15575 *with permission of Royal Society of Chemistry. Copyright 2016*

4.2.3 Solvatochromism of complex 20

During the course of the above experiments, it was noted that complex **20** assumed different colours in different solvents, as has been observed previously for complexes of transition metals (such as Pt) containing mixed bipyridine and catecholate ligand sets.[1,36-38] To probe this solvatochromic effect further, 5.0 mM solutions of compound **20** were made in solvents of various polarities and the position of the lowest energy absorption maximum, λmax (which falls between 640 and 760 nm), was plotted as a function of the ET(30) solvent polarity scale of Dimroth and Reichardt (see **Figure 4.7**)[39,40]

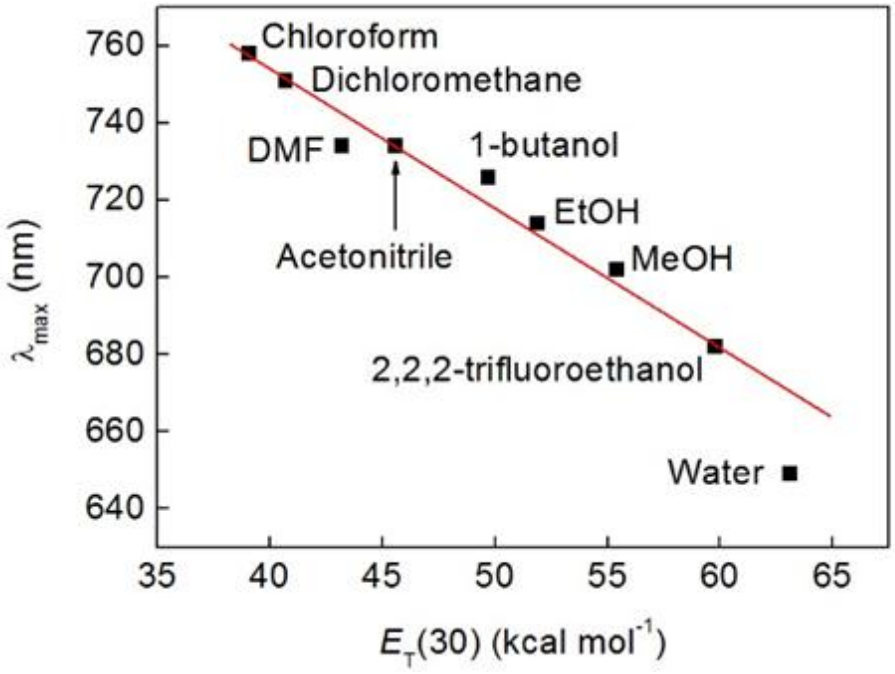

Figure 4.7: *Wavelength of the lowest energy absorption band of compound* ***20*** *as a function of solvent polarity, plotted on the Dimroth–Reichardt E_T scale. All solutions were at a concentration of 5 mM, except those in butanol, chloroform and dichloromethane (2.5 mM). The red line is a linear fit and is provided as a guide to the eye. Reproduced from Dalton Trans.*, **2016**,45, 15575 *with permission of Royal Society of Chemistry. Copyright 2016*

This revealed a clear correlation between solvent polarity and the wavelength of the first absorption, and implied that the excitation energy increased in more polar solvents (negative solvatochromism **Figure 4.8**).

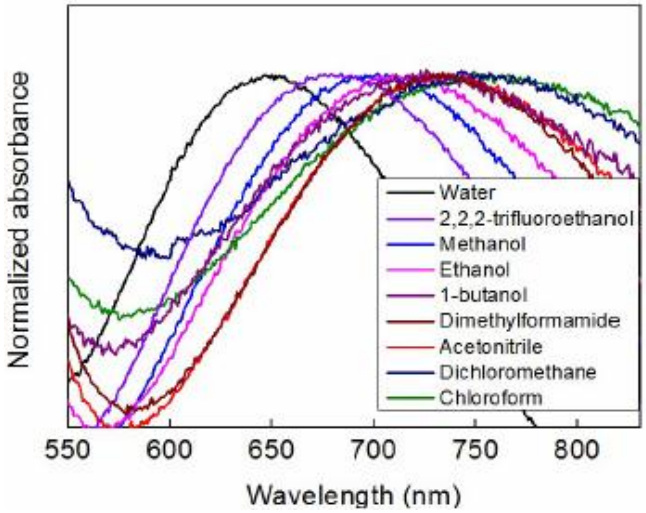

Figure 4.8: *Plot showing an overlay of the normalized absorption profiles (in the region 550-820 nm) of compound* ***20*** *in the solvents indicated, showing how the position of λmax within this range shifts. All spectra were measured at a concentration of 5 mM, except those in butanol, chloroform and dichloromethane (2.5 mM). Reproduced from Dalton Trans.*, **2016**,45, 15575 *with permission of Royal Society of Chemistry. Copyright 2016*

In methanol, this absorption was found to have an extinction coefficient of 171 (±6) M^{-1} cm^{-1} (**Figure 4.9**), which is in good agreement with the molar extinction coefficients (typically around 170 M^{-1} cm^{-1}) reported for the visible absorbances of complexes of the type $[Co^{III}(catecholate)(R)_2]^+$, where R is a saturated bidentate amine such as ethylenediamine.[4,38]

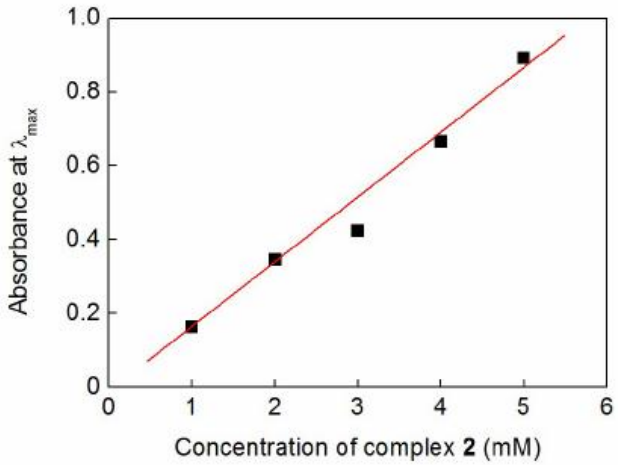

Figure 4.9: *Absorbance of the lowest energy absorption band of compound* ***20*** *in methanol as a function of concentration. The points at concentrations of 1, 2, 4 and 5 mM were averaged to give an extinction coefficient of 171 M–1 cm–1, with an error of ±6 M–1 cm–1. The red line is a linear fit and is provided as a guide to the eye. Reproduced from Dalton Trans.*, **2016**,45, 15575 *with permission of Royal Society of Chemistry. Copyright 2016*

To rationalize this trend further, we performed time-dependent density-functional theory (TD-DFT) calculations with a polarizable continuum model of the solvent to elucidate the nature of the excitation giving rise to the solvatochromic properties of compound **20**. These calculations suggested that the measured absorption band in the visible region was due to the lowest-energy singlet excitation (S_1) only. The S_2 excitation, which was 0.1 eV higher in energy and might therefore contribute to the same band, was calculated to have negligible intensity (oscillator strength $f \leq 10^{-4}$). Higher excitations were sufficiently separated in energy (S_3 was 0.3 eV above S_2), that they could be neglected. However, when the excitation energies calculated by TD-DFT were compared to those derived from the experimental absorption maxima, a linear correlation was only observed for solvents that were not significant hydrogen bond donors (black squares in **Figure 4.10**).

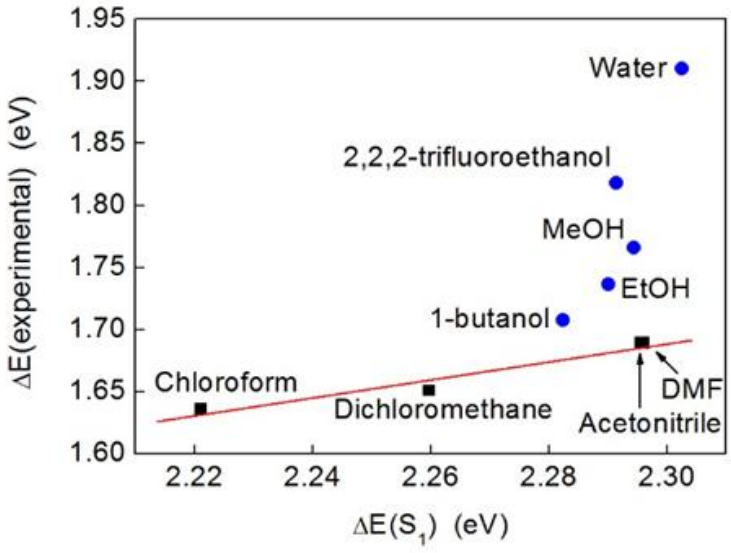

Figure 4.10:. *A plot of the experimental excitation energies (obtained from the band maxima given in* ***Figure 4.11****) and the energies of the lowest excited singlet state calculated by TD-DFT (ωB97-XD/def2-TZVP/PCM). Non-hydrogen bonding solvents are depicted with black squares and the linear trend is indicated by a red line as a guide to the eye. Hydrogen bonding solvents are shown as blue circles. Reproduced from Dalton Trans.*, **2016**,45, 15575 *with permission of Royal Society of Chemistry. Copyright 2016*

A very similar trend could be obtained by plotting the experimental excitation energies vs. the stabilization energy of a dipole sitting in a spherical cavity in a polarizable medium (the Onsager model of solvation[41]), which scales as $fO(\varepsilon) = (\varepsilon - 1)/(2\varepsilon + 1)$ with the dielectric constant of the solvent, ε (**Figure 4.11**).

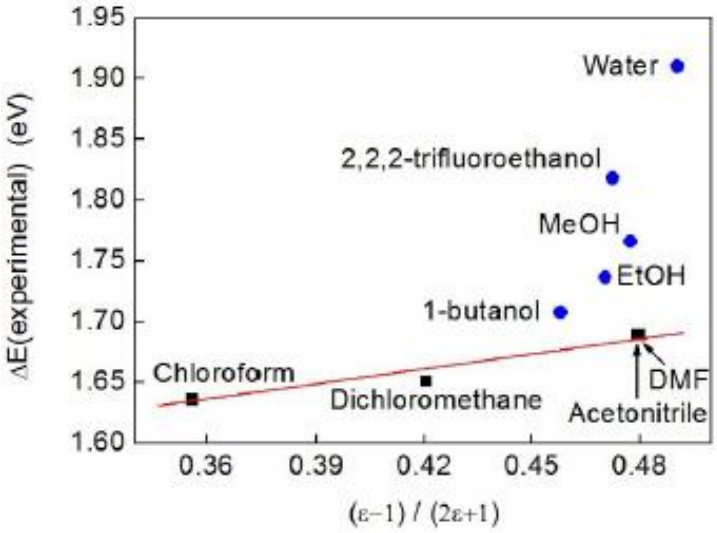

Figure 4.11: *Plot showing the relationship between the experimentally-determined excitation energies (ΔE(experimental)) and the stabilization energy of a dipole in a spherical cavity for the various solvents probed according to Onsager's model, fO(ε) = (ε – 1)/(2ε + 1). Non hydrogen bonding solvents are depicted with black squares and the linear trend is shown as a red line as a guide to the eye. Hydrogen bonding solvents are shown as blue circles. The trend is essentially the same as that shown in* ***Figure 4.10*** *in the main text. Reproduced from Dalton Trans.*, **2016**,45, 15575 *with permission of Royal Society of Chemistry. Copyright 2016*

Meanwhile, a plot of the excitation energies calculated by TD-DFT *vs.* $f_O(\varepsilon)$ was a straight line (**Figure 4.12**), which confirmed that the solvent model used in the calculations captured the purely electrostatic component of the solvents' influence on the excitation energy accurately.

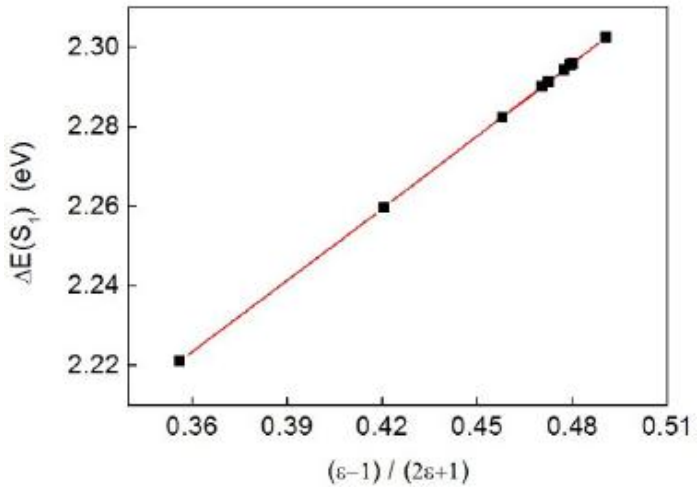

Figure 4.12: *Plot showing the linear relationship between the excitation energies determined by TD-DFT (ΔE(S1)) and the stabilization energy of a dipole in a spherical cavity for the various solvents probed according to Onsager's model, fO(ε) = (ε – 1)/(2ε + 1). Reproduced from Dalton Trans.*, **2016**,45, 15575 *with permission of Royal Society of Chemistry. Copyright 2016*

In these calculations, the solvent was considered to stabilize the solute by acting as a homogeneous polarizable medium. This was the only solvent effect included in the calculations and no specific solute–solvent interactions were considered. The effect of electrostatic solvation on an electronic excitation results from the differential stabilization of the ground and excited states and/or from the stabilization of the transition dipole moment. In the present case, the transition dipole moment was calculated to be negligible compared to the permanent dipole moment of the molecule, and so did not warrant further consideration. The dipole moments of complex **20** (in $CHCl_3$) were calculated to be μ_{S0} = 13.33 D and μ_{S1} = 9.26 D in the ground and first excited states, respectively. Hence, as the excited state has a smaller dipole moment than the ground state, it is expected to interact less with the solvent. With increasing polarity (greater dielectric constant, ε) of the solvent, the ground state should therefore be increasingly better solvated compared to S_1. Consequently, the excitation energy is expected to increase with increasing ε (i.e., the excitation energy blue-shifts). This explains the trend seen for non-hydrogen bonding solvents (**Figure 4.10** and **Figure 4.11**).

The fact that hydrogen bond-donating solvents do not conform to this simple model therefore suggests that other solvation effects, in particular hydrogen bonding, play a significant role in the solvatochromism displayed by complex **20**. Purely electrostatic solvent models, like the polarizable continuum model used is the calculations or the Onsager model, are only good predictors of the solvatochromism in non-hydrogen bonding solvents. By contrast, the empirical E_T scale accounts for all effects of the solvent, including hydrogen bonding.[42]

An explanation as to why hydrogen bonding should affect the absorption to such an extent can be found by considering the results of NTO (natural transition orbital) analysis of the $S_0 \rightarrow S_1$ excitation in complex **20**. This excitation is dominated (>90%) by the transition between one NTO donor–acceptor pair, as shown in **Figure 4.13**. Qualitatively, this excitation can be characterized as a d–d transition with significant admixture (~30%) from a filled catecholate π* orbital to the donor state: $Co(d_{yz}) - cat(\pi^*) \rightarrow Co(d_{z2})$. The catecholate π* orbital in turn is dominated by the two $O(p_z)$ contributions. We note that the solvent has negligible influence on orbital compositions and characters (the values given are for $CHCl_3$). Also note that we take the trans N–Co–N axis as the z-axis, with the y-axis along the C2 axis. (see **Appendix B2**)

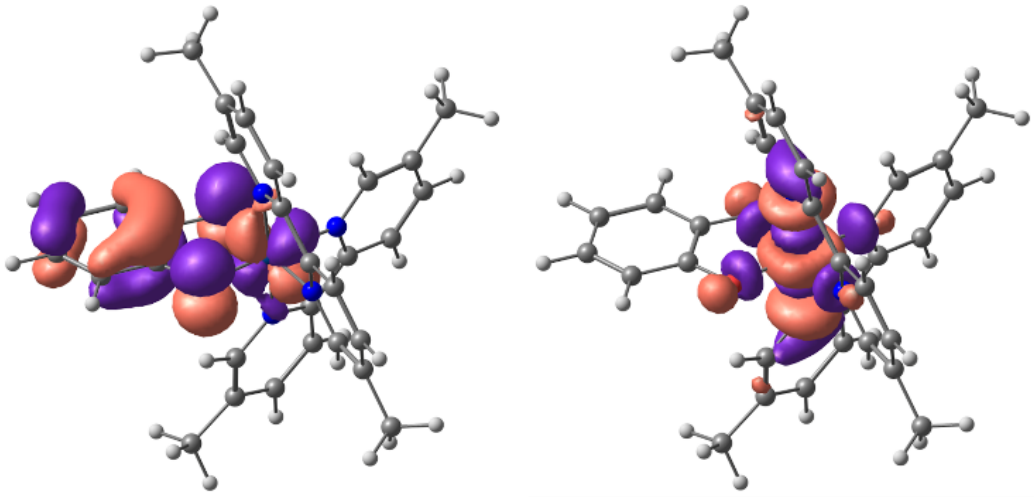

Figure 4.13: *The dominant NTO pair of the $S_0 \rightarrow S_1$ excitation of complex* ***20****, which accounts for >90% of the transition density. The donor orbital (left-hand side) has significant catecholate π* character, whereas the acceptor state (right-hand side) is mainly a metal-based d-orbital. Reproduced from Dalton Trans.*, **2016**,45, 15575 *with permission of Royal Society of Chemistry. Copyright 2016*

Hence, the electron density in the first excited state of **20** is shifted to a metal-centred d-orbital, which is largely isolated from the surrounding medium (and therefore largely inaccessible for specific interactions with the solvent). The donor NTO, however, has significant catecholate π*/O(p_z) character. The structure of complex **20** (see **Figure 4.1a**) suggests that the only sites available for accepting hydrogen bonds are the oxygen atoms of the catecholate ligands. Therefore, hydrogen bonding between the solvent and these oxygens is expected to remove electron density from the catecholate-based π* orbital, and therefore stabilize the donor NTO in hydrogen bond-donating solvents relative to solvents that cannot donate hydrogen bonds. Hence, hydrogen bond-donating solvents should indeed manifest increased negative solvatochromism (i.e. an increase in excitation energy with solvation strength) relative to solvents that cannot hydrogen bond, precisely as observed.

In further support of this, we fitted the experimental excitation energies with a linear model incorporating both fO(ε) and the Kamlet–Taft α-parameter,[43] which is a measure of the hydrogen bond donor ability of a solvent. This model should therefore account for the additional blue-shifting of the band in hydrogen bond-donating solvents.

As is evident from **Figure 4.14**, this model indeed reproduces the observed solvatochromic trend more closely than the purely electrostatic model of **Figure 4.10**, thus confirming that electrostatic stabilization and hydrogen bond donation are the two essential solvation components at play in this case. It is interesting to note that the empirical Dimroth–Reichardt $E_T(30)$ parameter, which captures the experimental trend very well (**Figure 4.7**), has long been recognized to correlate strongly with the hydrogen bond donation parameter, α.[44]

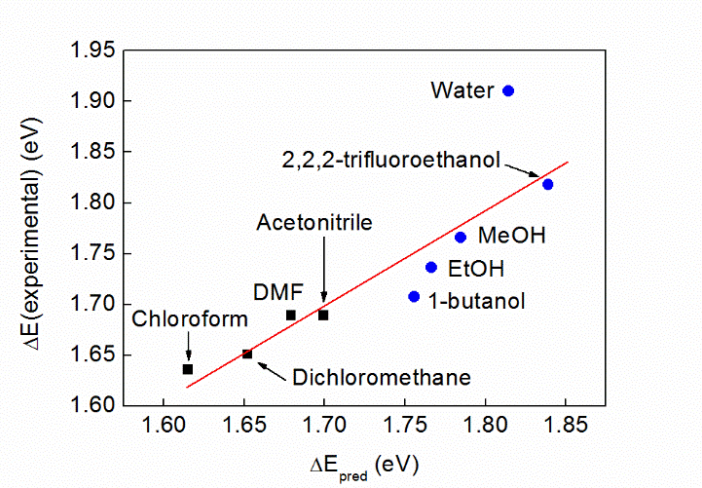

Figure 4.14: *A plot of the experimental excitation energies against the predictions from a linear model incorporating the Onsager function $f_O(\varepsilon)$ and the Kamlet–Taft α-parameter for hydrogen bond donor strength (taken from reference 44). The linear fit function is ΔE_{pred} = 1.345 eV + 0.695 $f_O(\varepsilon)$ + 0.109 α. Non-hydrogen bonding solvents are depicted with black squares, hydrogen bonding solvents with blue circles. Reproduced from Dalton Trans.*, **2016**,45, 15575 *with permission of Royal Society of Chemistry. Copyright 2016*

4.2.4 Prediction of the properties of complex 21 and its synthesis

In order to obtain an independent (experimental) verification of the effects that pure electrostatics (the Onsager model) and hydrogen bonding have upon the solvatochromism displayed by complex **20**, complex **21** was synthesized by the general route followed for complexes **19** and **20** (see below). The rationale behind this was both to test the applicability of the synthetic procedure to another class of bidentate ligand, and to replace the oxygen ligands of complex **20** with sulfur ligands. Sulfur is a weaker hydrogen bond acceptor than oxygen, as indicated by the positions of phenol (0.30) and thiophenol (0.16) on Abraham's hydrogen bond acceptor strength scale.[45] Hence, we hypothesized that any

solvatochromic shift due to hydrogen bonding interactions with the solvent should be much less pronounced for complex **21** than for complex **20**.

Prior to the synthesis of **21**, TD-DFT calculations were performed on the target structure in order to estimate the magnitude of the solvatochromic effect that might be expected on the basis of pure electrostatic solvation in the absence of hydrogen bonding. These calculations identified the $S_0 \rightarrow S_2$ excitation as being responsible for the visible absorption band of complex **21**. S_1, which was calculated to be 0.02 eV below S_2, had hardly any intensity ($f \approx 10^{-4}$) and the higher excited states were again well-separated (by ≥ 0.4 eV), as was also the case for complex **20**. When compared to complex **20**, the lowest energy absorption of complex **21** was ~0.06 eV lower in energy (in $CHCl_3$). The dipole moments for complex **21** in chloroform were calculated to be μ_{S0} = 13.84 D and μ_{S2} = 11.40 D (compared to μ_{S0} = 13.33 D, μ_{S1} = 9.26 D for complex **20** – see above). Hence, whilst complex **21** was predicted to display a negative solvatochromic shift (just as complex **20** does), this effect was predicted to be weaker for complex 2**1** than for complex **20** on account of the smaller difference in dipole moments between the ground and excited states in complex **21**.

NTO analysis of the $S_0 \rightarrow S_2$ excitation of complex **21** again showed domination (~90%) by one NTO donor–acceptor pair (**Figure 4.15**). Qualitatively, this excitation is a d–d transition with admixture of ~30% S(p_z) character to the donor NTO. Compared to complex **20**, there is a higher metal d contribution to the donor orbital (58% *vs.* 47%), at the expense of the benzene π* contribution, which is negligible in complex **21**.

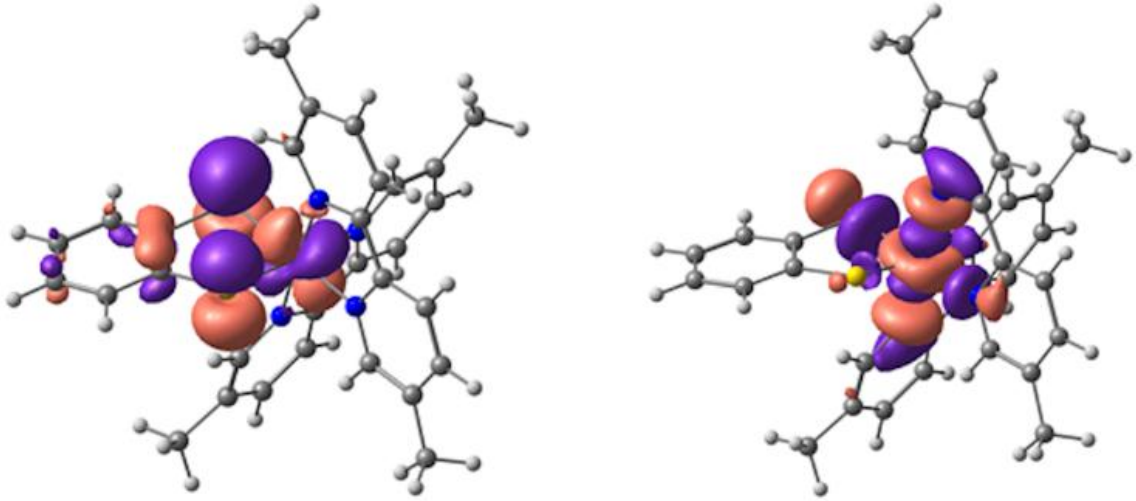

Figure 4.15: *The dominant NTO pair of the $S_0 \rightarrow S_2$ excitation of **21**, which accounts for ~90% of the transition density. The donor orbital is shown on the left-hand side and the acceptor is shown on the right-hand side. Reproduced from Dalton Trans.,* **2016**,45, 15575 *with permission of Royal Society of Chemistry. Copyright 2016*

The acceptor NTO has ~65% d character for both complex **20** and complex **21**. Overall, the calculations suggest that, compared to complex **20**, the visible band of complex **21** should be red-shifted and subject to a diminished negative solvatochromic effect, particularly in hydrogen bond-donating solvents.

Complex **21** was then synthesized by the route shown in **Scheme 4.2**. This was highly analogous to the route followed for the catecholate complexes, with the exception that upon addition of *o*-benzenedithiol the reaction mixture became dark green almost at once and the addition of Et_3N was not necessary in order to isolate the product (see **Section 4.4**).

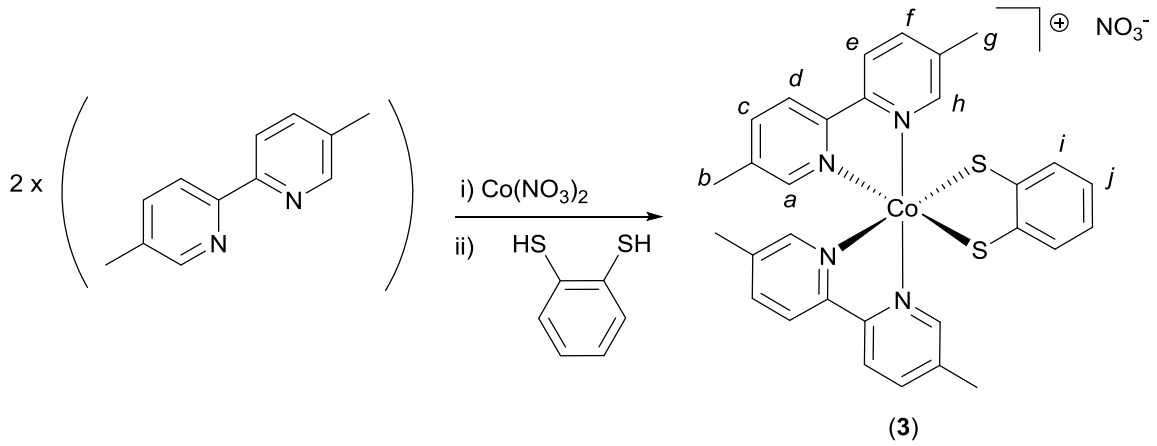

Scheme 4.2: *The synthetic route for the synthesis of compound **21** under air. Letters on the product structure correspond to the ^1H NMR signal assignments in the **Section 4.4.3.** Reproduced from Dalton Trans.,* **2016**,45, 15575 *with permission of Royal Society of Chemistry. Copyright 2016*

The yield of complex **21** was, however, consistently much lower than that obtained for the catecholate analogues (<20%). Again, the similarity between the ^1H NMR spectra of complexes **19**, **20** and **21** (see **Figures 4.16**) indicated that complex **21** shared the same basic structure as that found for complex **20**, with the cobalt present in the +III oxidation state.

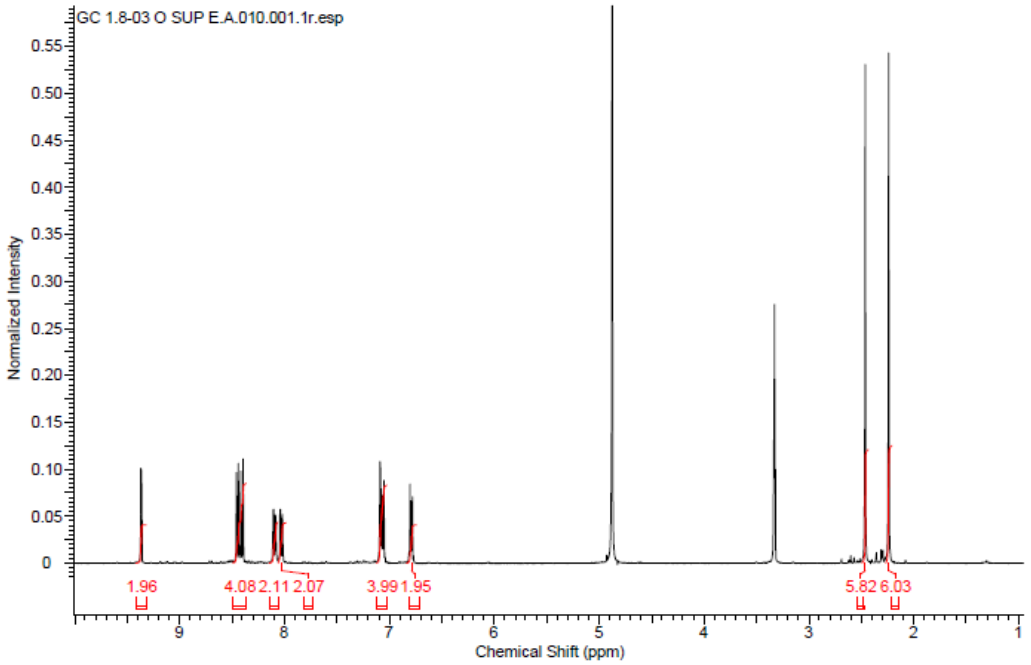

Figure 4.16: *1H NMR spectrum of compound* ***21*** *in MeOD Reproduced from Dalton Trans.,* **2016**,45, 15575 *with permission of Royal Society of Chemistry. Copyright 2016*

Complex **21** was not the only product of this synthesis since this compound was isolated via selective crystallization from a mixture containing mainly another product. In fact, the reaction mixture at the end of the reaction appears as a dark green solution and this initially confused us since we were expecting optical featrues analogous to compounds **19** and **20**. The following NMR analysis confirms the presence of the signal of compound **21** (shown in **Figure 4.16**) but also the presence of several other signals. However, we obtained computational data telling us that compound **21** should in fact be red (and not green) in this crude mixture, and so a purification via selective precipitation was carried out. Hence we added excess of diethyl ether until we started to see precipitation of a green solid and a dark orange supernatant solution that was separated via filtration. After a full characterization we realised it was an unreported di-cobalt complex (indicated as complex **24** in **Chapter 5**) showing different coordination environments of the two cobalt atoms. Results concerning this specie are detailed in **Chapter 5**. The synthetic procedure is detailed further in **Section 4.4**

4.2.5 Redox chemistry of complex 21

Figure 4.17 shows cyclic voltammograms for complex **21**. The full range CV (panel (**a**)) shows numerous irreversible and quasi-reversible processes. Panel (**b**) then

shows a scan-rate dependency assay on the first oxidative redox wave occurring at around +0.4 V *vs.* ferrocene/ferrocenium. At low scan rates (0.1 V s^{-1} and below) this wave appears to be largely irreversible. However, as the scan rate is increased, the wave becomes more reversible, being essentially fully reversible at 3 V s^{-1}. EPR spectroscopy was used to probe this behaviour further. Hence, compound **21** was oxidized chemically by treatment with $NOBF_4$, yielding a dark brown solution. In contrast to the EPR spectrum obtained when compound **20** was oxidized with $NOBF_4$, the spectrum of compound **21** upon oxidation revealed a single sharp line without hyperfine splitting at g ~2.006. This again is the hallmark of a ligand-centred oxidation, and the absence of ^{59}Co hyperfine coupling suggests that the signal stems from a trace amount of uncoordinated dithiobenzosemiquinone radical in the sample. This is consistent with the lifetime of the signal (which vanished after only two hours) and highlights the notable difference in stability between benzosemiquinone and dithiobenzosemiquinone radicals, with the former being considerably more long-lived than the latter.

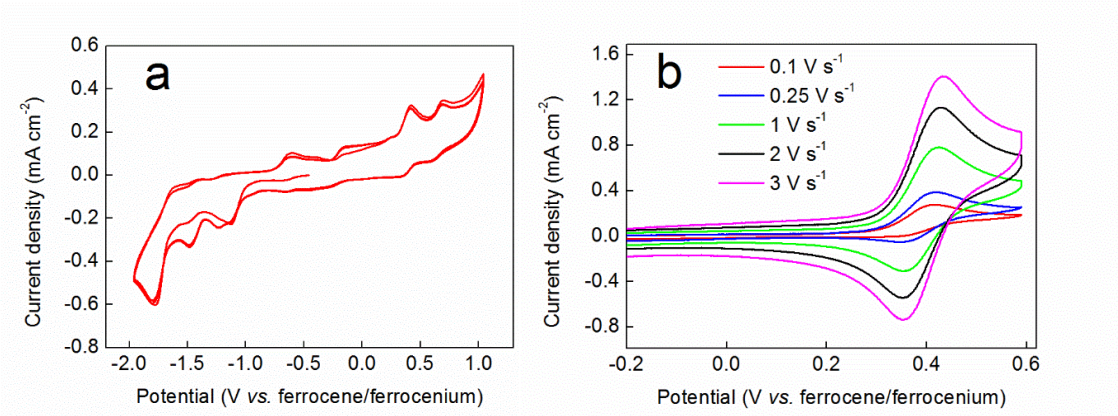

Figure 4.17: *Cyclic voltammograms of an 11 mM solution of the nitrate salt of complex* ***21*** *in 0.5 M TBA-PF_6 / acetonitrile run under the conditions detailed in* ***Section 2.6.2*** *(with the exception that a Pt counter electrode was used).* ***(a)*** *A full range cyclic voltammogram at a scan rate of 0.1 V s^{-1}.* ***(b)*** *CVs as in panel* ***(a)****, but at various scan rates as indicated. The ferrocene/ferrocenium couple is not shown for clarity. Reproduced from Dalton Trans.,* **2016**,45, 15575 *with permission of Royal Society of Chemistry. Copyright 2016*

On the basis of the EPR and electrochemical data, we therefore propose that the scan rate-dependent wave in the cyclic voltammogram is due to oxidation of the benzenedithiolate ligand, which is accompanied by dissociation of this ligand from the metal centre and consequent decomposition of complex **21**. However, the

electrochemistry suggests that if re-reduction follows oxidation rapidly enough, then dissociation of the benzenedithiolate ligand can be prevented and the structure of complex **21** can be preserved.

4.2.6 Solvatochromic behaviour of complex 21 and comparison to that of complex 20

Electronic spectra of complex **21** were collected in various solvents (see **Figure 4.10a** and **Figure 4.19**) and plotted on the $E_T(30)$ solvent polarity scale of Dimroth and Reichardt as for complex **20**. This revealed that the hydrogen bonding solvents ethanol and methanol did not conform to the linear trend predicted by this scale (we note that complex **21** is not soluble in water or 1-butanol). This is perhaps not unexpected, as the Dimroth-Reichardt scale reflects to a significant extent the effect of hydrogen bonding of the solvent to the solute.[39]

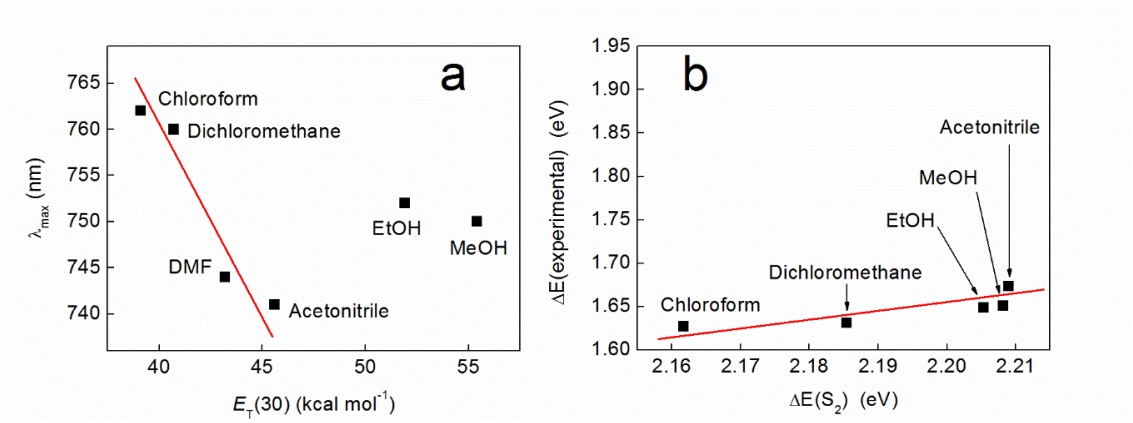

Figure 4.18: *(**a**) Wavelength of the lowest energy absorption band of compound **21** as a function of solvent polarity, plotted on the Dimroth–Reichardt E_T scale. Solutions were at a concentration of 1.9 mM for all samples, with the exception of those taken in acetonitrile and DMF (both 1.6 mM). (**b**) A plot of the experimental excitation energies (obtained from the band maxima given in panel (**a**)) and the energies of the S_2 excited singlet state calculated by TD-DFT (ωB97-XD/def2-TZVP/PCM). The scale has been chosen to allow comparison with Figure 5. The red lines in both panels are provided as guides to the eye. Reproduced from Dalton Trans.*, **2016**,45, 15575 *with permission of Royal Society of Chemistry. Copyright 2016*

Therefore, the fact that the positions of λ_{max} in methanol and ethanol predicted by the Dimroth-Reichardt scale do not agree with the observed positions of these absorbances serves as evidence that hydrogen bonding is insignificant for the solvatochromism displayed by complex **21**. Indeed, **Figure 4.18b** compares the experimental excitation

energies (ΔE(experimental), obtained from the λ_{max} values given in **Figure 18a**) with the S_2 excitation energies ($\Delta E(S_2)$) calculated for complex **21** on the basis of pure electrostatic solvation (*i.e.* in the absence of hydrogen bonding).

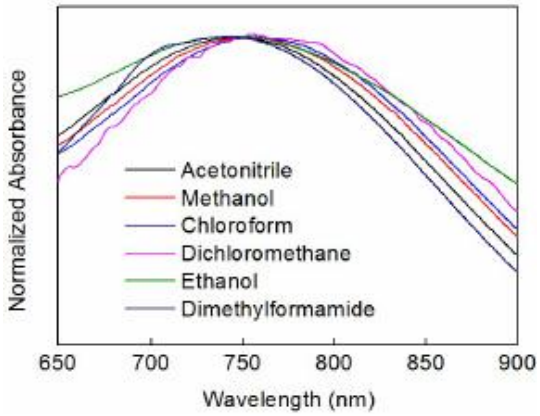

Figure 4.19: *Plot showing an overlay of the normalized absorption profiles (in the region 650-900 nm) of compound **21** in the solvents indicated, showing how the position of λmax within this range shifts. All spectra were measured at a concentration of 1.9 mM, with the exception of those taken in acetonitrile and DMF (both 1.6 mM). Reproduced from Dalton Trans.*, **2016**,45, 15575 *with permission of Royal Society of Chemistry. Copyright 2016*

When plotted on the same scale as the analogous data for complex **20** (see **Figure 4.10**), the positions of methanol and ethanol no longer appear anomalous, but are instead in agreement with what one might expect in the case of purely electrostatic solvation, where hydrogen bonding plays an insignificant role. Overall, therefore, these data suggest that complex **21** does indeed constitute a model for the behaviour of complex **20** but where the effects of hydrogen bonding have been eliminated.

It is interesting to note that a difference in solvatochromic behaviour between the catecholate and benzenedithiolate analogues of a transition metal-bipyridine complex such as that shown by complexes **20** and **21** is not a general phenomenon. For example, Kumar *et al.* observed a solvent-dependent shift in absorbance of 83 nm (from 495 nm in methanol to 578 nm in chloroform) with [Pt^{II}(2,2′-bipyridine)(*o*-catecholate)], but they also found an almost identical shift (76 nm) was obtained in these same solvents with the dithiolate analogue [Pt^{II}(2,2′-bipyridine)(3,4-dimercaptotoluene)].[37]

Having obtained these insights into the factors contributing to the solvent-dependent absorbances of complexes **20** and **21**, we chose to investigate the effects that mixed solvent systems had on the solvatochromism of complex **20**. **Figure 4.20** shows the outcome of these experiments, where complex **20** was dissolved in mixtures of

ethanol and water (**Figure 4.20a**) and mixtures of dichloromethane and methanol (**Figure 4.20b**).

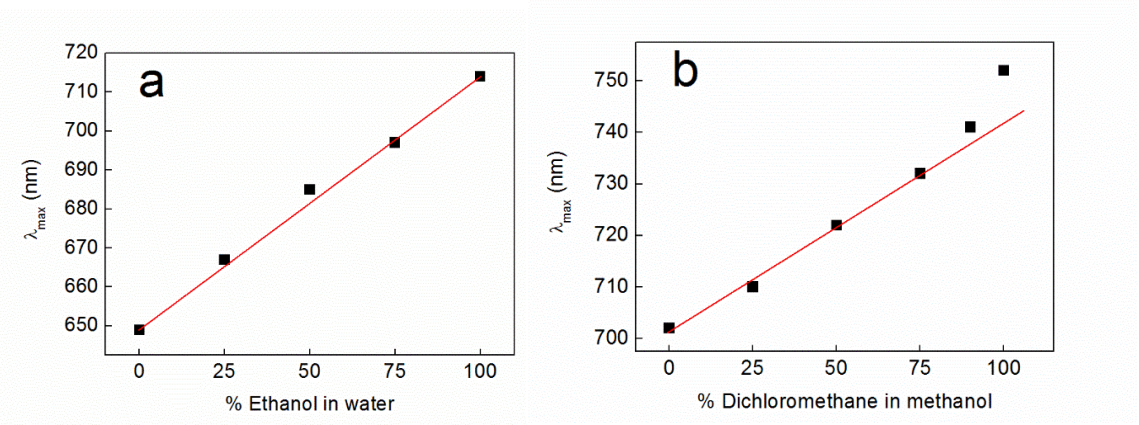

Figure 4.20. *(**a**) Shift of the lowest energy absorption band of compound **20** as a function of the percentage (by volume) of ethanol present in water in a mixed solvent system. (**b**) Shift of the lowest energy absorption band of compound **20** as a function of the percentage (by volume) of dichloromethane present in methanol in a mixed solvent system. The concentration of complex **20** was 5 mM in all the solvent mixtures investigated. The red lines in both panels are linear fits and are provided as guides to the eye. Reproduced from Dalton Trans.*, **2016**,45, 15575 *with permission of Royal Society of Chemistry. Copyright 2016*

In the case of the ethanol-water mixtures, the absorbance of complex **20** shifts in a linear fashion with the changing nature of the solvent over the whole range of compositions, indicating that there is no preferential solvation of complex **20** by either solvent (i.e. the composition of the solvent system in the cybotactic region of the solute is essentially the same as in the bulk).[46,47]

In the case of dichloromethane-methanol mixtures, the absorbance of complex **20** again shifts in a linear fashion over most of the compositional range, but there is now some deviation away from ideal behaviour at high ratios of dichloromethane to methanol (above 3:1). This suggests that some preferential solvation of complex **20** by methanol does indeed occur, which is perhaps unsurprising given that methanol is a hydrogen bond-donating solvent and the spectroscopic results described above show that complex **20** accepts hydrogen bonds through its catecholate oxygen atoms. However, even for these dichloromethane-methanol mixtures, the graph remains linear as far as a ratio of 3:1 dichloromethane to methanol. Hence, within the linear regions of these graphs at least, there remains the possibility that the percentage of each solvent in mixtures with intermediate compositions could be discerned on the basis of the absorbance of complex **20**. Whilst these results are

somewhat preliminary, we believe that this concept could be extended to allow molecular probes incorporating complex **20** to be used to determine solvent compositions on the basis of colour in a variety of mixed solvent systems.

4.3 Conclusions

In summary, we have synthesized three complexes of the type $[Co^{III}(L)(bipyridine)_2]^+$ (L = o-catecholato, o-benzenedithiolato) by a general and rapid one-pot reaction route, which is near-quantitative for the catecholate compounds. Complexes **20** and **21** were previously unreported and display intriguing differences in their solution-phase UV-vis absorption behaviour. Specifically, the position of λmax in complex **20** was highly sensitive to the hydrogen bond donation ability of the surrounding medium, whereas in the benzenedithiolate analogue **21** it was not. TD-DFT was used to compare the ground and excited state electronic structures of complexes **20** and **21**. Hence it was determined that complex **20** hydrogen-bonds to the solvent through the oxygen atoms on its catecholate ligand. This interaction removes electron density from the catecholate-based π^* orbital, thereby stabilizing the ground state with respect to the excited state (which is primarily metal-centred and hence more isolated from the solvent). This has the effect of increasing the excitation energy in hydrogen bond-donating solvents relative to those that cannot hydrogen bond. In complex **21** on the other hand, the sulfur atoms in the chelating benzenedithiolate ligand are much weaker hydrogen bond acceptors than oxygen, and so stabilization of the ground state through hydrogen bonding to the solvent is effectively eliminated. The (much smaller) solvatochromic effect that manifests in complex **21** can be explained on a purely electrostatic basis. Given the wide range of functionalized bipyridines, catechols and benzenedithiols that are available, we believe that the synthesis of an enormous diversity of allied complexes should be possible. In particular, we foresee potential for such compounds to be tailored for use as molecular probes[(48)] or solvatochromic indicators[(49)] that can give insight into different solvent and chemical environments by virtue of readily-observed spectroscopic changes.

4.4 Synthetic details

4.4.1 Synthesis of Compound 19

To a solution of 2,2′-bipyridine (0.233 g, 1.49 mmol, 2 eq.) in methanol (50 mL) was added a solution of $Co(NO_3)_2 \cdot 6H_2O$ (0.217 g, 0.746 mmol, 1 eq.) in methanol (10 mL) and the resulting orange solution stirred at room temperature open to air for 2 minutes. A solution of catechol (0.082 g, 0.746 mmol, 1 eq.) in 10 mL methanol was then added to the reaction. No colour change was observed. Excess triethylamine (3 mL) was then added to the reaction mixture, which was observed to darken immediately to red-brown upon addition of Et_3N. A precipitate was observed to form within 2 minutes. After 10 further minutes stirring open to air, the reaction mixture was filtered, washing the solid on the filter with diethyl ether. This solid was dried at 60 °C for 90 minutes, yielding compound **19** as a dark brown powder (0.375 g, 93%), m.p. = 240 °C (dec.). The complex is somewhat hygroscopic and turns greenish (indicating hydration, see below) when exposed to laboratory air. Indeed, a sample of dry mass 0.216 g was found to increase in mass by 12 mg after standing in air for 1 hour (upon further standing the mass did not increase further). This corresponds to a mass-gain of around 5%, corresponding to 1.5 molecules of H_2O per molecule of compound **19**. CHN analysis was then performed on this hydrated sample: Anal. calcd. For $C_{26}H_{20}CoN_5O_5 \cdot (1.5H_2O)$: C 54.94, H 4.08, N 12.32. Found: C 54.81, H 4.00, N 12.21. Yields for compound **19** are calculated from the dry (anhydrous) mass. ^{1}H NMR (90% MeOD / 10% D_2O, 400 MHz), δ = 8.91 (d, 2H, J = 5.6, H_a or H_h), 8.77 (d, 2H, J = 8.3, H_d or H_e), 8.70 (d, 2H, J = 8.0, H_d or H_e), 8.48 (dt, 2H, J_1 = 8.1, J_2 = 1.3, H_c or H_f), 8.34-8.27 (m, 2H, H_c or H_f), 7.92 (dt, 2H, J_1 = 5.7, J_2 = 1.1, H_b or H_g), 7.59-7.53 (m, 4H, H_b or H_g and H_a or H_h), 6.67-6.60 (m, 2H, H_i or H_j), 6.43-6.37 (m, 2H, H_i or H_j). Letter assignments correspond to those shown in **Figure 4.21**. ^{13}C NMR (90% MeOD / 10% D_2O, 100 MHz), δ = 157.6, 157.5, 157.3, 152.1, 150.7, 142.5, 142.1, 128.8, 128.6, 125.1, 124.7, 118.8, 116.2. ESI-LMMS (acetonitrile): *m/z* = 479.0699, $[M]^+$ (calcd. for $C_{26}H_{20}CoN_4O_2$; 479.0918).

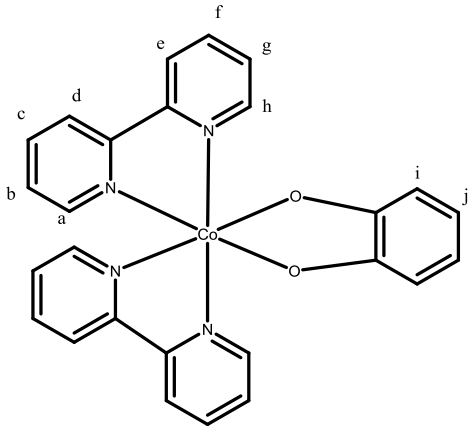

Figure 4.21: *Structure of compound **19**. Letters on the product structure correspond to the ^1H NMR signal assignments detailed in the text above.*

4.4.2 Synthesis of Compound 20

To a solution of 5,5′-dimethyl-2,2′-bipyridine (0.500 g, 2.71 mmol, 2 eq.) in methanol (50 mL) was added a solution of $Co(NO_3)_2 \cdot 6H_2O$ (0.395 g, 1.36 mmol, 1 eq.) in methanol (10 mL) and the resulting orange solution stirred at room temperature open to air for 2 minutes. A solution of catechol (0.149 g, 1.36 mmol, 1 eq.) in 10 mL methanol was then added to the reaction. No colour change was observed. Excess Et_3N (5 mL) was then added to the reaction mixture, which was observed to darken immediately to red-brown upon addition of Et_3N. After stirring in air for 3 minutes, the solution had changed to bottle-green. After a further 10 minutes stirring open to air, 100 mL of diethyl ether was added to induce precipitation of a green/grey solid, which was collected by filtration and washed on the filter with ether, and then dried at 100 °C to yield a dark brown powder (0.800 g, 98%). Subsequent recrystallization from DMF/diethylether afforded **20** as brown crystals, m.p. = 270 °C (dec.). The complex is somewhat hygroscopic and turns greenish (indicating hydration, see below) when exposed to laboratory air. Indeed, a sample of dry mass 0.128 g was found to increase in mass by 2.4 mg after standing in air for 1 hour (upon further standing the mass did not increase further). This corresponds to a mass-gain of around 2%, corresponding to ~0.67 molecules of H_2O per molecule of compound **20**. CHN analysis was then performed on this hydrated sample: Anal. calcd. for $C_{30}H_{28}CoN_5O_5 \cdot (2/3H_2O)$: C 59.12, H 4.85, N 11.49. Found: C 59.35, H 4.69, N 11.57. Yields for compound **20** are calculated from the dry (anhydrous) mass. ^1H NMR (MeOD, 400 MHz), δ = 8.68-8.66 (m, 2H, H_a or H_h), 8.59 (d, 2H, J = 8.2, H_d or H_e), 8.52 (d, 2H, J = 8.2, H_d or H_e), 8.29-8.24 (m, 2H, H_c or H_f), 8.12-8.07 (m, 2H, H_c or H_f), 7.28-7.24 (m, 2H, H_a or H_h), 6.65-6.60 (m, 2H, H_i or H_j), 6.43-6.37 (m, 2H, H_i or H_j), 2.50 (s, 6H, H_b or H_g), 2.26 (s, 6H, H_b or H_g).

Letter assignments correspond to those shown in **Figure 4.22**. ^{13}C NMR (MeOD, 100 MHz), δ = 157.0, 154.7, 154.6, 151.0, 149.7, 142.0, 141.6, 139.3, 139.0, 123.4, 123.0, 117.9, 115.3, 17.7, 17.1. ESI-LMMS (acetonitrile): *m/z* = 535.1305, $[M]^+$ (calcd. for $C_{30}H_{28}CoN_4O_2$, 535.1544).

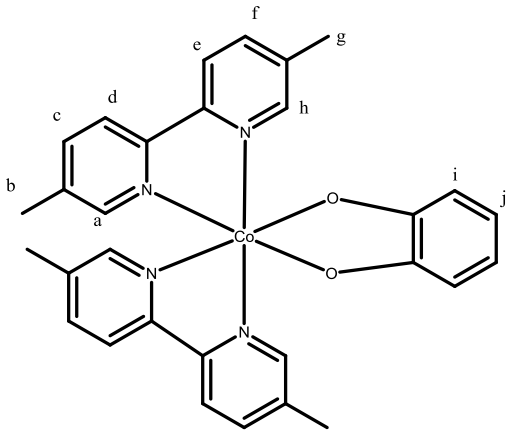

Figure 4.22: *Structure of compound **20**. Letters on the product structure correspond to the ^1H NMR signal assignments detailed in the text above.*

An exactly analogous synthetic route employing $CoCl_2 \cdot 6H_2O$ as the cobalt salt was found to be equally effective at generating compound **20**, and the characterization of the resulting chloride salt was in agreement with that reported here for the nitrate salt.

4.4.3 Synthesis of Compound 21

To a solution of 5,5′-dimethyl-2,2′-bipyridine (0.320 g, 1.74 mmol, 2 eq.) in methanol (20 mL) was added a solution of $Co(NO_3)_2 \cdot 6H_2O$ (0.254 g, 0.872 mmol, 1.2 eq.) in methanol (10 mL). To this was added a solution of benzene-1,2-dithiol (0.124 g, 0.872 mmol, 1 eq.) in 10 mL methanol. The reaction mixture was observed to turn dark green upon addition of the benzene-1,2-dithiol. After stirring in air for 60 minutes, the solvent was removed under reduced pressure and the resulting solid re-dissolved in 10 mL MeOH. Around 25 mL of diethyl ether were then added, inducing the formation of a dark green precipitate and a dark brown supernatant solution. After filtration, the green solid was kept, and re-dissolved in 5 mL of MeOH. To this green solution was then added a large excess diethyl ether, resulting in the formation of a green solid (the compound **24** detailed in **Chapter 5**) and an orange/brown supernatant solution. After a second filtration, the filtrate solution was kept and treated with excess petroleum ether, causing the precipitation of compound **21** as a yellow/orange solid. This was dried at 100 °C, giving a yield of 88 mg, (16%), m.p. = 212 °C (dec.). The complex is somewhat hygroscopic and hence absorbs water when exposed

to laboratory air. Indeed, a sample of dry mass 19.5 mg was found to increase in mass by 1.3 mg after standing in air for 1 hour (upon further standing the mass did not increase further). This corresponds to a mass-gain of around 6%, corresponding to around 2 molecules of H_2O per molecule of compound **21**. CHN analysis was then performed on this hydrated sample: Anal. calcd. for $C_{30}H_{28}CoN_5O_3S_2 \cdot (2H_2O)$: C 54.13, H 4.85, N 10.52. Found: C 54.10, H 4.83, N 10.30. Yields for compound **21** are calculated from the dry (anhydrous) mass. ^{1}H NMR (MeOD, 400 MHz), δ = 9.37-9.34 (m, 2H, H_a or H_h), 8.43 (d, 2H, *J* = 8.2, H_d or H_e), 8.39 (d, 2H, *J* = 8.2, H_d or H_e), 8.09-8.05 (m, 2H, H_c or H_f), 8.03-7.99 (m, 2H, H_c or H_f), 7.08-7.00 (m, 4H, H_a or H_h and H_i or H_j), 6.78-6.74 (m, 2H, H_i or H_j), 2.45 (s, 6H, H_b or H_g), 2.22 (s, 6H, H_b or H_g). Letter assignments correspond to those shown in **Figure 4.23** (see also **Scheme 4.2**). ^{13}C NMR (MeOD, 100 MHz), δ = 154.4, 153.9, 153.7, 148.9, 143.2, 140.7, 140.2, 138.7, 138.5, 126.4, 122.9, 122.8, 122.6, 17.6, 17.2. MS-FAB$^+$ (chloroform): *m/z* =567.1060 $[M]^+$ (calcd. for $C_{30}H_{28}CoN_4S_2$; 567.1087).

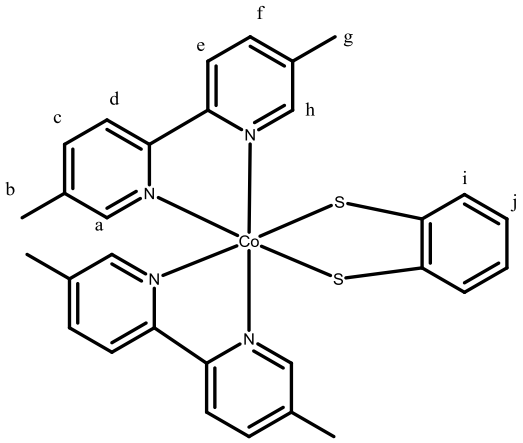

Figure 4.23: *Structure of compound **21**. Letters on the product structure correspond to the ^{1}H NMR signal assignments detailed in the text above.*

4.5 References

[1] W. Paw and R. Eisenberg, *Inorg. Chem.* 1997, **36**, 2287.

[2] D. Ruiz-Molina, L. N. Zakharov, A. L. Rheingold and D. N. Hendrickson, *J. Phys. Chem. Solids,* 2004, **65**, 831.

[3] A. Panja, *RSC Adv.* 2013, **3**, 4954.

[4] Y. Suenaga and C. G. Pierpont, *Inorg. Chem.* 2005, **44**, 6183.

[5] Y. Suenaga, Y. Umehata, Y. Hirano, T. Minematsu and C. G. Pierpont, *Inorg. Chim. Acta*, 2008, **361**, 2941.

[6] Y. Suenaga, Y. Hirano, Y. Umehata and T. Minematsu, *Inorg. Chim. Acta*, 2011, **365**, 505.

[7] D. Ruiz, J. Yoo, I. A. Guzei, A. L. Rheingold and D. N. Hendrickson, *Chem. Commun.* 1998, 2089.

[8] A. Witt, F. W. Heinemann, S. Sproules and M. M. Khusniyarov, *Chem. Eur. J.* 2014, **20**, 11149.

[9] W. Kaim, *Inorg. Chem.* 2011, **50**, 9752.

[10] V. Lyaskovskyy and B. de Bruin, *ACS Catal.* 2012, **2**, 270.

[11] M. Affronte, A. Beni, A. Dei and L. Sorace, *Dalton Trans.* 2007, 5253.

[12] V. K. Andrä and F. Fleischer, *Z. Anorg. Allg. Chem*. 1982, **486**, 210.

[13] N. G. Connelly, J. A. McCleverty and C. J. Winscom, *Nature*, 1967, **216**, 999.

[14] J. A. McCleverty, N. M. Atherton, N. G. Connelly and C. J. Winscom, *J. Chem. Soc. A*, 1969, 2242.

[15] J. A. McCleverty, *Prog. Inorg. Chem.* 1968, **10**, 49.

[16] S. Sproules and K. Wieghardt, *Coord. Chem. Rev.* 2010, **254**, 1358.

[17] F. H. Allen, *Acta Cryst. B*, 2002, **58**, 380.

[18] C. R. Groom, I. J. Bruno, M. P. Lightfoot and S. C. Ward, *Acta Cryst. B*, 2016, **72**, 171.

[19] S. N. Brown, *Inorg. Chem.* 2012, **51**, 1251.

[20] See, for example: J. J. Loughrey, N. J. Patmore, A. Baldansuren, A. J. Fielding, E. J. L. McInnes, M. J. Hardie, S. Sproules and M. A. Halcrow, *Chem. Sci.* 2015, **6**, 6935.

[21] C. G. Pierpont and R. M. Buchanan, *Coord. Chem. Rev.* 1981, **38**, 45.

[22] C. G. Pierpont, *Coord. Chem. Rev.* 2001, **216-217**, 99.

[23] C. G. Pierpont, *Coord. Chem. Rev.* 2001, **219-221**, 415.

[24] C. G. Pierpont, S. K. Larsen and S. R. Boone, *Pure Appl. Chem.* 1988, **60**, 1331.

[25] C. G. Pierpont and C. W. Lange, *Prog. Inorg. Chem.* 1994, **41**, 331.

[26] P. A. Wicklund, L. S. Beckmann and D. G. Brown, *Inorg. Chem.* 1976, **15**, 1996.

[27] A. Vlček Jr., J. Klíma and A. A. Vlček, *Inorg. Chim. Acta*, 1983, **69**, 191.

[28] R. M. Buchanan and C. G. Pierpont, *J. Am. Chem. Soc.* 1980, **102**, 4951.

[29] S. Arzberger, J. Soper, O. P. Anderson, A. la Cour and M. Wicholas, *Inorg. Chem.* 1999, **38**, 757.

[30] C. Milsmann, E. Bothe, E. Bill, T. Weyhermüller and K. Wieghardt, *Inorg. Chem.* 2009, **48**, 6211.

[31] L. I. Simándi, T. Barna, G. Argay and T. L. Simándi, *Inorg. Chem.* 1995, **34**, 6337.

[32] A. Bencini, C. A. Daul, A. Dei, F. Mariotti, H. Lee, D. A. Shultz and L. Sorace, *Inorg. Chem.* 2001, **40**, 1582.

[33] K. S. Min, A. G. DiPasquale, J. A. Golen, A. L. Rheingold and J. S. Miller, *J. Am. Chem. Soc.* 2007, **129**, 2360.

[34] K. G. Alley, G. Poneti, P. S. D. Robinson, A. Nafady, B. Moubaraki, J. B. Aitken, S. C. Drew, C. Richie, B. F. Abrahams, R. K. Hocking, K. S. Murray, A. M. Bond, H. H. Harris, L. Sorace and C. Boskovic, *J. Am. Chem. Soc.* 2013, **135**, 8304.

[35] A. Hudson and G. R. Luckhurst, *Chem. Rev.* 1969, **69**, 191.

[36] A. Vogler and H. Kunkely, *J. Am. Chem. Soc.* 1981, **103**, 1559.

[37] L. Kumar, K. H. Puthraya and T. S. Srivastava, *Inorg. Chim. Acta*, 1984, **86**, 173.

[38] K. H. Puthraya and T. S. Srivastava, *Polyhedron*, 1985, **4**, 1579.

[39] C. Reichardt, *Chem. Rev.* 1994, **94**, 2319.

[40] C. Reichardt and T. Welton, *Solvents and Solvent Effects in Organic Chemistry, 4th edn.* Wiley-VCH, Weinheim, 2011.

[41] L. Onsager, *J. Am. Chem. Soc.* 1936, **58**, 1486.

[42] J. P. Cerón-Carrasco, D. Jacquemin, C. Laurence, A. Planchat, C. Reichardt and K. Sraïdi, *J. Phys. Org. Chem.* 2014, **27**, 512.

[43] M. J. Kamlet, J.-L. M. Abboud, M. H. Abraham and R. W. Taft, *J. Org. Chem.* 1983, **48**, 2877.

[44] Y. Marcus, *Chem. Soc. Rev.* 1993, **22**, 409.

[45] M. H. Abraham, *Chem. Soc. Rev.* 1993, **22**, 73.

[46] P. M. E. Mancini, A. Terenzani, M. G. Gasparri and L. R. Vottero, *J. Phys. Org. Chem.* 1995, **8**, 617.

[47] F. Gharib, A. Shamel, F. Jaberi and A. Farajtabar, *J. Solution Chem.* 2013, **42**, 1083

[48] S. Herrmann, J. T. Margraf, T. Clark and C. Streb, *Chem. Commun.* 2015, **51**, 13702.

[49] P. L. Silva, E. L. Bastos and O. A. El Seoud, *J. Phys. Chem. B*, 2007, **111**, 6173.

Unprecedented Inequivalent Metal Coordination Environments in a Mixed-Ligand Dicobalt Complex

Published as "*Unprecedented Inequivalent Metal Coordination Environments in a Mixed-Ligand Dicobalt Complex"*

Giacomo Cioncoloni, Stephen Sproules, Claire Wilson and Mark D. Symes,

Eur. J. Inorg. Chem. ***2017****, 3707–3713*

Acknowledgments and declaration

The project covered in this chapter was a collaboration with several researchers from other groups at University of Glasgow. I carried out all the synthesis work presented in this chapter as well as the UV-Vis IR and all the electrochemical studies.
Dr. Stephen Sproules performed all the theoretical studies; Dr. Claire Wilson performed the crystallographic study.

Synopsis

Bimetallic complexes of the transition metals containing mixed diimine and dithiolate ligands are of fundamental interest on account of their intriguing electronic properties. Almost always, such complexes are isolated as species in which both the metal centers are in identical coordination environments – this means that the two metals often have identical redox properties. In contrast, mixed-diimine/dithiolate bimetallic complexes of the first row transition metals where the two metals are in dissimilar coordination environments are exceedingly rare, and are only known for nickel. Herein, we report the first ever example of a mixed-diimine/dithiolate dicobalt complex where the two cobalt centers are in different coordination environments. The synthesis of this compound is straightforward, and produces a complex in which the two cobalt centers display very different redox properties.

5.1 Introduction

Transition metal complexes containing mixed chelating diimine and dithiolate ligand sets have long been recognized to be of interest on account of their varied physical properties, which include luminescence, non-linear optical behavior, intense coloration and multi-electron redox chemistry.[1-5] Within this class of compounds, multimetallic complexes containing dithiolene ligands show particular promise for the development of new materials with exciting properties.[6] In such multimetallic complexes containing dithiolene ligands, the metal centers normally all coordinate to the dithiolene ligands in the same manner, regardless of whether other types of ligand are present or not. This then leads to multimetallic complexes where all the metal ions are in the same coordination environment. For bimetallic species, commonly-observed coordination motifs involving dithiolene ligands include $[M_2(\text{dithiolene})_4]$ (M = Mn,[7,8] Fe,[9-11] Co,[7,11,12] Ni[13,14]), $[M_2(\text{dithiolene})_5]$ (M = Mo, Rh, Re),[15] and $[M_2(Cp)_2(\text{dithiolene})_2]$ (Cp = cyclopentadenyl, M = V, Cr, Fe, Co, Mo, Rh).[16] In such complexes, the coordination environment around one metal center is almost always the same as that around the other metal center, and this is especially true when the metals in question are drawn from the first row of the d-block. Indeed, extensive searching of the Cambridge Crystallographic Database (and other databases) returned only two examples of bimetallic complexes of first row transition metals containing dithiolene ligands where the two metal ions were *not* in the same coordination environment. Both of these are di-nickel complexes reported by Bachman in the late 1990s,[17] whereby aerial oxidation of the monomeric complex [Ni(bdt)(bpy)] in DMF leads to the generation of mixtures of $[(bpy)_2Ni(bdtO_2)Ni(bdt)]$ and $[(bpy)_2Ni(bdtO_4)Ni(bdt)]$ (**22**) (bpy = 2,2′-bipyridine, bdt^{2-} = benzene-1,2-dithiolate; **Figure 5.1a**. Hence one of the nickel centers in these complexes is octahedral, coordinating to both of the bipyridine ligands and forming interactions with the two dithiolene-derived ligands, whilst the second nickel coordinates only to these dithiolene-derived ligands and adopts a square planar geometry. Meanwhile, Wacholtz, Mague and co-workers have reported two allied tri-zinc complexes where one zinc center is coordinated by two dithiolenes whilst the other two zinc centers each coordinate to one diimine ligand, with a bridging dithiolene ligand and bonds to the dithiolenes on the first zinc (**23**) as shown in **Figure 5.1b**.[18,19]

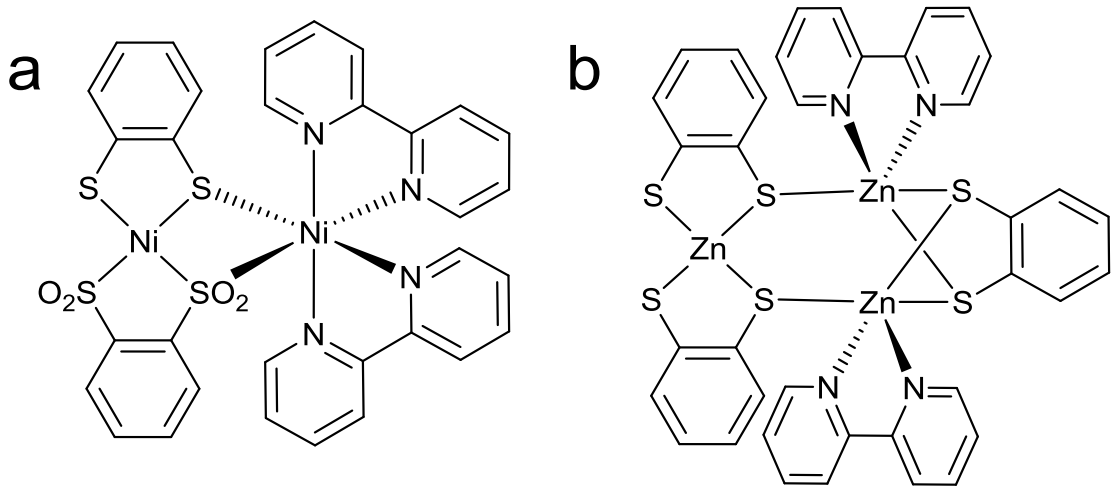

Figure 5.1: *Simplified structures showing the coordination geometry around the metal centers in (**a**) Bachman's di-nickel complexes (**22**) and (**b**) the tri-zinc complexes (**23**) reported by Wacholtz, Mague and co-workers.Reproduced from Eur. J. Inorg. Chem. **2017**, 3707wih permission of John Wiley and sons. Copyright 2017.*

Beyond these examples, however, we could find no other instances of bimetallic complexes of first row transition metals containing dithiolene ligands where the two metal centers were in different coordination environments (and hence where the two metal ions could be expected to exhibit differing redox activity).

Herein, we report a dicobalt complex, discovered coincidentally during the synthesis of compound **21**, detailed in **Chapter 4**. This complex incorporates diimine and dithiolate ligands with an unprecedented coordination motif, whereby the first cobalt center coordinates to one diimine ligand and two dithiolenes, whilst the other cobalt coordinates to two diimine ligands and completes its octahedral geometry by virtue of forming single bonding interactions with both of the dithiolenes that coordinate to the first metal center. The unusual structure of this complex ($[Co_2(bdt)_2(Me_2bpy)_3]^{2+}$, $[\mathbf{24}]^{2+}$) was determined by single crystal X-ray diffraction, and NMR and mass spectrometry indicate that this species is also stable in solution. Furthermore, electrochemical analysis of complex $[\mathbf{24}]^{2+}$ indicates that it undergoes a reversible one-electron reduction reaction at very modest cathodic potentials, producing a mixed-valence $Co^{III}Co^{II}$ species, the likely nature of which we have rationalized using computational methods.

5.2 Results and Discussion

5.2.1 Synthesis and structure of complex [24]$^{2+}$

A general route to the synthesis of dicobalt complex [**24**]$^{2+}$ is given in **Scheme 5.1**. Hence, addition of one equivalent of $Co(NO_3)_2 \cdot 6H_2O$ to two equivalents of 5,5′-dimethyl-2,2′-bipyridine (Me_2bpy) in methanol resulted in the formation of an orange solution, the color of which rapidly turned to dark green upon the addition of one equivalent of *o*-benzenedithiol under air. After removal of some of the solvent, a dark green solid could be precipitated from the remainder of the dark green solution by addition of diethyl ether. Subsequent recrystallization of this solid from MeOH/diethylether then afforded green crystals of [**24**]$(NO_3)_2$ suitable for X-ray diffraction (**Figure 5.2**).

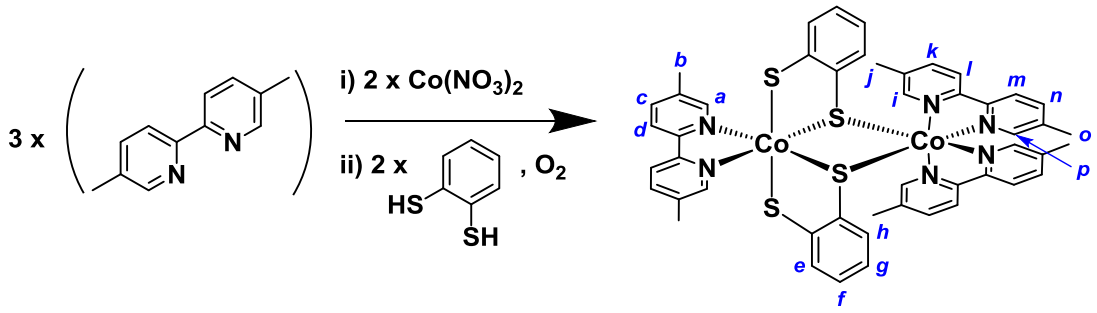

Scheme 5.1 *The general synthetic route followed to synthesize compound [**24**](NO$_3$)$_2$. Italic letters on the product structure correspond to the ^{1}H NMR signal assignments in the Experimental Section. Reproduced from Eur. J. Inorg. Chem.* ***2017****, 3707 wih permission of John Wiley and sons. Copyright 2017.*

The connectivity of [**24**]$^{2+}$ is evident from **Figure 5.2**, which shows that two bipyridine moieties are coordinated in a *cis* fashion around one of the Co centers (Co2), the octahedral geometry of which is completed by coordination to sulfurs from each of the dithiolene ligands. These dithiolene ligands themselves coordinate to the other Co center (Co1) in a *cis* fashion, with the result that one sulfur on each dithiolene acts as a bridge between the two cobalt centers. The octahedral coordination environment of Co1 is then completed by bidentate coordination to a unique bipyridine ligand. The Co−S bond lengths in **Figure 5.2** are Co1–S1 = 2.2222(7) Å, Co1–S2 = 2.2688(7) Å, Co1–S3 = 2.2251(8) Å, Co1–S4 = 2.2709(8) Å, Co2–S1 = 2.2663(8) Å and Co2–S3 = 2.2620(7) Å, and hence the Co–S bond lengths for Co2 are both of approximately the same length as each other (and the same length as between Co1 and the non-bridging sulfurs), whilst the Co–S bond lengths between Co1 and the bridging sulfur atoms are noticeably shorter in length.

The coordination sphere for Co2 is nearly identical to that observed in [Co(Tab)(4,4′-dmbpy)]$(PF_6)_3$, where Tab is 4-(trimethylammonio)benzenethiolate) and 4,4′-dmbpy is 4,4′-dimethylbipyridine.[20] Most of the angles around Co2 are within the range $85 < \theta < 95°$, with the exception of the S3–Co2–S1, N3–Co2–N4 and N5–Co2–N6 angles, all of which are closer to 82° (see **Table 5.1** and **Appendix A3**). The maximum deviation from 90° for the bond angles around Co1 are for the N1–Co1–N2 angle (83°) and the N2–Co1–S1 angle (97°). These Co–S–Co angles are therefore similar to related edge-sharing bi-octahedron (ESBO) dicobalt complexes with bridging thiolate ligands.[21-23]

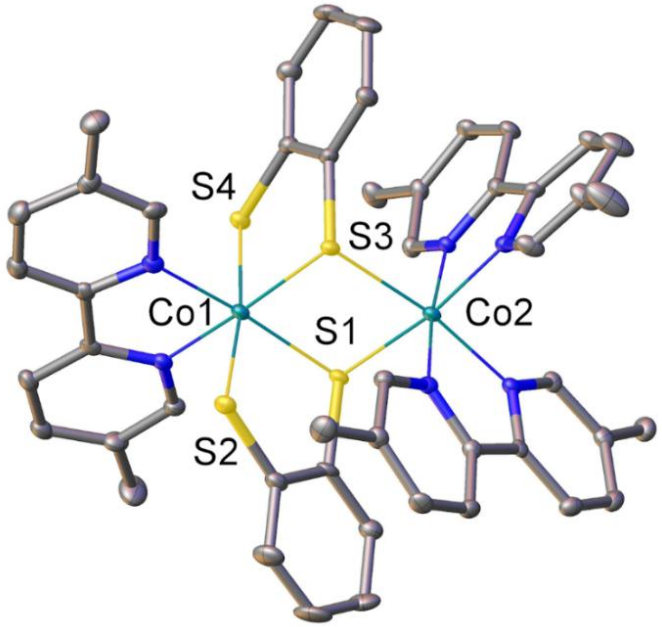

Figure 5.2. *The molecular structure of the di-cationic complex in crystals of* $[Co_2(bdt)_2(Me_2bpy)_3](NO_3)_2$. *Hydrogen atoms, solvent and counterions have been omitted from the structure. Further crystallographic details can be found in the Supporting Information. Color scheme: C = grey, N = blue, S = yellow, Co = cyan. For selected bond lengths and angles, see* ***Table 1****. Reproduced from Eur. J. Inorg. Chem.* ***2017****, 3707 wih permission of John Wiley and sons. Copyright 2017.*

The complex has no Co–Co bond given the long intermetal distance of 3.63 Å. This is a consistent feature of ESBO dicobalt(III) complexes, where the intermetal distance is a function of the donor atoms that comprise the $\{Co_2X_2\}$ diamond core, ranging from 2.863(2) – 2.951(1) Å for hydroxo-bridged,[24] 2.885(5) – 2.9842(6) Å for alkoxo-bridged,[25] 2.926(1) Å for imido-bridged,[26] 2.874(1) – 2.977(2) Å for OH^-/NH_2^--bridged,[27] to 3.35(1) – 3.3441(2) Å with the larger thiolato ligands.[21-23] Akin to other bimetallic complexes with five chelating ligands,[15] the chirality about

each Co center in $[\mathbf{1}]^{2+}$ is the same (ΛΛ) for each tris-chelate Co ion. The only exception to this rule for bimetallic complexes with five chelating ligands is $[Co_2(Et_2dtc)_5]^{1+}$ (Et_2dtc^{1-} = diethyldithiocarbamato), where the each Co center has an opposing chirality.[27a]

The solution-phase ^{1}H NMR of complex $[\mathbf{24}]^{2+}$ supports the hypothesis that the structure shown in **Figure 5.2** is maintained in solution (see **Figures 5.3**).

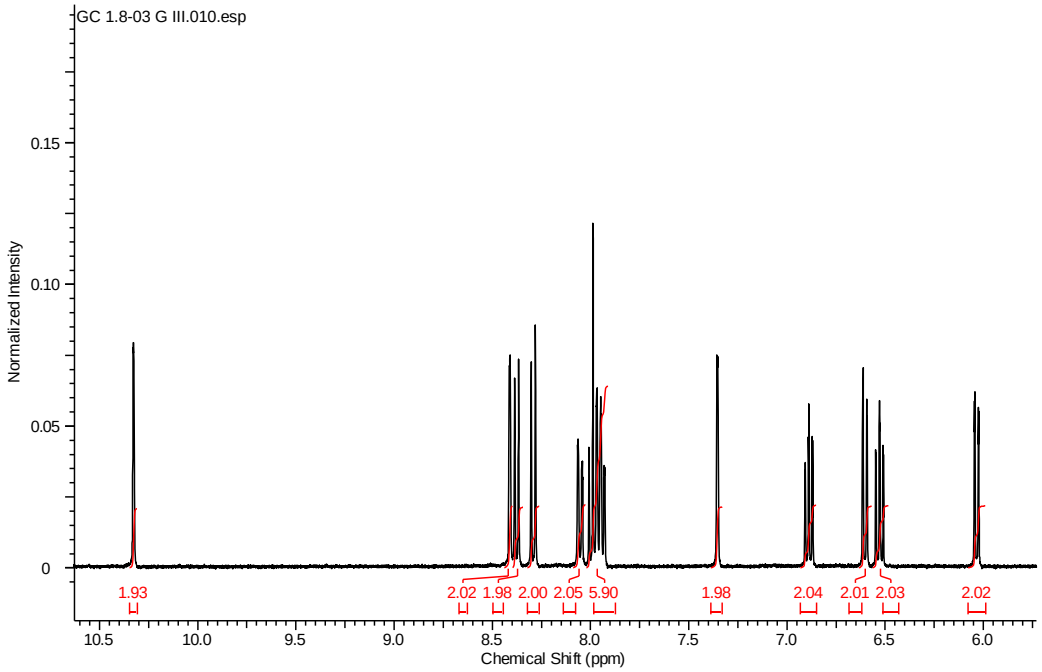

Figure 5.3: *Expansion of the aromatic region of the ^{1}H NMR spectrum of $[\mathbf{24}]^{2+}$. Full spectrum is shown in* ***Figure 5.10*** *(****Section 5.4****) Reproduced from Eur. J. Inorg. Chem.* ***2017****, 3707 wih permission of John Wiley and sons. Copyright 2017.*

Hence the bipyridine units around Co2 adopt the characteristic pattern for a *cis* arrangement of these ligands observed in species such as (**21**),[28] whilst the unique bipyridine coordinated to Co1 sits in a more symmetrical chemical environment. Meanwhile, the peaks corresponding to the dithiolate ligands also show a pattern consistent with their inequivalent binding to the two cobalt centers. Moreover, the fact that the spectrum is sharp and well-resolved serves as good evidence that both the cobalt ions are in the low-spin Co(III) oxidation state. Meanwhile, mass spectrometry indicates a peak with *m/z* = 475.1, which matches exactly that expected for the $[Co_2(bdt)_2(Me_2bpy)_3]^{2+}$ ion (ion mass = 950.1174 with a +2 charge). Hence it seems highly likely that the structure shown in **Figure 5.2** is also the structure found in solution.

5.2.2 Redox Behavior

Cyclic voltammetry was performed on complex [**24**]$^{2+}$ in acetonitrile containing 1 M tetabutylammonium hexafluorophosphate (TBA-PF_6) as the supporting electrolyte (see **Figure 5.4**). This evinced an irreversible oxidative process peaking at around +0.7 V (*vs.* ferrocenium/ferrocene), which we attribute to oxidation of the benzenedithiolate ligands by analogy to the behavior observed for the monomeric species [Co^{III}(bdt)(Me_2bpy)$_2$]$^+$ (**21**)in this solvent system (see below).[28] In terms of reductive electrochemistry, the sample displayed an irreversible wave at −1.4 V, followed by a more reversible wave at around −1.8 V, with this latter value agreeing well with the position of the couple for the reduction of free Me_2bpy in acetonitrile as determined by Saji and Aoyagui.[29] It seems, therefore, that the reductive process at −1.4 V leads to decomposition of the complex and the consequent liberation of free 5,5′-dimethyl-2,2′-bipyridine. Meanwhile, complex [**24**]$^{2+}$ also possesses a reversible wave ($E_{1/2}$ = −0.63 V), evident over both the wide and narrow potential windows scanned in **Figure 5.4**. Controlled potential electrolysis of this reversible wave at −1.0 V (*vs.* ferrocenium/ferrocene) indicated that it corresponded to a one-electron redox process (1.44 C were passed, out of a theoretical maximum of 1.53 C for a one-electron process). Hence it appears that this wave may correspond to the reversible reduction (to Co^{II}) and re-oxidation (to Co^{III}) of only one of the two cobalt centers in the complex (*vide infra*).

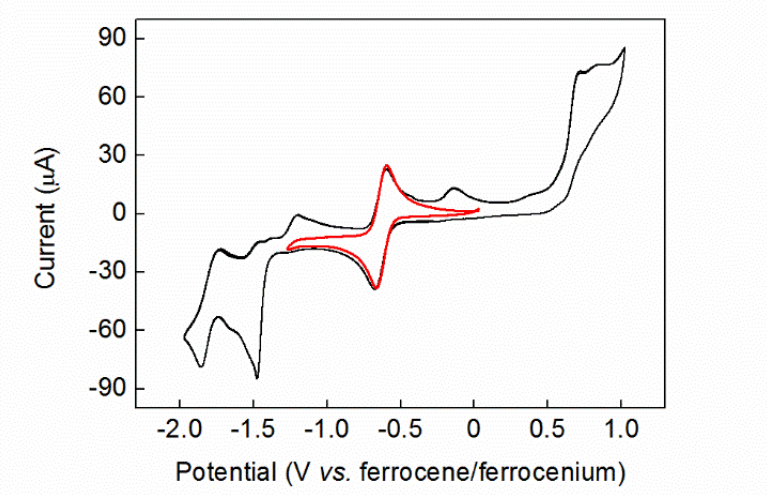

Figure 5.4: *Cyclic voltammogram of a 2.3 mM acetonitrile solution of complex [**24**]$^{2+}$ containing 1 M TBA-PF_6 run under the conditions detailed in the Experimental Section. The black trace shows the behavior over the potential range +1 to −2 V vs. reference, and the red trace shows the reversible nature of the one-electron Co^{III}/Co^{II} wave over a narrower potential window. Reproduced from Eur. J. Inorg. Chem.* ***2017****, 3707 wih permission of John Wiley and sons. Copyright 2017.*

5.2.3 Calculations

In order to elucidate the nature of the species giving rise to the redox waves observed in **Figure 5.4**, the electronic structures for this electron transfer series were investigated by DFT calculations. The geometry-optimized structure of $[\mathbf{24}]^{2+}$ at the BP86 level of theory revealed average Co–S and Co–N bond lengths of 2.276 Å and 1.973 Å, which are ~0.02 Å and 0.009 Å longer, respectively, than the experimental data (see **Table 5.1**, and **Figure 5.6** and **Appendix B3**). The optimized structure nicely reproduces the bonding pattern of the first coordination sphere, with the Co2–N4 and Co2–N5 bonds that are *trans* to the bridging sulfur atoms being longer than the other two Co–N bonds about Co2 (**Figure 5.2**). Similarly, lengths of the Co1–S bonds to the bridging atoms are *ca*. 0.05 Å shorter than the Co1–S2 and Co1–S4 distances, just as seen experimentally. The dimensions of the $\{Co_2S_2\}$ diamond core are also well-reproduced in the optimized structure, with a slight overestimation of the Co···Co separation by 0.08 Å due to a minute expansion of the Co–S–Co angles.

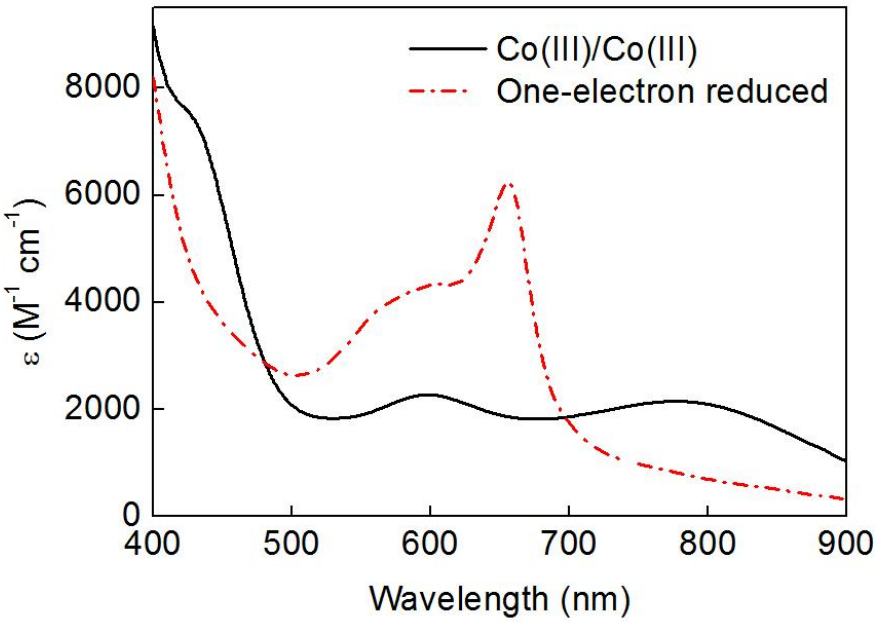

Figure 5.5: *UV-vis spectra of complex* $[\mathbf{24}]^{2+}$ *in acetonitrile (black line) and of this complex after one-electron reduction to* $[\mathbf{24}]^{+}$ *(also in acetonitrile, red dashed line). Individual spectra were collected at a range of concentrations from 0.03 to 0.3 M and the data reported here are averaged curves. Reproduced from Eur. J. Inorg. Chem.* ***2017****, 3707 wih permission of John Wiley and sons. Copyright 2017.*

Table 5.1: *Experimental and Calculated Bond Distances (Å) and Angles (°) in* $[Co_2(bdt)_2(Me_2bpy)_3]^z$ *(z = 2+, 1+) Reproduced from Eur. J. Inorg. Chem.* ***2017****, 3707 wih permission of John Wiley and sons. Copyright 2017.*

	$[Co^{III,III}{}_2(bdt)_2(Me_2bpy)_3]^{2+}$ ($S = 0$)		$[Co^{III,II}{}_2(bdt)_2(Me_2bpy)_3]^{1+}$ ($S = {}^1/_2$)
	exptl	calcd	calcd
Co(1)–N(1)	1.940(2)	1.961	1.976
Co(1)–N(2)	1.952(3)	1.960	1.973
Co(2)–N(3)	1.961(2)	1.964	1.940
Co(2)–N(4)	1.983(2)	1.995	2.102
Co(2)–N(5)	1.986(3)	1.993	1.980
Co(2)–N(6)	1.957(2)	1.962	1.943
Co(1)–S(1)	2.2222(7)	2.239	2.247
Co(1)–S(2)	2.2688(7)	2.289	2.287
Co(1)–S(3)	2.2251(8)	2.239	2.247
Co(1)–S(4)	2.2709(8)	2.288	2.280
Co(2)–S(1)	2.2663(8)	2.302	2.333
Co(2)–S(3)	2.2620(7)	2.300	2.735
S(1)–Co(1)–S(2)	89.61(3)	88.4	88.2
S(3)–Co(1)–S(4)	88.81(3)	88.4	88.6
S(1)–Co(1)–S(3)	83.83(3)	82.9	86.5
S(1)–Co(2)–S(3)	82.00(3)	80.2	74.4
Co(1)–S(1)–Co(2)	97.06(3)	98.4	105.5
Co(1)–S(3)–Co(2)	97.10(3)	98.5	93.6
Co(1)···Co(2)	3.363	3.438	3.646
S(1)···S(3)	2.971	2.965	3.080

The molecular orbital (MO) manifold presented in **Figure 5.6** for complex $[\mathbf{24}]^{2+}$ depicts two octahedral low-spin Co^{III} centers, each with a filled t_{2g} set of orbitals and empty e_g orbitals. The relative energies of these MOs reflects their individual coordination spheres; the d orbital manifold for Co2 is stabilized with respect to Co1 as it has fewer π-donating sulfur ligands. Thus, the e_g MOs of Co2, specifically the $d_{x^2-y^2}$ (where the N3–Co2–N6 vector is defined as the *z*-axis in this ESBO complex), represent the lowest unoccupied orbitals (LUMO) with more coordinating 2p donor atoms than for Co1. The highest occupied orbitals (HOMO) are ligand-based; specifically, the π_3 orbital of the bdt ligand (**Figure 5.6**).[4,30] This supports the assignment of the oxidation of $[\mathbf{24}]^{2+}$ (see **Figure 5.4** and associated discussion) as being ligand-centered, and that the process is irreversible; a bdt

radical anion ligand is incapable of bridging two Co^{III} ions, as was also observed with the monocobalt complex.[28]

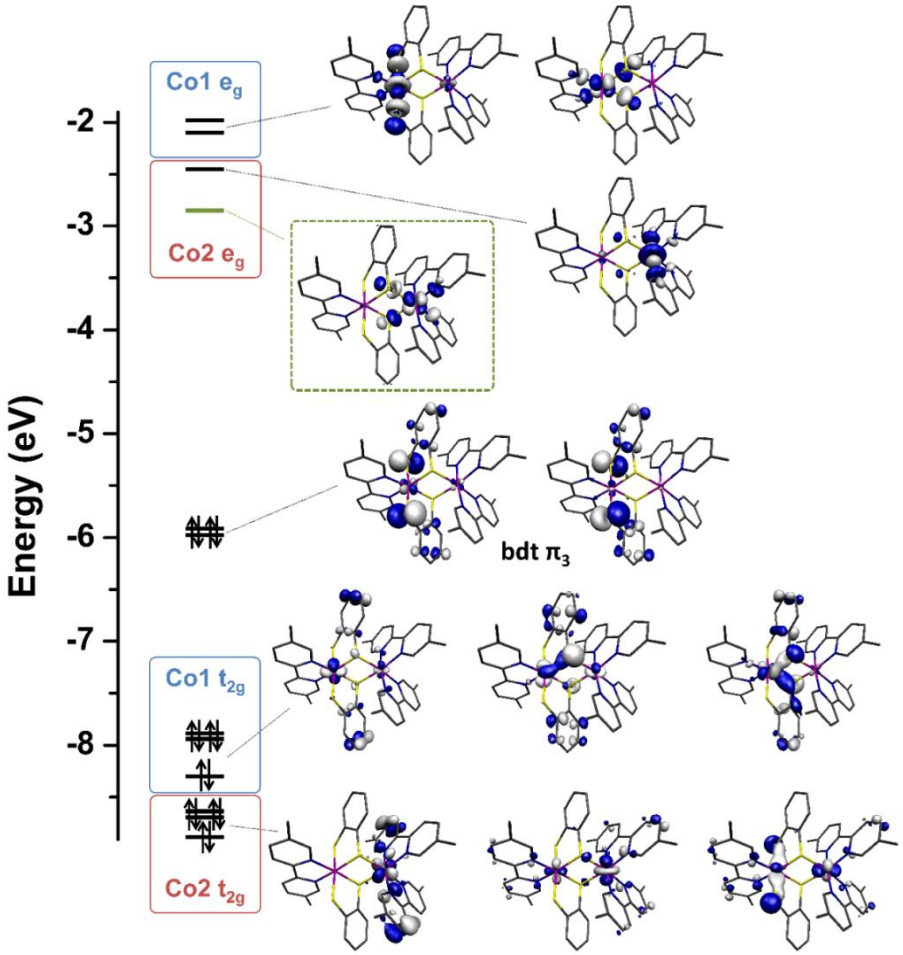

Figure 5.6: *Qualitative MO scheme depicting the ordering of the frontier orbitals for* $[\mathbf{1}]^{2+}$ *showing two low-spin* Co^{III} *ions, with the LUMO highlighted in the green dashed box. Reproduced from Eur. J. Inorg. Chem.* ***2017****, 3707 wih permission of John Wiley and sons. Copyright 2017.*

Complex $[\mathbf{24}]^{2+}$ exhibits a reversible one-electron reduction at −0.63 V (*vs.* ferrocenium/ferrocene), which was tentatively assigned as metal-centered on account of the mild potential relative to that typically observed for bpy ligands in homoleptic complexes.(31) This assignment is confirmed by these calculations. The geometry-optimized structure of the one-electron reduced species $[Co_2(bdt)_2(Me_2bpy)_3]^+$ (denoted $[\mathbf{24}]^+$) retained the ESBO connectivity (**Figure 5.7** and **Appendix B3**).

Complex $[\mathbf{24}]^+$ is a $Co^{III/II}$ mixed-valence complex where the singly-occupied orbital (SOMO) is the σ* MO of Co2. The low-spin $S = {}^1/_2$ solution is 12.8 kcal mol^{-1} more stable than the corresponding high-spin $S = {}^3/_2$ configuration of the Co^{II} ion, a consequence of the

relatively strong ligand field comprising bridging thiolate donors and π-accepting Me_2bpy ligands.

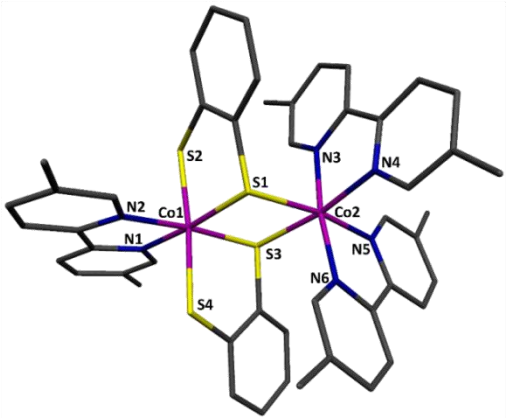

Figure 5.7: *Geometry optimized structure of $[Co^{III,III}_2(bdt)_2(Me_2bpy)_3]^{2+}$ Reproduced from Eur. J. Inorg. Chem.* ***2017****, 3707 wih permission of John Wiley and sons. Copyright 2017.*

The Mulliken spin population analysis confirms this compound as class I mixed-valency, given the inequivalence of the Co ions as defined by their respective first coordination spheres (**Figure 5.8**).[32] The reduction of Co2 to a low-spin d^7 ion gives rise to a Jahn-Teller distortion along what is defined as the *x*-axis, with the elongation of the Co2–S3 and Co2–N4 bond lengths by 0.44 Å and 0.11 Å, respectively (**Table 5.1**). The other bonds about Co2 are marginally shorter as expected for a distortion of this type, and those about Co1 remain unchanged. Further reduction of this complex to the neutral species is predicted to sever the Co2–S3 bond, giving square pyramidal and octahedral Co^{II} ions (possibly evinced by the irreversible reductive process at −1.4 V in the cyclic voltammogram in **Figure 5.4**).

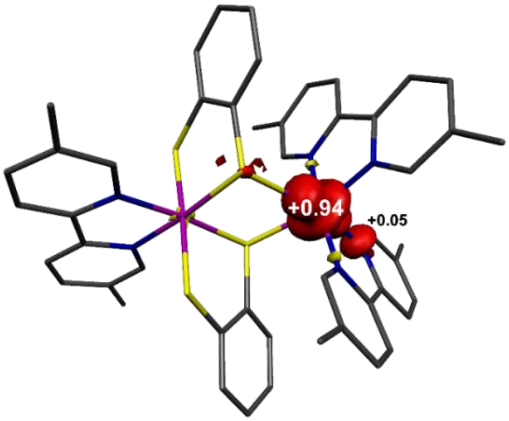

Figure 5.8: *Mulliken spin population analysis for* ***[1]***$^+$ *(red: α-spin; yellow: β-spin). Reproduced from Eur. J. Inorg. Chem.* ***2017****, 3707 wih permission of John Wiley and sons. Copyright 2017.*

The above calculations allow the electronic spectra of complex $[\mathbf{1}]^{2+}$ before and after one-electron reduction to be interpreted (see **Figure 5.9**). Hence the as-isolated dicobalt(III) form displays two low energy LMCT bands ascribed as S → Co2 at 776 nm (ε = 2200 M^{-1} cm^{-1}) and S → Co1 at 598 nm (ε = 2300 M^{-1} cm^{-1}).[12e,33] The latter is the characteristic band seen in many monometallic Co(III) complexes with sulfur donor ligands.[28] The shift to lower energy for the S → Co2 band stems from the stabilization of the e_g orbitals of Co2 by the two Me_2bpy ligands (**Figure 5.4**). After reduction by one electron, a new 'sharp' peak appears at *ca.* 650 nm, which is assigned as S → Co2 LMCT as previously reported in mixed-valence Co^{III}/Co^{II} species,[34] and which sits adjacent to the S → Co1 LMCT that is retained in the one-electron reduced complex.

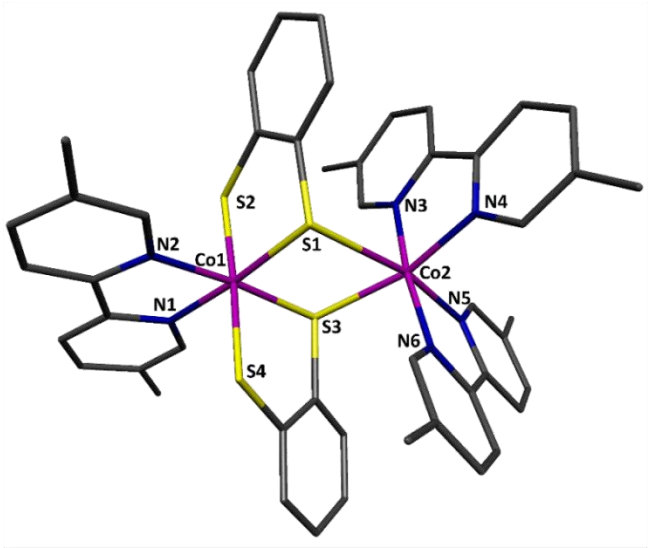

Figure 5.9: *Geometry optimized structure of* $[Co^{III,II}{}_2(bdt)_2(Me_2bpy)_3]^{1+}$. *Reproduced from Eur. J. Inorg. Chem.* ***2017****, 3707 wih permission of John Wiley and sons. Copyright 2017.*

5.3 Conclusions

In summary, we have presented the first known example of a mixed diimine/dithiolate dicobalt complex where the two cobalt centers are in dissimilar coordination environments (complex $[\mathbf{24}]^{2+}$). This complex was discovered coincidently during the synthesis of **21** detailed in **Chapter 4**. The structure of complex $[\mathbf{24}]^{2+}$ was determined by single crystal X-ray diffraction studies, whilst NMR and mass spectrometry data imply that this structure is maintained in solution. The different coordination environments around the two cobalt centers then cause these two centers to have differing redox activity, as shown by the experimental electrochemical analyses. Finally, DFT calculations on complex $[\mathbf{24}]^{2+}$ and its one-

electron reduced analog (complex [**24**]$^{+}$) help to rationalize the redox behavior observed by cyclic voltammetry, and show that the metal center coordinated to two diimine units is the easier of the centers to reduce, with subsequent reduction of the second cobalt center leading to irreversible decomposition of the complex.

5.4 Synthesis of $[Co^{III}_2(bdt)_2(Me_2bpy)_3](NO_3)_2$, [24](NO$_3$)$_2$

Compound [**24**](NO$_3$)$_2$ is obtained as a green microcrystalline solid following the procedure detailed in **Section 4.2.4** and **Section 4.4.4** for the synthesis of compound **21**. Product **24** obtained was carefully dried at 150 °C overnight to give a final anhydrous mass yield of 0.385 g (41%). Complex [**24**](NO$_3$)$_2$ is somewhat hygroscopic and hence absorbs water when exposed to laboratory air. Indeed, a sample of dry mass 364 mg was found to increase in mass by 25 mg after standing in air for 1 day (upon further standing the mass did not increase further). This corresponds to a mass-gain of around 6%, corresponding to around 3.5 molecules of H_2O per formula unit of [**24**](NO$_3$)$_2$.

CHN analysis was then performed on this hydrated sample: Anal. calcd. for $C_{48}H_{44}Co_2N_8O_6S_4\cdot(3.5H_2O)$: C 50.66, H 4.52, N 9.85. Found: C 50.61, H 4.40, N 10.35. Yields are calculated from the dry (anhydrous) mass.

^{13}C NMR (MeOD, 400 MHz), δ = 159.5, 156.0, 155.9, 155.0, 153.1, 151.7, 149.2, 143.2, 142.8, 141.2, 140.7, 138.7, 138.5, 132.7, 132.4, 130.6, 129.8, 125.4, 125.1, 124.8, 123.2, 19.5, 18.9, 18.6. IR (solid state, cm^{-1}) ν = 3041 (w), 1473 (w), 1432 (w), 1331 (s), 1236 (m), 825 (m), 734 (m). ESI-LMMS (methanol): *m/z* = 475.0508 [M]$^{2+}$ (calcd. for $C_{48}H_{44}Co_2N_6S_4$; 475.0587).

The full ^{1}H NMR spectrum of this compound is shown in **Figure 5.10.**

^{1}H NMR (MeOD, 400 MHz), δ = 10.34-10.32 (m, 2H, H_a or H_i or H_p), 8.44-8.40 (m, 2H, H_a or H_i or H_p), 8.38 (d, 2H, J = 8.2, H_d or H_l or H_m), 8.29 (d, 2H, J = 8.3, H_d or H_l or H_m), 8.08-8.03 (m, 2H, H_c or H_k or H_n), 8.02-7.91 (m, 6H, H_d or H_l or H_m and H_c and/or H_k and/or H_n), 7.38-7.34 (m, 2H, H_a or H_i or H_p), 6.92-6.86 (m, 2H, H_e or H_f or H_g or H_h), 6.60 (dd, 2H, J_1 = 8.0, J_2 = 0.8, H_e or H_f or H_g or H_h), 6.56-6.50 (m, 2H, H_e or H_f or H_g or H_h), 6.03 (dd, 2H, J_1 = 7.8, J_2 = 0.9, H_e or H_f or H_g or H_h), 2.67 (s, 6H, H_b or H_j or H_o), 2.29 (s, 6H, H_b or H_j or H_o), 2.26 (s, 6H, H_b or H_j or H_o).

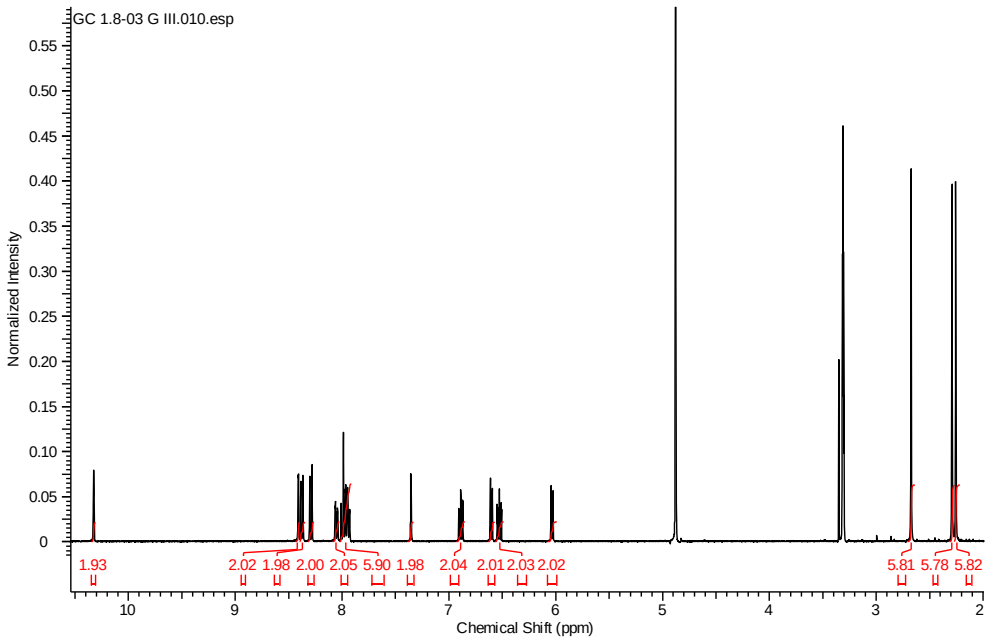

Figure 5.10: *^{1}H NMR full spectrum of compound [**24**]$^{2+}$ in MeOD. Reproduced from Eur. J. Inorg. Chem.* ***2017****, 3707 wih permission of John Wiley and sons. Copyright 2017.*

Assignments of signals to groups of protons are based on 2D (COSY) spectra and the expected coupling patterns of the peaks, although the symmetry of the molecule prevents unambiguous assignments. Letter codes correspond to those shown in **Figure 5.11** and **Scheme 5.1**.

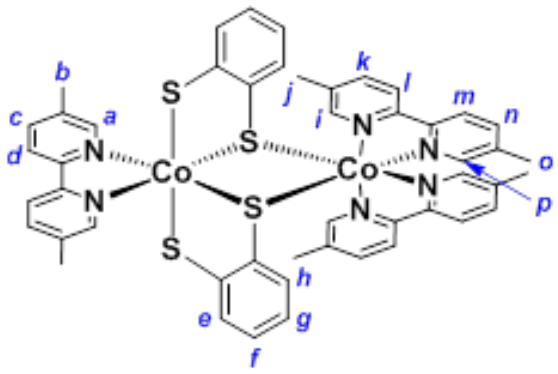

Figure 5.11: *Structure of compound* ***24****. Letters on the product structure correspond to the ^{1}H NMR signal assignments detailed in the text above. Readapted from Eur. J. Inorg. Chem.* ***2017****, 3707 wih permission of John Wiley and sons. Copyright 2017.*

5.5 References:

[1] T. R. Miller, I. G. Dance, *J. Am. Chem. Soc*. **1973**, 95, 6970.

[2] W. Paw, S. D. Cummings, M. A. Mansour, W. B. Connick, D. K. Geiger, R. Eisenberg, *Coord. Chem. Rev.* **1998**, 171, 125.

[3] C. A. Mitsopoulou, *Coord. Chem. Rev.* **2010**, 254, 1448.

[4] Dithiolene Chemistry: Synthesis, Properties, and Applications, E. I. Stiefel (Ed.), Prog. *Inorg. Chem*. **2003**, 52, 1.

[5] R. Sakamoto, S. Tsukada, H. Nishihara, *Dalton Trans*. **2012**, 41, 10123.

[6] M. L. Mercuri, P. Deplano, L. Pilia, A. Serpe, F. Artizzu, *Coord. Chem. Rev*. **2010**, 254, 1419.

[7] S. Friedle, D. V. Partyka, M. V. Bennett, R. H. Holm, *Inorg. Chim. Acta* **2006**, 359, 1427.

[8] (a) C.-H. Lin, C.-G. Chen, M.-L. Tsai, G.-H. Lee, W.-F. Liaw, *Inorg. Chem*. **2008**, 47, 11435; (b) H. Tamura, S. Tanaka, G. Matsubayashi, W. Mori, *Inorg. Chim. Acta* **1995**, 232, 51.

[9] (a) H. Alves, D. Simão, H. Novais, I. C. Santos, C. Giménez-Saiz, V. Gama, J. C. Waerenborgh, R. T. Henriques, M. Almeida, *Polyhedron* **2003**, 22, 2481; (b) K. Awaga, T. Okuno, Y. Maruyama, A. Kobayashi, H. Kobayashi, S. Schenk, A. E. Underhill, *Inorg. Chem.* **1994**, 33, 5598; (c) S. Benmansour, D. Delgado, C. J. Gómez-García, D. Hernández, E. Hernández, A. Martin, J. Perles, F. Zamora, *Inorg. Chem.* **2015**, 54, 2243; (d) S. Bruña, I. Cuadrado, D. Delgado, C. J. Gómez-García, D. Hernández, E. Hernández, R. Llusar, A. Martín, N. Menéndez, V. Polo, F. Zamora, *Dalton Trans.* **2014**, 43, 13187; (e) O. Castillo, E. Delgado, D. Hernández, E. Hernández, A. Martin, I. Martín, F. Zamora, *Cryst. Growth Des.* **2016**, 16, 5466; (f) A. C. Cerdeira, D. Belo, S. Rabaça, L. C. J. Pereira, J. T. Coutinho, D. Simão, R. T. Henriques, O. Jeannin, M. Fourmigué, M. Almeida, *Eur. J. Inorg. Chem.* **2013**, 4612; (g) A. C. Cerdeira, D. Simão, I. C. Santos, A. Machado, L. C. J. Pereira, J. C. Waerenborgh, R. T. Henriques, M. Almeida, *Inorg. Chim. Acta* **2008**, 361, 3836; (h) M. Fettouhi, A. Waheed, S. Golhen, N. Helou, L. Ouahab, P. Molinie, *Synth. Met.* **1999**, 102, 1764; (i) F. E. Hahn, T. Eiting, W. W. Seidel, T. Pape, *Eur. J. Inorg. Chem.* **2010**, 2393; (j) W. C. Hamilton, I. Bernal, *Inorg. Chem.* **1967**, 6, 2003; (k) U. Jayarathne, K. Williams, V. M. Kasyanenko, J. T. Mague, I. V. Rubtsov, J. P. Donahue, *Polyhedron* **2012**, 31, 98; (l) M. G. Kanatzidis, D. Coucouvanis, *Inorg. Chem*. **1984**, 23, 403; (m) B. S. Kang, L. H. Weng, D. X. Wu, F. Wang, Z. Guo, L. R. Huang, Z. Y. Huang, H. Q. Liu, *Inorg. Chem*. **1988**, 27, 1128; (n) H. Lv, T. P. A. Ruberu, V. E. Fleischauer, W. W. Brennessel, M. L. Neidig, R. Eisenberg, *J. Am.*

Chem. Soc. **2016**, 138, 11654; (o) A. I. S. Neves, I. C. Santos, D. Belo, M. Almeida, *Cryst. Eng. Comm*. **2009**, 11, 1046; (p) A. K. Patra, E. Bill, T. Weyhermüller, K. Stobie, Z. Bell, M. D. Ward, J. A. Mccleverty, K. Wieghardt, *Inorg. Chem*. **2006**, 45, 6541.

[10] (a) L. Pilia, C. Faulmann, I. Malfant, V. Collière, M. L. Mercuri, P. Deplano, P. Cassoux, *Acta Crystallogr., Sect. C: Cryst. Struct. Commun.* **2002**, 58, m240; (b) K. Ray, E. Bill, T. Weyhermüller, K. Wieghardt, *J. Am. Chem. Soc.* **2005**, 127, 5641; (c) X. Ren, P. Wu, W. Zhang, Q. Meng, X. Chen, *Transition Met. Chem.* **2002**, 27, 394; (d) D. T. Sawyer, G. S. Srivatsa, M. E. Bodini, W. P. Schaefer, R. M. Wing, *J. Am. Chem. Soc.* **1986**, 108, 936; (e) A. J. Schultz, R. Eisenberg, *Inorg. Chem.* **1973**, 12, 518; (f) D. Simão, J. A. Ayllon, S. Rabaça, M. J. Figueira, I. C. Santos, R. T. Henriques, M. Almeida, *Cryst. Eng. Comm.* **2006**, 8, 658; (g) S. Tanaka, G. Matsubayashi, *J. Chem. Soc., Dalton Trans*. **1992**, 2837; (h) T. Yamaguchi, S. Masaoka, K. Sakai, *Acta Crystallogr., Sect. E: Struct. Rep. Online* **2008**, 64, m1557; (i) T. Yamaguchi, S. Masaoka, K. Sakai, *Acta Crystallogr., Sect. E: Struct. Rep.* Online **2009**, 65, m77; (j) B. Zhou, S. Ogura, N. Kato, Y. Idobata, A. Kobayashi, H. Kobayashi, *Chem. Lett.* **2013**, 42, 977.

[11] (a) D. Bellamy, N. G. Connelly, G. R. Lewis, A. G. Orpen, *Cryst. Eng. Comm*. **2002**, 4, 51; (b) M. Fettouhi, L. Ouahab, M. Hagiwara, E. Codjovi, O. Kahn, H. Constant-Machado, F. Varret, *Inorg. Chem.* **1995**, 34, 4152; (c) J. V. Rodrigues, I. C. Santos, V. Gama, R. T. Henriques, J. C. Waerenborgh, M. T. Duarte, M. Almeida, *J. Chem. Soc., Dalton Trans.* **1994**, 2655; (d) R. Yu, K. Arumugam, A. Manepalli, Y. Tran, R. Schmehl, H. Jacobsen, J. P. Donahue, *Inorg. Chem.* **2007**, 46, 5131.

[12] (a) H. Alves, D. Simão, I. C. Santos, V. Gama, R. T. Henriques, H. Novais, M. Almeida, *Eur. J. Inorg. Chem.* **2004**, 1318; (b) M. J. Baker-Hawkes, Z. Dori, R. Eisenberg, H. B. Gray, *J. Am. Chem. Soc.* **1968**, 90, 4253; (c) E. E. Eduok, M. Krawiec, Y.-S. L. Buisson, C. J. O'Conner, D. Sun, W. H. Watson, *J. Chem. Cryst.* **1996**, 26, 621; (d) J. H. Enemark, W. N. Lipscomb, *Inorg. Chem.* **1965**, 4, 1729; (e) T. Fogeron, J.-P. Porcher, M. Gomez-Mingot, T. K. Todorova, L.-M. Chamoreau, C. Mellot-Draznieks, Y. Li, M. Fontecave, *Dalton Trans.* **2016**, 45, 14754; (f) E. Fujiwara, K. Hosoya, A. Kobayashi, H. Tanaka, M. Tokumoto, Y. Okano, H. Fujiwara, H. Kobayashi,

Y. Fujishiro, E. Nishibori, M. Takata, M. Sakata, *Inorg. Chem.* **2008**, 47, 863; (g) V. Gama, R. T. Henriques, M. Almeida, L. Veiros, M. J. Calhorda, A. Meetsma, J. L. de Boer, *Inorg. Chem.* **1993**, 32, 3705; (h) C. S. Letko, J. A. Panetier, M. Head-Gordon, T. D. Tilley, *J. Am. Chem. Soc.* **2014**, 136, 9364; (i) G. R. Lewis, I. Dance, *J. Chem. Soc., Dalton Trans.* **2000**, 3176; (j) T. Mochida, K. Takazawa, H. Matsui, M. Takahashi, M. Takeda, M. Sato, Y. Nishio, K. Kajita, H. Mori, *Inorg. Chem.* **2005**, 44, 8628; (k) T. Mochida, K. Takazawa, M. M. Matsushita, T. Sugawara, *Acta Crystallogr., Sect.C: Cryst. Struct. Commun.* **2002**, 58, m431; (l) R. A. L. Silva, I. C. Santos, E. B. Lopes, S. Rabaça, S. Galindo, M. Mas-Torrent, C. Rovira, M. Almeida, D. Belo, *Eur. J. Inorg. Chem*. **2015**, 5003; (m) H. Tanaka, H. Kobayashi, A. Kobayashi, *Synth. Met*. **2003**, 135, 549; (n) J. H. Welch, R. D. Bereman, P. Singh, C. Moreland, *Inorg. Chim. Acta* **1989**, 158, 17; (o) S. Zurcher, B. Gramlich, D. Von Arx, A. Togni, *Inorg. Chem.* **1998,** 37, 4015.

[13] X.-X. Chen, F. Qiao, C.-F. Wang, Y.-H. Chi, E. Cottrill, N. Pan, J.-M. Shi, W.-W. Zhu-Ge, Y.-X. Fu, J. Xu, X.-P. Qian, *J. Mol. Struct.* **2016**, 1107, 157.

[14] a) E. B. Lopes, H. Alves, I. C. Santos, D. Graf, J. S. Brooks, E. Canadell, M. Almeida, *J. Mater. Chem.* **2008**, 18, 2825; (b) D. Simão, H. Alves, D. Belo, S. Rabaça, E. B. Lopes, I. C. Santos, V. Gama, M. T. Duarte, R. T. Henriques, H. Novais, M. Almeida, *Eur. J. Inorg. Chem*. **2001**, 3119; (c) S. Takaishi, M. Hada, N. Ishihara, B. K. Breedlove, K. Katoh, M. Yamashita, *Polyhedron* **2013**, 52, 333.

[15] (a) G. Matsubayashi, T. Maikawa, H. Tamura, M. Nakano, R. Arakawa, *J. Chem. Soc., Dalton Trans*. **1996**, 1539; (b) T. J. Morsing, S. N. Macmillan, J. W. H. Uebler, T. Brock-Nannestad, J. Bendix, K. M. Lancaster, *Inorg.Chem*. **2015**, 54, 3660; (c) Y. Yan, J. T. Mague, J. P. Donahue, S. Sproules, *Chem. Commun*. **2015**, 51, 5482.

[16] (a) H. Adams, M. J. Morris, A. E. Riddiough, L. J. Yellowlees, A. B. P. Lever, *Inorg. Chem*. **2007**, 46, 9790; (b) M.-J. Don, K. Yang, S. G. Bott, M. G. Richmond, *J. Organomet. Chem.* **1997**, 544, 15; (c) K. Kawabata, M. Nakano, H. Tamura, G. Matsubayashi, *J. Organomet. Chem*. **2004**, 689, 405; (d) D. H. Kim, J.-H. Kim, T. H. Kim, D. M. Kang, Y. H. Kim, Y.-B. Shim, S. C. Shin, *Chem. Mater*. **2003**, 15, 825; (e) J.-J. Liu, Y.-J. Lin, G.-X. Jin, *Dalton Trans*. **2015**, 44, 10281; (f) E. J. Miller, T. B. Brill, A. L. Rheingold,

W. C. Fultz, *J. Am. Chem. Soc*. **1983**, 105, 7580; (g) W. K. Miller, R. C. Haltiwanger, M. C. Vanderveer, M. Rakowski Dubois, *Inorg. Chem*. **1983**, 22, 2973; (h) M. Nomura, T. Sasao, T. Hashimoto, T. Sugiyama, M. Kajitani, *Inorg. Chim. Acta* **2010**, 363, 3647; (i) M. Nomura, E. Tsukano, C. Fujita-Takayama, T. Sugiyama, M. Kajitani, J. *Organomet. Chem*. **2009**, 694, 3116; (j) O. A. Rajan, M. McKenna, J. Noordik, R. C. Haltiwanger, M. Rakowski Dubois, *Organometallics* 1984, 3, 831; (k) K. Roesselet, K. E. Doan, S. D. Johnson, P. Nicholls, G. L. Miessler, R. Kroeker, S. H. Wheeler, *Organometallics* **1987**, 6, 480; (l) D. W. Stephan, *Inorg. Chem.* **1992**, 31, 4218; (m) K. Sukcharoenphon, T. D. Ju, K. A. Abboud, C. D. Hoff, *Inorg. Chem*. **2002**, 41, 6769; (n) R. T. Weberg, R. C. Haltiwanger, M. Rakowski Dubois, *Organometallics* **1988**, 4, 1315; (o) R. Xi, M. Abe, T. Suzuki, T. Nishioka, K. Isobe, *J. Organomet. Chem*. **1997**, 549, 117; (p) R. Ziessel, M.-T. Youinou, F. Balegroune, D. Grandjean, *J. Organomet. Chem*. **1992**, 441, 143.

[17] T. M. Cocker, R. E. Bachman, *Chem. Commun.* **1999**, 875.

[18] K. Halvorsen, G. A. Crosby, W. F. Wacholtz, *Inorg. Chim. Acta* **1995**, 228, 81.

[19] D. M. Hatch, W. F. Wacholtz, J. T. Mague, *J. Chem. Crystallogr.* **2005**, 35, 327.

[20] A.-X. Zheng, J. Si, X.-Y. Tang, L.-L. Miao, M. Yu, K.-P. Hou, F. Wang, H.-X. Li, J.-P. Lang, *Inorg. Chem.* **2012**, 51, 10262.

[21] (a) A. R. Hendrickson, R. L. Martin, *J. Chem. Soc., Dalton Trans*. **1975**, 2182; (b) B. W. Smucker, M. J. Vanstipdonk, D. M. Eichhorn, *J. Inorg. Biochem.* **2007**, 101, 1537; (c) T. Suzuki, H. D. Takagi, K. Kashiwabara, *Acta Crystallogr., Sect. C: Cryst. Struct. Commun.* **2002**, 58, m95.

[22] (a) T. C. Higgs, D. Ji, R. S. Czernuszewicz, K. Spartalian, C. J. O'Connor, C. Seip, C. J. Carrano, *J. Chem. Soc., Dalton Trans*. **1999**, 807; (b) R. J. Pleus, H. Waden, W. Saak, D. Haase, S. Pohl, *J. Chem. Soc., Dalton Trans*. **1999**, 2601.

[23] T. Konno, K.-i. Okamoto, *Chem. Lett*. **1995**, 24, 675.

[24] (a) C. Cappelli, C. Duce, M. Formica, V. Fusi, L. Ghezzi, L. Giorgi, M. Micheloni, P. Paoli, P. Rossi, M. R. Tiné, *Inorg. Chim. Acta* **2014**, 417, 230; (b) M.-Q. Chen, J.-J. Liu, Z.-W. Mao, Q.-W. Hang, W.-X. Tang, *Acta*

Crystallogr., Sect. C: Cryst. Struct. Commun. **1995**, 51, 1080; (c) K. Hamada, E. Ohta, T. Fujiwara, T. Ama, *Bull. Chem. Soc. Jpn.* **1989**, 62, 1328; (d) T. Ishizuka, A. Watanabe, H. Kotani, D. Hong, K. Satonaka, T. Wada, Y. Shiota, K. Yoshizawa, K. Ohara, K. Yamaguchi, S. Kato, S. Fukuzumi, T. Kojima, *Inorg. Chem.* **2016**, 55, 1154; (e) J. Qian, X. Ma, W. Gu, J. Shang, X. Liu, S. Yan, *J. Inorg. Biochem.* **2010**, 104, 993; (f) D. Schweinfurth, J. Klein, S. Hohloch, S. Dechert, S. Demeshko, F. Meyer, B. Sarkar, *Dalton Trans.* **2013**, 42, 6944; (g) U. Thewalt, M. Zehnder, *Helv. Chim. Acta* **1977**, 60, 2000; (h) K. Wieghardt, W. Schmidt, B. Nuber, J. Weiss, *Chem. Ber*. **1979**, 112, 2220.

[25] (a) F. Sama, I. A. Ansari, M. Raizada, M. Ahmad, C. M. Nagaraja, M. Shahid, A. Kumar, K. Khan, Z. A. Siddiqi, *New J. Chem.* **2017**, 41, 1959; (b) J. Welby, L. N. Ruserem, J. M. Tanski, L. A. Tyler, *Inorg. Chim. Acta* **2009**, 362, 1405.

[26] A. Panja, P. Guionneau, *Dalton Trans.* **2013**, 42, 5068.

[27] (a) N. W. Alcock, I. I. Creaser, N. J. Curtis, L. Roecker, A. M. Sargeson, A. C. Wills, Aust. *J. Chem.* **1990**, 43, 643; (b) U. Thewalt, R. E. Marsh, *Inorg. Chem.* **1971**, 10, 1789.

[28] G. Cioncoloni, H. M. Senn, S. Sproules, C. Wilson, M. D. Symes, *Dalton Trans.* **2016**, 45, 15575.

[29] T. Saji, S. Aoyagui, *J. Electroanal. Chem.* **1975**, 60, 1.

[30] (a) S. Sproules, *Prog. Inorg. Chem*. **2014**, 58, 1; (b) S. Sproules, K. Wieghardt, *Coord. Chem. Rev.* **2011**, 255, 837.

[31] (a) C. C. Scarborough, S. Sproules, T. Weyhermüller, S. DeBeer, K. Wieghardt, *Inorg. Chem*. **2011**, 50, 12446; (b) J. England, C. C. Scarborough, T. Weyhermüller, S. Sproules, K. Wieghardt, *Eur. J. Inorg. Chem.* **2012**, 4065; (c) A. C. Bowman, S. Sproules, K. Wieghardt, *Inorg. Chem.* **2011**, 50, 3707.

[32] M. B. Robin, P. Day, *Adv. Inorg. Chem. Radiochem.* **1967,** 10, 247.

[33] P. Chakraborty, S. K. Chandra, A. Chakravorty, *Inorg. Chem.* **1994**, 33, 4959.

[34] D. Bonnet, P. Leduc, E. Bill, G. Chottard, D. Mansuy, I. Artaud, *Eur. J. Inorg. Chem*. **2001**, 1449.

Exploiting sonication to fix nitrogen

Acknowledgments and declaration

The project covered in this chapter is in partnership with the Cavlab in the school of Engineering at the University of Glasgow. I would like to thank Dr. Paul Prentice and Dr. Jae Hae Song for the availability, preparation of the set-up of acoustic instruments and for all the acoustic measurements.

Synopsis

It is known that irradiation of water saturated with air with ultrasound leads to the formation of nitrate and especially nitrite in the liquid, via a phenomenon called cavitation. In this chapter is investigated the cavitation phenomenon and how to exploit different sources of cavitation in order to magnify the yield of NO_x. A more promising pathway to increase the yield of nitrogen fixation via cavitation involves pulsed irradiation with high frequency ultrasound. The study of different parameters involved as for example frequency and amplitude of ultradound applied and the interval between pulses allows us to obtain an improvement in the process since the yield we obtained is one order of magnitude bigger than in the previous work, although it is still too low compared to other methods commonly used to fix nitrogen at a larger scale.

6.1 Nitrogen fixation via cavitation

As introduced already in **Chapter 1** nitrogen can be fixed thermally by energetically violent processes that require large energies. This is in fact what happens in presence of lightning and explosions where the energy is high enough to allow the breakage of the strong triple bond in the dinitrogen molecule. Under these conditions dinitrogen is broken to give two atoms of radical nitrogen, that (as with all radical species) are so reactive that they will react very rapidly with other species to give more stable products. This phenomenon was exploited by Birkeland and Eyde but as already presented in **Chapter 1** it was uneconomical and energetically non sustainable.(1)

The process happening in the atmosphere during a lightning strike is described by a mechanism introduced for the study of weapons explosions by Yakov Zeldovich in 1946 and can be summarised in two basic steps as per **Scheme 6.1.** The first step is the generation of nitric oxide via reaction of atomic nitrogen with an atomic diradical oxygen atom generated in the same way. The second step is the radical propagation of the reaction, where the nitric oxide generated reacts with other species present in order to give as the final product nitrogen oxides (NO_x)(2)

First step:

$$^{\cdot}O^{\cdot} + N_2 \rightarrow {}^{\cdot}NO + {}^{\cdot}N$$

$$^{\cdot}N + O_2 \rightarrow {}^{\cdot}NO + {}^{\cdot}O^{\cdot}$$

Second step:

$$^{\cdot}NO + {}^{\cdot}O^{\cdot} \rightarrow NO_2^{\cdot}$$

$$2\ {}^{\cdot}NO + O_2 \rightarrow 2NO_2^{\cdot}$$

$$2NO_2^{\cdot} + H_2O \rightarrow HNO_3 + HNO_2$$

$$NO_2^{\cdot} + {}^{\cdot}OH \rightarrow HNO_3$$

$$^{\cdot}NO + NO_2^{\cdot} \rightarrow N_2O_3$$

$$N_2O_3 + H_2O \rightarrow 2HNO_2$$

Scheme 6.1 *Summary of the reactions involved in the Zeldovich mechanism*

Since this thermal approach is hard to implement in a conventional reactor in a sustainable and environmentally friendly manner capitalising on the famous quotation from Richard Feynman ("There's Plenty of Room at the Bottom"), it is possible to exploit an approach that allows us to have billions of micrometric explosions each leading to a pressure gradient comparable with an atomic explosion. This phenomenon is called cavitation. Cavitation is an interesting input of energy to a reaction medium and is studied because it is useful for generating high temperatures and pressures under otherwise ambient conditions. This is very useful for facilitating chemical processes. The possibility to exploit this phenomenon stems from the fact that millions of cavities (bubbles) in liquid grow and collapse simultaneously in the liquid medium when irradiated with ultrasound.

In 1936 Schultes and Gohr recognised that irradiation of air-saturated water with ultrasound leads to formation of nitrite and nitrate.[3] Ultrasound is inaudible sound and its frequency of oscillation is above 20 kHz (20,000 oscillations per second)[4].

When a liquid is irradiated with these frequencies we have the formation and collapse of bubbles from the gas dissolved in the liquid. The whole process of nucleation, growth and collapse of cavities happens on a timescale of few microseconds. The temperature and pressure inside the bubbles increases to thousands of Kelvin and thousands of bars, respectively with the consequence that water vapour, nitrogen, oxygen and other gaseous species, if present, are dissociated inside a bubble and oxidants such as $^{\cdot}OH$, $O^{\cdot}$, and H_2O_2 are produced, in a sonochemical reaction.[5] When the pressure amplitude of an acoustic wave in a liquid or solid exceeds the atmospheric pressure, during the rarefaction phase of an acoustic wave the instantaneous pressure, defined as the force acting on the surface of a liquid element per surface area to expand the element, becomes negative.[6,7] **Figure 6.1** describes graphically what happens during this process.

When the instantaneous local pressure becomes negative in a liquid irradiated by ultrasound, the formation of bubbles is observed since gas dissolved in the liquid can no longer remain dissolved in the liquid under negative pressure. This phenomenon takes the name of acoustic cavitation. [8,9] Indeed, in static conditions, generation of vapour bubbles occurs when the static pressure becomes lower than the saturated vapour pressure, giving rise to the boiling phenomenon.

A bubble generated when ultrasound is applied expands during the rarefaction phase (negative pressure) and collapses during the compression phase. The speed of the bubble

collapse increases and reaches the speed of sound in liquid. Accordingly, the bubble collapse is a quasi-adiabatic process where "quasi" means that considerable thermal conduction takes place between the interior of a bubble and the surrounding liquid. The temperature and pressure inside a bubble increase to thousands of Kelvin (between 2000 and 5000 K) and thousands of bars, respectively at the end of the bubble collapse.[10] Moreover, a collapsing bubble emits a shock wave into the surrounding liquid just after the end of the bubble collapse.[11-14] The magnitude of the shockwave is estimated to be of the order of the order of several thousands of atmospheres, comparable with the shockwave released during a nuclear explosion

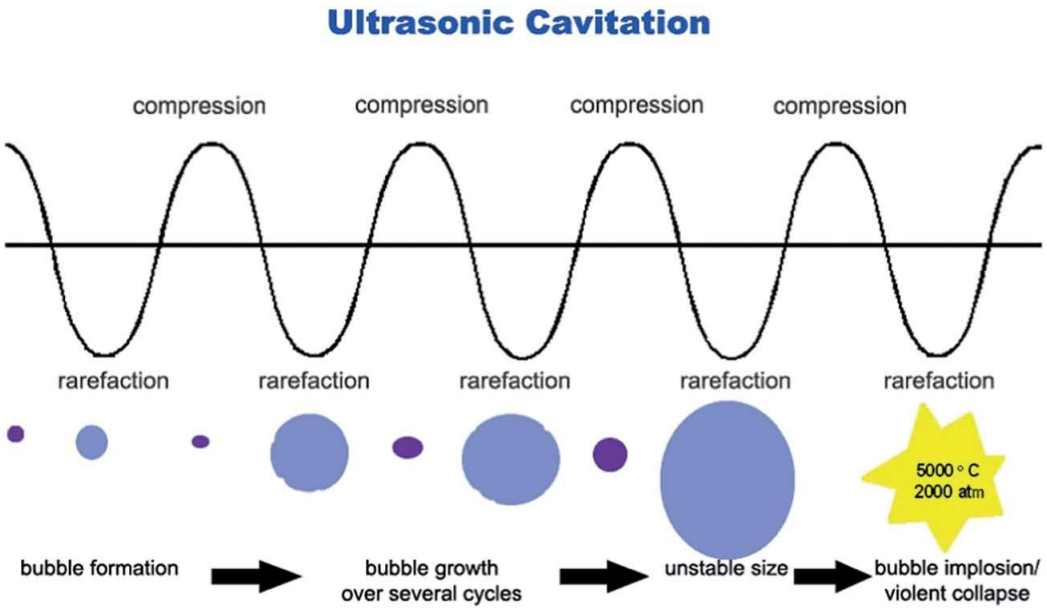

Figure 6.1: *Scheme for the formation and collapse of a bubble following the application of ultrasounds. Adapted from RSC Adv.,* ***2015****, 5, 48281 with permission from the Centre National de la Recherche Scientifique (CNRS) and The Royal Society of Chemistry.*

There are three mechanisms explaining the nucleation of a bubble in the presence of applied ultrasound.[15] The first one takes into account the nucleation occurring at the surface of solids such as a liquid container or, if present, in particles dispersed in the liquid. Nucleation occurs preferentially at crevices because the surface of a gas pocket is concave and the surface tension of a gas pocket reduces the pressure inside the pocket. This fact means that a gas pocket is stabilized against dissolution into the liquid because the partial pressure of dissolved gas in the liquid can be higher than that in a gas pocket. The second mechanism for nucleation involves the initially-present bubble nuclei, stabilized against dissolution. Without surfactants, a bubble with radius smaller than 1 mm should dissolve within a few seconds in the absence of ultrasound unless the liquid is supersaturated with

gas.[16] The third mechanism for nucleation involves the fragmentation of active cavitation bubbles.[17] A shape-unstable bubble is fragmented into several daughter bubbles which can act as new nuclei for cavitation bubbles. An asymmetric acoustic environment promotes the shape-instability of a bubble.[18-20] This mechanism becomes important after acoustic cavitation is fully started and gives a significant contribution in the experiments carried out with a pulsed ultrasound source. From **Figure 6.2** it is possible to distinguish three sites where a chemical reaction may take place[21]. The first one is the interior of a bubble, then there is is the interfacial region between the liquid and the bubble surface and the third one is represented by the liquid region outside the interface.

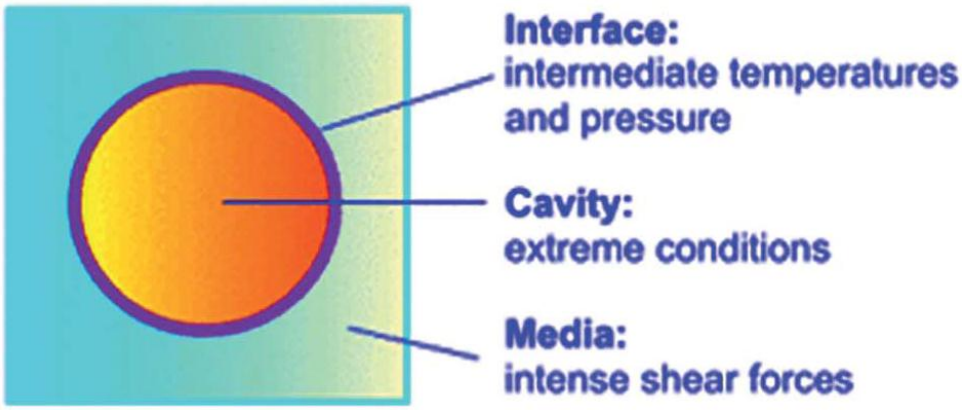

Figure 6.2: *Three sites for chemical reactions for a cavitation bubble. Adapted from RSC Adv.* ***2015****, 5, 48281 with permission from the Centre National de la Recherche Scientifique (CNRS) and The Royal Society of Chemistry.*

The liquid region is at room temperature and species with a relatively long lifetime diffuse out of the interface region and react with solutes.

In the interface region, the temperature increases dramatically due to the thermal conduction from the interior of a bubble where the temperature of thousands of degrees cause formation of radicals with a relatively short lifetime such as ·OH and ·O that react with solutes or themselves. However, the actual temperature in the interface region is not known even though some researchers have tried to estimate it.[22]

6.2 Experimental

In all the measurements ultrapure deionised water (18.2 MΩ cm resistivity) was used, obtained from a Sartorius Arium Comfort combined water system. The detection of nitrite produced during the reaction was done exploiting a variation of the Griess test [23] that

allows us to detect trace nitrite with a detection limit of about $5*10^{-7}$mol/L and based on the reaction schematized in **Figure 6.3:**

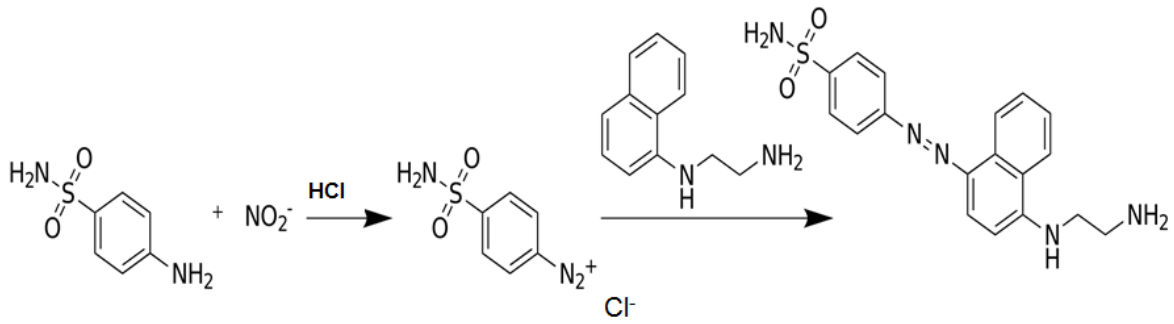

Figure 6.3: *The Diazotation reaction exploited to quantify nitrite produced sonochemically.*

For the continuous sonication input experiment, the set up consists of a 250mL beaker filled with 100 mL of ultrapure water and saturated with air via bubbling with compressed air for a period of 20 minutes. Two methods were used: the first way consisted of a cannula immersed in the liquid, the second in a fine-bubbles diffuser immersed into the liquid and directly connected with the compressed air source.

For the pulsed sonication input experiment, the reactor setup consists of a cylinder of borosilicate glass with 1 cm of diameter and about 5 cm of length. On the bottom it presents a sintering glass septum where the compressed air coming from a cylinder passes through it and is flushed inside the liquid as small bubbles. The reactor is filled with 3mL of ultrapure water and saturated with compressed air for 2 minutes before starting the sonication, and immersed in a tank of ultrapure degassed water where ultrasound is focused inside the cylinder. A schematic representation of the experimental setting is shown in **Figure 6.4**.

The remaining experimental arrangement consists of a long working distance microscope objective lens (50 × 0.42 NA Mitutoyo Kawasaki Japan) and a HIFU (High intensity focused ultrasounds) transducer, are arranged within a custom built chamber measuring 420x438x220mm^3, such that the optical and acoustic foci are aligned. The chamber has two recessed walls to allow the placement of an imaging optic (Monozoom 7 lens system, Bausch and Lomb, Rochester USA) in closer proximity to the combined foci, and filled with degassed deionized water.

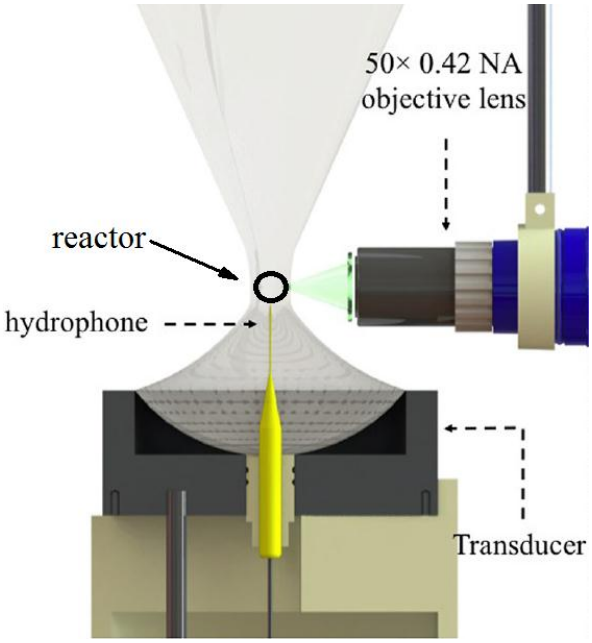

Figure 6.4: *Scheme of the experimental set-up for the experiment with pulsed irradiation with ultrasound. Repreoduced from J. Acoust. Soc. Am.* ***2016****, 140 with the permission of the editor.*

Bubble activity is imaged with a Shimadzu HPV-X2 (Shimadzu Corp, Kyoto, Japan) high-speed camera, at 1×10^6 frames per second, and with 10 ns synchronous laser pulses (CAVILUX Smart, Cavitar, Tampere, Finland), providing the illumination and shadowgraphic capability for shock wave visualisation.

The HIFU transducer operates at a fundamental frequency of f_0 = 220 kHz and is geometrically focused to 68 mm, with an outer diameter of 110 mm and a 20 mm central hole through the body. The Y107 PCD is geometrically focused to 68 mm, and designed for insertion within the hole through the transducer.

For the various testing with pulsed frequency input, the swPCD occupied the hole through the transducer, with Y-107 and the calibrated needle hydrophone (Complex calibration bandwidth is 125 kHz – 20 MHz, 1.0 mm diameter, PVdF, Precision Acoustics, Dorchester, UK) arranged orthogonally to the axis of HIFU propagation, mounted on an xyz-manipulator and positioned 68± 1mm from the bubble activity. [25-26]

6.3 Sonochemical reactions with continuous irradiation with ultrasound

Sonication of water saturated with compressed air gives nitrite as the main product and a lower amount nitrate. The reaction will follow the mechanism proposed by Zeldovich [2] for combustion in the atmosphere (shown in **Scheme 6.1**). During our investigations, it was

found that the saturation level of the solution was relevant in order to maximise the yield of the reaction. In fact where the solution was exposed to air it was possible to see a better yield than in the absence of preliminary bubbling of air before starting sonication experiments. Results obtained using a frequency of 35 kHz, were in good agreement with literature for a saturated solution.[27] On the basis of what was introduced in the previous section, cavities are formed preferentially close to surface defects (**Figure 6.2**). In order to exploit this factor, and also in order to maximise the contribution coming from the hydrodynamic cavitation [28, 29] instead of using a single injector of air we tried to exploit a fine bubbles diffuser, in order to increase the surface in contact with the solution and also to exploit the effect of the hydrodynamic cavitation due to the high number of holes in the diffuser. This is explained in **Figure 6.5**.

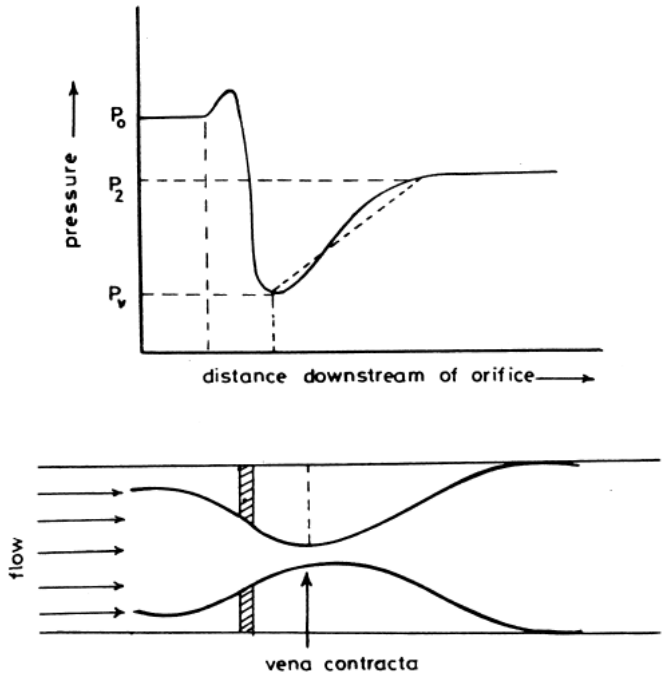

Figure 6.5: *Graph of the pressure for a flowing liquid close to an orifice [29]. The rapid change of pressure causes the generation of cavitation phenomena. Reproduced from Ultrasonics Sonochemistry 6 (**1999**) 53, 3707 wih permission of Elsevier. Copyright 1999.*

The difficulties related to the cleaning of the diffuser have hitherto prevented the study of saline saturated solutions but are planned in the future. As shown in **Figure 6.6 right** the nitrite concentration is about 3 times bigger than in the previous case and in literature.

A study involving control of the temperature showed that at lower temperatures the yield of NO_2^- increases. Systematic studies are ongoing to see the influence of the temperature and also to see the effect of various salts on the nitrite yield. These intriguing results led us

to continue to investigate this phenomenon and to start collaboration with the Cavlab in the school of Engineering at University of Glasgow.

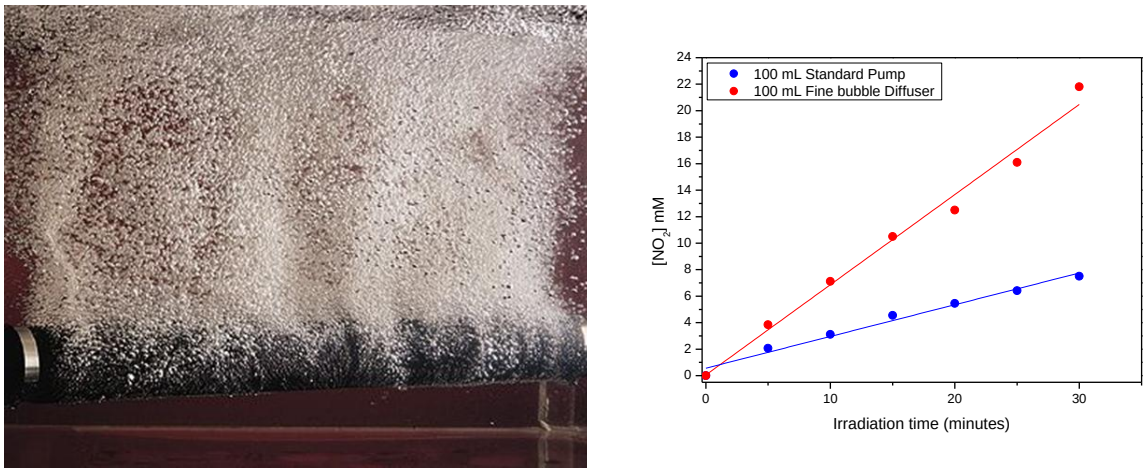

***Figure 6.6**: On the **left** side a Fine bubbler diffurser working, on the **right** side comparison between [NO_2^-] trend vs time for the synthesis of NO_2^- in 100 mL of H_2O using a fine bubbler diffuser (red) and using the previous pump (blue)*

6.4 Sonochemical reaction with pulsed irradiation of ultrasound

Since it was realised that saturation of the liquid with air was one of the limiting factors, another mode of sonication was investigated: instead of irradiating with continuous ultrasound, we irradiated the solution with small pulses of ultrasound followed by variable intervals of quiet time in order to allow the gas to diffuse again into the liquid medium. The scheme of the experiment including the important parameters is shown in **Figure 6.7**.

Pulse duration is the interval of time over which the ultrasound is applied, pulse interval is the interval of time when no ultrasound is applied and no cavitation phenomena are observed in the liquid medium. Amplitude of pulse is representative of the applied ultrasound energy and is measured in Pa.

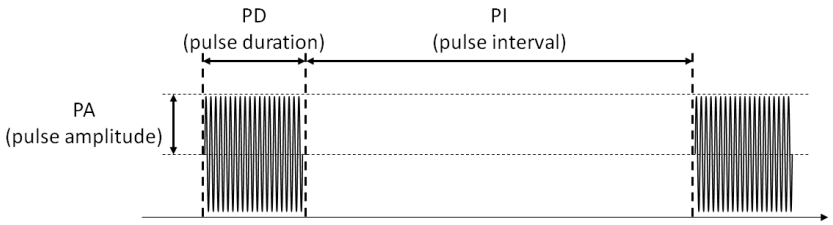

Figure 6.7: *Scheme of the typical pulsed sonochemical experiment carried out to generate nitrate.*

It was also possible to follow the experiment not only via acoustic measurements, indispensable if we want to quantify the effect of cavitation, but also with a special camera, able to collect pictures on the nanoseconds timescale. This imaging proved to be really useful since it allows us to see intuitively the extent of the cavitation phenomena inside the reactor. A picture taken during the collapse of a bubble due to the application of ultrasound is shown in **Figure 6.8.**

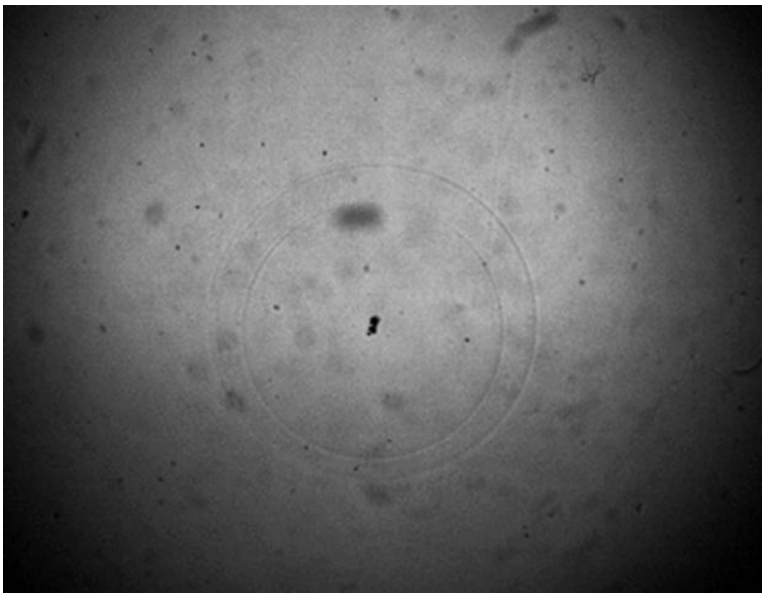

Figure 6.8: *Collapse of a bubble following the application of ultrasound to a solution saturated with air. It is possible to see the shockwave originating from the bubble collapse.*

The presence of shockwaves is proof of the bubble collapse following the irradiation with highly energetic ultrasound happening as described in **section 6.1.**

Acoustic measurements allow us to understand the magnitude of the cavitation and to optimise the pulse length and the interval between two different pulses of ultrasound. These results are shown in **Figure 6.9**. From the comparison of the detected amplitude it is found that for degassed deionised water (red trace) no cavitation is observed following irradiation with ultrasound. This is in perfect agreement with our supposition since no gas

is dissolved into the liquid. The situation dramatically changes when this deionised water is bubbled with compressed air. In this case (black trace) significant cavitation was observed during the first 10-20 msec and then the cavitation observed decrease asymptotically with time.

Moreover, similar measurements done in non-degassed deionised solution give comparable results, with a small amount of cavitation observed for the sample that was not exposed to compressed air (green trace) and with a result comparable to the black trace (blue trace) for the case where the liquid was bubbled for 1 minute with compressed air.

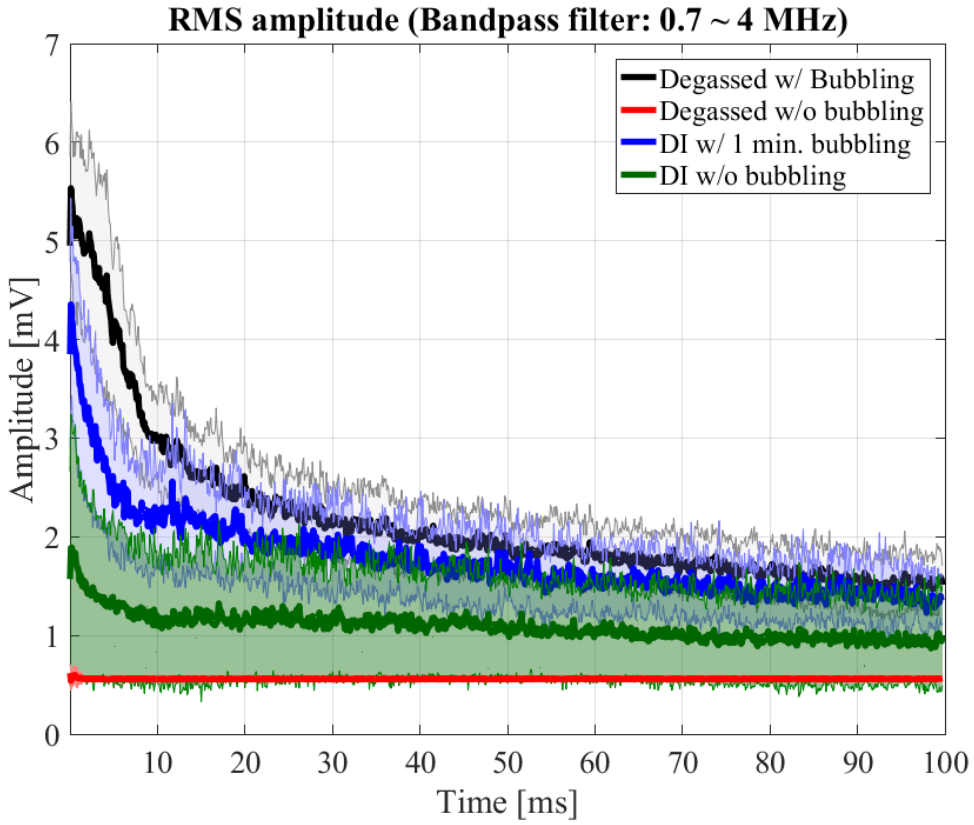

Figure 6.9: *Trend of the detected cavitation in the reactor filled with ultrapure deionized and degassed water.*

These measurements allow us to know that most of the cavitation occurs in the first 20 msec, and hence the burst's length was optimised taking this fact into account.

In a second study we investigated the effect of the interval between two pulses. This is also fundamental in order to maximise the yield of the process since an appropriate interval allows the gas time to diffuse again into the liquid and to improve the final yield of nitrite produced. In **Figure 6.10** is shown the yield of nitrite detected as a function of changing the

interval of time between two bursts. It is easy to see that when the time interval between two pulses is too short, the detected amount of nitrite is smaller.

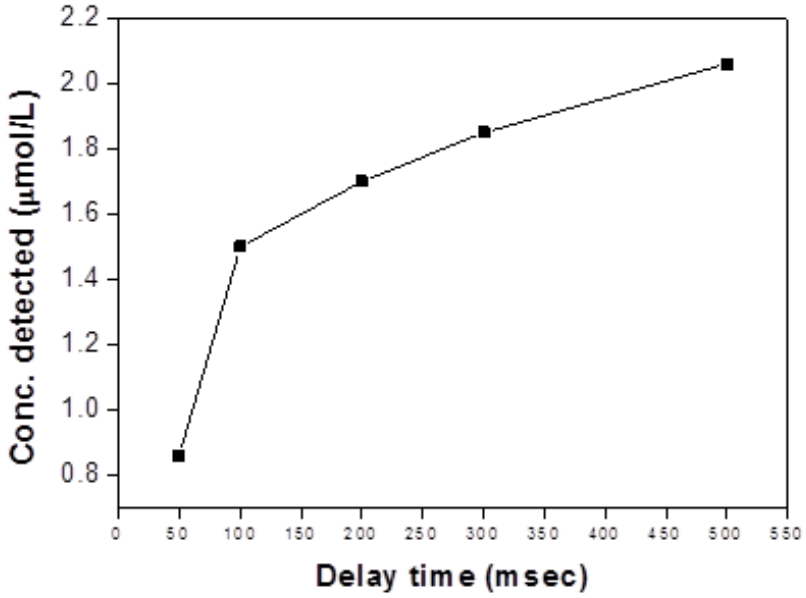

Figure 6.10: *plot showing the detected concentration of nitrite increasing with the interval time between two ultrasounds pulses. The pulse length was 10 msec in all the experiments.*

From **Figure 6.10** is possible to note that there is a strong change in the concentration detected on going from an interval of 50 msec to 10 msec. For longer intervals, it is noticed that the detected concentration grew again but with a less drastic trend. This indicates that under a continous gas flow, it is necessary to comprise on a time between 100 and 500 msec to make the solution saturated again when ultrasound at 200 kHz and with 600mV_{pp} are applied.

The other parameter to study is the amplitude, and as anticipated this is relative to the power of ultrasound applied. From **Figure 6.11** it is possible to appreciate that the concentration of nitrite detected increases linearly with the increase of the power of ultrasound applied. This graph can be misleading since in terms of energy per mole of nitrite produced we observed that the best results are obtained for 300 mV_{pp}, the lowest amplitude used. This is not surprising since the power of ultrasound with 300 mVpp of amplitude is ¼ of the ultrasonic power compared to when the amplitude is 600 mV_{pp}. Moreover since the power applied is lower, also the fraction of gas reacting during the burst is smaller and so we studied the optimal length of bursts for the new settings.

Experiments carried at $1V_{pp}$ give a value of energy per mole that is less favourable when compared with experiment carried out with lower ultrasound amplitude.

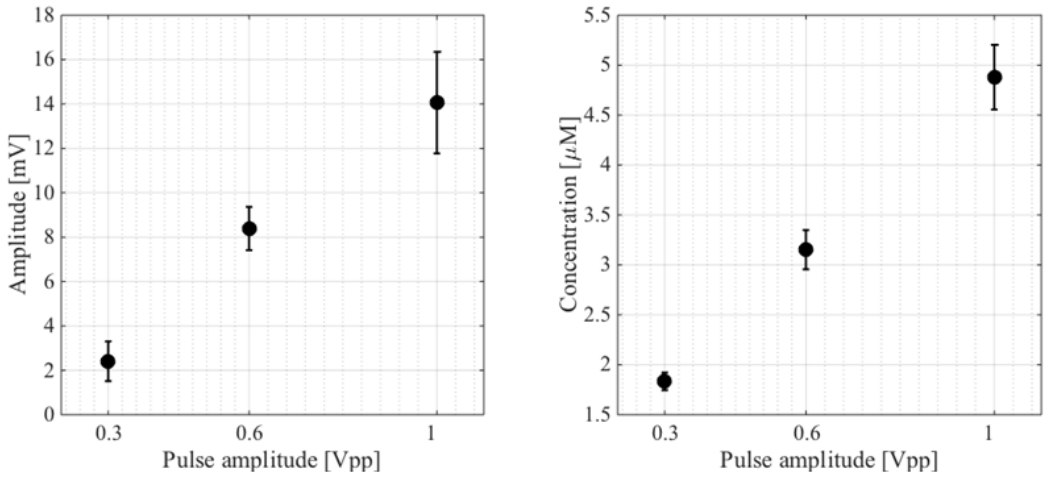

Figure 6.11: *Comparison between (**A**) the amplitude of the detected cavitation and (**B**) the concentration of nitrite detected from these experiments. Every single point was the average of 5 different experiments with the same features.*

For the experiment carried using ultrasound with amplitude of 300 mV_{pp} the study described previously in this section was repeated. The length of pulse was carefully investigated again and a maximum was found for a value of 20 msec as shown in **Figure 6.12.**

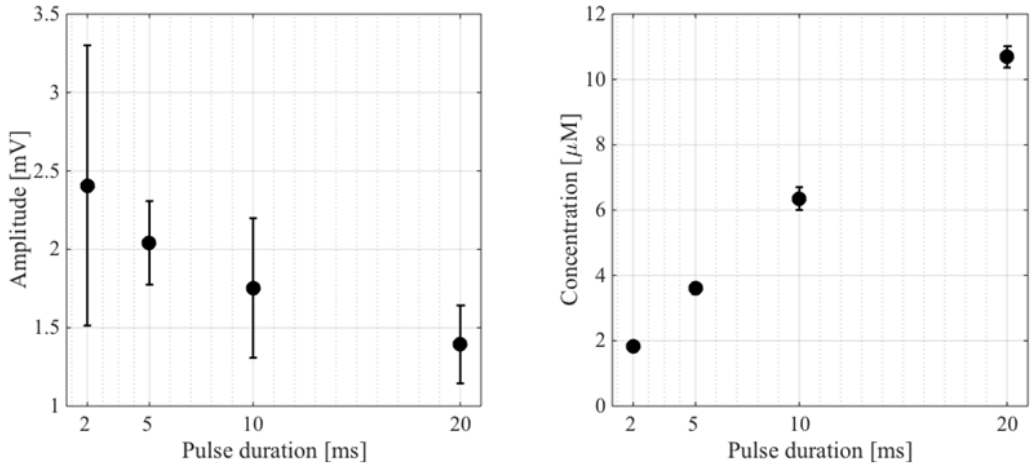

Figure 6.12: *Plot of the detected amplitude vs the pulse length **(A)** and detected concentration of nitrite vs length of pulse (B). Is easy to note that, for a longer pulse length it a better yield both in terms of concentration and also in terms of energy per mole of product.*

Concerning the interval between two pulses in the case of 300 mV_{pp} amplitude, it was possible to see the same trend as that observed in **Figure 6.10**. However the curve reached a

plateau earlier since it is possible to see no obvious changes between the data collected with 50 msec of interval and 100-200 msec of interval between two pulses. (**Figure 6.13**)

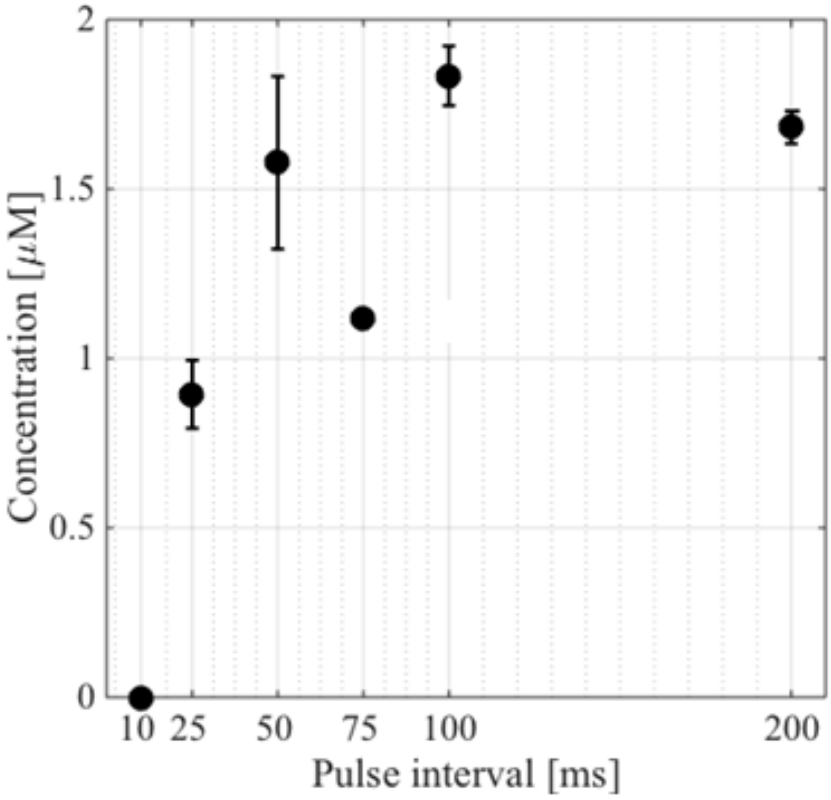

Figure 6.13: *Plot of the detected concentration of nitrite for different intervals between two pulses using 300 mV_{pp} amplitude*

6.5 Conclusions and future work

In this chapter was presented our study on the sonochemical generation of nitrite. This was focused on two different sources of cavitation: a continuous source, consisting of a sonicating bath producing ultrasounds with a frequency of 35 KHz and a pulsed ultrasound source described in the experimental section. Exploiting the sonicating bath was not possible to know the exact power involved in the process since was not possible to carry acoustic measurements in the sonication environment.

On the other hand, the application of pulsed ultrasound allows us to study more precisely the phenomenon. In first instance the adopted method allows us to know with great precision the power involved in the process and to realise that the pulsed method gives rise to show the best yield for this kind of phenomenon when compared with previous studies on the topic listed in **Table 6.1**

Table 6.1: *Comparison between different work concerning sonochemical nitrogen fixation and our experiment.In the table is reported our best value obtained with the pulsed method.*

Paper	Mode	freq (kHz)	rate of Nox formation (M min^{-1})	rate of Nox formation (M s^{-1})	ultrasonic power density (W L^{-1})	Rate of Nox formation (mol min^{-1} W^{-1})	Formation yield (mol J^{-1})	Energy per mol (kJ/mol)
Supeno (air)	Batch	900	2.00E-06	3.33E-08	270	7.41E-09	1.23E-10	8.10E+06
Wakeford	Batch	35	3.00E-07	5.00E-09		-	-	-
Mead	Batch	447	1.00E-05	1.67E-07	1000	1.00E-08	1.67E-10	6.00E+06
Virtnen (pH 7)	Batch	300	2.40E-06	4.00E-08	1400	1.71E-09	2.86E-11	3.50E+07
Koda	Batch	33	8.00E-10	1.33E-11	10	8.00E-11	1.33E-12	7.50E+08
Hart (N_2 only, best at 50:50 N_2:Ar)	Batch	300	6.00E-06	1.00E-07	320	1.88E-08	3.13E-10	3.20E+06
Parke	Batch	500	1.00E-06	1.67E-08		-	-	-
de la Rochebrochard…	Batch	367	4.00E-07	6.67E-09	14	2.86E-08	4.76E-10	2.10E+06
Our work (small amp, nitrite only)	**Batch**	**200**	**1.05E-05**	**1.75E-07**	**149**	**7.05E-08**	**1.17E-09**	**8.51E+05**

The first thing to notice is since the original report in 1936[3] there are relatively few publications concerning this topic where the phenomenon was deeply investigated, since only eight publications concerning this topic were found in literature. If we look at the rate of formation and the power density for the ultrasound used, it is possible to note that better yield always corresponds to a bigger power density.[30, 31] Another point to clarify concerns the precision with which the authors measured the power density of ultrasound. From **Table 6.1** we can see in two cases[27, 32] no values concerning the power densities and in the other cases this value is not measured with good accuracy. Because of this, we started a partnership with the Cavlab in the school of Engineering in order to obtain more accurate measurements.

Moreover due to the great differences in the reaction settings and in the power exploited none of the previous studies focus their attention on minimising the energy involved to fix nitrogen, a parameter of fundamental importance for large industrial applications. Comparing our results with other studies is possible to see that the energy necessary to fix a mole of nitrogen is about one order of magnitude smaller than any other analogous work we found in the literature and of course this is due to the optimization of the sonication,

reducing the effective time of ultrasound application and optimizing the interval between bursts. In this way we had a great reduction of the effective time of irradiation and, together with the interval where the gas can be dissolved again in the liquid, we were able to make the process more efficient than continuous irradiation with ultrasound.
However, even if the results shown in this chapter represent a noticeable improvement in sonochemical nitrogen fixation, a comparison of efficiencies with the Haber-Bosch method is found to be unflattering. Exploiting the Haber-Bosch process the energy required to fix a mole of nitrogen is 485 kJ/mol whereas for sonochemical nitrogen fixation, following our optimised pathway, the energy necessary results to be 851000 kJ/mol, about 1700 times bigger than if one exploits the Haber-Bosch process that at the state of the art and the most effective way to fix nitrogen industrially. To conclude, the use of a sonochemical reaction at the moment is not a convenient way to fix nitrogen if compared with the methods currently in use.

As future work we are interested to see if nitrate is produced during our sonochemical experiments since at the moment we have available only data concerning the detection of nitrite, although it is known that also nitrate is made during this process. [2, 27, 33] The plan is to carry out Ion chromatography measurements in order to have a value for nitrate produced during the process and also to have an external confirmation for our nitrite detection method based on the Griess test.

Moreover, further investigations are planned to investigate the anomalous effect of the fine bubble diffuser on the yield of the sonochemical reaction and to try to understand if the increase of the reaction yield is due to an increase in of the exposed surface or just due to a larger number of fine bubbles being produced by the diffuser and then undergoing cavitational collapse in solution.

6.6 References

[1] S. Eyde, *Journal of the Royal Society of Arts*, **1909**,57, 568

[2] J. Zeldovich, *Acta Physiochim USSR*, **1946**, 21, 577

[3] H. Schultes, H. Gohr, *Angew. Chem*, **1936**, 49, 420.

[4] J.D.N. Cheeke , *Fundamentals and applications of ultrasonic waves*. **2002**, CRC Press, Boca Raton

[5] Pankaj, M. Ashokkumar, *Theoretical and Experimental Sonochemistry Involving Inorganic Systems*, **2010** Springer

[6] H. Maris, S. Balibar, *Phys Today*, **2000**, 53 29

[7] K. Yasui, T. Tuziuti, M. Sivakumar, Y. Iida, *Appl Spectrosc Rev*. **2004**, 39, 399

[8] E.A. Neppiras, *Phys Rep*, **1980**, 61 159

[9] F.R. Young, *Cavitation, **1999***, Imperial College, London

[10] K.S. Suslick, D.J. Flannigan, *Ann Rev Phys Chem*, **2008**, 59, 659

[11] R. Pecha, B. Gompf, *Phys Rev Lett*, **2000**, 84, 1328

[12] J. Holzfuss, M. Reuggeberg, A. Billo, *Phys Rev Lett* **1998**, 81, 5434

[13] K.R. Weninger, G.C. Camara, S.J. Putterman, *Phys Rev E*, **2001**, 6, 16310

[14] S. Fujikawa, T. Akamatsu , *J Fluid Mech*, **1980**, 97, 481

[15] A. Henglein, *Contributions to various aspects of cavitation chemistry*. In: T.J. Mason (ed) *Advances in Sonochemistry*, vol. 3,17–83, JAI Press, **1993**, London

[16] D.E. Yount, E.W. Gillary, D.C. Hoffman, *J Acoust Soc Am*, **1984**, 76, 1511

[17] K. Yasui, *J Acoust Soc Am*, **2002**, 112, 1405

[18] N. Bremond, M. Arora, S.M. Dammer, D. Lohse, *Phys Fluids*, **2006**, 18, 121505

[19] M.L. Calvisi, O. Lindau, J.R. Blake, A.J. Szeri, *Phys Fluids*, **2007**, 19, 047101

[20] E. Wang, W. Chen, M. Lu, R. Wei, *J Acoust Soc Am*, **2003**, 114:1898–1904

[21] T. J. Mason, *Sonochemistry*. **1999**, Oxford University Press, Oxford

[22] K. S. Suslick, D. A. Hammerton, R. E. Cline, *J Am Chem Soc* **1986**, 108, 5641

[23] M. B. Shiny, *Ind. Eng. Chem. Anal.* Ed., **1941**, 13, 33

[24] J. H. Song, K. Johansen, and P. Prentice, *J. Acoust. Soc. Am*. **2016**, 140

[25] K. Johansen, J. H. Song, P. Prentice, *Ultrasonics – Sonochemistry*, **2018**, 43, 146

[26] K. Johansen, J. H.Song, K. Johnston, P. Prentice, *Ultrasonics* 73 **2017**, 73, 144

[27] C.A.Wakeford, R. Blackburn, P.D. Lickiss: *Ultrasonics Sonochemistry*, **1999**, 6, 141

[28] K. Yasui, *J Chem Phys*, **2002**, 116, 2945

[29] V.S. Moholkar, P. S. Kumar, A.B. Pandit, *Ultrasonics Sonochemistry* **1999**, 6, 53

[30] E.L. Mead, R.G. Sutherland, R.E. Verrall, *Can. J. Chem, **1976**, 54, 1114*

[31] A.I. Virtanen, N. Ellfolk, *Acta Chem. Scand*, **1950**, 4, 93.

[32] A.V.M. Parke, D. Taylor, *J. Chem. Soc*, **1956**, 4, 4442.

[33] Supeno and P. Kruus, *Ultrasonics Sonochemistry*, **2000**, 7, 109

CONCLUSIONS AND FUTURE WORK

The experimental work described in this thesis has covered a detailed study concerning the development of two new copper-tripod catalysts that mimic the active site of the copper nitrite reductase class of enzymes promoting the electro-reduction of nitrite to NO with essentially full Faradaic efficiency for NO production. Our results presented in **Chapter 3** also highlight the central role of proton-coupled-electron transfer in the reduction of nitrite to NO (and in the activation of small molecules in general). We showed in fact that incorporation of a proton-relaying moiety into the secondary coordination sphere of one of these complexes (**18**) enhances the electrocatalytic nitrite reduction rate displayed by this complex by a factor of two when compared to the analogous complex that lacks this functionality (**complex 3**). On the basis of what we have seen in **Chapter 1**, this could have important implications for the development of new catalysts for the selective interconversions of the nitrogen oxides and other substrates.

Regarding the product of this reaction, nitric oxide, it is important to note that in the presence of oxygen NO has a very short lifetime and so needs to be generated *in situ* when it is required (e.g. for medical applications). In order to create medical devices that can generate NO with the lowest toxicity and impact on the body, the best way to do this is to use something similar to what we find in nature, and hence mimic a natural system able to promote nitric oxide formation from a source that is abundant in the body (such as nitrate). Devices for the treatment of pathologies like heart disease, that exploit these properties are under study[1,2] and the class of catalysts presented in **Chapter 3** make good starting points for these applications (for example, as part of a set of catalysts that might convert nitrate to nitrite, and then nitrite to NO).

The results detailed in **Chapter 4** describe the synthesis of three complexes of the type $[Co^{III}(L)(bipyridine)_2]^+$ (L = catecholato **20**, *o*-benzenedithiolato **21**) by a general and rapid one-pot reaction route which is near-quantitative for the catecholate compounds but non-quantitative for o-benzenedithiolato analogue. In this last case, in addition to the complex **21** we were able to isolate the previously unreported bis-chelate dimer $[Co_2(bdt)_2(Me_2bpy)_3]^{2+}$ (**24**) as the main product

(**Chapter 5**)**.** This complex displays a most uncommon arrangement in which the two cobalt centers are in dissimilar coordination environments. DFT calculations on this species helped to rationalize the redox behaviour observed by cyclic voltammetry, and showed that the metal center coordinated to two diimine units was the easier of the centers to reduce, with subsequent reduction of the second cobalt center leading to irreversible decomposition of the complex.

An interesting fact is that **21** and **20** display intriguing differences in their solution-phase UV-vis absorption behaviour since the position of λ_{max} in both complexes was sensitive to the polarity of the surrounding medium. In the case of **20**, the position of λ_{max} was also highly sensitive to the hydrogen bond donation ability of the solvent, whereas in the benzenedithiolate analogue **21** it was not. The theoretical model developed via TD-DFT calculations was used to explain these intriguing optical properties, and by comparing the ground and excited state electronic structures of the two complexes it was found that complex **20** hydrogen-bonds to the solvent through the oxygen atoms on its catecholate ligand.

This interaction was found to remove electron density from the catecholate-based π^* orbital, in a similar manner to that seen in **Chapter 1** and **Chapter 3**, where in those cases the stabilization of the ground state led to a higher catalytic activity, thereby stabilizing the ground state with respect to the excited state (which is primarily metal-centred and hence more isolated from the solvent) with the effect of increasing the excitation energy in hydrogen bond-donating solvents relative to those that cannot hydrogen bond.

In complex **21** on the other hand, the sulfur atoms in the chelating benzenedithiolate ligand are much weaker hydrogen bond acceptors than oxygen, and so preferential stabilization contributions through hydrogen bonding, important in the previous case, are eliminated. The solvatochromic effect that manifests in complex **21** is much smaller and can be explained on a purely electrostatic basis. We believe that the synthesis of an enormous diversity of allied complexes should be possible, given the wide range of functionalized bipyridines, catechols and benzenedithiols that are available. In particular, we foresee potential for such compounds to be tailored for use as molecular probes or solvatochromic indicators that can give insight into different solvent and chemical environments by virtue of readily-observed spectroscopic changes.

Finally, in **Chapter 6** we described the optimization of the sonochemical fixation of nitrogen. In our experiments we managed to increase the yield of the sonochemical reaction in two different ways. Firstly, we optimised the aeration of the solution and maximized the hydrodynamic contribution to the overall cavitation, and secondly we optimized the application of the ultrasound itself by developing a pulsed sequence of focused high frequency ultrasound. In this last case we found better yields of nitrite when the time between a given pulse and the following one was long enough to allow the solution to become re-aerated. Although the energetic yield was about one order of magnitude bigger than in the previous works reported in the literature, it is still too low compared to other methods commonly used to fix nitrogen at a larger scale for this ultrasound route to be economically viable at the current time.

A lot of work needs to be done if we want to increase the yield of the sonochemical nitrogen fixation reaction, but it is possible to obtain further improvements in the process by working at lower temperature (since gas dissolves better in colder liquids) and by minimising the power density of the system (e.g. by increasing the volume). The development of this procedure may produce something of practical interest since, if we manage to make this process more efficient, it has the advantages of requiring only air, water and electricity as inputs, and uses only equipment which could be operated by a non-expert. Hence there is some scope for small-scale NO_x production by this route. If the nitrite generated could be converted to nitrate *in situ*, then decentralised fertiliser production that avoids the traditional Haber Bosch/Ostwald route could one day be feasible.

References:

[1] H.Ren, J. Wu, C. Xi, N. Lehnert, T. Major, R.H. Bartlett, M.E. Meyerho, *Applied Materials & Interfaces*, **2014,** 6
[2] P.N. Coneski, M.H. Schoenfisch, *Chem. Soc. Rev*. **2012**, 41

Appendix A: Crystallographic data

1 Crystallography for complex [3-CH_3CN]$^{2+}$

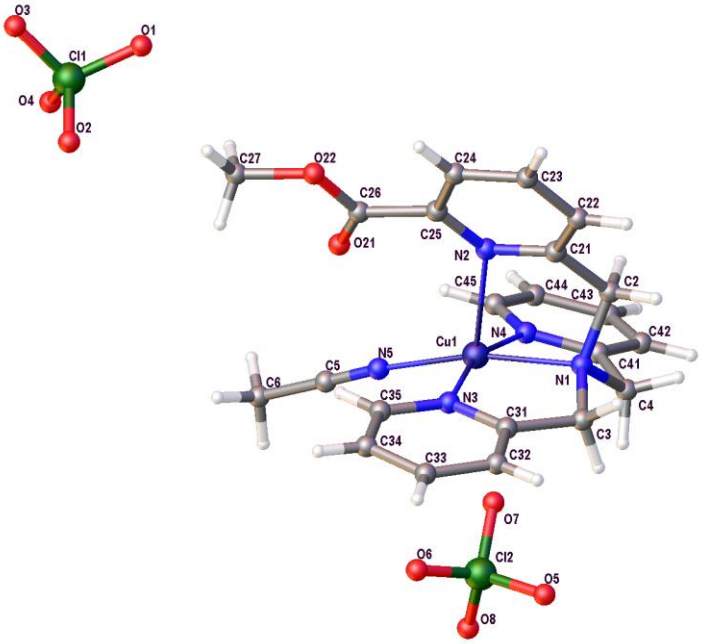

Refinement

Crystal data, data collection and structure refinement details are summarized in Table 1.

Computing details

Data collection: *APEX2* (Bruker, 2013); cell refinement: *SAINT* v8.34A (Bruker, 2013); data reduction: *SAINT* v8.34A (Bruker, 2013); program(s) used to solve structure: Superflip (Palatinus & Chapuis, 2007;Palatinus & van der Lee, 2008; Palatinus *et al.*, 2012); program(s) used to refine structure: *SHELXL* (Sheldrick, 2015); molecular graphics: Olex2 (Dolomanov *et al.*, 2009); software used to prepare material for publication: Olex2 (Dolomanov *et al.*, 2009).

References

Palatinus, L.; Chapuis, G. SUPERFLIP – a Computer Program for the Solution of Crystal Structures by Charge Flipping in Arbitrary Dimensions. *J. Appl. Cryst.* **2007**, *40*, 786–790.

Palatinus, L.; van der Lee, A. Symmetry Determination following Structure Solution in P1. *J. Appl. Cryst.* **2008**, *41*, 975-984.

Palatinus, L.; Prathapa, S. J.; van Smaalen, S. *EDMA*: a Computer Program for Topological Analysis of Discrete Electron Densities. *J. Appl. Cryst.* **2012**, *45*, 575-580.

Sheldrick, G. M. Crystal Structure Refinement with SHELXL. *Acta Cryst. C,* **2015**, *71*, 3-8.

Dolomanov, O. V.; Bourhis, L. J.; Gildea, R. J.; Howard, J. A. K.; Puschmann, H. OLEX2: a Complete Structure Solution, Refinement and Analysis Program. *J. Appl. Cryst.* **2009**, *42*, 339-341.

(2015gu0016_0m) *Crystal data*

$C_{22}H_{23}CuN_5O_2 \cdot 2(ClO_4)$	$Z = 2$
$M_r = 651.89$	$F(000) = 666$
Triclinic, $P\bar{1}$	$\rho_{calcd} = 1.687$ g cm^{-3}
$a = 8.4706(7)$ Å	Mo $K\alpha$ radiation, $\lambda = 0.71073$ Å
$b = 8.8319(8)$ Å	Cell parameters from 9963 reflections
$c = 17.982(2)$ Å	$\theta = 2.3–27.4°$
$\alpha = 95.471(2)°$	$\mu = 1.13$ mm^{-1}
$\beta = 99.637(2)°$	$T = 100$ K
$\gamma = 102.415(2)°$	Block, blue
$V = 1283.2(2)$ Å^3	0.42 × 0.4 × 0.31 mm

Data collection

Bruker APEX-II CCD diffractometer	5061 reflections with $I > 2\sigma(I)$
ϕ and ω scans	$R_{int} = 0.068$
Absorption correction: multi-scan *SADABS2012*/1 (Bruker,2012) was used for absorption correction. wR2(int) was 0.1364 before and 0.1085 after correction. The Ratio of minimum to maximum transmission is 0.7665. The l/2 correction factor is 0.0015.	$\theta_{max} = 27.4°$, $\theta_{min} = 1.2°$
$T_{min} = 0.570$, $T_{max} = 0.744$	$h = -10 \rightarrow 10$
15864 measured reflections	$k = -10 \rightarrow 11$
5798 independent reflections	$l = -23 \rightarrow 23$

Refinement

Refinement on F^2	0 restraints
Least-squares matrix: full	Hydrogen site location: inferred from neighbouring sites
$R[F^2 > 2\sigma(F^2)] = 0.062$	H-atom parameters constrained
$wR(F^2) = 0.171$	$w = 1/[\sigma^2(F_o^2) + (0.111P)^2 + 0.251P]$ where $P = (F_o^2 + 2F_c^2)/3$
$S = 1.10$	$(D/s)_{max} = 0.001$
5798 reflections	$\Delta\rangle_{max} = 0.90$ e Å^{-3}
363 parameters	$\Delta\rangle_{min} = -0.76$ e Å^{-3}

Fractional atomic coordinates and isotropic or equivalent isotropic displacement parameters (Å^2)

	x	*y*	*z*	U_{iso}*/U_{eq}
Cu1	0.76353 (4)	0.48129 (4)	0.21221 (2)	0.01254 (14)

O21	0.5874 (3)	0.3790 (3)	0.35445 (13)	0.0224 (5)
O22	0.6696 (3)	0.4223 (3)	0.48150 (13)	0.0260 (5)
N1	0.9611 (3)	0.6545 (3)	0.20430 (13)	0.0118 (5)
N2	0.8382 (3)	0.6299 (3)	0.34173 (14)	0.0136 (5)
N3	0.9316 (3)	0.3792 (3)	0.26086 (13)	0.0128 (5)
N4	0.6435 (3)	0.5945 (3)	0.14090 (13)	0.0129 (5)
N5	0.5760 (3)	0.2951 (3)	0.19422 (14)	0.0169 (5)
C2	0.9772 (4)	0.7921 (3)	0.26125 (16)	0.0152 (6)
H2A	0.8913	0.8456	0.2450	0.018*
H2B	1.0826	0.8642	0.2639	0.018*
C3	1.1105 (3)	0.5903 (3)	0.21524 (17)	0.0143 (6)
H3A	1.2036	0.6709	0.2434	0.017*
H3B	1.1351	0.5601	0.1659	0.017*
C4	0.9222 (4)	0.7005 (3)	0.12620 (16)	0.0140 (6)
H4A	0.9857	0.8055	0.1251	0.017*
H4B	0.9513	0.6294	0.0892	0.017*
C5	0.4696 (4)	0.1874 (4)	0.17718 (16)	0.0153 (6)
C6	0.3314 (4)	0.0524 (4)	0.1553 (2)	0.0243 (7)
H6A	0.2303	0.0854	0.1546	0.036*
H6B	0.3400	-0.0203	0.1914	0.036*
H6C	0.3322	0.0028	0.1056	0.036*
C21	0.9648 (4)	0.7475 (3)	0.33940 (17)	0.0152 (6)
C22	1.0778 (4)	0.8277 (4)	0.40399 (18)	0.0178 (6)
H22	1.1679	0.9054	0.3996	0.021*
C23	1.0531 (4)	0.7893 (4)	0.47466 (18)	0.0230 (7)
H23	1.1238	0.8435	0.5189	0.028*
C24	0.9207 (4)	0.6682 (4)	0.47831 (18)	0.0219 (7)
H24	0.9013	0.6395	0.5250	0.026*
C25	0.8175 (4)	0.5906 (4)	0.41063 (17)	0.0161 (6)
C26	0.6783 (4)	0.4535 (4)	0.41080 (17)	0.0162 (6)
C27	0.5427 (5)	0.2866 (4)	0.4879 (2)	0.0306 (8)
H27A	0.5514	0.1976	0.4551	0.046*
H27B	0.4361	0.3076	0.4731	0.046*
H27C	0.5568	0.2651	0.5396	0.046*
C31	1.0876 (4)	0.4494 (3)	0.25799 (16)	0.0134 (6)
C32	1.2191 (4)	0.3904 (4)	0.28880 (17)	0.0165 (6)
H32	1.3265	0.4410	0.2873	0.020*
C33	1.1874 (4)	0.2544 (4)	0.32198 (17)	0.0185 (6)
H33	1.2735	0.2104	0.3413	0.022*
C34	1.0270 (4)	0.1845 (3)	0.32620 (16)	0.0172 (6)
H34	1.0042	0.0953	0.3499	0.021*
C35	0.9012 (4)	0.2495 (3)	0.29457 (16)	0.0147 (6)
H35	0.7931	0.2024	0.2967	0.018*

C41	0.7419 (4)	0.6948 (3)	0.10658 (15)	0.0127 (5)
C42	0.6781 (4)	0.7808 (4)	0.05323 (17)	0.0180 (6)
H42	0.7478	0.8526	0.0316	0.022*
C43	0.5079 (4)	0.7572 (4)	0.03279 (18)	0.0212 (7)
H43	0.4623	0.8116	-0.0036	0.025*
C44	0.4074 (4)	0.6523 (4)	0.06707 (19)	0.0225 (7)
H44	0.2934	0.6348	0.0537	0.027*
C45	0.4784 (4)	0.5736 (4)	0.12146 (18)	0.0185 (6)
H45	0.4108	0.5045	0.1452	0.022*
Cl1	0.44967 (9)	0.11291 (8)	0.67584 (4)	0.01835 (19)
O1	0.5086 (3)	0.2783 (3)	0.67660 (15)	0.0322 (6)
O2	0.5841 (3)	0.0377 (3)	0.67260 (15)	0.0334 (6)
O3	0.3870 (3)	0.0837 (3)	0.74409 (16)	0.0332 (6)
O4	0.3197 (3)	0.0510 (3)	0.61061 (16)	0.0392 (7)
Cl2	0.94664 (9)	0.22457 (8)	0.07214 (4)	0.01578 (19)
O5	1.1129 (3)	0.3118 (3)	0.07336 (16)	0.0335 (6)
O6	0.9493 (3)	0.1198 (3)	0.12837 (13)	0.0258 (5)
O7	0.8466 (3)	0.3332 (3)	0.08829 (13)	0.0233 (5)
O8	0.8773 (3)	0.1369 (3)	-0.00227 (13)	0.0255 (5)

Atomic displacement parameters (Å^2)

	U^{11}	U^{22}	U^{33}	U^{12}	U^{13}	U^{23}
Cu1	0.0092 (2)	0.0112 (2)	0.0168 (2)	0.00127 (15)	0.00116 (15)	0.00536 (14)
O21	0.0225 (12)	0.0230 (12)	0.0178 (11)	-0.0020 (10)	0.0033 (9)	0.0013 (9)
O22	0.0271 (13)	0.0294 (13)	0.0173 (11)	-0.0045 (10)	0.0057 (10)	0.0059 (10)
N1	0.0101 (11)	0.0107 (11)	0.0143 (11)	0.0011 (9)	0.0022 (9)	0.0034 (9)
N2	0.0145 (12)	0.0130 (12)	0.0138 (11)	0.0053 (10)	0.0013 (9)	0.0020 (9)
N3	0.0147 (12)	0.0097 (11)	0.0141 (11)	0.0035 (9)	0.0027 (9)	0.0021 (9)
N4	0.0114 (12)	0.0133 (12)	0.0134 (11)	0.0025 (9)	0.0013 (9)	0.0025 (9)
N5	0.0172 (13)	0.0170 (13)	0.0163 (12)	0.0027 (11)	0.0030 (10)	0.0050 (10)
C2	0.0171 (14)	0.0122 (13)	0.0155 (14)	0.0028 (11)	0.0016 (11)	0.0019 (11)
C3	0.0084 (13)	0.0162 (14)	0.0183 (14)	0.0035 (11)	0.0015 (11)	0.0037 (11)
C4	0.0141 (14)	0.0142 (14)	0.0136 (13)	0.0022 (11)	0.0028 (11)	0.0046 (11)
C5	0.0165 (15)	0.0187 (15)	0.0105 (13)	0.0052 (13)	-0.0006 (11)	0.0046 (11)
C6	0.0193 (16)	0.0196 (16)	0.0274 (17)	-0.0020 (13)	-0.0056 (13)	0.0044 (13)
C21	0.0155 (14)	0.0143 (14)	0.0158 (14)	0.0053 (11)	0.0019 (11)	0.0006 (11)
C22	0.0147 (14)	0.0156 (15)	0.0201 (15)	0.0014 (12)	-0.0010 (12)	0.0004 (12)
C23	0.0236 (17)	0.0241 (17)	0.0182 (15)	0.0058 (14)	-0.0024 (13)	-0.0010 (13)
C24	0.0237 (17)	0.0265 (17)	0.0148 (14)	0.0056 (14)	0.0024 (13)	0.0025 (12)
C25	0.0172 (15)	0.0173 (14)	0.0140 (14)	0.0055 (12)	0.0029 (11)	0.0000 (11)
C26	0.0163 (14)	0.0176 (15)	0.0157 (14)	0.0061 (12)	0.0037 (11)	0.0010 (11)

C27	0.0299 (19)	0.035 (2)	0.0242 (17)	-0.0046 (16)	0.0083 (15)	0.0118 (15)
C31	0.0153 (14)	0.0117 (13)	0.0136 (13)	0.0047 (11)	0.0030 (11)	-0.0004 (10)
C32	0.0137 (14)	0.0190 (15)	0.0161 (14)	0.0052 (12)	0.0004 (11)	0.0001 (11)
C33	0.0203 (15)	0.0174 (15)	0.0182 (14)	0.0094 (12)	-0.0009 (12)	0.0020 (11)
C34	0.0259 (16)	0.0134 (14)	0.0128 (13)	0.0066 (12)	0.0019 (12)	0.0038 (11)
C35	0.0175 (14)	0.0140 (14)	0.0132 (13)	0.0046 (11)	0.0027 (11)	0.0032 (11)
C41	0.0153 (14)	0.0120 (13)	0.0109 (12)	0.0032 (11)	0.0031 (11)	0.0003 (10)
C42	0.0216 (16)	0.0176 (15)	0.0163 (14)	0.0053 (12)	0.0056 (12)	0.0059 (11)
C43	0.0238 (17)	0.0240 (16)	0.0184 (15)	0.0103 (14)	0.0015 (13)	0.0095 (13)
C44	0.0151 (15)	0.0268 (17)	0.0266 (17)	0.0072 (13)	0.0012 (13)	0.0086 (14)
C45	0.0132 (14)	0.0212 (16)	0.0236 (15)	0.0057 (12)	0.0058 (12)	0.0078 (12)
Cl1	0.0146 (4)	0.0157 (4)	0.0228 (4)	0.0008 (3)	0.0019 (3)	0.0022 (3)
O1	0.0327 (14)	0.0191 (12)	0.0376 (15)	-0.0044 (11)	-0.0029 (12)	0.0093 (11)
O2	0.0268 (13)	0.0417 (15)	0.0371 (14)	0.0175 (12)	0.0095 (11)	0.0039 (12)
O3	0.0318 (14)	0.0383 (15)	0.0368 (15)	0.0113 (12)	0.0184 (12)	0.0135 (12)
O4	0.0294 (14)	0.0343 (15)	0.0393 (16)	-0.0012 (12)	-0.0138 (12)	-0.0109 (12)
Cl2	0.0165 (4)	0.0168 (4)	0.0132 (3)	0.0030 (3)	0.0026 (3)	0.0002 (3)
O5	0.0212 (13)	0.0343 (14)	0.0402 (15)	-0.0045 (11)	0.0112 (11)	-0.0027 (12)
O6	0.0380 (14)	0.0223 (12)	0.0181 (11)	0.0110 (11)	0.0009 (10)	0.0066 (9)
O7	0.0263 (12)	0.0263 (12)	0.0195 (11)	0.0144 (10)	0.0014 (9)	0.0011 (9)
O8	0.0346 (14)	0.0235 (12)	0.0141 (11)	0.0038 (11)	0.0000 (10)	-0.0030 (9)

Geometric parameters (Å, º) for (2015gu0016_0m)

Cu1—N1	2.045 (2)	C22—C23	1.384 (5)
Cu1—N2	2.473 (2)	C23—H23	0.9300
Cu1—N3	1.972 (2)	C23—C24	1.389 (5)
Cu1—N4	1.981 (2)	C24—H24	0.9300
Cu1—N5	1.984 (3)	C24—C25	1.394 (4)
O21—C26	1.203 (4)	C25—C26	1.498 (4)
O22—C26	1.337 (4)	C27—H27A	0.9600
O22—C27	1.456 (4)	C27—H27B	0.9600
N1—C2	1.479 (4)	C27—H27C	0.9600
N1—C3	1.486 (3)	C31—C32	1.384 (4)
N1—C4	1.503 (3)	C32—H32	0.9300
N2—C21	1.333 (4)	C32—C33	1.386 (4)
N2—C25	1.347 (4)	C33—H33	0.9300
N3—C31	1.345 (4)	C33—C34	1.384 (5)
N3—C35	1.343 (4)	C34—H34	0.9300
N4—C41	1.349 (4)	C34—C35	1.383 (4)
N4—C45	1.351 (4)	C35—H35	0.9300
N5—C5	1.138 (4)	C41—C42	1.390 (4)
C2—H2A	0.9700	C42—H42	0.9300

C2—H2B	0.9700	C42—C43	1.391 (5)
C2—C21	1.509 (4)	C43—H43	0.9300
C3—H3A	0.9700	C43—C44	1.382 (5)
C3—H3B	0.9700	C44—H44	0.9300
C3—C31	1.519 (4)	C44—C45	1.384 (4)
C4—H4A	0.9700	C45—H45	0.9300
C4—H4B	0.9700	Cl1—O1	1.437 (2)
C4—C41	1.497 (4)	Cl1—O2	1.442 (3)
C5—C6	1.450 (4)	Cl1—O3	1.440 (3)
C6—H6A	0.9600	Cl1—O4	1.440 (3)
C6—H6B	0.9600	Cl2—O5	1.448 (3)
C6—H6C	0.9600	Cl2—O6	1.435 (2)
C21—C22	1.395 (4)	Cl2—O7	1.450 (2)
C22—H22	0.9300	Cl2—O8	1.442 (2)
N1—Cu1—N2	77.49 (9)	C22—C23—C24	118.7 (3)
N3—Cu1—N1	84.54 (10)	C24—C23—H23	120.6
N3—Cu1—N2	79.14 (9)	C23—C24—H24	120.7
N3—Cu1—N4	161.90 (10)	C23—C24—C25	118.7 (3)
N3—Cu1—N5	96.55 (10)	C25—C24—H24	120.7
N4—Cu1—N1	82.62 (10)	N2—C25—C24	123.0 (3)
N4—Cu1—N2	110.26 (9)	N2—C25—C26	116.0 (3)
N4—Cu1—N5	92.90 (10)	C24—C25—C26	121.0 (3)
N5—Cu1—N1	166.01 (10)	O21—C26—O22	124.1 (3)
N5—Cu1—N2	116.45 (9)	O21—C26—C25	124.4 (3)
C26—O22—C27	115.9 (3)	O22—C26—C25	111.5 (3)
C2—N1—Cu1	110.15 (17)	O22—C27—H27A	109.5
C2—N1—C3	111.9 (2)	O22—C27—H27B	109.5
C2—N1—C4	108.5 (2)	O22—C27—H27C	109.5
C3—N1—Cu1	108.18 (17)	H27A—C27—H27B	109.5
C3—N1—C4	112.4 (2)	H27A—C27—H27C	109.5
C4—N1—Cu1	105.63 (17)	H27B—C27—H27C	109.5
C21—N2—Cu1	105.15 (18)	N3—C31—C3	116.5 (2)
C21—N2—C25	117.5 (3)	N3—C31—C32	121.4 (3)
C25—N2—Cu1	133.1 (2)	C32—C31—C3	122.0 (3)
C31—N3—Cu1	114.65 (19)	C31—C32—H32	120.6
C35—N3—Cu1	125.5 (2)	C31—C32—C33	118.7 (3)
C35—N3—C31	119.8 (2)	C33—C32—H32	120.6
C41—N4—Cu1	113.94 (19)	C32—C33—H33	120.2
C41—N4—C45	119.3 (3)	C34—C33—C32	119.6 (3)
C45—N4—Cu1	126.7 (2)	C34—C33—H33	120.2
C5—N5—Cu1	173.8 (2)	C33—C34—H34	120.6
N1—C2—H2A	109.1	C35—C34—C33	118.8 (3)

N1—C2—H2B	109.1	C35—C34—H34	120.6
N1—C2—C21	112.3 (2)	N3—C35—C34	121.6 (3)
H2A—C2—H2B	107.9	N3—C35—H35	119.2
C21—C2—H2A	109.1	C34—C35—H35	119.2
C21—C2—H2B	109.1	N4—C41—C4	115.9 (2)
N1—C3—H3A	109.3	N4—C41—C42	121.7 (3)
N1—C3—H3B	109.3	C42—C41—C4	122.3 (3)
N1—C3—C31	111.7 (2)	C41—C42—H42	120.7
H3A—C3—H3B	107.9	C41—C42—C43	118.7 (3)
C31—C3—H3A	109.3	C43—C42—H42	120.7
C31—C3—H3B	109.3	C42—C43—H43	120.3
N1—C4—H4A	109.9	C44—C43—C42	119.4 (3)
N1—C4—H4B	109.9	C44—C43—H43	120.3
H4A—C4—H4B	108.3	C43—C44—H44	120.4
C41—C4—N1	109.1 (2)	C43—C44—C45	119.2 (3)
C41—C4—H4A	109.9	C45—C44—H44	120.4
C41—C4—H4B	109.9	N4—C45—C44	121.7 (3)
N5—C5—C6	178.7 (3)	N4—C45—H45	119.2
C5—C6—H6A	109.5	C44—C45—H45	119.2
C5—C6—H6B	109.5	O1—Cl1—O2	109.11 (17)
C5—C6—H6C	109.5	O1—Cl1—O3	109.84 (16)
H6A—C6—H6B	109.5	O1—Cl1—O4	109.63 (16)
H6A—C6—H6C	109.5	O3—Cl1—O2	109.11 (16)
H6B—C6—H6C	109.5	O4—Cl1—O2	109.97 (16)
N2—C21—C2	115.3 (3)	O4—Cl1—O3	109.17 (18)
N2—C21—C22	123.4 (3)	O5—Cl2—O7	109.09 (15)
C22—C21—C2	121.3 (3)	O6—Cl2—O5	109.47 (17)
C21—C22—H22	120.7	O6—Cl2—O7	110.00 (14)
C23—C22—C21	118.7 (3)	O6—Cl2—O8	109.82 (14)
C23—C22—H22	120.7	O8—Cl2—O5	109.68 (15)
C22—C23—H23	120.6	O8—Cl2—O7	108.76 (14)
Cu1—N1—C2—C21	47.5 (3)	C3—C31—C32—C33	-175.1 (3)
Cu1—N1—C3—C31	-22.4 (3)	C4—N1—C2—C21	162.6 (2)
Cu1—N1—C4—C41	37.2 (2)	C4—N1—C3—C31	-138.6 (2)
Cu1—N2—C21—C2	23.1 (3)	C4—C41—C42—C43	173.7 (3)
Cu1—N2—C21—C22	-158.0 (2)	C21—N2—C25—C24	0.7 (4)
Cu1—N2—C25—C24	153.6 (2)	C21—N2—C25—C26	-177.5 (2)
Cu1—N2—C25—C26	-24.5 (4)	C21—C22—C23—C24	2.6 (5)
Cu1—N3—C31—C3	-2.7 (3)	C22—C23—C24—C25	-0.3 (5)
Cu1—N3—C31—C32	-179.2 (2)	C23—C24—C25—N2	-1.5 (5)
Cu1—N3—C35—C34	178.9 (2)	C23—C24—C25—C26	176.6 (3)
Cu1—N4—C41—C4	1.6 (3)	C24—C25—C26—O21	-178.0 (3)

Cu1—N4—C41—C42	178.2 (2)	C24—C25—C26—O22	0.8 (4)
Cu1—N4—C45—C44	-175.7 (2)	C25—N2—C21—C2	-177.0 (2)
N1—C2—C21—N2	-48.4 (3)	C25—N2—C21—C22	1.9 (4)
N1—C2—C21—C22	132.8 (3)	C27—O22—C26—O21	1.4 (5)
N1—C3—C31—N3	17.4 (3)	C27—O22—C26—C25	-177.4 (3)
N1—C3—C31—C32	-166.1 (3)	C31—N3—C35—C34	-0.6 (4)
N1—C4—C41—N4	-26.9 (3)	C31—C32—C33—C34	-2.5 (4)
N1—C4—C41—C42	156.5 (2)	C32—C33—C34—C35	2.3 (4)
N2—C21—C22—C23	-3.5 (4)	C33—C34—C35—N3	-0.8 (4)
N2—C25—C26—O21	0.2 (4)	C35—N3—C31—C3	176.9 (2)
N2—C25—C26—O22	179.0 (2)	C35—N3—C31—C32	0.4 (4)
N3—C31—C32—C33	1.1 (4)	C41—N4—C45—C44	0.1 (5)
N4—C41—C42—C43	-2.7 (4)	C41—C42—C43—C44	1.5 (5)
C2—N1—C3—C31	99.1 (3)	C42—C43—C44—C45	0.4 (5)
C2—N1—C4—C41	-80.9 (3)	C43—C44—C45—N4	-1.2 (5)
C2—C21—C22—C23	175.2 (3)	C45—N4—C41—C4	-174.7 (3)
C3—N1—C2—C21	-72.9 (3)	C45—N4—C41—C42	1.9 (4)
C3—N1—C4—C41	154.9 (2)		

Hydrogen-bond geometry (Å, º) for (2015gu0016_0m)

D—H···*A*	*D*—H	H···*A*	*D*···*A*	*D*—H···*A*
C2—H2*A*···O3^{i}	0.97	2.60	3.479 (4)	151
C3—H3*A*···O1^{ii}	0.97	2.54	3.376 (4)	144
C3—H3*B*···O5	0.97	2.58	3.377 (4)	140
C4—H4*B*···O7	0.97	2.57	3.152 (4)	119
C6—H6*A*···O6^{iii}	0.96	2.44	3.379 (4)	167
C6—H6*B*···O2^{iv}	0.96	2.45	3.270 (4)	143
C6—H6*B*···O3^{iv}	0.96	2.61	3.257 (4)	125
C6—H6*C*···O8^{v}	0.96	2.37	3.118 (4)	134
C22—H22···O2^{ii}	0.93	2.63	3.418 (4)	142
C27—H27*C*···O1	0.96	2.56	3.460 (5)	156
C32—H32···O21^{vi}	0.93	2.53	3.172 (4)	127
C32—H32···O1^{ii}	0.93	2.53	3.247 (4)	134
C35—H35···N5	0.93	2.69	3.156 (4)	112
C35—H35···O3^{iv}	0.93	2.62	3.325 (4)	133

Symmetry codes: (i) -*x*+1, -*y*+1, -*z*+1; (ii) -*x*+2, -*y*+1, -*z*+1; (iii) *x*-1, *y*, *z*; (iv) -*x*+1, -*y*, -*z*+1; (v) -*x*+1, -*y*, -*z*; (vi) *x*+1, *y*, *z*.

Document origin: *publCIF* [Westrip, S. P. publCIF: Software for Editing, Validating and Formatting Crystallographic Information Files. *J. Apply. Cryst.* **2010**, *43*, 920-925].

2 Crystallography for complex [4-NO_2]

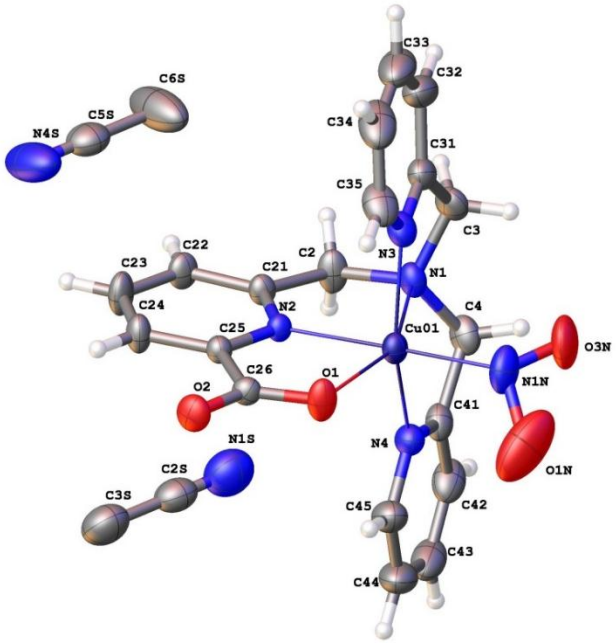

View of the structure with one disorder component of the NO_2 group omitted and displacement ellipsoids drawn at 30% probability level. Both MeCN molecules are modelled as 0.5-occupied.

Refinement

Crystal data, data collection and structure refinement details are summarized in Table 1.

Computing details

Data collection: *APEX3* Ver. 2016.9-0 (Bruker-AXS, 2016); cell refinement: *SAINT* V8.37A (Bruker-AXS, 2016); data reduction: *APEX3* Ver. 2016.9-0 (Bruker-AXS, 2016); program(s) used to solve structure: XT (Sheldrick, 2015); program(s) used to refine structure: XL (Sheldrick, 2008); molecular graphics: Olex2 (Dolomanov *et al.*, 2009); software used to prepare material for publication: Olex2 (Dolomanov *et al.*, 2009).

References

Dolomanov, O. V.; Bourhis, L. J.; Gildea, R. J.; Howard, J. A. K.; Puschmann, H. OLEX2: a Complete Structure Solution, Refinement and Analysis Program. *J. Appl. Cryst.* **2009**, *42*, 339-341.

Sheldrick, G. M. A Short History of SHELX. *Acta Cryst. A,* **2008**, *64*, 112-122.

Sheldrick, G. M. *SHELXT* – Integrated Space-Group and Crystal-Structure Determination. *Acta Cryst. A*, **2015**, *71*, 3–8.

(gc_3_1_cu_carbno2)

Crystal data

$C_{19}H_{17}CuN_5O_4 \cdot 0.5(C_2H_3N)$	ρ_{calcd} = 1.404 g cm^{-3}
M_r = 463.44	Mo $K\alpha$ radiation, λ = 0.71073 Å
Orthorhombic, *Pbcn*	Cell parameters from 8296 reflections
a = 14.817(8) Å	θ = 2.2–31.9°
b = 19.01(1) Å	μ = 1.03 mm^{-1}
c = 15.569(9) Å	T = 298 K
V = 4386(4) Å^3	Block, green
Z = 8	0.39 × 0.33 × 0.16 mm
F(000) = 1904	

Data collection

Bruker D8 VENTURE diffractometer	5403 independent reflections
Radiation source: microfocus sealed tube, INCOATEC Iμs 3.0	4657 reflections with $I > 2\sigma(I)$
Multilayer mirror optics monochromator	R_{int} = 0.037
Detector resolution: 7.4074 pixels mm^{-1}	θ_{max} = 28.3°, θ_{min} = 2.2°
ϕ and ω scans	h = -19→19
Absorption correction: multi-scan *SADABS2016*/2 (Bruker,2016/2) was used for absorption correction. wR2(int) was 0.0898 before and 0.0529 after correction. The Ratio of minimum to maximum transmission is 0.8335. The λ/2 correction factor is Not present.	k = -25→25
T_{min} = 0.623, T_{max} = 0.747	l = -20→20
71877 measured reflections	

Refinement

Refinement on F^2	Primary atom site location: dual
Least-squares matrix: full	Hydrogen site location: inferred from neighbouring sites
$R[F^2 > 2\sigma(F^2)]$ = 0.044	H-atom parameters constrained
$wR(F^2)$ = 0.141	$w = 1/[\sigma^2(F_o^2) + (0.079P)^2 + 2.190P]$ where $P = (F_o^2 + 2F_c^2)/3$
S = 1.05	$(\Delta/\sigma)_{max}$ = 0.004
5403 reflections	$\Delta\rangle_{max}$ = 0.56 e Å^{-3}
301 parameters	$\Delta\rangle_{min}$ = -0.48 e Å^{-3}
1 restraint	

Special details

Geometry. All esds (except the esd in the dihedral angle between two l.s. planes) are estimated using the full covariance matrix. The cell esds are taken into account individually in the estimation of esds in distances, angles and torsion angles; correlations between esds in cell parameters are only used when they are defined by crystal symmetry. An approximate (isotropic) treatment of cell esds is used for estimating esds involving l.s. planes.

Fractional atomic coordinates and isotropic or equivalent isotropic displacement parameters (Å^2)

	x	*y*	*z*	U_{iso}*/U_{eq}	Occ. (<1)
Cu01	0.26261 (2)	0.37064 (2)	0.53241 (2)	0.03993 (12)	
O1	0.25122 (14)	0.47893 (9)	0.48287 (11)	0.0609 (5)	
O2	0.23277 (13)	0.59071 (9)	0.52628 (11)	0.0574 (5)	
N1	0.27069 (14)	0.28446 (9)	0.64337 (13)	0.0476 (4)	
N2	0.25809 (10)	0.42997 (8)	0.64080 (10)	0.0348 (3)	
N3	0.12982 (14)	0.34556 (11)	0.55205 (13)	0.0540 (5)	
N4	0.39746 (15)	0.35236 (11)	0.54591 (13)	0.0531 (5)	
C2	0.2794 (2)	0.32233 (12)	0.72471 (15)	0.0597 (6)	
H2A	0.340117	0.315473	0.746507	0.072*	
H2B	0.237968	0.301823	0.765919	0.072*	
C3	0.1869 (2)	0.24452 (12)	0.63354 (17)	0.0599 (6)	
H3A	0.171132	0.223027	0.688005	0.072*	
H3B	0.196004	0.207211	0.591931	0.072*	
C4	0.35166 (19)	0.24511 (12)	0.62077 (17)	0.0582 (6)	
H4A	0.337606	0.211308	0.576068	0.070*	
H4B	0.373288	0.219509	0.670578	0.070*	
C21	0.26091 (13)	0.40110 (11)	0.71908 (13)	0.0406 (4)	
C22	0.25084 (17)	0.44222 (14)	0.79240 (14)	0.0523 (5)	
H22	0.251938	0.421905	0.846725	0.063*	

C23	0.2391 (2)	0.51438 (15)	0.78268 (16)	0.0655 (7)	
H23	0.232634	0.542717	0.830975	0.079*	
C24	0.23702 (18)	0.54430 (13)	0.70165 (16)	0.0561 (6)	
H24	0.229690	0.592549	0.694738	0.067*	
C25	0.24615 (12)	0.50034 (11)	0.63096 (12)	0.0366 (4)	
C26	0.24261 (13)	0.52638 (11)	0.53886 (13)	0.0399 (4)	
C31	0.11040 (18)	0.29136 (13)	0.60409 (16)	0.0570 (6)	
C32	0.0213 (2)	0.27625 (18)	0.6260 (2)	0.0820 (9)	
H32	0.007655	0.238757	0.662154	0.098*	
C33	-0.0459 (2)	0.3179 (3)	0.5932 (3)	0.1032 (14)	
H33	-0.105701	0.308777	0.607350	0.124*	
C34	-0.0257 (3)	0.3726 (2)	0.5399 (3)	0.1023 (16)	
H34	-0.071343	0.400777	0.517601	0.123*	
C35	0.0625 (2)	0.38544 (18)	0.5198 (2)	0.0762 (9)	
H35	0.076453	0.422462	0.483116	0.091*	
C41	0.42448 (17)	0.29517 (12)	0.58939 (16)	0.0555 (5)	
C42	0.5144 (2)	0.28077 (18)	0.6024 (2)	0.0751 (8)	
H42	0.532128	0.241365	0.633511	0.090*	
C43	0.5776 (2)	0.3258 (2)	0.5684 (2)	0.0918 (12)	
H43	0.638786	0.316677	0.575532	0.110*	
C44	0.5501 (3)	0.3843 (2)	0.5241 (3)	0.0955 (13)	
H44	0.592461	0.415372	0.501675	0.115*	
C45	0.4593 (2)	0.39668 (18)	0.5130 (2)	0.0740 (8)	
H45	0.440521	0.436063	0.482416	0.089*	
O2N	0.1967 (5)	0.3253 (4)	0.3690 (3)	0.137 (3)	0.5
O3N	0.2589 (4)	0.2550 (3)	0.4197 (4)	0.1055 (19)	0.5
N1N	0.2627 (2)	0.31953 (16)	0.42141 (18)	0.0823 (8)	

N1S	0.500000	0.4289 (7)	0.750000	0.123 (4)	0.5
C2S	0.500000	0.4862 (7)	0.750000	0.081 (2)	0.5
C3S	0.500000	0.5624 (7)	0.750000	0.109 (4)	0.5
N4S	0.000000	0.6189 (6)	0.750000	0.156 (6)	0.5
C5S	0.000000	0.5596 (6)	0.750000	0.081 (2)	0.5
C6S	0.000000	0.4828 (7)	0.750000	0.169 (8)	0.5
O1N	0.3269 (4)	0.3343 (3)	0.3641 (2)	0.185 (2)	

Atomic displacement parameters (Å^2)

	U^{11}	U^{22}	U^{33}	U^{12}	U^{13}	U^{23}
Cu01	0.05371 (19)	0.03560 (17)	0.03048 (16)	0.00093 (9)	-0.00097 (9)	-0.00111 (8)
O1	0.1086 (15)	0.0429 (9)	0.0311 (7)	0.0053 (8)	0.0015 (7)	0.0044 (6)
O2	0.0758 (12)	0.0378 (8)	0.0587 (10)	0.0065 (7)	0.0014 (8)	0.0117 (7)
N1	0.0666 (12)	0.0331 (8)	0.0429 (9)	-0.0010 (7)	-0.0041 (8)	0.0010 (7)
N2	0.0423 (8)	0.0333 (7)	0.0287 (7)	-0.0006 (6)	-0.0007 (5)	-0.0013 (6)
N3	0.0548 (11)	0.0507 (10)	0.0564 (11)	-0.0001 (9)	-0.0101 (9)	-0.0102 (9)
N4	0.0520 (11)	0.0472 (10)	0.0600 (11)	-0.0015 (8)	0.0064 (9)	-0.0073 (9)
C2	0.102 (2)	0.0417 (11)	0.0358 (10)	0.0061 (12)	-0.0078 (11)	0.0066 (8)
C3	0.0740 (16)	0.0433 (11)	0.0625 (14)	-0.0128 (11)	0.0062 (12)	0.0055 (10)
C4	0.0702 (15)	0.0391 (10)	0.0653 (14)	0.0085 (10)	-0.0136 (12)	0.0004 (10)
C21	0.0525 (11)	0.0385 (10)	0.0308 (9)	-0.0018 (8)	-0.0029 (7)	0.0008 (8)
C22	0.0735 (14)	0.0538 (13)	0.0295 (10)	0.0003 (10)	-0.0026 (9)	-0.0016 (9)
C23	0.108 (2)	0.0509 (13)	0.0376 (12)	0.0040 (12)	0.0007 (11)	-0.0141 (10)
C24	0.0852 (17)	0.0374 (10)	0.0456 (12)	0.0026 (10)	0.0003 (10)	-0.0089 (9)
C25	0.0411 (9)	0.0336 (9)	0.0350 (9)	-0.0006 (7)	-0.0005 (7)	-0.0008 (7)
C26	0.0443 (10)	0.0372 (10)	0.0383 (10)	0.0008 (7)	0.0012 (7)	0.0055 (7)
C31	0.0598 (13)	0.0554 (13)	0.0559 (13)	-0.0102 (10)	0.0077 (10)	-0.0146 (10)

C32	0.0699 (19)	0.091 (2)	0.085 (2)	-0.0210 (16)	0.0244 (16)	-0.0257 (17)
C33	0.0540 (17)	0.127 (3)	0.129 (3)	-0.007 (2)	0.0120 (19)	-0.058 (3)
C34	0.062 (2)	0.105 (3)	0.140 (4)	0.0169 (19)	-0.031 (2)	-0.049 (3)
C35	0.0633 (17)	0.0718 (18)	0.094 (2)	0.0072 (14)	-0.0292 (15)	-0.0152 (15)
C41	0.0590 (13)	0.0506 (12)	0.0569 (13)	0.0063 (10)	-0.0100 (10)	-0.0159 (10)
C42	0.0644 (17)	0.086 (2)	0.0748 (18)	0.0154 (15)	-0.0203 (14)	-0.0268 (15)
C43	0.0525 (15)	0.120 (3)	0.103 (3)	0.0037 (18)	-0.0067 (16)	-0.053 (2)
C44	0.0646 (19)	0.105 (3)	0.117 (3)	-0.027 (2)	0.0273 (19)	-0.035 (2)
C45	0.0679 (17)	0.0654 (16)	0.089 (2)	-0.0100 (14)	0.0233 (16)	-0.0078 (16)
O2N	0.161 (6)	0.191 (7)	0.059 (3)	-0.078 (6)	-0.003 (3)	-0.033 (4)
O3N	0.155 (5)	0.079 (3)	0.082 (4)	-0.007 (3)	0.001 (3)	-0.047 (3)
N1N	0.113 (2)	0.0772 (19)	0.0565 (15)	0.0109 (14)	-0.0051 (14)	-0.0269 (14)
N1S	0.129 (9)	0.137 (9)	0.103 (7)	0.000	0.021 (6)	0.000
C2S	0.061 (5)	0.103 (7)	0.079 (6)	0.000	0.013 (4)	0.000
C3S	0.104 (8)	0.123 (9)	0.099 (8)	0.000	0.032 (6)	0.000
N4S	0.104 (8)	0.095 (7)	0.269 (18)	0.000	0.075 (10)	0.000
C5S	0.053 (4)	0.100 (7)	0.089 (6)	0.000	0.010 (4)	0.000
C6S	0.089 (8)	0.079 (7)	0.34 (2)	0.000	0.033 (12)	0.000
O1N	0.212 (5)	0.260 (5)	0.084 (2)	0.090 (4)	0.010 (3)	-0.023 (3)

Geometric parameters (Å, º) for (gc_3_1_cu_carbno2)

Cu01—O1	2.205 (2)	C23—H23	0.9300
Cu01—N1	2.384 (2)	C23—C24	1.384 (4)
Cu01—N2	2.0309 (18)	C24—H24	0.9300
Cu01—N3	2.047 (2)	C24—C25	1.389 (3)
Cu01—N4	2.039 (2)	C25—C26	1.518 (3)

Cu01—N1N	1.983 (3)	C31—C32	1.394 (4)
O1—C26	1.261 (3)	C32—H32	0.9300
O2—C26	1.247 (3)	C32—C33	1.370 (6)
N1—C2	1.462 (3)	C33—H33	0.9300
N1—C3	1.463 (3)	C33—C34	1.363 (6)
N1—C4	1.457 (3)	C34—H34	0.9300
N2—C21	1.337 (3)	C34—C35	1.366 (6)
N2—C25	1.358 (3)	C35—H35	0.9300
N3—C31	1.342 (3)	C41—C42	1.375 (4)
N3—C35	1.350 (4)	C42—H42	0.9300
N4—C41	1.342 (3)	C42—C43	1.375 (5)
N4—C45	1.347 (4)	C43—H43	0.9300
C2—H2A	0.9700	C43—C44	1.371 (6)
C2—H2B	0.9700	C44—H44	0.9300
C2—C21	1.525 (3)	C44—C45	1.376 (5)
C3—H3A	0.9700	C45—H45	0.9300
C3—H3B	0.9700	O2N—N1N	1.278 (6)
C3—C31	1.513 (4)	O3N—N1N	1.228 (6)
C4—H4A	0.9700	N1N—O1N	1.335 (6)
C4—H4B	0.9700	N1S—C2S	1.091 (14)
C4—C41	1.520 (4)	C2S—C3S	1.448 (17)
C21—C22	1.392 (3)	N4S—C5S	1.127 (13)
C22—H22	0.9300	C5S—C6S	1.460 (16)
C22—C23	1.391 (4)		
O1—Cu01—N1	154.03 (7)	C21—C22—H22	120.7
N2—Cu01—O1	76.67 (7)	C23—C22—C21	118.6 (2)

N2—Cu01—N1	77.37 (8)	C23—C22—H22	120.7
N2—Cu01—N3	88.49 (7)	C22—C23—H23	119.8
N2—Cu01—N4	92.37 (7)	C24—C23—C22	120.5 (2)
N3—Cu01—O1	101.32 (8)	C24—C23—H23	119.8
N3—Cu01—N1	77.29 (8)	C23—C24—H24	120.9
N4—Cu01—O1	105.68 (8)	C23—C24—C25	118.2 (2)
N4—Cu01—N1	76.05 (8)	C25—C24—H24	120.9
N4—Cu01—N3	152.45 (10)	N2—C25—C24	121.09 (19)
N1N—Cu01—O1	98.79 (11)	N2—C25—C26	115.62 (17)
N1N—Cu01—N1	107.14 (11)	C24—C25—C26	123.3 (2)
N1N—Cu01—N2	175.21 (10)	O1—C26—C25	114.59 (18)
N1N—Cu01—N3	90.94 (11)	O2—C26—O1	127.2 (2)
N1N—Cu01—N4	90.34 (11)	O2—C26—C25	118.18 (19)
C26—O1—Cu01	115.72 (14)	N3—C31—C3	118.3 (2)
C2—N1—Cu01	107.07 (13)	N3—C31—C32	120.6 (3)
C3—N1—Cu01	103.79 (15)	C32—C31—C3	121.0 (3)
C3—N1—C2	114.9 (2)	C31—C32—H32	120.8
C4—N1—Cu01	102.67 (14)	C33—C32—C31	118.5 (3)
C4—N1—C2	112.9 (2)	C33—C32—H32	120.8
C4—N1—C3	114.0 (2)	C32—C33—H33	119.7
C21—N2—Cu01	121.89 (14)	C34—C33—C32	120.6 (3)
C21—N2—C25	120.74 (17)	C34—C33—H33	119.7
C25—N2—Cu01	117.24 (13)	C33—C34—H34	120.5
C31—N3—Cu01	118.36 (17)	C35—C34—C33	119.0 (4)
C31—N3—C35	119.8 (3)	C35—C34—H34	120.5
C35—N3—Cu01	121.6 (2)	N3—C35—C34	121.4 (4)
C41—N4—Cu01	118.85 (17)	N3—C35—H35	119.3

C41—N4—C45	119.7 (3)	C34—C35—H35	119.3
C45—N4—Cu01	121.4 (2)	N4—C41—C4	117.2 (2)
N1—C2—H2A	108.6	N4—C41—C42	121.6 (3)
N1—C2—H2B	108.6	C42—C41—C4	121.1 (3)
N1—C2—C21	114.70 (17)	C41—C42—H42	120.7
H2A—C2—H2B	107.6	C41—C42—C43	118.6 (3)
C21—C2—H2A	108.6	C43—C42—H42	120.7
C21—C2—H2B	108.6	C42—C43—H43	120.1
N1—C3—H3A	109.4	C44—C43—C42	119.8 (3)
N1—C3—H3B	109.4	C44—C43—H43	120.1
N1—C3—C31	111.22 (19)	C43—C44—H44	120.2
H3A—C3—H3B	108.0	C43—C44—C45	119.5 (4)
C31—C3—H3A	109.4	C45—C44—H44	120.3
C31—C3—H3B	109.4	N4—C45—C44	120.7 (4)
N1—C4—H4A	109.7	N4—C45—H45	119.7
N1—C4—H4B	109.7	C44—C45—H45	119.7
N1—C4—C41	109.92 (18)	O2N—N1N—Cu01	120.9 (4)
H4A—C4—H4B	108.2	O2N—N1N—O1N	95.8 (4)
C41—C4—H4A	109.7	O3N—N1N—Cu01	120.5 (3)
C41—C4—H4B	109.7	O1N—N1N—Cu01	118.7 (3)
N2—C21—C2	117.45 (18)	N1S—C2S—C3S	180.0
N2—C21—C22	120.9 (2)	N4S—C5S—C6S	180.0
C22—C21—C2	121.60 (19)		

Document origin: *publCIF* [Westrip, S. P. publCIF: Software for Editing, Validating and Formatting Crystallographic Information Files. *J. Apply. Cryst.* **2010**, *43*, 920-925].

3 Crystallography for complex [CoIII(o-catecholate)(5,5'-dimethyl-2,2'-bipyridine)$_2$]$^+$

Refinement

Crystal data, data collection and structure refinement details are summarized in the tables below.

Computing details

Data collection: *CrystalClear*-SM Expert 2.1 b31 (Rigaku, 2014); cell refinement: *CrysAlis PRO* 1.171.38.41 (Rigaku OD, 2015); data reduction: *CrysAlis PRO* 1.171.38.41 (Rigaku OD, 2015); program used to solve the structure: SuperFlip (Palatinus & Chapuis, 2007); program(s) used to refine structure: *SHELXL* (Sheldrick, 2015); molecular graphics: Olex2 (Dolomanov *et al.*, 2009); software used to prepare material for publication: Olex2 (Dolomanov *et al.*, 2009).

References

Dolomanov, O. V., Bourhis, L. J., Gildea, R. J., Howard, J. A. K. & Puschmann, H. (2009). *J. Appl. Cryst.* **42**, 339–341.

Sheldrick, G. M. (2015). *Acta Cryst.* C**71**, 3–8.

Palatinus, L., Chapuis, G. (2007). *J. Appl. Cryst.* **40**, 786-790.

Crystal data

$C_{30}H_{28}CoN_4O_2 \cdot 1(NO_3)$	D_x = 1.057 Mg m^{-3}
M_r = 597.50	Mo $K\alpha$ radiation, λ = 0.71075 Å
Trigonal, $P\bar{3}c1$	Cell parameters from 5011 reflections
a = 21.2619 (15) Å	θ = 2.2–25.1°
c = 14.3882 (10) Å	μ = 0.49 mm^{-1}
V = 5633.0 (7) Å^3	T = 100 K
Z = 6	Plate, brown
F(000) = 1860	0.06 × 0.06 × 0.01 mm

Data collection

Rigaku AFC12 (Right) diffractometer	3339 independent reflections
Radiation source: rotating anode, FR-E+ SuperBright	1325 reflections with $I > 2\sigma(I)$
Detector resolution: 28.5714 pixels mm^{-1}	R_{int} = 0.240

ω scans	θ_{max} = 25.1°, θ_{min} = 1.9°
Absorption correction: multi-scan *CrysAlis PRO* 1.171.38.41 (Rigaku Oxford Diffraction, 2015) Empirical absorption correction using spherical harmonics, implemented in SCALE3 ABSPACK scaling algorithm.	*h* = -24→25
T_{min} = 0.357, T_{max} = 1.000	*k* = -25→25
40590 measured reflections	*l* = -12→17

Refinement

Refinement on F^2	13 restraints
Least-squares matrix: full	Hydrogen site location: inferred from neighbouring sites
$R[F^2 > 2\sigma(F^2)]$ = 0.126	H-atom parameters constrained
$wR(F^2)$ = 0.403	$w = 1/[\sigma^2(F_o^2) + (0.2P)^2]$ where $P = (F_o^2 + 2F_c^2)/3$
S = 1.11	$(\Delta/\sigma)_{max}$ = 0.002
3339 reflections	$\Delta\rangle_{max}$ = 0.89 e Å^{-3}
197 parameters	$\Delta\rangle_{min}$ = -0.41 e Å^{-3}

Special details

Geometry. All esds (except the esd in the dihedral angle between two l.s. planes) are estimated using the full covariance matrix. The cell esds are taken into account individually in the estimation of esds in distances, angles and torsion angles; correlations between esds in cell parameters are only used when they are defined by crystal symmetry. An approximate (isotropic) treatment of cell esds is used for estimating esds involving l.s. planes.
Refinement. Overall data quality not high, probably due to large solvent accessible voids (19% of cell) and solvent loss. The electron density in the channels was accounted for using SQUEEZE which calculated a void volume of 1149 Å^3 containing 214 electrons which could correspond to 5 molecules of Et_2O. There are two nitrate anion sites modelled. One is 1/6 occupied and the second is disordered around a 3-fold axis. There is one central orientation with the nitrogen on the 3-fold axis which is 1/6 occupied and 3 equivalent orientations which have 2 oxygens common with the first orientation and third which lies on the 3-fold axis. Distance restraints were applied and partially occupied atoms refined with isotropic adps.

Fractional atomic coordinates and isotropic or equivalent isotropic displacement parameters (Å²)

	x	*y*	*z*	U_{iso}*/U_{eq}	Occ. (<1)
Co1	0.48521 (10)	0.48521 (10)	0.2500	0.0611 (8)	
O1	0.3985 (4)	0.4449 (4)	0.1799 (4)	0.0663 (19)	
N1	0.5275 (4)	0.5716 (5)	0.1714 (5)	0.062 (2)	
N2	0.5253 (4)	0.4489 (5)	0.1587 (5)	0.064 (2)	
C2	0.3533 (7)	0.3780 (6)	0.2113 (6)	0.070 (3)	
C3	0.2856 (6)	0.3325 (7)	0.1729 (8)	0.082 (3)	
H3	0.2698	0.3484	0.1207	0.098*	
C4	0.2403 (7)	0.2635 (7)	0.2102 (8)	0.096 (4)	
H4	0.1943	0.2322	0.1828	0.116*	
C11	0.5254 (6)	0.6322 (6)	0.1845 (6)	0.071 (3)	
H11	0.5002	0.6357	0.2370	0.085*	
C12	0.5582 (6)	0.6897 (6)	0.1250 (7)	0.078 (3)	
C13	0.5927 (6)	0.6855 (6)	0.0501 (7)	0.083 (4)	
H13	0.6146	0.7248	0.0075	0.100*	
C14	0.5963 (5)	0.6236 (7)	0.0352 (6)	0.071 (3)	
H14	0.6222	0.6204	-0.0167	0.085*	
C15	0.5620 (5)	0.5659 (6)	0.0964 (6)	0.062 (3)	
C16	0.5594 (5)	0.4963 (6)	0.0873 (6)	0.063 (3)	
C17	0.5875 (5)	0.4728 (7)	0.0141 (6)	0.073 (3)	
H17	0.6118	0.5045	-0.0365	0.088*	
C18	0.5799 (6)	0.4055 (6)	0.0157 (7)	0.075 (3)	
H18	0.5972	0.3898	-0.0350	0.090*	
C19	0.5474 (6)	0.3599 (7)	0.0897 (7)	0.078 (3)	
C20	0.5210 (6)	0.3850 (7)	0.1600 (6)	0.068 (3)	
H20	0.4985	0.3543	0.2120	0.082*	
C21	0.5497 (8)	0.7563 (6)	0.1430 (8)	0.118 (5)	
H21A	0.4998	0.7403	0.1625	0.177*	
H21B	0.5606	0.7851	0.0860	0.177*	
H21C	0.5834	0.7861	0.1922	0.177*	
C22	0.5397 (8)	0.2863 (7)	0.0940 (8)	0.102 (4)	
H22A	0.5719	0.2856	0.1422	0.153*	
H22B	0.5528	0.2746	0.0337	0.153*	
H22C	0.4893	0.2503	0.1089	0.153*	

O10N	0.862 (2)	0.732 (3)	0.033 (3)	0.15 (2)*	0.1667
O11N	0.7705 (17)	0.669 (2)	0.122 (2)	0.067 (11)*	0.1666
O12N	0.866 (2)	0.662 (3)	0.137 (4)	0.14 (2)*	0.1667
N10N	0.8335 (16)	0.6894 (17)	0.098 (2)	0.11 (2)*	0.1667
O1N	0.3677 (6)	0.6302 (6)	0.2000 (8)	0.106 (4)*	0.7221
O2N	0.3333	0.6667	0.0961 (14)	0.156 (9)*	0.8333
N1N	0.3333	0.6667	0.1992 (17)	0.034 (6)*	0.1666
N2N	0.3199 (6)	0.6405 (8)	0.1753 (12)	0.034 (6)*	0.2778

Atomic displacement parameters ($Å^2$)

	U^{11}	U^{22}	U^{33}	U^{12}	U^{13}	U^{23}
Co1	0.0788 (12)	0.0788 (12)	0.0266 (10)	0.0401 (12)	-0.0038 (4)	0.0038 (4)
O1	0.077 (5)	0.075 (5)	0.037 (4)	0.030 (4)	-0.009 (3)	0.004 (3)
N1	0.081 (6)	0.075 (6)	0.025 (4)	0.035 (5)	-0.007 (4)	0.008 (4)
N2	0.082 (6)	0.080 (6)	0.032 (4)	0.041 (5)	-0.010 (4)	-0.005 (4)
C2	0.086 (8)	0.082 (8)	0.043 (6)	0.043 (7)	0.002 (6)	0.001 (5)
C3	0.081 (9)	0.098 (9)	0.063 (7)	0.044 (8)	-0.007 (6)	0.002 (7)
C4	0.087 (9)	0.094 (9)	0.093 (9)	0.034 (8)	-0.030 (7)	-0.007 (8)
C11	0.116 (9)	0.061 (7)	0.035 (5)	0.043 (7)	-0.010 (5)	0.000 (5)
C12	0.124 (10)	0.063 (7)	0.035 (6)	0.038 (7)	0.001 (6)	-0.001 (5)
C13	0.115 (10)	0.068 (8)	0.038 (6)	0.025 (7)	-0.018 (6)	0.006 (5)
C14	0.069 (7)	0.094 (9)	0.030 (5)	0.026 (7)	-0.012 (5)	-0.005 (6)
C15	0.074 (7)	0.064 (7)	0.030 (5)	0.023 (6)	-0.008 (5)	0.004 (5)
C16	0.050 (6)	0.091 (8)	0.033 (6)	0.025 (6)	-0.007 (5)	0.006 (5)
C17	0.061 (7)	0.126 (10)	0.025 (5)	0.041 (7)	-0.005 (4)	0.012 (6)
C18	0.122 (10)	0.091 (9)	0.046 (6)	0.078 (8)	-0.024 (6)	-0.011 (6)
C19	0.111 (9)	0.109 (9)	0.039 (6)	0.075 (8)	-0.016 (6)	-0.004 (6)
C20	0.093 (8)	0.087 (9)	0.032 (5)	0.051 (7)	-0.007 (5)	0.001 (5)
C21	0.200 (15)	0.074 (8)	0.060 (7)	0.054 (9)	-0.003 (9)	0.003 (6)
C22	0.183 (13)	0.128 (11)	0.055 (7)	0.123 (10)	0.000 (8)	0.000 (7)

*Geometric parameters (Å, º) for complex **2***

Co1—O1	1.889 (6)	C17—C18	1.359 (14)
Co1—O1^{i}	1.889 (6)	C18—H18	0.9500
Co1—N1	1.951 (8)	C18—C19	1.371 (14)

Co1—N1^{i}	1.951 (8)	C19—C20	1.387 (13)
Co1—N2	1.926 (8)	C19—C22	1.491 (15)
Co1—N2^{i}	1.926 (8)	C20—H20	0.9500
O1—C2	1.335 (11)	C21—H21A	0.9800
N1—C11	1.325 (11)	C21—H21B	0.9800
N1—C15	1.344 (11)	C21—H21C	0.9800
N2—C16	1.366 (11)	C22—H22A	0.9800
N2—C20	1.315 (12)	C22—H22B	0.9800
C2—C2^{i}	1.439 (19)	C22—H22C	0.9800
C2—C3	1.386 (13)	O10N—N10N	1.239 (10)
C3—H3	0.9500	O11N—N10N	1.231 (10)
C3—C4	1.400 (14)	O12N—N10N	1.238 (10)
C4—C4^{i}	1.43 (2)	O1N—N1N	1.306 (7)
C4—H4	0.9500	O1N—N2N^{ii}	1.198 (9)
C11—H11	0.9500	O1N—N2N^{iii}	1.823 (17)
C11—C12	1.365 (13)	O1N—N2N	1.197 (9)
C12—C13	1.332 (14)	O2N—N2N^{iii}	1.238 (10)
C12—C21	1.535 (16)	O2N—N2N	1.238 (10)
C13—H13	0.9500	O2N—N2N^{ii}	1.238 (10)
C13—C14	1.372 (15)	N1N—O1N^{iii}	1.306 (7)
C14—H14	0.9500	N1N—O1N^{ii}	1.306 (7)
C14—C15	1.385 (13)	N2N—O1N^{iii}	1.198 (9)
C15—C16	1.458 (14)	N2N—O1N^{ii}	1.823 (17)
C16—C17	1.419 (14)	N2N—N2N^{ii}	0.84 (3)
C17—H17	0.9500	N2N—N2N^{iii}	0.84 (3)
O1—Co1—O1^{i}	88.8 (4)	C18—C17—C16	120.6 (10)
O1^{i}—Co1—N1^{i}	90.2 (3)	C18—C17—H17	119.7
O1—Co1—N1	90.2 (3)	C17—C18—H18	119.6
O1—Co1—N1^{i}	176.6 (3)	C17—C18—C19	120.7 (10)
O1^{i}—Co1—N1	176.6 (3)	C19—C18—H18	119.6
O1—Co1—N2^{i}	92.8 (3)	C18—C19—C20	116.9 (10)
O1—Co1—N2	88.9 (3)	C18—C19—C22	121.8 (10)
O1^{i}—Co1—N2	92.8 (3)	C20—C19—C22	121.4 (11)
O1^{i}—Co1—N2^{i}	88.9 (3)	N2—C20—C19	123.6 (10)
N1—Co1—N1^{i}	91.0 (4)	N2—C20—H20	118.2
N2^{i}—Co1—N1^{i}	83.9 (4)	C19—C20—H20	118.2

N2—Co1—N1	83.9 (4)	C12—C21—H21A	109.5
N2—Co1—N1^{i}	94.4 (3)	C12—C21—H21B	109.5
N2^{i}—Co1—N1	94.4 (3)	C12—C21—H21C	109.5
N2^{i}—Co1—N2	177.6 (5)	H21A—C21—H21B	109.5
C2—O1—Co1	108.9 (6)	H21A—C21—H21C	109.5
C11—N1—Co1	127.5 (7)	H21B—C21—H21C	109.5
C11—N1—C15	119.1 (9)	C19—C22—H22A	109.5
C15—N1—Co1	113.3 (7)	C19—C22—H22B	109.5
C16—N2—Co1	113.2 (7)	C19—C22—H22C	109.5
C20—N2—Co1	126.0 (7)	H22A—C22—H22B	109.5
C20—N2—C16	120.7 (9)	H22A—C22—H22C	109.5
O1—C2—C2^{i}	116.8 (5)	H22B—C22—H22C	109.5
O1—C2—C3	123.5 (9)	O11N—N10N—O10N	120.8 (13)
C3—C2—C2^{i}	119.7 (7)	O11N—N10N—O12N	118.9 (13)
C2—C3—H3	119.7	O12N—N10N—O10N	120.0 (13)
C2—C3—C4	120.6 (10)	N2N—O1N—N2N^{iii}	21.6 (8)
C4—C3—H3	119.7	N2N^{ii}—O1N—N2N^{iii}	21.6 (8)
C3—C4—C4^{i}	119.7 (6)	N2N—O1N—N2N^{ii}	40.8 (14)
C3—C4—H4	120.2	N2N^{iii}—O2N—N2N	39.4 (13)
C4^{i}—C4—H4	120.2	N2N^{iii}—O2N—N2N^{ii}	39.4 (13)
N1—C11—H11	118.9	N2N—O2N—N2N^{ii}	39.4 (13)
N1—C11—C12	122.2 (10)	O1N^{iii}—N1N—O1N^{ii}	119.99 (4)
C12—C11—H11	118.9	O1N^{iii}—N1N—O1N	119.99 (4)
C11—C12—C21	118.5 (11)	O1N^{ii}—N1N—O1N	119.99 (4)
C13—C12—C11	119.9 (10)	O1N—N2N—O1N^{ii}	94.7 (9)
C13—C12—C21	121.5 (11)	O1N—N2N—O1N^{iii}	141.5 (17)
C12—C13—H13	120.4	O1N^{iii}—N2N—O1N^{ii}	94.7 (9)
C12—C13—C14	119.2 (10)	O1N—N2N—O2N	109.3 (10)
C14—C13—H13	120.4	O1N^{iii}—N2N—O2N	109.2 (10)
C13—C14—H14	120.2	O2N—N2N—O1N^{ii}	78.3 (11)
C13—C14—C15	119.5 (10)	N2N^{ii}—N2N—O1N^{iii}	126.5 (11)
C15—C14—H14	120.2	N2N^{ii}—N2N—O1N	69.7 (12)
N1—C15—C14	120.0 (10)	N2N^{iii}—N2N—O1N^{ii}	31.9 (6)
N1—C15—C16	114.7 (9)	N2N^{iii}—N2N—O1N^{iii}	69.5 (12)
C14—C15—C16	125.3 (10)	N2N^{iii}—N2N—O1N	126.6 (11)
N2—C16—C15	114.8 (9)	N2N^{ii}—N2N—O1N^{ii}	31.8 (6)
N2—C16—C17	117.4 (10)	N2N^{iii}—N2N—O2N	70.3 (7)

C17—C16—C15	127.9 (10)	N2N^{ii}—N2N—O2N	70.3 (7)
C16—C17—H17	119.7	N2N^{iii}—N2N—N2N^{ii}	60.000 (10)
Co1—O1—C2—C2^{i}	1.5 (13)	C15—N1—C11—C12	-1.1 (15)
Co1—O1—C2—C3	-177.9 (9)	C15—C16—C17—C18	-179.3 (9)
Co1—N1—C11—C12	179.0 (8)	C16—N2—C20—C19	-2.4 (14)
Co1—N1—C15—C14	-178.4 (7)	C16—C17—C18—C19	-2.5 (15)
Co1—N1—C15—C16	1.6 (10)	C17—C18—C19—C20	2.2 (15)
Co1—N2—C16—C15	2.9 (10)	C17—C18—C19—C22	-178.8 (10)
Co1—N2—C16—C17	-176.9 (6)	C18—C19—C20—N2	0.3 (15)
Co1—N2—C20—C19	176.3 (8)	C20—N2—C16—C15	-178.2 (8)
O1^{i}—Co1—O1—C2	-0.5 (5)	C20—N2—C16—C17	2.0 (12)
O1—C2—C3—C4	-178.9 (10)	C21—C12—C13—C14	-177.5 (10)
N1—Co1—O1—C2	176.2 (6)	C22—C19—C20—N2	-178.7 (10)
N1—C11—C12—C13	1.1 (17)	N2N^{ii}—O1N—N2N—O1N^{iii}	-124 (2)
N1—C11—C12—C21	177.1 (10)	N2N^{iii}—O1N—N2N—O1N^{iii}	-104 (3)
N1—C15—C16—N2	-3.0 (11)	N2N^{iii}—O1N—N2N—O1N^{ii}	0.0 (4)
N1—C15—C16—C17	176.8 (8)	N2N^{ii}—O1N—N2N—O1N^{ii}	-20.0 (10)
N2—Co1—O1—C2	92.3 (6)	N2N^{iii}—O1N—N2N—O2N	79.3 (13)
N2^{i}—Co1—O1—C2	-89.4 (6)	N2N^{ii}—O1N—N2N—O2N	59.3 (12)
N2—C16—C17—C18	0.4 (13)	N2N^{ii}—O1N—N2N—N2N^{iii}	-20.0 (10)
C2^{i}—C2—C3—C4	1.7 (19)	N2N^{iii}—O1N—N2N—N2N^{ii}	20.0 (10)
C2—C3—C4—C4^{i}	1 (2)	N2N^{iii}—O2N—N2N—O1N^{ii}	-32.1 (7)
C11—N1—C15—C14	1.6 (13)	N2N^{ii}—O2N—N2N—O1N^{iii}	123.0 (13)
C11—N1—C15—C16	-178.4 (8)	N2N^{iii}—O2N—N2N—O1N	-123.1 (13)
C11—C12—C13—C14	-1.6 (17)	N2N^{iii}—O2N—N2N—O1N^{iii}	58.8 (15)
C12—C13—C14—C15	2.2 (15)	N2N^{ii}—O2N—N2N—O1N	-58.9 (15)
C13—C14—C15—N1	-2.2 (14)	N2N^{ii}—O2N—N2N—O1N^{ii}	32.0 (7)
C13—C14—C15—C16	177.8 (9)	N2N^{ii}—O2N—N2N—N2N^{iii}	64.2 (3)
C14—C15—C16—N2	177.0 (8)	N2N^{iii}—O2N—N2N—N2N^{ii}	-64.2 (3)
C14—C15—C16—C17	-3.2 (15)		

Symmetry codes: (i) *y*, *x*, -*z*+1/2; (ii) -*y*+1, *x*-*y*+1, *z*; (iii) -*x*+*y*, -*x*+1, *z*.

Document origin: *publCIF* [Westrip, S. P. (2010). *J. Appl. Cryst.*, **43**, 920-925].

4 Crystallography for complex $[Co_2(bdt)_2(Me_2bpy)_3]^{2+}$

Refinement

Crystal data, data collection and structure refinement details are summarized below.

Computing details

Data collection: *CrystalClear*-SM Expert 3.1 b27 (Rigaku, 2013); cell refinement: *CrysAlis PRO* 1.171.38.43 (Rigaku OD, 2015); data reduction: *CrysAlis PRO* 1.171.38.43 (Rigaku OD, 2015); program(s) used to solve structure: ShelXT (Sheldrick, 2015); program(s) used to refine structure: *SHELXL* (Sheldrick, 2015); molecular graphics: Olex2 (Dolomanov *et al.*, 2009); software used to prepare material for publication: Olex2 (Dolomanov *et al.*, 2009).

References

Dolomanov, O. V., Bourhis, L. J., Gildea, R. J., Howard, J. A. K. & Puschmann, H. (2009). *J. Appl. Cryst.* **42**, 339–341.

Sheldrick, G. M. (2015). *Acta Cryst.* A**71**, 3–8.

Sheldrick, G. M. (2015). *Acta Cryst.* C**71**, 3–8.

Crystal data

$C_{48}H_{44}Co_2N_6S_4 \cdot 2(NO_3) \cdot 1.25(H_2O) \cdot 0.25(CH_3OH)$	$F(000) = 2284$
$M_r = 1105.54$	$D_x = 1.530$ Mg m^{-3}
Monoclinic, $P2_1/n$	Mo $K\alpha$ radiation, $\lambda = 0.71073$ Å
$a = 12.6021$ (3) Å	Cell parameters from 24504 reflections
$b = 22.7893$ (5) Å	$\theta = 1.9–27.5°$
$c = 17.1872$ (6) Å	$\mu = 0.93$ mm^{-1}
$\beta = 103.500$ (3)°	$T = 100$ K
$V = 4799.7$ (2) Å^3	Cut Block, opaque dark blue
$Z = 4$	0.10 × 0.09 × 0.02 mm

Data collection

Rigaku FRE+ equipped with VHF Varimax confocal mirrors and an AFC10 goniometer and HG Saturn 724+ detector diffractometer	11002 independent reflections

Radiation source: Rotating Anode, Rigaku FRE+	8780 reflections with $I > 2\sigma(I)$
Confocal mirrors, VHF Varimax monochromator	$R_{int} = 0.053$
Detector resolution: 28.5714 pixels mm^{-1}	$\theta_{max} = 27.5°$, $\theta_{min} = 2.4°$
ω scans	$h = -16 \rightarrow 15$
Absorption correction: multi-scan *CrysAlis PRO* 1.171.38.43 (Rigaku Oxford Diffraction, 2015) Empirical absorption correction using spherical harmonics, implemented in SCALE3 ABSPACK scaling algorithm.	$k = -28 \rightarrow 29$
$T_{min} = 0.538$, $T_{max} = 1.000$	$l = -22 \rightarrow 20$
59216 measured reflections	

Refinement

Refinement on F^2	Primary atom site location: dual
Least-squares matrix: full	Hydrogen site location: mixed
$R[F^2 > 2\sigma(F^2)] = 0.043$	H atoms treated by a mixture of independent and constrained refinement
$wR(F^2) = 0.097$	$w = 1/[\sigma^2(F_o^2) + (0.037P)^2 + 6.005P]$ where $P = (F_o^2 + 2F_c^2)/3$
$S = 1.06$	$(\Delta/\sigma)_{max} = 0.001$
11002 reflections	$\Delta\rangle_{max} = 0.50$ e Å^{-3}
670 parameters	$\Delta\rangle_{min} = -0.39$ e Å^{-3}
3 restraints	

Special details

Geometry. All esds (except the esd in the dihedral angle between two l.s. planes) are estimated using the full covariance matrix. The cell esds are taken into account individually in the estimation of esds in distances, angles and torsion angles; correlations between esds in cell parameters are only used when they are defined by crystal symmetry. An approximate (isotropic) treatment of cell esds is used for estimating esds involving l.s. planes.
Refinement. A region containing solvent was modelled as 0.75 H2O with hydrogens located in difference Fourier map, 0.25 MeOH and 0.25 H2O and a further separate 0.25 H2O all of which were modelled without H-atoms. The H were included in the unit cell contents and all values dervied from them. One of the NO3- anions was modelled with the oxygen atoms over 2 partially occupied sites with the occupancy refining to 0.9/0.1.

Fractional atomic coordinates and isotropic or equivalent isotropic displacement parameters (Å²)

	x	*y*	*z*	U_{iso}*/U_{eq}	Occ. (<1)
Co1	0.54995 (3)	0.70078 (2)	0.50482 (2)	0.01185 (8)	
Co2	0.37780 (3)	0.76246 (2)	0.60399 (2)	0.01115 (8)	
S1	0.41693 (5)	0.76699 (2)	0.48192 (4)	0.01213 (12)	

S2	0.67458 (5)	0.77413 (2)	0.53444 (4)	0.01385 (13)	
S3	0.51514 (5)	0.69616 (2)	0.62584 (4)	0.01206 (12)	
S4	0.43999 (5)	0.62172 (3)	0.46839 (4)	0.01580 (13)	
N1	0.67428 (16)	0.64808 (8)	0.52709 (13)	0.0141 (4)	
N2	0.57015 (16)	0.69755 (8)	0.39575 (13)	0.0154 (4)	
N3	0.26599 (16)	0.70239 (8)	0.56724 (12)	0.0125 (4)	
N4	0.34346 (16)	0.74519 (8)	0.70875 (13)	0.0132 (4)	
N5	0.48038 (16)	0.82532 (8)	0.64835 (12)	0.0121 (4)	
N6	0.27371 (16)	0.82901 (8)	0.57922 (13)	0.0138 (4)	
C1	0.7278 (2)	0.62953 (10)	0.59915 (16)	0.0175 (5)	
H1	0.705975	0.643295	0.643916	0.021*	
C2	0.8147 (2)	0.59054 (11)	0.61024 (17)	0.0199 (6)	
C3	0.8445 (2)	0.57065 (11)	0.54205 (17)	0.0209 (6)	
H3	0.899972	0.543064	0.546652	0.025*	
C4	0.7925 (2)	0.59136 (10)	0.46759 (17)	0.0178 (5)	
H4	0.814743	0.579197	0.422219	0.021*	
C5	0.7065 (2)	0.63069 (10)	0.46111 (16)	0.0151 (5)	
C6	0.64727 (19)	0.65830 (10)	0.38622 (16)	0.0151 (5)	
C7	0.6659 (2)	0.64753 (11)	0.31154 (17)	0.0190 (5)	
H7	0.718005	0.620111	0.305352	0.023*	
C8	0.6066 (2)	0.67784 (11)	0.24596 (17)	0.0206 (6)	
H8	0.618845	0.670726	0.195490	0.025*	
C9	0.5287 (2)	0.71896 (11)	0.25514 (16)	0.0182 (5)	
C10	0.5134 (2)	0.72674 (10)	0.33182 (16)	0.0165 (5)	
H10	0.461008	0.753587	0.339224	0.020*	
C11	0.5981 (2)	0.83620 (10)	0.49671 (15)	0.0147 (5)	
C12	0.6492 (2)	0.88993 (11)	0.49032 (17)	0.0198 (6)	
H12	0.724804	0.892852	0.505596	0.024*	
C13	0.5872 (2)	0.93861 (11)	0.46131 (17)	0.0239 (6)	
H13	0.621806	0.974257	0.457975	0.029*	
C14	0.4745 (2)	0.93533 (11)	0.43706 (17)	0.0219 (6)	
H14	0.433882	0.968416	0.417207	0.026*	
C15	0.4228 (2)	0.88253 (10)	0.44262 (16)	0.0170 (5)	
H15	0.347312	0.879674	0.425812	0.020*	
C16	0.4846 (2)	0.83374 (10)	0.47351 (15)	0.0141 (5)	
C17	0.4308 (2)	0.59203 (10)	0.56019 (16)	0.0172 (5)	
C18	0.3898 (2)	0.53558 (11)	0.56629 (18)	0.0255 (6)	
H18	0.369445	0.512155	0.520950	0.031*	
C19	0.3796 (3)	0.51461 (12)	0.63966 (19)	0.0313 (7)	
H19	0.351272	0.477211	0.642642	0.038*	
C20	0.4103 (2)	0.54764 (12)	0.70874 (18)	0.0254 (6)	
H20	0.402000	0.532799	0.757371	0.030*	

C21	0.4536 (2)	0.60310 (11)	0.70463 (17)	0.0185 (5)	
H21	0.476832	0.625435	0.750757	0.022*	
C22	0.46196 (19)	0.62514 (10)	0.63040 (16)	0.0151 (5)	
C23	0.58775 (19)	0.82023 (10)	0.68042 (15)	0.0138 (5)	
H23	0.617659	0.782800	0.688807	0.017*	
C24	0.6565 (2)	0.86836 (10)	0.70174 (15)	0.0149 (5)	
C25	0.6096 (2)	0.92350 (11)	0.69214 (16)	0.0174 (5)	
H25	0.653222	0.956740	0.704031	0.021*	
C26	0.4975 (2)	0.92923 (10)	0.66477 (16)	0.0157 (5)	
H26	0.464910	0.966047	0.661645	0.019*	
C27	0.43487 (19)	0.87975 (10)	0.64225 (15)	0.0139 (5)	
C28	0.3173 (2)	0.88103 (10)	0.60833 (15)	0.0147 (5)	
C29	0.2533 (2)	0.93085 (11)	0.60350 (17)	0.0199 (6)	
H29	0.282924	0.965850	0.626709	0.024*	
C30	0.1446 (2)	0.92771 (12)	0.56356 (19)	0.0274 (7)	
H30	0.100549	0.960791	0.559966	0.033*	
C31	0.1013 (2)	0.87555 (12)	0.52896 (19)	0.0255 (6)	
C32	0.1690 (2)	0.82697 (11)	0.53962 (17)	0.0206 (6)	
H32	0.140404	0.791273	0.518266	0.025*	
C33	0.38776 (19)	0.77026 (10)	0.77916 (15)	0.0145 (5)	
H33	0.436908	0.800879	0.780352	0.017*	
C34	0.3639 (2)	0.75276 (11)	0.85075 (16)	0.0168 (5)	
C35	0.2887 (2)	0.70755 (11)	0.84741 (16)	0.0182 (5)	
H35	0.269152	0.695296	0.893741	0.022*	
C36	0.2433 (2)	0.68089 (11)	0.77507 (16)	0.0172 (5)	
H36	0.194057	0.650170	0.772605	0.021*	
C37	0.27176 (19)	0.70036 (10)	0.70607 (15)	0.0135 (5)	
C38	0.23024 (19)	0.67529 (10)	0.62701 (15)	0.0135 (5)	
C39	0.1608 (2)	0.62748 (10)	0.61195 (16)	0.0169 (5)	
H39	0.137227	0.609361	0.653389	0.020*	
C40	0.1270 (2)	0.60705 (10)	0.53431 (16)	0.0181 (5)	
H40	0.081923	0.574281	0.523625	0.022*	
C41	0.1598 (2)	0.63514 (10)	0.47245 (16)	0.0164 (5)	
C42	0.22858 (19)	0.68338 (10)	0.49189 (15)	0.0144 (5)	
H42	0.249636	0.703366	0.450773	0.017*	
C43	0.8719 (3)	0.57173 (14)	0.69321 (19)	0.0339 (7)	
H43A	0.948297	0.580435	0.702127	0.051*	
H43B	0.862211	0.530295	0.698904	0.051*	
H43C	0.841619	0.592439	0.731632	0.051*	
C44	0.4642 (2)	0.75424 (13)	0.18627 (17)	0.0247 (6)	
H44A	0.435897	0.728670	0.141884	0.037*	
H44B	0.510683	0.783154	0.170736	0.037*	

H44C	0.404823	0.773434	0.202184	0.037*	
C45	0.7764 (2)	0.85857 (11)	0.73320 (18)	0.0225 (6)	
H45A	0.807587	0.891674	0.764953	0.034*	
H45B	0.810648	0.853973	0.689215	0.034*	
H45C	0.787678	0.823790	0.765594	0.034*	
C46	-0.0149 (2)	0.87065 (13)	0.4802 (2)	0.0421 (9)	
H46A	-0.014920	0.855976	0.427847	0.063*	
H46B	-0.048752	0.908628	0.475571	0.063*	
H46C	-0.054846	0.844216	0.506254	0.063*	
C47	0.4207 (2)	0.78189 (12)	0.92722 (16)	0.0212 (6)	
H47A	0.421650	0.823570	0.919294	0.032*	
H47B	0.494271	0.767607	0.943237	0.032*	
H47C	0.382706	0.773179	0.968165	0.032*	
C48	0.1282 (2)	0.61436 (12)	0.38797 (17)	0.0231 (6)	
H48A	0.059866	0.593877	0.379190	0.035*	
H48B	0.183412	0.588405	0.377795	0.035*	
H48C	0.120978	0.647430	0.352515	0.035*	
O5	0.7153 (16)	0.6497 (9)	0.7930 (12)	0.028 (6)*	0.101 (5)
O6	0.7516 (2)	0.69832 (13)	0.78350 (15)	0.0418 (8)	0.899 (5)
O7	0.712 (3)	0.7421 (16)	0.807 (2)	0.075 (11)*	0.101 (5)
O8	0.6385 (2)	0.74196 (12)	0.83989 (16)	0.0402 (8)	0.899 (5)
O9	0.611 (2)	0.7023 (12)	0.8585 (16)	0.047 (7)*	0.101 (5)
O10	0.6569 (2)	0.64822 (11)	0.85058 (17)	0.0471 (9)	0.899 (5)
O1W	0.6996 (3)	0.53314 (16)	0.8143 (3)	0.0542 (10)	0.75
H1WA	0.662 (3)	0.523 (2)	0.7691 (17)	0.036 (15)*	0.75
H1WB	0.683 (5)	0.5676 (13)	0.822 (4)	0.08 (2)*	0.75
N7	0.68209 (19)	0.69516 (11)	0.82444 (15)	0.0258 (5)	
O1	0.35197 (17)	0.93560 (8)	0.78680 (13)	0.0306 (5)	
O2	0.36252 (16)	1.02680 (8)	0.75128 (12)	0.0264 (4)	
O3	0.43001 (15)	0.99950 (8)	0.87446 (12)	0.0244 (4)	
N8	0.38117 (17)	0.98773 (10)	0.80437 (14)	0.0207 (5)	
O1M	0.1509 (8)	0.9946 (5)	0.3668 (6)	0.051 (3)*	0.25
C1M	0.0885 (11)	1.0326 (6)	0.4003 (9)	0.040 (3)*	0.25
O3W	0.5864 (15)	0.5406 (8)	0.8878 (11)	0.119 (6)*	0.25
O2W	0.6435 (9)	0.4947 (4)	0.6541 (6)	0.052 (3)	0.25

Atomic displacement parameters (Å^2)

	U^{11}	U^{22}	U^{33}	U^{12}	U^{13}	U^{23}
Co1	0.01222 (16)	0.00785 (15)	0.01577 (19)	0.00024 (11)	0.00386 (13)	0.00025 (12)
Co2	0.01133 (16)	0.00735 (14)	0.01484 (18)	-0.00088 (11)	0.00320 (13)	0.00023 (12)

S1	0.0124 (3)	0.0084 (3)	0.0158 (3)	-0.0004 (2)	0.0038 (2)	0.0012 (2)
S2	0.0126 (3)	0.0105 (3)	0.0186 (3)	-0.0008 (2)	0.0039 (2)	0.0000 (2)
S3	0.0128 (3)	0.0074 (3)	0.0159 (3)	-0.0003 (2)	0.0033 (2)	0.0005 (2)
S4	0.0180 (3)	0.0109 (3)	0.0185 (3)	-0.0027 (2)	0.0042 (3)	-0.0016 (2)
N1	0.0144 (10)	0.0085 (9)	0.0198 (12)	-0.0007 (7)	0.0050 (9)	-0.0003 (8)
N2	0.0150 (11)	0.0114 (10)	0.0196 (12)	-0.0032 (8)	0.0037 (9)	-0.0007 (8)
N3	0.0114 (10)	0.0106 (9)	0.0153 (11)	0.0009 (7)	0.0026 (8)	0.0017 (8)
N4	0.0126 (10)	0.0098 (9)	0.0175 (12)	0.0009 (7)	0.0043 (8)	0.0007 (8)
N5	0.0138 (10)	0.0083 (9)	0.0144 (11)	-0.0009 (7)	0.0040 (8)	-0.0006 (8)
N6	0.0137 (10)	0.0116 (9)	0.0162 (12)	-0.0003 (8)	0.0037 (8)	0.0014 (8)
C1	0.0183 (13)	0.0141 (11)	0.0209 (15)	0.0016 (9)	0.0063 (11)	0.0032 (10)
C2	0.0180 (13)	0.0165 (12)	0.0251 (15)	0.0022 (10)	0.0047 (11)	0.0056 (11)
C3	0.0172 (13)	0.0129 (12)	0.0344 (17)	0.0029 (9)	0.0096 (12)	0.0018 (11)
C4	0.0182 (13)	0.0117 (11)	0.0249 (15)	0.0003 (9)	0.0080 (11)	-0.0030 (10)
C5	0.0168 (12)	0.0080 (10)	0.0210 (14)	-0.0039 (9)	0.0054 (10)	-0.0024 (9)
C6	0.0140 (12)	0.0107 (11)	0.0214 (14)	-0.0029 (9)	0.0057 (10)	-0.0010 (10)
C7	0.0188 (13)	0.0139 (12)	0.0257 (16)	-0.0015 (9)	0.0083 (11)	-0.0037 (10)
C8	0.0223 (14)	0.0218 (13)	0.0192 (15)	-0.0048 (10)	0.0081 (11)	-0.0027 (11)
C9	0.0157 (13)	0.0188 (12)	0.0202 (15)	-0.0062 (10)	0.0041 (11)	0.0007 (10)
C10	0.0123 (12)	0.0145 (11)	0.0228 (15)	-0.0023 (9)	0.0044 (10)	0.0034 (10)
C11	0.0173 (13)	0.0121 (11)	0.0158 (14)	-0.0005 (9)	0.0061 (10)	0.0006 (9)
C12	0.0173 (13)	0.0164 (12)	0.0260 (16)	-0.0046 (10)	0.0056 (11)	0.0001 (11)
C13	0.0287 (15)	0.0121 (12)	0.0307 (17)	-0.0066 (10)	0.0066 (13)	0.0029 (11)
C14	0.0266 (15)	0.0111 (12)	0.0281 (16)	0.0012 (10)	0.0066 (12)	0.0058 (11)
C15	0.0152 (12)	0.0138 (12)	0.0220 (15)	-0.0005 (9)	0.0042 (10)	0.0010 (10)
C16	0.0166 (12)	0.0105 (11)	0.0172 (14)	-0.0030 (9)	0.0078 (10)	0.0004 (9)
C17	0.0165 (13)	0.0111 (11)	0.0241 (15)	-0.0003 (9)	0.0048 (11)	0.0001 (10)
C18	0.0351 (16)	0.0128 (12)	0.0267 (17)	-0.0078 (11)	0.0032 (13)	-0.0035 (11)
C19	0.0420 (18)	0.0129 (13)	0.0356 (19)	-0.0099 (12)	0.0023 (14)	0.0052 (12)
C20	0.0306 (16)	0.0194 (13)	0.0251 (17)	-0.0047 (11)	0.0044 (12)	0.0092 (11)
C21	0.0185 (13)	0.0150 (12)	0.0216 (15)	-0.0002 (9)	0.0037 (11)	0.0026 (10)
C22	0.0138 (12)	0.0066 (10)	0.0247 (15)	0.0007 (8)	0.0039 (10)	0.0026 (9)
C23	0.0133 (12)	0.0134 (11)	0.0146 (13)	0.0014 (9)	0.0032 (10)	-0.0002 (9)
C24	0.0142 (12)	0.0139 (11)	0.0170 (14)	-0.0008 (9)	0.0044 (10)	-0.0027 (9)
C25	0.0191 (13)	0.0128 (11)	0.0206 (14)	-0.0039 (9)	0.0053 (11)	-0.0039 (10)
C26	0.0163 (12)	0.0096 (11)	0.0213 (14)	0.0003 (9)	0.0047 (10)	0.0005 (10)
C27	0.0151 (12)	0.0112 (11)	0.0162 (13)	0.0009 (9)	0.0051 (10)	0.0005 (9)
C28	0.0153 (12)	0.0113 (11)	0.0179 (14)	-0.0019 (9)	0.0049 (10)	0.0014 (9)
C29	0.0207 (14)	0.0114 (11)	0.0260 (16)	0.0003 (9)	0.0021 (11)	0.0003 (10)
C30	0.0219 (15)	0.0141 (12)	0.0422 (19)	0.0042 (10)	-0.0008 (13)	0.0017 (12)
C31	0.0172 (14)	0.0188 (13)	0.0353 (18)	0.0022 (10)	-0.0044 (12)	0.0003 (12)
C32	0.0168 (13)	0.0135 (12)	0.0288 (16)	-0.0010 (9)	-0.0004 (11)	-0.0006 (11)

C33	0.0124 (12)	0.0137 (11)	0.0170 (14)	0.0013 (9)	0.0024 (10)	-0.0007 (9)
C34	0.0159 (12)	0.0163 (12)	0.0178 (14)	0.0050 (9)	0.0029 (10)	0.0004 (10)
C35	0.0171 (13)	0.0208 (13)	0.0176 (14)	0.0042 (10)	0.0060 (10)	0.0052 (10)
C36	0.0141 (12)	0.0159 (12)	0.0218 (15)	-0.0009 (9)	0.0044 (10)	0.0041 (10)
C37	0.0125 (12)	0.0104 (11)	0.0180 (14)	0.0026 (9)	0.0044 (10)	0.0006 (9)
C38	0.0119 (12)	0.0122 (11)	0.0163 (13)	0.0007 (9)	0.0031 (10)	0.0001 (9)
C39	0.0169 (13)	0.0139 (12)	0.0212 (15)	-0.0015 (9)	0.0073 (11)	0.0025 (10)
C40	0.0150 (12)	0.0126 (11)	0.0260 (15)	-0.0041 (9)	0.0034 (11)	-0.0021 (10)
C41	0.0149 (12)	0.0137 (11)	0.0203 (14)	-0.0015 (9)	0.0035 (10)	-0.0024 (10)
C42	0.0138 (12)	0.0124 (11)	0.0173 (14)	0.0001 (9)	0.0041 (10)	0.0009 (9)
C43	0.0308 (17)	0.0374 (17)	0.0339 (19)	0.0183 (13)	0.0084 (14)	0.0117 (14)
C44	0.0234 (15)	0.0289 (15)	0.0209 (16)	-0.0001 (11)	0.0035 (12)	0.0050 (12)
C45	0.0172 (13)	0.0169 (12)	0.0325 (17)	-0.0028 (10)	0.0039 (12)	-0.0054 (11)
C46	0.0244 (16)	0.0229 (15)	0.066 (3)	0.0031 (12)	-0.0152 (16)	-0.0028 (15)
C47	0.0239 (14)	0.0231 (13)	0.0174 (14)	0.0023 (10)	0.0060 (11)	-0.0003 (11)
C48	0.0237 (14)	0.0223 (13)	0.0230 (16)	-0.0083 (11)	0.0049 (12)	-0.0059 (11)
O6	0.0293 (14)	0.070 (2)	0.0274 (15)	0.0030 (12)	0.0101 (11)	-0.0012 (13)
O8	0.0452 (17)	0.0358 (15)	0.0332 (16)	0.0181 (12)	-0.0035 (12)	-0.0092 (12)
O10	0.0465 (17)	0.0364 (15)	0.0481 (19)	-0.0161 (12)	-0.0098 (13)	0.0154 (13)
O1W	0.048 (2)	0.035 (2)	0.084 (3)	0.0054 (17)	0.024 (2)	-0.004 (2)
N7	0.0233 (13)	0.0278 (13)	0.0220 (14)	0.0057 (10)	-0.0038 (10)	-0.0054 (10)
O1	0.0408 (12)	0.0223 (10)	0.0328 (13)	-0.0170 (9)	0.0172 (10)	-0.0099 (9)
O2	0.0304 (11)	0.0211 (10)	0.0286 (12)	0.0009 (8)	0.0083 (9)	-0.0011 (8)
O3	0.0231 (10)	0.0223 (10)	0.0267 (12)	-0.0026 (8)	0.0034 (8)	-0.0075 (8)
N8	0.0173 (11)	0.0199 (11)	0.0273 (14)	-0.0032 (9)	0.0099 (10)	-0.0059 (10)
O2W	0.078 (8)	0.032 (5)	0.049 (7)	-0.009 (5)	0.020 (6)	-0.018 (5)

Geometric parameters (Å, º) for (2016ncs0400)

Co1—S1	2.2212 (6)	C23—H23	0.9300
Co1—S2	2.2688 (6)	C23—C24	1.393 (3)
Co1—S3	2.2261 (7)	C24—C25	1.382 (3)
Co1—S4	2.2702 (7)	C24—C45	1.497 (3)
Co1—N1	1.940 (2)	C25—H25	0.9300
Co1—N2	1.951 (2)	C25—C26	1.388 (4)
Co2—S1	2.2668 (7)	C26—H26	0.9300
Co2—S3	2.2620 (6)	C26—C27	1.379 (3)
Co2—N3	1.960 (2)	C27—C28	1.460 (3)
Co2—N4	1.987 (2)	C28—C29	1.384 (3)
Co2—N5	1.9608 (19)	C29—H29	0.9300
Co2—N6	1.985 (2)	C29—C30	1.383 (4)
S1—C16	1.766 (2)	C30—H30	0.9300

S2—C11	1.749 (2)	C30—C31	1.383 (4)
S3—C22	1.760 (2)	C31—C32	1.384 (4)
S4—C17	1.745 (3)	C31—C46	1.512 (4)
N1—C1	1.333 (3)	C32—H32	0.9300
N1—C5	1.350 (3)	C33—H33	0.9300
N2—C6	1.359 (3)	C33—C34	1.392 (4)
N2—C10	1.340 (3)	C34—C35	1.391 (4)
N3—C38	1.362 (3)	C34—C47	1.497 (4)
N3—C42	1.342 (3)	C35—H35	0.9300
N4—C33	1.337 (3)	C35—C36	1.382 (4)
N4—C37	1.358 (3)	C36—H36	0.9300
N5—C23	1.342 (3)	C36—C37	1.389 (3)
N5—C27	1.360 (3)	C37—C38	1.454 (3)
N6—C28	1.352 (3)	C38—C39	1.383 (3)
N6—C32	1.337 (3)	C39—H39	0.9300
C1—H1	0.9300	C39—C40	1.383 (4)
C1—C2	1.389 (3)	C40—H40	0.9300
C2—C3	1.387 (4)	C40—C41	1.384 (4)
C2—C43	1.502 (4)	C41—C42	1.392 (3)
C3—H3	0.9300	C41—C48	1.490 (4)
C3—C4	1.378 (4)	C42—H42	0.9300
C4—H4	0.9300	C43—H43A	0.9600
C4—C5	1.391 (3)	C43—H43B	0.9600
C5—C6	1.470 (4)	C43—H43C	0.9600
C6—C7	1.380 (4)	C44—H44A	0.9600
C7—H7	0.9300	C44—H44B	0.9600
C7—C8	1.383 (4)	C44—H44C	0.9600
C8—H8	0.9300	C45—H45A	0.9600
C8—C9	1.393 (4)	C45—H45B	0.9600
C9—C10	1.387 (4)	C45—H45C	0.9600
C9—C44	1.503 (4)	C46—H46A	0.9600
C10—H10	0.9300	C46—H46B	0.9600
C11—C12	1.400 (3)	C46—H46C	0.9600
C11—C16	1.394 (3)	C47—H47A	0.9600
C12—H12	0.9300	C47—H47B	0.9600
C12—C13	1.381 (4)	C47—H47C	0.9600
C13—H13	0.9300	C48—H48A	0.9600
C13—C14	1.387 (4)	C48—H48B	0.9600
C14—H14	0.9300	C48—H48C	0.9600
C14—C15	1.382 (3)	O5—N7	1.28 (2)
C15—H15	0.9300	O6—N7	1.247 (3)
C15—C16	1.390 (3)	O7—N7	1.19 (4)

C17—C18	1.399 (3)	O8—N7	1.256 (3)
C17—C22	1.399 (4)	O9—N7	1.19 (3)
C18—H18	0.9300	O10—N7	1.230 (3)
C18—C19	1.382 (4)	O1W—H1WA	0.839 (19)
C19—H19	0.9300	O1W—H1WB	0.83 (2)
C19—C20	1.383 (4)	O1—N8	1.259 (3)
C20—H20	0.9300	O2—N8	1.257 (3)
C20—C21	1.385 (3)	O3—N8	1.247 (3)
C21—H21	0.9300	O1M—C1M	1.384 (13)
C21—C22	1.398 (4)		
S1—Co1—S2	89.63 (2)	C19—C20—C21	119.2 (3)
S1—Co1—S3	83.83 (2)	C21—C20—H20	120.4
S1—Co1—S4	95.94 (2)	C20—C21—H21	120.4
S2—Co1—S4	173.08 (3)	C20—C21—C22	119.3 (3)
S3—Co1—S2	95.87 (3)	C22—C21—H21	120.4
S3—Co1—S4	88.82 (2)	C17—C22—S3	119.36 (19)
N1—Co1—S1	175.44 (6)	C21—C22—S3	118.8 (2)
N1—Co1—S2	85.81 (6)	C21—C22—C17	121.8 (2)
N1—Co1—S3	96.47 (7)	N5—C23—H23	118.5
N1—Co1—S4	88.62 (6)	N5—C23—C24	123.1 (2)
N1—Co1—N2	83.43 (9)	C24—C23—H23	118.5
N2—Co1—S1	96.76 (6)	C23—C24—C45	119.4 (2)
N2—Co1—S2	90.27 (6)	C25—C24—C23	117.5 (2)
N2—Co1—S3	173.84 (6)	C25—C24—C45	123.1 (2)
N2—Co1—S4	85.02 (6)	C24—C25—H25	120.0
S3—Co2—S1	81.99 (2)	C24—C25—C26	120.0 (2)
N3—Co2—S1	91.66 (6)	C26—C25—H25	120.0
N3—Co2—S3	92.96 (6)	C25—C26—H26	120.4
N3—Co2—N4	82.03 (8)	C27—C26—C25	119.3 (2)
N3—Co2—N5	174.02 (8)	C27—C26—H26	120.4
N3—Co2—N6	94.31 (8)	N5—C27—C26	121.4 (2)
N4—Co2—S1	171.18 (6)	N5—C27—C28	114.8 (2)
N4—Co2—S3	92.13 (6)	C26—C27—C28	123.8 (2)
N5—Co2—S1	93.47 (6)	N6—C28—C27	114.7 (2)
N5—Co2—S3	90.80 (6)	N6—C28—C29	121.1 (2)
N5—Co2—N4	93.19 (8)	C29—C28—C27	124.3 (2)
N5—Co2—N6	82.41 (8)	C28—C29—H29	120.6
N6—Co2—S1	92.43 (6)	C30—C29—C28	118.9 (2)
N6—Co2—S3	170.96 (6)	C30—C29—H29	120.6
N6—Co2—N4	94.18 (8)	C29—C30—H30	119.9
Co1—S1—Co2	97.08 (3)	C31—C30—C29	120.2 (2)

C16—S1—Co1	103.94 (8)	C31—C30—H30	119.9
C16—S1—Co2	109.18 (9)	C30—C31—C32	117.5 (2)
C11—S2—Co1	102.71 (8)	C30—C31—C46	122.4 (2)
Co1—S3—Co2	97.08 (3)	C32—C31—C46	120.1 (2)
C22—S3—Co1	104.19 (9)	N6—C32—C31	123.0 (2)
C22—S3—Co2	109.70 (8)	N6—C32—H32	118.5
C17—S4—Co1	102.90 (9)	C31—C32—H32	118.5
C1—N1—Co1	126.13 (17)	N4—C33—H33	118.4
C1—N1—C5	120.1 (2)	N4—C33—C34	123.2 (2)
C5—N1—Co1	113.81 (17)	C34—C33—H33	118.4
C6—N2—Co1	113.47 (17)	C33—C34—C47	119.4 (2)
C10—N2—Co1	127.20 (18)	C35—C34—C33	117.5 (2)
C10—N2—C6	119.2 (2)	C35—C34—C47	123.1 (2)
C38—N3—Co2	114.39 (16)	C34—C35—H35	120.1
C42—N3—Co2	126.90 (16)	C36—C35—C34	119.8 (2)
C42—N3—C38	118.5 (2)	C36—C35—H35	120.1
C33—N4—Co2	127.04 (16)	C35—C36—H36	120.3
C33—N4—C37	119.1 (2)	C35—C36—C37	119.5 (2)
C37—N4—Co2	113.72 (17)	C37—C36—H36	120.3
C23—N5—Co2	127.35 (16)	N4—C37—C36	120.9 (2)
C23—N5—C27	118.5 (2)	N4—C37—C38	114.8 (2)
C27—N5—Co2	114.10 (16)	C36—C37—C38	124.3 (2)
C28—N6—Co2	113.52 (16)	N3—C38—C37	114.6 (2)
C32—N6—Co2	127.36 (17)	N3—C38—C39	121.5 (2)
C32—N6—C28	119.1 (2)	C39—C38—C37	123.9 (2)
N1—C1—H1	118.6	C38—C39—H39	120.5
N1—C1—C2	122.8 (2)	C40—C39—C38	119.0 (2)
C2—C1—H1	118.6	C40—C39—H39	120.5
C1—C2—C43	120.1 (3)	C39—C40—H40	119.8
C3—C2—C1	117.0 (2)	C39—C40—C41	120.3 (2)
C3—C2—C43	123.0 (2)	C41—C40—H40	119.8
C2—C3—H3	119.7	C40—C41—C42	117.5 (2)
C4—C3—C2	120.6 (2)	C40—C41—C48	122.8 (2)
C4—C3—H3	119.7	C42—C41—C48	119.6 (2)
C3—C4—H4	120.4	N3—C42—C41	123.1 (2)
C3—C4—C5	119.2 (2)	N3—C42—H42	118.5
C5—C4—H4	120.4	C41—C42—H42	118.5
N1—C5—C4	120.2 (2)	C2—C43—H43A	109.5
N1—C5—C6	114.7 (2)	C2—C43—H43B	109.5
C4—C5—C6	125.0 (2)	C2—C43—H43C	109.5
N2—C6—C5	114.1 (2)	H43A—C43—H43B	109.5
N2—C6—C7	120.8 (2)	H43A—C43—H43C	109.5

C7—C6—C5	125.2 (2)	H43B—C43—H43C	109.5
C6—C7—H7	120.3	C9—C44—H44A	109.5
C6—C7—C8	119.5 (2)	C9—C44—H44B	109.5
C8—C7—H7	120.3	C9—C44—H44C	109.5
C7—C8—H8	119.8	H44A—C44—H44B	109.5
C7—C8—C9	120.3 (3)	H44A—C44—H44C	109.5
C9—C8—H8	119.8	H44B—C44—H44C	109.5
C8—C9—C44	122.5 (3)	C24—C45—H45A	109.5
C10—C9—C8	116.9 (2)	C24—C45—H45B	109.5
C10—C9—C44	120.7 (2)	C24—C45—H45C	109.5
N2—C10—C9	123.3 (2)	H45A—C45—H45B	109.5
N2—C10—H10	118.3	H45A—C45—H45C	109.5
C9—C10—H10	118.3	H45B—C45—H45C	109.5
C12—C11—S2	120.86 (19)	C31—C46—H46A	109.5
C16—C11—S2	120.90 (18)	C31—C46—H46B	109.5
C16—C11—C12	118.2 (2)	C31—C46—H46C	109.5
C11—C12—H12	120.0	H46A—C46—H46B	109.5
C13—C12—C11	120.0 (2)	H46A—C46—H46C	109.5
C13—C12—H12	120.0	H46B—C46—H46C	109.5
C12—C13—H13	119.4	C34—C47—H47A	109.5
C12—C13—C14	121.2 (2)	C34—C47—H47B	109.5
C14—C13—H13	119.4	C34—C47—H47C	109.5
C13—C14—H14	120.3	H47A—C47—H47B	109.5
C15—C14—C13	119.5 (2)	H47A—C47—H47C	109.5
C15—C14—H14	120.3	H47B—C47—H47C	109.5
C14—C15—H15	120.2	C41—C48—H48A	109.5
C14—C15—C16	119.5 (2)	C41—C48—H48B	109.5
C16—C15—H15	120.2	C41—C48—H48C	109.5
C11—C16—S1	119.61 (18)	H48A—C48—H48B	109.5
C15—C16—S1	118.86 (18)	H48A—C48—H48C	109.5
C15—C16—C11	121.5 (2)	H48B—C48—H48C	109.5
C18—C17—S4	121.8 (2)	H1WA—O1W—H1WB	107 (6)
C18—C17—C22	117.7 (2)	O6—N7—O8	118.0 (3)
C22—C17—S4	120.42 (18)	O7—N7—O5	118 (2)
C17—C18—H18	120.0	O9—N7—O5	132.4 (17)
C19—C18—C17	120.1 (3)	O9—N7—O7	108 (2)
C19—C18—H18	120.0	O10—N7—O6	122.1 (3)
C18—C19—H19	119.1	O10—N7—O8	119.9 (3)
C18—C19—C20	121.9 (2)	O2—N8—O1	120.0 (2)
C20—C19—H19	119.1	O3—N8—O1	119.0 (2)
C19—C20—H20	120.4	O3—N8—O2	121.0 (2)

Document origin: *publCIF*.

Appendix B: Theoretical calculation.

B.1 Geometry optimization for molecules presented in Chapter 3

Geometry Optimized Coordinates for **3-NCCH$_3$**

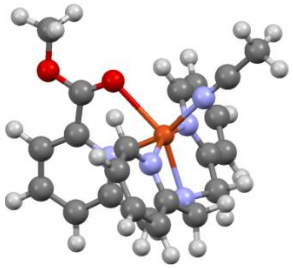

Cu	4.87284655224627	3.33140880847674	4.22629351366373
O	3.33531153342869	2.55191157120005	5.99206898847816
O	2.74320742352666	3.12587433938695	8.10565895283937
N	6.45289172385105	4.77981802851929	3.43848008896325
N	5.07651402993155	4.63855531507252	5.88319366458611
N	6.55015642604935	2.34416733313080	4.80540270917570
N	3.66978314442972	4.67644197982296	3.30017687125026
N	4.24597983973340	1.80188727907542	3.06909793874787
C	6.72079937571425	5.80400034380670	4.46449752619783
C	7.58820443400991	3.86961896539606	3.19105070420524
C	5.78442196347605	5.30603408138571	2.23171365032976
C	3.91508683543081	0.92609205295350	2.37157162759800
C	3.50210985532852	-0.16211836077182	1.51009661708014
C	5.94745997824215	5.64576886254855	5.76942648892773
C	6.14389030933079	6.55249466580748	6.83571381074852
C	5.41467879104905	6.38173036957348	8.01699405772446
C	4.50266256470939	5.31493632537815	8.11965705617993
C	4.36340410964136	4.45991275381151	7.01877614796732
C	3.43164780717201	3.28218473330040	6.98051874273785
C	1.81584418025281	2.01356253843556	8.16303829161324
C	7.70802910509400	2.80386623793987	4.26387379870975
C	8.94167097428173	2.25184762837162	4.64583064719851
C	8.96591524743189	1.20596076398672	5.58098944400420
C	7.75666515322248	0.73812624750310	6.11938483437429
C	6.56231143046186	1.34190716053363	5.70770614737338
C	4.30405231343903	5.54038010132666	2.46515768313152
C	3.58651712654320	6.55528997311354	1.81058876294678
C	2.20186662798067	6.65964377492180	2.01528706508935
C	1.56511659757774	5.75171411021091	2.87683539089325
C	2.34050317210317	4.77072083863017	3.50768516710968
H	6.49609208854211	6.81389210533899	4.05760408301024
H	7.80480875068086	5.82286060602305	4.70779234064941
H	8.55169028396489	4.41472465105760	3.08493110173286
H	7.41019270065369	3.35440805157947	2.22297312542874
H	6.26395066989958	6.23559966659906	1.85393458558531
H	5.88718159855072	4.54973074533492	1.42400784283381
H	3.62345077454578	0.13451758249342	0.44886960586176
H	2.43846077493741	-0.40724131280951	1.70166373418405
H	4.12485242157814	-1.05600023239045	1.71236507553874
H	6.86303758356647	7.37836495165741	6.72801626598519
H	5.55239187861976	7.07510515604867	8.86013775497657
H	3.91295763958690	5.14678793386890	9.03036148261573
H	2.35539602652092	1.06050705593096	8.00378516313487
H	1.03184759345455	2.13246244527486	7.39064195903667
H	1.37533655525052	2.04771311536670	9.17320034512547
H	9.87128759300053	2.64298875378447	4.20775347208799
H	9.92369424678427	0.76213852872602	5.89025766170434
H	7.73012315957214	-0.07943463120607	6.85385702687377
H	5.58659929069701	1.02197549295584	6.10376787655905
H	4.11632925271394	7.25474838425547	1.14699529430638
H	1.62526172726812	7.44899045043332	1.50987044807400
H	0.48377806586124	5.80007249888189	3.06969225678675
H	1.89486273006073	4.03756920494744	4.19779913806259

Total energy = -2915.40844804 E_h

Geometry Optimized Coordinates for **3-NO$_2$**

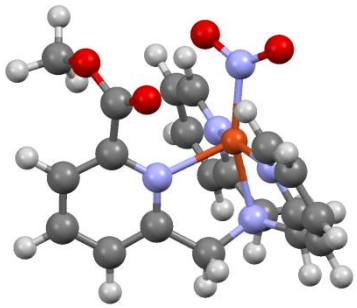

Cu	4.88638274159058	3.44302081310105	3.84616413518408
O	1.99989688332982	3.60672198394599	5.66442187091510
O	2.46624450424157	2.30047342791385	7.39626015444346
N	6.44362147237406	4.93648233081863	3.50673617044044
N	4.69838916088201	4.54053719886914	5.75262456984429
N	6.50411530532503	2.36542137492410	4.56222281723419
N	3.84744365402201	4.72785858549332	2.63358438883829
N	3.63951177163808	1.85147234301636	3.57930169515418
C	6.32430721820973	5.94996906471198	4.58511782966974
C	7.73207069370123	4.20885461271000	3.52798085091557
C	6.10894651777712	5.49614441378930	2.17365503816009
O	3.07017193170261	1.71085792989210	2.49115152464394
C	5.68006692061713	5.45647765958499	5.87056845853912
C	6.00886754175038	6.03557649434136	7.11238687064948
C	5.28257413659576	5.65670621096538	8.24837695421799
C	4.24818739268188	4.71580677785135	8.11769299101358
C	3.98698631080547	4.17837914975463	6.84498111639967
C	2.76147660044686	3.32205682148965	6.57476186211411
C	3.42368552032399	1.70356530478919	8.29677379974867
C	7.69895754338288	2.99816348896245	4.43350613759614
C	8.86029758023471	2.49938576885059	5.04632546906724
C	8.78637864549894	1.31411971432818	5.79277757760734
C	7.54765603277828	0.66442291610404	5.91380904306526
C	6.42812579444437	1.23002233605747	5.29062451055493
C	4.61344978604350	5.66962045998031	2.02530733395195
C	4.03753968677430	6.70304062959175	1.26958004949616
C	2.64061414709043	6.75183311211423	1.13665450394639
C	1.85995100667549	5.77648339525917	1.77662711715554
C	2.50360022003456	4.78185179494414	2.52504026179378
H	5.67377306495268	6.76877829970195	4.21033252294887
H	7.31105577814877	6.41071982001176	4.80046092662814
H	8.57484518390565	4.87768900403012	3.80411194408747
H	7.93908343851734	3.84978748817202	2.49780184402448
H	6.64034044451531	6.45219705662067	1.97410342291452
H	6.45364418416817	4.77054644743140	1.40766371330088
H	6.81615358041521	6.78005672049617	7.17975010712699
H	5.51321969963095	6.09535046808775	9.23030415765634
H	3.64408729438980	4.42446393681251	8.98795047594097
H	3.29160009475530	2.10945173207611	9.31847991314096
H	4.46482308788868	1.86717317921543	7.95768223042073
H	3.20598852535096	0.61963365757802	8.30468464906663
H	9.81148220489091	3.04001562914536	4.93222118544481
H	9.68561901308474	0.90591094305541	6.27775132169547
H	7.43989920965569	-0.26716160247947	6.48696985631257
H	5.42713483650659	0.77494538517446	5.35684283982565
H	4.68064784096301	7.45821882764826	0.79405524562275
H	2.16638973117393	7.55173888088287	0.54778031719114
H	0.76218269832453	5.78360419078949	1.70839251829821
H	1.93610193120125	4.00969322787513	3.06300531464275
O	3.48650569158774	1.05178071951984	4.51827251734896

Total energy = -2987.88711566 E_h

Geometry Optimized Coordinates for **3-ONO**

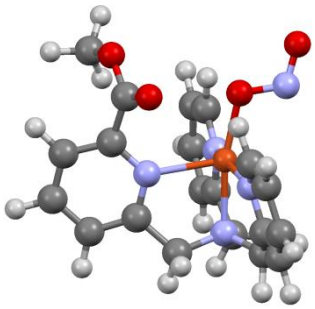

Cu	4.88204934683998	3.48294651621388	3.85742974091325
O	1.95397479518961	3.66882807172419	5.84008172924750
O	2.60051533657341	2.25574269039836	7.42469630333415
N	6.41553495992518	4.94092624653983	3.52925454970557
N	4.68865495886424	4.58965279110716	5.79542009870341
N	6.43710894856202	2.37706097099780	4.55269169377518
N	3.83986833738567	4.71264249954318	2.65129869978975
O	3.63292741708426	1.94658299880681	3.81227000607062
C	6.27761366200519	5.98696055364665	4.57837236038621
C	7.71267060525726	4.21772792324111	3.58988933314086
C	6.09602553181296	5.47345982930448	2.17533306241862
N	3.70567885975717	1.32533526333470	2.64414653621539
O	3.00981813037412	0.32324688063407	2.57346124210341
C	5.66949702694999	5.50910560343508	5.88588668440412
C	6.02657480605479	6.09956038765107	7.11327610971719
C	5.32808840347673	5.72532171283749	8.26900368171974
C	4.29605161524483	4.77840370853309	8.16990554828346
C	4.00657671778875	4.23237169480841	6.90648004583793
C	2.78878069907041	3.35457872997867	6.67145769936223
C	3.61012572778719	1.71161829457233	8.30218802146509
C	7.64798993090636	2.98170844102374	4.46071677000132
C	8.78425940572418	2.42145155434275	5.06678380035517
C	8.65830662737147	1.20775702945350	5.75965749754160
C	7.40053981730479	0.58527468895328	5.83273098108838
C	6.30823342347903	1.20993267246623	5.21901370645950
C	4.60054074395238	5.63723961280418	2.00988936946469
C	4.01124991864094	6.63116937930898	1.21412342222921
C	2.61293413503622	6.65251714554883	1.08016463364930
C	1.84177000613552	5.69264001451378	1.75543212837255
C	2.49606676394276	4.73618367104727	2.54328984244362
H	5.59437716277681	6.76932228198881	4.18477064591838
H	7.25367384305239	6.48251728937021	4.76030045768399
H	8.53286012117172	4.89050281579704	3.91564006088867
H	7.96636163076972	3.88595199149018	2.56139997290286
H	6.62965673613487	6.42604122787788	1.96926005746124
H	6.45318092036276	4.73375869572754	1.42894775250172
H	6.83339213222386	6.84627652793662	7.15602037964543
H	5.58055868284869	6.17062898542131	9.24250328619369
H	3.71684012998871	4.48612749596873	9.05677046063112
H	3.47921301309766	2.10790513688131	9.32785297569739
H	4.63325821856782	1.93330142054053	7.94086010562186
H	3.45102062282358	0.61777091997340	8.31114792121472
H	9.75517903324151	2.93237050393522	4.98882429485393
H	9.53663454084755	0.75105495087431	6.23952250449830
H	7.26185875309601	-0.36947763546297	6.35877820498106
H	5.29518975444426	0.77687504585683	5.24211608050245
H	4.64247703942788	7.37715986810447	0.70945155632934
H	2.12843439519870	7.42184291888344	0.45989302932109
H	0.74443765009773	5.68274668882986	1.68203708765142
H	1.94818599333034	3.97200131423437	3.11517989430228

Total energy = -2987.88573455 E_h

Geometry Optimized Coordinates for **3-κ^2-ONO**

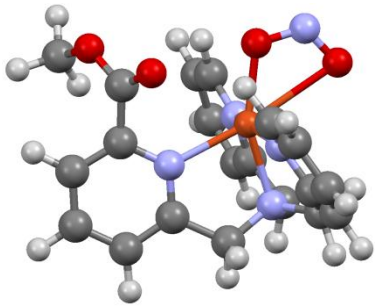

Cu	4.80567020283487	3.42497633912103	3.89769418951981
O	2.10090969574632	3.31750804473616	5.75026944570470
O	2.70322945614451	2.14275078074174	7.53061257379760
N	6.39516336450192	4.89472698198458	3.56256847763443
N	4.69272663802596	4.52278602687533	5.81968618329165
N	6.33576329518193	2.30228160039924	4.59154790612324
N	3.76947799943629	4.72001253126201	2.76263973161227
C	6.28804274567925	5.93857179872376	4.60563123411808
C	7.65555122060693	4.12185711899002	3.61706556583275
C	6.04356141909653	5.40044636127584	2.21274344687616
O	4.79145759652112	1.83467676889922	1.68289910955215
C	5.61815464512008	5.49671642819170	5.89861614770213
C	5.88280593687329	6.17040430742969	7.10865889960265
C	5.15234159866787	5.82199507127610	8.25088331455343
C	4.18672475322814	4.80515105630447	8.16347426928378
C	3.99053918350437	4.17487863535304	6.92318995112349
C	2.87308754176599	3.17544067186872	6.68449022835290
C	3.66711147575889	1.75441236476295	8.53467673783585
C	7.55761543441161	2.88484724998651	4.49010780926367
C	8.68638024373348	2.30292218319262	5.09125274208718
C	8.54467069796579	1.09391653103295	5.78870787977352
C	7.27654402336395	0.49429939505769	5.86995850167136
C	6.19277974405130	1.13704047120713	5.26020291720787
C	4.54713925119691	5.60835097171156	2.09057703824977
C	3.97262209209478	6.61768036506548	1.30235055855411
C	2.57339064548943	6.69343445290498	1.20547282412008
C	1.78534863966220	5.77005250315572	1.91137283959945
C	2.42463371014062	4.79600995170030	2.68995546957528
H	5.66725066188789	6.76613297504884	4.20066764903732
H	7.28259386459456	6.38110509404254	4.82584074956927
H	8.51055470075078	4.75428141486803	3.93810828966931
H	7.89175743027481	3.77782867446311	2.58794674478239
H	6.59313695360721	6.33134842349680	1.95121291720156
H	6.34532785921963	4.62795833092413	1.47477688967879
H	6.64547387558266	6.96274552210600	7.14518994586898
H	5.33126896253500	6.33647182552347	9.20656489371712
H	3.58961081451176	4.52388734231852	9.04164929586936
H	3.40866949346441	2.21311683664715	9.50870836020775
H	4.69965767060393	2.03402168808331	8.24800460737963
H	3.59196772728688	0.65503508877604	8.62063621016993
H	9.66605712440934	2.79593536251109	5.00593513855564
H	9.41785125095173	0.62313304050296	6.26437512001603
H	7.12338181803543	-0.45729654083359	6.39782306179727
H	5.17651064647897	0.71310520361450	5.28749632487365
H	4.61802786180038	7.33535117880492	0.77465630362099
H	2.10219687070055	7.47586545018284	0.59130828344053
H	0.68669193855709	5.80261177139539	1.86924567629724
H	1.86382845120630	4.05953232921295	3.28503524254962
O	3.62081624008114	1.79364690718980	3.49090735500684
N	3.90654955665523	1.29499352691072	2.34602448507141

Total energy = - 2987.88936649 E_h

Geometry Optimized Coordinates for **4-NCCH$_3$**

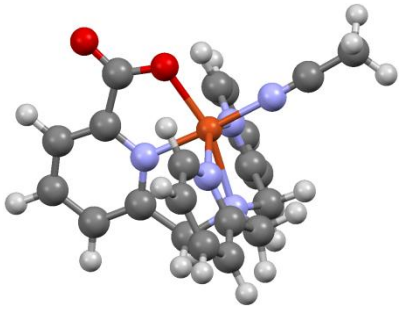

Cu	4.10906098088123	7.18965140794255	7.97804309889327
O	3.96549600911600	9.05208561285357	7.08673186967324
O	3.78060550296617	11.23374089826750	7.62161630859023
N	4.22022551314495	5.56211371098069	9.58803784620991
N	4.05013917008877	8.29679367368644	9.58484083511364
N	1.85827004691063	6.59172962588441	8.39309419228455
N	6.39992215241810	6.77473888175315	8.28650545115534
C	4.28410622684777	6.26250741245125	10.90462216952884
C	3.00505544216225	4.72739095428335	9.45927782757271
C	5.44981514352598	4.78313909469272	9.32109385454937
C	4.08867235347178	7.75802638822571	10.81129939358132
C	3.98023879116147	8.58332914560903	11.93741945393905
C	3.83878810712988	9.95938794325828	11.76033408369038
C	3.80552148929287	10.49416766182931	10.46761530361981
C	3.91173744505255	9.62266580458983	9.39037948197864
C	3.88115342117482	10.03304587649053	7.92877226944812
C	1.74830676743877	5.54519269082578	9.23092365483669
C	0.52786258759148	5.18126196123724	9.80751635009624
C	-0.61496757971066	5.91795558253949	9.48966751244842
C	-0.50141056616097	6.99812005114133	8.61288545452892
C	0.75804922160234	7.30269723503380	8.09456745425985
C	6.64094224474003	5.67240514717616	9.01954102383163
C	7.92957235113008	5.32682273283402	9.43753916987443
C	9.00011751466355	6.14368086323563	9.06960708851407
C	8.74956194974538	7.28403311146248	8.30384792754246
C	7.43179888590763	7.56309524339950	7.94010446893383
N	4.12407328867102	6.17320165264870	6.30268489293713
H	5.26592914671691	6.07489642577778	11.36669556751174
H	3.54031988888162	5.83744849416689	11.59628259648051
H	2.87334313721458	4.07540012015918	10.33960028903204
H	3.14894277797913	4.07185442843893	8.58658941652938
H	5.25387220655602	4.15271164970851	8.44015732492516
H	5.69139853120592	4.10657764349877	10.15856806911018
H	4.00731265732441	8.14633418042619	12.93592307702761
H	3.75159327174991	10.61376686563618	12.62804317143152
H	3.69462716264103	11.56281495569851	10.28473045479008
H	0.47648993811635	4.33206996233948	10.49055974539407
H	-1.57906707648801	5.65415543522705	9.92572022103129
H	-1.36647915056293	7.60134205267854	8.33805835673794
H	0.89690852217288	8.14604002234706	7.41386569725162
H	8.08716871475110	4.43130974463664	10.03995988239720
H	10.01487428728468	5.89582970031467	9.38306381498046
H	9.55457533764145	7.95190324410908	7.99783790433968
H	7.18747949208824	8.44905429407598	7.34967655875816
C	4.13528527705486	5.61514689272854	5.28818113796750
C	4.14965770759972	4.91919105435136	4.02131345211553
H	5.09108910435509	5.13035150780114	3.49528408681534
H	4.06396488121097	3.83748324477497	4.19402746669064
H	3.30472383154212	5.25757443777220	3.40584502405017

Total energy = -2875.70768268 E_h

Geometry Optimized Coordinates for **4-NO_2**

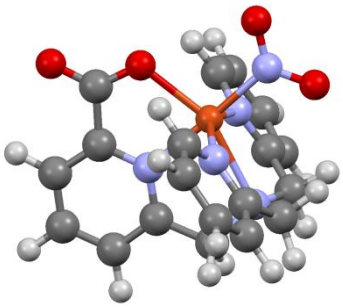

Cu	3.87114090915277	7.16115317440806	8.20319905294980
O	3.76042396174829	9.20313384618232	7.46638504249254
O	3.62368815723732	11.33230604264626	8.21759028833679
N	3.97605832240462	5.43733128521276	9.93734542357519
N	3.83622425986199	8.22428363509036	9.94301454656573
N	1.79722348675576	6.59563025641399	8.52756394587920
N	5.98352404970908	6.72246210860548	8.42198817668447
C	4.04651588242778	6.13694530951869	11.22897831246329
H	5.02959981312173	5.95095179669372	11.69247983683096
H	3.30561729593419	5.72428306701940	11.93461961675857
C	2.73959510828805	4.67801162453301	9.73807015790123
H	2.46325211838162	4.07946288644052	10.62584616464185
H	2.91318731220903	3.97085938881520	8.91251828352671
C	5.20306254468213	4.71292940980925	9.59252232752760
H	4.96891685177667	4.05675576503258	8.74069569089389
H	5.56671328725508	4.07025026555573	10.41575957102444
C	3.85793985685913	7.64385533569971	11.15129442320564
C	3.74295623794590	8.41579790548145	12.31536480382338
H	3.75399636783999	7.92990313927965	13.29205499725978
C	3.61621868601091	9.79884774258057	12.20484363860764
H	3.52397765201930	10.41453741907097	13.10045705148996
C	3.60493133247566	10.38601135508704	10.93625243592337
H	3.50829591530104	11.46219573243997	10.79620603896679
C	3.71347065641460	9.56298149139338	9.81841333582966
C	3.69728889980828	10.09305454728658	8.38695033757968
C	1.55763361688620	5.54775483236855	9.34115665864633
C	0.25925728142135	5.22762465300257	9.75044464586789
H	0.09702600880042	4.38010393082990	10.41806292944781
C	-0.81119624412037	5.99735130670867	9.29478599829271
H	-1.83017251022681	5.76215012342332	9.60440126086965
C	-0.55576944169867	7.07522556652263	8.44444772142429
H	-1.35907166241080	7.70642384562167	8.06570173508633
C	0.76572699070708	7.34181100886316	8.09103029342322
H	1.02198731046458	8.17982690757514	7.43960083549483
C	6.32248122354694	5.64154389591299	9.15416359778038
C	7.65891110853203	5.35396373467748	9.44879637538462
H	7.90250444401941	4.47977019246288	10.05396583243500
C	8.66228782200236	6.19230406946989	8.96226974511474
H	9.70991958308578	5.98306049272120	9.18267548924056
C	8.30358080433657	7.30488573596319	8.19808024494847
H	9.05214492032070	7.98992008837564	7.80103623833601
C	6.95036097882517	7.53472961950329	7.95664670980043
H	6.61481184065556	8.39597342593164	7.37552590670841
O	3.89367523464616	4.94267027147606	6.47012615480280
N	3.86063537326349	6.19276474415153	6.44853680905472
O	3.82150635132190	6.81536702414196	5.37274131710267

Total energy = -2948.20587828 E_h

Geometry Optimized Coordinates for **4-ONO**

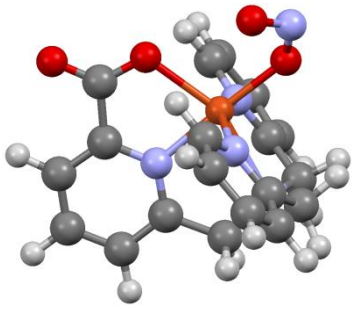

Cu	4.10742560396053	7.24469283491183	7.98073417742103
O	3.85833732688062	9.32216461960790	7.27321777841704
O	3.71730107968256	11.43226274454934	8.08090428916716
N	4.22869653870486	5.50242518095590	9.69566806501755
N	4.07107082516957	8.29469600392368	9.73589673448339
N	2.06386441400788	6.70975317097201	8.30747924387094
N	6.17966435717363	6.86385739628378	8.17556721288893
C	4.34486729505492	6.18892945730061	10.98734810741618
C	2.97950254691164	4.76595171077166	9.51076158830928
C	5.44479291798528	4.79903100804089	9.28270131253854
C	4.13012389518039	7.69535134841926	10.93408919914255
C	4.02493681318304	8.44632969457480	12.11245402308122
C	3.86814936047367	9.82815714791180	12.02708865046477
C	3.81092801591044	10.43303346319054	10.76848475283895
C	3.90944341470860	9.63042199556405	9.63427844759176
C	3.82229934225656	10.18923426060666	8.21265564898783
C	1.80868846535592	5.64495599334956	9.09415264434061
C	0.50096387483286	5.31223172186785	9.46244154846270
C	-0.56065511207883	6.08538144214694	8.99333504478049
C	-0.28781999092874	7.18063316800435	8.17074620346770
C	1.04078356766938	7.46023526343858	7.85784657873701
C	6.54472628862775	5.75660859713790	8.85619016497544
C	7.88884849770666	5.47974733646107	9.12316436394666
C	8.87193387379417	6.36092879278063	8.67273677743867
C	8.48475258185826	7.50473573667774	7.97135349007490
C	7.12674052051441	7.71848705171430	7.74540393606499
O	3.97482364002134	6.08518149142748	6.32600051184898
H	5.34998836593589	6.01282537477708	11.40524982471875
H	3.64073088911489	5.76033955758509	11.72085167302730
H	2.69005825626653	4.19395840849966	10.41182760713120
H	3.13563980023417	4.02869814060275	8.70768207721595
H	5.19066673118399	4.17116474963424	8.41453756813070
H	5.83998517949876	4.12427477206513	10.06522787951662
H	4.06586290328152	7.94475910933797	13.08049743538085
H	3.78450541020781	10.42815586008954	12.93414979725797
H	3.68321685225141	11.50813407845489	10.64680738188033
H	0.32488398883804	4.45172355949557	10.10959703583101
H	-1.58631406841846	5.83963870550964	9.27129579097143
H	-1.08398023250868	7.81561633774312	7.78343574674865
H	1.31313809346906	8.31224865883434	7.23213564695152
H	8.15361884588668	4.58223991888760	9.68335319357791
H	9.92525200330263	6.16145581358345	8.87447007598239
H	9.21650756672229	8.22489191088168	7.60635089206685
H	6.76784820872754	8.59223998655069	7.20126868170379
N	4.60091257283862	6.31314403753943	5.21070700000846
O	5.30537486954992	7.31943507433697	5.13211123112299

Total energy = -2948.20029723 E_h

Geometry Optimized Coordinates for [**4-H$_c$-NO$_2$**]$^+$

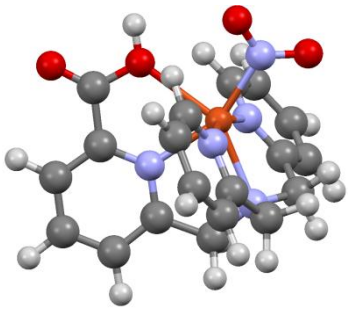

Cu	3.77412092461018	6.91765305938431	8.34027045617462
O	3.70729684321831	9.29724014373265	7.59795332891554
O	4.08154959847273	11.40748196907348	8.34886281859978
N	3.86140455412441	5.42083128486451	10.09016226399244
N	3.85368484953712	8.24844412449956	10.03484229574950
N	1.78573543461016	6.47097890647031	8.54518448879374
N	5.80265989185973	6.65374692452046	8.43983968980065
C	3.63299668209645	6.16962733839928	11.33450114887618
C	2.74303475460602	4.53840276376879	9.71335301329683
C	5.20246955894449	4.82861369375246	9.97859872280427
C	3.91109758406296	7.66446418341783	11.24503051433656
C	4.14669218371802	8.42226652534885	12.41282795975921
C	4.30852186409401	9.80893145044550	12.30999751763612
C	4.23497393360698	10.41121911646721	11.04356131703715
C	4.00943810613957	9.58967985507864	9.92914802106736
C	3.94078921230625	10.21609210534282	8.56245774385564
C	1.53656259682713	5.33300067939618	9.24121289669959
C	0.21921092624162	4.89961153485893	9.46680619049498
C	-0.84845543144385	5.65172864737811	8.95268105565268
C	-0.57346589990362	6.82774694987702	8.23635001482998
C	0.76406748047652	7.20418228295057	8.05762413762863
C	6.23601142105871	5.76337372239553	9.36604375168519
C	7.60382097390357	5.65280749784032	9.67115935504012
C	8.52753293193811	6.46249695256579	8.99327253525487
C	8.06319501275079	7.36318222329439	8.02058429214683
C	6.68559831451614	7.43011524835991	7.77717286032870
O	3.27610924748137	5.30767113653593	6.03168251346502
N	3.74927406878054	6.39991816547066	6.36458280254260
O	4.26936532979364	7.18657372328533	5.55840005538998
H	4.21427893639744	5.73840073969176	12.17916987632808
H	2.56460201768252	6.06502360124806	11.62310195519503
H	2.44012477373901	3.84440421433025	10.53012814055488
H	3.08092037572579	3.90671532584952	8.86400062598285
H	5.13547775063067	3.94235390356436	9.31198833591826
H	5.57455247487456	4.45183158024169	10.95663474965672
H	4.20104070995469	7.91861893108931	13.38966303258714
H	4.49526847263159	10.41712780340167	13.20723720849367
H	4.35584542842506	11.49447453508481	10.90316087030173
H	0.03947670460438	3.97976169151278	10.04224828954931
H	-1.88652690377142	5.32615226547939	9.11828738314576
H	-1.37801785775627	7.45233544594293	7.82333023664492
H	1.03264779676014	8.12176075450824	7.51109210814898
H	7.93533854647764	4.93223374190780	10.43368248506162
H	9.60153647306496	6.39104697325874	9.22353194417360
H	8.75090736808488	8.01215565209144	7.45984009293550
H	6.26085840780128	8.11106146637491	7.02226744755037
H	3.70280682824500	9.73284072964701	6.71499737691683

Total energy = -2948.64047176 E_h

Geometry Optimized Coordinates for [**4-H_f-NO_2**]$^+$

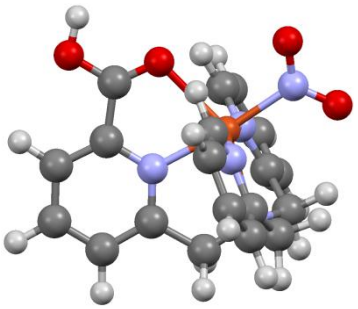

Cu	3.77412092461018	6.91765305938431	8.34027045617462
O	3.70729684321831	9.29724014373265	7.59795332891554
O	4.08154959847273	11.40748196907348	8.34886281859978
N	3.86140455412441	5.42083128486451	10.09016226399244
N	3.85368484953712	8.24844412449956	10.03484229574950
N	1.78573543461016	6.47097890647031	8.54518448879374
N	5.80265989185973	6.65374692452046	8.43983968980065
C	3.63299668209645	6.16962733839928	11.33450114887618
C	2.74303475460602	4.53840276376879	9.71335301329683
C	5.20246955894449	4.82861369375246	9.97859872280427
C	3.91109758406296	7.66446418341783	11.24503051433656
C	4.14669218371802	8.42226652534885	12.41282795975921
C	4.30852186409401	9.80893145044550	12.30999751763612
C	4.23497393360698	10.41121911646721	11.04356131703715
C	4.00943810613957	9.58967985507864	9.92914802106736
C	3.94078921230625	10.21609210534282	8.56245774385564
C	1.53656259682713	5.33300067939618	9.24121289669959
C	0.21921092624162	4.89961153485893	9.46680619049498
C	-0.84845543144385	5.65172864737811	8.95268105565268
C	-0.57346589990362	6.82774694987702	8.23635001482998
C	0.76406748047652	7.20418228295057	8.05762413762863
C	6.23601142105871	5.76337372239553	9.36604375168519
C	7.60382097390357	5.65280749784032	9.67115935504012
C	8.52753293193811	6.46249695256579	8.99327253525487
C	8.06319501275079	7.36318222329439	8.02058429214683
C	6.68559831451614	7.43011524835991	7.77717286032870
O	3.27610924748137	5.30767113653593	6.03168251346502
N	3.74927406878054	6.39991816547066	6.36458280254260
O	4.26936532979364	7.18657372328533	5.55840005538998
H	4.21427893639744	5.73840073969176	12.17916987632808
H	2.56460201768252	6.06502360124806	11.62310195519503
H	2.44012477373901	3.84440421433025	10.53012814055488
H	3.08092037572579	3.90671532584952	8.86400062598285
H	5.13547775063067	3.94235390356436	9.31198833591826
H	5.57455247487456	4.45183158024169	10.95663474965672
H	4.20104070995469	7.91861893108931	13.38966303258714
H	4.49526847263159	10.41712780340167	13.20723720849367
H	4.35584542842506	11.49447453508481	10.90316087030173
H	0.03947670460438	3.97976169151278	10.04224828954931
H	-1.88652690377142	5.32615226547939	9.11828738314576
H	-1.37801785775627	7.45233544594293	7.82333023664492
H	1.03264779676014	8.12176075450824	7.51109210814898
H	7.93533854647764	4.93223374190780	10.43368248506162
H	9.60153647306496	6.39104697325874	9.22353194417360
H	8.75090736808488	8.01215565209144	7.45984009293550
H	6.26085840780128	8.11106146637491	7.02226744755037
H	3.70280682824500	9.73284072964701	6.71499737691683

Total energy = -2948.64477513 E_h

Geometry Optimized Coordinates for [$Cu^{I}H_{c}$-NO_2]

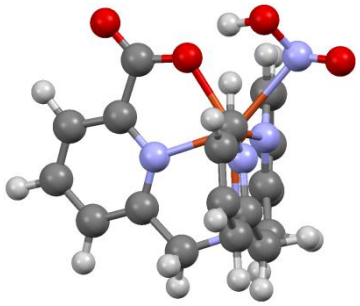

Cu	3.96286269039093	7.05588426936271	8.36344334969348
O	3.72592259912090	9.11881164019711	7.72596815807839
O	3.42956369845638	11.25529167352872	8.46544412879668
N	4.06950352962710	5.35699817676304	10.30740769745248
N	3.84227474123336	8.16665483722262	10.20643966096584
N	2.04437687272728	6.38009874168490	8.48414984269870
N	5.85934412879011	6.42941072812418	8.25057569682374
C	4.28700946000752	6.14235577448843	11.51450884510351
C	2.76066015787577	4.73451381311557	10.17324852049495
C	5.22379668974186	4.62372036395005	9.80028616334750
C	3.84180648231787	7.60403379629742	11.42776615182954
C	3.52163087218896	8.35111452918385	12.57657196910080
C	3.22414888680514	9.71791104330137	12.43609786630118
C	3.24943598415348	10.29557285919348	11.15829965097666
C	3.55276444945753	9.47693183862146	10.05715303044758
C	3.56905661895527	10.04022781285987	8.62510777638383
C	1.67659211763533	5.60001961664257	9.53147157818711
C	0.33680651510739	5.50669884956324	9.94479052183632
C	-0.65297601689239	6.21526266386756	9.24532768817044
C	-0.26703325570753	6.99845631850104	8.14552731868261
C	1.09067672982341	7.05780294740768	7.80570402810698
C	6.28688728539258	5.50239207739042	9.15199403803157
C	7.65258093714011	5.30468075508133	9.41170021523905
C	8.60935530527267	6.05606344669233	8.70988428306633
C	8.16119863747154	6.98489508134959	7.75822168381147
C	6.78260789944457	7.14346448799151	7.56338922239579
O	4.20958846204457	6.10861601245047	5.14259503282883
N	3.85377213880095	7.01796154675171	5.84076363119507
O	4.47354190160121	8.23010458384499	5.50515322097142
H	5.37929447304890	6.15238366624685	11.72587581500409
H	3.80736238177512	5.66751382898256	12.40610804351786
H	2.37769371950267	4.35467423148826	11.15185726025430
H	2.87589092831754	3.84126254561890	9.52014732247616
H	4.85605068905126	3.93156627839647	9.01182311846028
H	5.71798933636838	3.98546130773224	10.57655337392922
H	3.50977983455676	7.86877186626251	13.56710685905643
H	2.97025871519112	10.32246763945351	13.32090897933521
H	3.03383080291937	11.35695814235088	10.96852823829272
H	0.07545241733910	4.87512422094138	10.80859513723278
H	-1.70734967263598	6.15931268841276	9.55708331393863
H	-1.00300141941215	7.56795636806903	7.55936225819214
H	1.45637187979480	7.67299560197428	6.96787637721630
H	7.95869872947711	4.55319026466175	10.15630224865561
H	9.68413919860992	5.91482755343542	8.90191197360835
H	8.86544061795854	7.58982799989351	7.16852597101675
H	6.38248520085399	7.85256612497954	6.81845491418056
H	4.13005920329965	8.83517259667089	6.27187635061469

Total energy = -2948.78512718 E_h

Geometry Optimized Coordinates for [$Cu^{I}H_{f}$-NO_2]

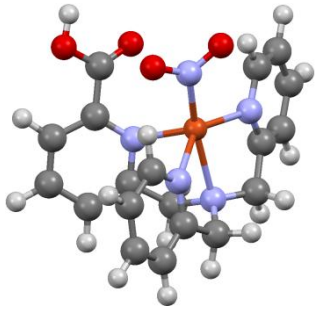

Cu	3.60460330251767	6.91156005565482	8.35897887412370
O	2.15770551504425	9.88661661911764	8.20241392367164
O	3.79618795126904	11.45305366122544	8.30247126619340
N	3.73247258448074	5.35673209518412	10.19416949694942
N	3.65627350647640	8.28460022299498	9.96802151876725
N	1.77329423471524	5.89526035312802	8.22622194856728
N	5.75386029648218	6.46137309489596	8.55795154586740
C	3.59286736525814	6.27107532897016	11.33787334845731
C	2.58964804751173	4.45064948428979	10.02035271275626
C	5.04469572660638	4.71038340976284	10.10925660662826
C	4.13829318768560	7.66849535789514	11.07816377905468
C	5.00860832198405	8.31131207995631	11.97215403481514
C	5.40727308711671	9.63479909248708	11.70865046938955
C	4.87526548487627	10.28752695948797	10.58802680756826
C	3.97474310573042	9.58848558233380	9.75903878959869
C	3.21639673659199	10.28526923938222	8.66576855998554
C	1.43567232334715	5.11322263587258	9.28427959460906
C	0.09525887751369	4.86491533906819	9.62620340333111
C	-0.92778575789248	5.41636329881419	8.83695902921460
C	-0.57286545589049	6.20166663649040	7.72636942764348
C	0.78678726868822	6.42016810176385	7.46217609116590
C	6.12278831511178	5.63075794041325	9.56187345925351
C	7.44786259389873	5.56740972852778	10.02962011119597
C	8.42495683000986	6.37653910228461	9.42937644489142
C	8.03885940283099	7.23584406973779	8.38745937009393
C	6.69277184459320	7.25196442550099	7.99277286237821
O	3.05118728524931	7.60373682249312	5.56085951369266
N	3.71171318765497	7.94232956580674	6.57723151980928
O	4.51737511566642	8.90643256588386	6.44943021946184
H	4.04852745903156	5.85018229984763	12.26360294675743
H	2.50750298121425	6.39082176994131	11.53934530815305
H	2.22778672685122	4.01180953301460	10.97878683164312
H	2.93344825329405	3.59686412792997	9.39769815253917
H	4.95007631338150	3.85483287141723	9.40600523997660
H	5.37850597924941	4.28539448238032	11.08528809582794
H	5.36583968499499	7.78063467299487	12.86720396149537
H	6.10705050411646	10.15436480801638	12.38053050010655
H	5.12519245350495	11.33331979148241	10.36454604511358
H	-0.13866330865021	4.23984118704242	10.50194337317002
H	-1.98457973472481	5.23572615780997	9.08694761828395
H	-1.33703413425809	6.64494491114061	7.07085874713973
H	1.13566397370539	7.02720008602940	6.60981363025687
H	7.70410197424416	4.88615341129031	10.85592616556515
H	9.46864531846014	6.34471073916557	9.77829518590866
H	8.76516620767518	7.89460703210332	7.88843919400508
H	6.32390278701337	7.93589958400683	7.20865180062667
H	3.21413535776832	11.86233640096311	7.62327126729635

Total energy = -2948.77898676 E_h

Geometry Optimized Coordinates for $[Cu^{I}\text{-}NO_2]^-$

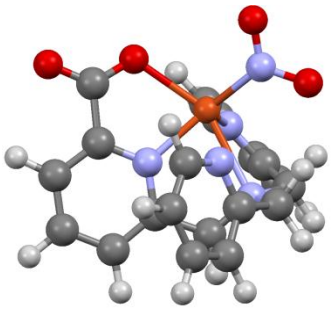

Cu	3.13831428282906	7.23449339161025	7.88339596290869
O	2.86225291136756	9.40139080364186	7.27118811029543
O	3.59191317078551	11.45508935005999	7.90788580703768
N	3.83740300664216	5.46460762369298	9.53282099231451
N	3.83715485842830	8.26234393923082	9.50860198851965
N	1.33908208063434	6.53142273894211	8.59038566008049
N	6.46273684366869	6.61565641172526	8.19656802700069
C	3.83812352535873	6.17199014453275	10.80604316891841
H	4.51874785522333	5.70920039121029	11.55978562012923
H	2.82069953789765	6.10163789040984	11.25135464492549
C	2.68512572470853	4.60133366700458	9.27118484422892
H	2.60992312212823	3.72977363561549	9.97070413270932
H	2.83737436614654	4.20736084960747	8.24051337918500
C	5.10689098680956	4.82169100204114	9.16705504880573
H	4.98522934687246	4.48485464115594	8.11707783166342
H	5.31125052319362	3.93194876208270	9.81853860897026
C	4.14856608324083	7.66532993754190	10.68134530908831
C	4.63506458408808	8.40616998215386	11.77326382365225
H	4.89660532946479	7.89260369678863	12.71195802977950
C	4.77527968194954	9.80007470657277	11.65064360761186
H	5.15941992117157	10.39737473718540	12.49252223157592
C	4.40273658597124	10.41193826118298	10.44264004288144
H	4.46556896431466	11.49829187266861	10.28300491788912
C	3.92640391907259	9.60996259674350	9.39215528939945
C	3.42732546437706	10.21740328610501	8.07183589497236
C	1.36527669078764	5.35269793095680	9.26851212958904
C	0.21296745232650	4.84328824507558	9.89342947643114
H	0.26785890738190	3.89155399146160	10.44369117694435
C	-0.99527524161873	5.55659845207150	9.80472972713194
H	-1.90834070094501	5.17019859624712	10.28267998432037
C	-1.00994648257803	6.77508707246397	9.10573575300183
H	-1.92860827540292	7.37410738554082	9.01668701935589
C	0.18259322988503	7.22631004823872	8.52197603034445
H	0.23215459260207	8.18387517371424	7.97785569564528
C	6.31028667044331	5.74850852394817	9.22229276620765
C	7.23596005760260	5.67904568770888	10.28601537759817
H	7.09193191176235	4.94768521943959	11.09725185114308
C	8.34046865023692	6.54672307884698	10.29445792154531
H	9.07615353519963	6.50890077071649	11.11392261692179
C	8.48440602185944	7.46009674356782	9.23879188964418
H	9.33226314319720	8.16160940167096	9.19735647693676
C	7.51712077697190	7.44702912021728	8.21659123150448
H	7.60769048760289	8.14282986985696	7.36168505376886
O	3.73914744494979	5.01793731499516	6.20845822313127
N	3.61861795813630	6.28806987840608	6.22448587478660
O	3.61014049325457	6.86306317534916	5.10553074950448

Total energy = -2948.31647908 E_h

Geometry Optimized Coordinates for [**Cu^{I}-ONO**]$^{-}$

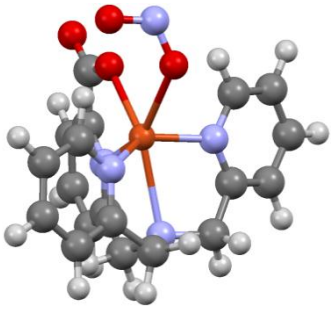

Cu	4.29811033531996	7.27520460566712	8.14739940427821
O	3.89624927617382	9.38616721917197	7.58124440942029
O	3.22572195621963	11.39407711943228	8.40090997561893
N	4.38592309311415	5.52288387341475	10.09208520108051
N	4.05905481448012	8.32628256021009	10.03415138996186
N	2.41645405439003	6.48521053911516	8.18382308741538
N	6.13815587030461	6.47721214251669	7.97578690101822
C	4.66039354994155	6.31216810062571	11.28284988613981
C	3.05408497028675	4.94149563824813	10.01207885064184
C	5.50336650361538	4.73231954652581	9.59564499705486
C	4.08155781370316	7.72125946377461	11.23949911686165
C	3.64769997212162	8.38059620061856	12.40537832851045
C	3.19699990490988	9.70873332056105	12.31077172355120
C	3.18077465420486	10.32874809873376	11.05176273903326
C	3.61024196829088	9.59657452555889	9.93081970015819
C	3.57516659249124	10.18981208964109	8.51487790917860
C	2.00546070550128	5.76153482547794	9.25687406078762
C	0.64455172097276	5.67011055433430	9.60360736636798
C	-0.31816487902514	6.31514723526228	8.81071213086588
C	0.11322484017454	7.03081685295572	7.67862756430418
C	1.48557595359987	7.09128409208286	7.40622775992581
C	6.56959622328877	5.54684210441287	8.87154487755726
C	7.93643701667435	5.26657720392452	9.04352680682140
C	8.88656827528475	5.93555335486872	8.25314587647902
C	8.42781515317370	6.85119933130309	7.29019401250536
C	7.04996785538706	7.09075639035427	7.17870771467615
O	4.14956598201838	7.20843567118613	5.62579084917147
H	5.76351750741339	6.41650526673364	11.38013790588182
H	4.31319166148324	5.80396241485529	12.21671769420456
H	2.65036528744257	4.69544138433764	11.02301435569476
H	3.13157183122095	3.96789734016136	9.47893253158674
H	5.09805528273174	4.00928345507072	8.85430570125660
H	5.99925473238929	4.11988625693221	10.38967548131193
H	3.66705963020322	7.85619832269915	13.37383054303208
H	2.85409479273262	10.24570463299840	13.20896126091828
H	2.83438742493124	11.36118134538456	10.90233872088284
H	0.34603311843872	5.08815337560333	10.49010749621111
H	-1.38678999439785	6.25837539217519	9.07081820058810
H	-0.60249494395343	7.53951756477225	7.01532968778861
H	1.89803177517162	7.62777538629213	6.53630634463081
H	8.24685722915587	4.51645929214094	9.78794380832481
H	9.96202597797501	5.73423785768867	8.37879704670244
H	9.12868923870183	7.37758597570309	6.62396047764673
H	6.61676410479425	7.75235560963796	6.39779191993039
N	4.35956891159884	8.14060200399969	4.78697080822661
O	5.51234844634892	8.66223714983533	4.79027441079529

Total energy = -2948.30740048 E_h

B.2 Natural transition orbitals described in Chapter 4

When expressed in terms of canonical molecular orbitals, a particular electronic excitation often has contributions from many transitions between filled and vacant MOs. NTO analysis transforms the transitions between canonical MOs into transitions between pairs of donor/acceptor NTOs that maximally account for the excitation (by diagonalizing the transition density matrix). Very often, a single NTO pair is sufficient to characterize an excitation in terms of its orbital character.

Table S1 lists the MO transitions contributing significantly to S_1 of complex **2** and S_2 of complex **3**; the dominant NTOs are presented in the main text.

Table S1. MO transitions with >10% weight contributing to the relevant excitations of complexes **2** and **3**; H = HOMO, L = LUMO.

Complex **2**	Donor MO	Acceptor MO	Weight	Complex **3**	Donor MO	Acceptor MO	Weight
S_1	H	L + 7	26%	S_2	H	L + 4	30%
	H	L + 3	25%		H – 9	L + 4	10%
	H – 5	L + 7	13%		H	L + 6	9%
	H – 5	L + 3	10%		H – 18	L + 4	7%
					H – 7	L + 4	5%

Axis system: The complex has C_2 symmetry; by convention, the *z*-axis is taken along the C_2 axis (*i.e.*, bisecting X–Co–X, X = O or S). However, it is more convenient here to define *z* along the *trans* N–Co–N axis, with *y* along the C_2 axis. Note that with this choice, the *x*- and *y*-axes do not coincide with Co–L bonds, but bisect them; the lobes of the d_{xy} orbital therefore point towards the ligands and the d_{x2-y2} lobes point in-between.

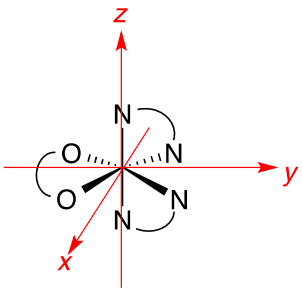

Linear fit of solvatochromic trend: The experimental excitation energies of complex **2** were used to fit a linear model of the form

$$\Delta E_{pred} = a + b\, f_O(\varepsilon) + c\, \alpha$$

which predicts the excitation energy, ΔE_{pred}, as a linear function of the Onsager function $f_O(\varepsilon) = (\varepsilon - 1)/(2\varepsilon + 1)$ and the Kamlet–Taft hydrogen-bonding strength parameter α. The fit parameters a, b, c were determined using the LinearModelFit function in *Mathematica* v. 10.3.1; quality of fit: $R^2 = 0.771$; Adjusted $R^2 = 0.694$.

B.3 Geometry optimization for molecules presented in Chapter 5

Table S1. Geometry Optimized Coordinates for $[Co^{III,III}_2(bdt)_2(Me_2bpy)_3]^{2+}$

Co	3.61899346119338	15.90726059976303	8.31231950541295
Co	6.23341988657192	17.34313766711827	6.60197370641610
S	4.55720566189833	15.80116403769830	6.28194666261943
S	5.23699206287823	17.41182566329741	8.67634691276545
S	2.21080340590054	17.63771690748266	7.80147162542675
S	4.88220845156091	14.09918523581835	8.92173346160170
N	2.90117664397900	15.85290092439353	10.13524747981487
N	5.13347067495755	18.80378105292830	5.88469202766038
N	7.47516710753037	18.84873571003959	7.01768989265288
N	2.09640124917064	14.72839976932640	7.94366558981507
N	7.06370200887420	16.98441801611920	4.82618642180616
N	7.53699354316524	15.99764763960575	7.18534185733393
C	8.30868080458708	15.48686721447891	6.17968895070585
C	1.32863689122513	14.45618010340736	9.03436680776577
C	6.99527052684614	20.07004445404711	6.66549677194113
C	8.03274110298449	16.03261885912571	4.85522393988345
C	3.42494687130051	16.44854163665736	11.22216385998768
H	4.33126909708044	17.03319775059662	11.06313664877911
C	1.78876912672188	15.07991126214599	10.27135392874491
C	2.87254008033982	16.33774153986289	12.50215548267862
C	5.68829384734796	20.04554687792828	6.01773842314422
C	6.74638474158586	17.55671072930949	3.64899881702236
H	5.95879552297743	18.30739477033191	3.66717740398010
C	4.33363436626188	21.23944327920996	9.66798258811733
H	4.83606718059951	22.09107569044768	10.12755745782306
C	5.59018249265124	13.61615313853699	4.95161346068051
H	5.45119937401329	14.20345039402216	4.04218504220692
C	2.33231760967382	20.24111999655431	8.71086663875176
H	1.28197873941151	20.32224982499428	8.42543818040002
C	1.17730891720142	14.92265379829939	11.51958063620504
H	0.28556567602779	14.30552659034895	11.61712099378272
C	3.24829383049003	19.77951835194339	4.71534116286522
C	7.73706175341354	21.23125401023651	6.91042649223751
H	7.33916052165746	22.20350325585101	6.62682469644637
C	0.19380527708626	13.64569840664213	8.92453133585755
H	-0.41165731199933	13.43410263420523	9.80426951508526
C	5.35162166602649	13.40879131206745	7.38477773780481
C	8.36258048403892	16.24586205722181	2.47718578834325
H	8.87644172559010	15.94717080040138	1.56258382366571
C	3.81905119658155	21.04745409692451	4.87075461091251
H	3.31582709121456	21.93046370344923	4.47450841713569
C	7.36356219641629	17.23024241416545	2.43809372152776
C	8.69634622611561	15.64844670534927	3.68428268782739
H	9.47001902447158	14.88321073367625	3.71903928060397

C	4.36737731888685	18.94419890993852	8.89910095087296
C	2.99074378080747	21.33353903591303	9.27353188753064
H	2.44515162922907	22.26736476519132	9.42088434340312
C	3.01045976097091	19.02066833967950	8.51466250526246
C	5.04415515783440	21.17828194897253	5.51562226241702
H	5.50749294639076	22.15772194924254	5.61826489717751
C	9.30802792335911	14.54883569221823	6.44736634859335
H	9.92233409934603	14.16177317355340	5.63699200465729
C	1.73733290589706	14.23021032508543	6.74644727514314
H	2.36892494411999	14.50354619430429	5.90053979845111
C	-0.15870153782631	13.12101898492657	7.68793019098084
H	-1.04404146473654	12.48974505817101	7.59734751061228
C	5.87558530207805	12.10259941511448	7.29552107249897
H	5.97527197685613	11.50252964417670	8.20185065762808
C	3.95629941175745	18.68910766764587	5.23846726812996
H	3.57059748588395	17.68071640077714	5.10712321964442
C	1.71650577682884	15.55349150696244	12.63309711484438
H	1.24424895021334	15.43106142739236	13.60893177357329
C	0.61769168797150	13.41435569847599	6.55634277450258
C	9.52634723279291	14.12468496468141	7.75388588363583
H	10.30895262111979	13.39453943985398	7.96595092517925
C	5.02126647185397	20.04056175608745	9.48208232518369
H	6.06079146547633	19.94388213557587	9.79971449072615
C	5.22711720843808	14.15891543594415	6.19405259850509
C	6.10910162377376	12.32342697605795	4.88442158346502
H	6.38638429538462	11.89718817790788	3.92014264071830
C	8.75305104194319	14.65280523341184	8.79305283456931
C	8.97990491570433	21.13605723547484	7.52006732064587
H	9.56024319993028	22.03886010485963	7.71471381813538
C	8.68269558341432	18.76773053800017	7.60942698837873
H	9.02670393008676	17.77206976740324	7.87969223450948
C	3.49944591375386	17.03702496798452	13.67354523547603
H	4.45825447835935	17.49608335061819	13.40330038984299
H	3.67068236408612	16.33353276086682	14.50085231937450
H	2.83443143569770	17.82850929718911	14.05161253834091
C	6.96898674942986	17.91613471769104	1.16323048514813
H	6.72119893913484	17.17892478714695	0.38622474215283
H	7.80216568057924	18.52472145542077	0.77965368684567
H	6.10293408132953	18.57371117529344	1.30888170357931
C	7.77262825386882	15.59340369897216	8.44930031420613
H	7.17240201115312	16.05876827251540	9.22747808650853
C	8.92351964713934	14.23221513570729	10.22330139502063
H	8.24445830968309	13.39610757212883	10.45548320750614
H	8.68305011521431	15.05058328564262	10.91486871231161
H	9.94901664467952	13.89322544132838	10.41704554458770
C	1.92450442553698	19.56645271218897	4.04238545597634
H	1.10986914452686	19.61511506421825	4.78296294575768
H	1.87189566794786	18.58152447337284	3.56062673383130
H	1.73514953103927	20.34164488120600	3.28894293557706
C	6.25434609043749	11.57472459807875	6.06207926786953
H	6.65500446775764	10.56089919402845	6.01580183543552
C	9.48478595975985	19.87850853058812	7.88554593795242
C	0.27517158792888	12.88507664259708	5.19381647175901
H	0.95752835952255	13.27416095877769	4.42793328595534
H	-0.75219666178762	13.16182802457402	4.91601131043741
H	0.33040531779022	11.78592792676203	5.17984431139848
C	10.82647839710323	19.71641260866221	8.53811503955495
H	11.00740356890897	18.67720936071169	8.83875613060271
H	10.90525842751167	20.35611130183858	9.42828060041100
H	11.62864663850042	20.01828628486027	7.84798043076544

Table S2. Geometry Optimized Coordinates for $[Co^{III,II}_2(bdt)_2(Me_2bpy)_3]^{1+}$

Co	3.52839390506793	15.80798856453735	8.22893019260935
Co	6.33770385871764	17.41413457052274	6.54888522320445
S	4.32542967716209	15.60736442424291	6.13808937855687
S	5.16742399816154	17.30752304029672	8.56410738194709
S	2.14619784791926	17.54618665928048	7.68289181401158
S	4.82997486317344	14.03706652767722	8.83652271685341
N	2.86363089487044	15.82523557792804	10.08634714580560
N	5.28905971349519	18.90749874686861	5.88895810044976
N	7.60451256838767	18.99281019340525	7.11658148161365
N	1.97090953436931	14.61986357863675	7.97037372197028
N	7.12285885335829	17.03129055734736	4.77252121766647
N	7.57376930935533	16.01921262541751	7.09899990446885
C	8.30803901090394	15.46190282170583	6.08792244787507
C	1.21938045892706	14.43130872888577	9.08898549041546
C	7.10449794236690	20.20408670772940	6.77054740293244
C	8.02753332197682	16.01157032376945	4.76853545584471
C	3.43404518189848	16.43603710248238	11.14159251160406
H	4.35741630567264	16.97830615463528	10.93503178815073
C	1.72875303833281	15.09900245888219	10.28341866942972
C	2.91161119709482	16.39200263603463	12.43818551039499
C	5.81782374363625	20.15568071148398	6.06969557813069
C	6.82775801934052	17.62752620602810	3.59707083342642
H	6.10600248775752	18.44179142370522	3.63893841468927
C	4.23593567316409	21.12468157718847	9.63544104673383
H	4.73500304952123	21.96807715789638	10.11490201435184
C	5.47695942999624	13.43300546348449	4.87659053915908
H	5.28949792164620	13.97300748027656	3.94620959677408
C	2.25511759071756	20.14150843922531	8.63197974494820
H	1.20909092835423	20.22575726625869	8.32968565670968
C	1.14290255527737	15.00872629921416	11.55130176892971
H	0.23436797265928	14.42557669680366	11.69191594709655
C	3.40980273865676	19.87981215152396	4.70267643349553
C	7.79741747341260	21.38557264597263	7.06948956450373
H	7.38573710128835	22.35445468946937	6.79190761711572
C	0.06072436145716	13.64670745481386	9.05284975464098
H	-0.53194161966341	13.50608083127393	9.95542111457947
C	5.30433593931389	13.31062670976765	7.30809132301219
C	8.30623884088163	16.19883169265250	2.37944197849622
H	8.76928565204920	15.86292621755064	1.45050870136582
C	3.95827738589003	21.15441802243012	4.89556658356316
H	3.44956180039995	22.03836133726062	4.50766895098351
C	7.38455341612573	17.25867139199977	2.37128418863766
C	8.62697338351871	15.57947619389598	3.57933001798551
H	9.34186556452016	14.75779861710174	3.59527859954828
C	4.28689577048633	18.83634189356202	8.82804737389280
C	2.90077630675706	21.22827632602908	9.22340953949418
H	2.35125385593382	22.15911504285338	9.37834854605826
C	2.93554015591934	18.92444098967796	8.42693697330647
C	5.16301865352190	21.28846564392332	5.57497454631993
H	5.60404239372798	22.27402935273732	5.71391156446247
C	9.27685023414066	14.48768218193858	6.34639194965653
H	9.85271312002089	14.06379472741646	5.52562966496896
C	1.57855806192783	14.04742237936088	6.81796099960938
H	2.21457435354532	14.25261167821062	5.95482911833457
C	-0.33145683698702	13.05421838937667	7.85942694899859
H	-1.23496445705746	12.44304429805703	7.82567696038595
C	5.92982813142193	12.05002388228352	7.26289996352591
H	6.10259743956358	11.50717643474279	8.19490443871565
C	4.12315911441321	18.79227874517176	5.21730826787217
H	3.75417936379133	17.77802201069633	5.07913580160352
C	1.73052965901106	15.65925038687902	12.62852600447774
H	1.27824913632761	15.59115326395425	13.61937446406664

C	0.43533126742234	13.25018677033469	6.70070667859373
C	9.51408320040991	14.07795266789397	7.65268799022881
H	10.27302648655029	13.32127582268194	7.86005944475898
C	4.92458800668827	19.92509724705410	9.43838403756433
H	5.96176254375647	19.82592278694288	9.76425908434975
C	5.08281698507370	14.00518591237833	6.09662223745352
C	6.09839790157326	12.18100652284376	4.84727519812678
H	6.39618365546601	11.74522292886027	3.89231182745308
C	8.78338952708111	14.65485739147630	8.69983972944640
C	9.01691353990336	21.31321835484510	7.73065970972463
H	9.56174147934153	22.22842812422424	7.96755385730890
C	8.78501741488547	18.93727376780194	7.75736419938555
H	9.14443076216880	17.93981867541171	8.01594628001050
C	3.59507811936186	17.11080614659554	13.56683390102003
H	4.57502989656998	17.49757690465888	13.26147117442161
H	3.73728170260881	16.44238060684914	14.42813334046441
H	2.98543162354946	17.95991890657219	13.91195488485341
C	7.00794891984678	17.97663648980685	1.10645174312075
H	6.63434080387238	17.26912847656962	0.35141440136868
H	7.88233065203296	18.48238608416863	0.66938232685996
H	6.23180369671023	18.73122138237334	1.28759445685593
C	7.82761789805683	15.61858491968398	8.36362224795245
H	7.23731804304053	16.09689860554368	9.14323716322617
C	8.98605270251985	14.25245852808308	10.13295226297138
H	8.51516765915106	13.27656808716478	10.33032175798631
H	8.54242089042614	14.98212327773275	10.82217123373777
H	10.05487786639145	14.15154485302875	10.36759086864515
C	2.10185663815578	19.66745987278827	3.99593811612203
H	1.26120510348692	19.85323058210465	4.68309701867812
H	2.00686798052307	18.63899339922640	3.62587159710985
H	1.99300181611512	20.35890781937962	3.14942943689138
C	6.32505939589254	11.49086116252935	6.04524664611442
H	6.80300351478236	10.50966286073593	6.03263566481103
C	9.54420256618400	20.06259155192429	8.09338115177462
C	0.05943610373610	12.63549906946401	5.38220087059040
H	0.74600084863259	12.94695627039965	4.58491172683553
H	-0.96146491979945	12.92473455442322	5.09248331571231
H	0.07931246832804	11.53665885667834	5.44459329142527
C	10.85977876800065	19.92747623301193	8.80650388829222
H	11.10067356069118	18.87602504358874	9.00773314158436
H	10.84301948318512	20.46710075350748	9.76478991671847
H	11.67556008002890	20.35998142422307	8.20818452901959